



Oxide and composite electron transport layers for efficient dye-sensitized solar cells

Yuly Kusumawati

► To cite this version:

Yuly Kusumawati. Oxide and composite electron transport layers for efficient dye-sensitized solar cells. Inorganic chemistry. Université Pierre et Marie Curie - Paris VI; Institut teknologi Bandung, 2015. English. NNT : 2015PA066240 . tel-01232187

HAL Id: tel-01232187

<https://theses.hal.science/tel-01232187>

Submitted on 23 Nov 2015

HAL is a multi-disciplinary open access archive for the deposit and dissemination of scientific research documents, whether they are published or not. The documents may come from teaching and research institutions in France or abroad, or from public or private research centers.

L'archive ouverte pluridisciplinaire **HAL**, est destinée au dépôt et à la diffusion de documents scientifiques de niveau recherche, publiés ou non, émanant des établissements d'enseignement et de recherche français ou étrangers, des laboratoires publics ou privés.

Université Pierre et Marie Curie
Insitut Teknologi Bandung

Ecole doctorale chimie physique et analytique (ED 388)

***OXIDE AND COMPOSITE ELECTRON TRANSPORT LAYERS
FOR EFFICIENT DYE-SENSITIZED SOLAR CELLS***

par

Yuly KUSUMAWATI

Thèse de doctorat

Présentée et soutenue publiquement le 10 Juin 2015

Devant un jury compose de:

Dr. Thierry Pauportè	Directeur de Recherche-CNRS	Directeur de thèse
Dr. M. A. Martoprawiro	Professeur – ITB	Co-directeur de these
Prof. Fabrice Goubard	Professeur Université Cergy-Pontoise	Rapporteur
Prof. Gilles Wallez	Professeur – UPMC	Examineur
Dr. Samir Farhat	Maître de Conférence – Université Paris XIII	Examineur
Prof. Dr. Ir. Akhmad Herman Yuwono, M.Phil.Eng	Professeur – UI	Rapporteur
Dr. Eng. Ferry Iskandar	Professeur – ITB	Examineur
Veinardi Suendo, Ph. D	Professur - ITB	Examineur

ACKNOWLEDGEMENT

It would not have been possible to write this doctoral thesis without the help and support of the kind people around me to only some of them it is possible to give particular mention here.

I would like to express the deepest appreciation to my supervisor in France, Dr. Thierry Pauporté, for his guidance and advice during finishing the research and writing publications in France, also for his patience to correct my thesis.

I would also like to express my sincere gratitude to my supervisors in ITB Dr. M. A. Martoprawiro, Prof. Dr. Ing. Cynthia L. Radiman and Dr. Bambang Prijamboedi. Without them I cannot pass the tricky administration that let the student to graduate. There are no words to express my grateful to Prof. Dr. Ing. Cynthia L. Radiman's patience. I would also like to thank Dr. Bambang Prijamboedi for the intense discussion and for correcting my draft.

Dr. Samir Farhat and Prof. Nouredin Jouni from *Laboratoire des Sciences des Procédés et des Matériaux*, LSPM UPR 3407, Université Paris 13, Villetaneuse, France, are acknowledged for providing ZnO nanorod-like particles and Dr. Celine Olivier from *Institut des Sciences moléculaires*, Université de Bordeaux, France is acknowledged for providing carbazole dye sensitizer.

I would like to acknowledge Prof. Dr. Djulia Onggo, the head of doctoral school chemistry, ITB, for her time and her effort in manage the academic and administration requirement. I would also like to acknowledge Prof. Dr. Ir. Triyogi Yuwono, the rector ITS (Institut Teknologi Sepuluh Nopember), Prof. Dr. Perry Burhan (Dean of Mathematics and Natural Science Faculty, ITS) and Hamzah Fansury, Ph.D (Head of Chemistry Departement, ITS), who have gave me the permission to take a study.

I would like to acknowledge the financial support from Campus France and the Higher Education Ministry of Indonesian (DIKTI) government in the framework of the DDIP collaboration program. I would also like to acknowledge Prof. Fida Madayanti Warganegara and Mrs. Tri for their effort to manage the program and DDIP's students, including me.

In addition, of course I would like to thank to all my friends in MPOE, Chimie-Paristech. Thank you Mongia for the dinner in your home, thank you Alexandra for keeping your finger crossed for me, thanks also to Jie, Ricardo, Xue, Frederic, Dora and Sana. Special

thank to all my friends the DDIP scholarship holder and my friends in computational chemistry group ITB. Big thank is addressed to Atthar for helping the calculation and Hasan for keeping the HPC work well. The last, there are no words that can describe the support of my family, my husband, my mother, my father, my sisters and my daughter.

ABSTRACT

OXIDE AND COMPOSITE ELECTRON TRANSPORT LAYERS FOR EFFICIENT DYE-SENSITIZED SOLAR CELLS

Dye-sensitized solar cell (DSSC) is built with combining many components in order to convert the solar energy to electricity. One of the DSSC components is a metal oxide semiconductor which plays the role of electron transport layer (ETL). It receives electrons from photoexcited dyes attached on its surface and ensures the electron transfer to the back contact of the solar cell. Developing the metal oxide that fulfills the requirements as an ETL is one of the effort to increase the DSSC power conversion efficiency. Three kinds of ETL have been developed and studied in this present work as a photoelectrode in DSSC. Those composed of (1) two kinds of TiO_2 -brookite nanoparticles, ($\text{TiO}_2\text{-B1}$ and $\text{TiO}_2\text{-B2}$), (2) the composite of anatase and graphene ($\text{TiO}_2\text{-Gr}$) and (3) the nanorods like ZnO nanoparticles (ZnO-NR), respectively. All photoelectrode are prepared by doctor blading technique. The morphology of photoelectrodes have been characterized using transmission electron microscopy (TEM) and scanning electron microscopy (SEM). The layer thicknesses were measured using profilometry. For the film structural characterizations, a high-resolution X-ray diffractometer was used. The Fourier transform infrared (FTIR) and micro Raman measurement have been carried out to verify the $\text{TiO}_2\text{-Gr}$ composite preparation. The optical film properties (total transmission and total reflection) were recorded with a spectrophotometer equipped with an integrating sphere techniques. The cell performances were obtained by measuring the I-V curves of the cells under calibrated illumination. To achieve an in-deep understanding of the cell functioning, the impedance spectroscopy (IS) technique has been studied over a large applied potential range. By doing IS study, the electronic structure, charge carrier lifetime (τ_n), transport/collection time (τ_{tr}) and electron transport parameters of the layers have been determined.

The IS study of brookite-based photoelectrode has revealed that, compared to anatase, the brookite surface is less active for the recombination side reaction. A large charge transfer resistance, R_{ct} , is shown which explains the high open circuit voltage of the brookite cells. However, the charge transport is much slower in the brookite phase due to a lower electrical conductivity. The computational study that has been performed, are in excellent agreement with the experimental results.

The incorporation of 1.2 wt% of graphene into TiO₂ photoelectrode led to an increase in conductivity by 60%. This increase induced a faster electron transport in photoelectrode. Moreover, the addition of graphene provoked the improvement in sensitized-layer sensitization and light absorbance. Both improvements resulted in a J_{sc} enlargement which is promising to apply in cobalt-based DSSCs. The composite of anatase and graphene, TiO₂_Gr12 photoelectrode, that was sensitized by the Z907 and was coupled with [Co(phen)₃]^{2+/3+}, showed better cell performance compared to that the one coupled with I₃⁻/I redox couple. This cell had performances comparable to the TiO₂_A (as reference cell composed of pure anatase) photoelectrode that was sensitized using the Z907 and was coupled with I₃⁻/I. The ZnO_NR showed good cell performances. D149 sensitized ZnO_NR cell coupled with I₃⁻/I redox-couple had Power Conversion Efficiency (PCE) of 4.82%. The TG6 sensitized ZnO-NR cell showed the best ZnO-based DSSC performances and reached a PCE of 5.3%. We observed that, the outstanding properties of ZnO_NR lie in their large pores size that facilitates more dye to attach to their surface upon the sensitization process. Their advantages then become an interesting point to apply this photoelectrode in cobalt-based DSSC. The cobalt redox-couple species have bulky structures, they need large pores in order to transport through the photoelectrode. Our test employing carbazole dyes as the sensitizer revealed that the ZnO_NR photoelectrode has good performances with cobalt-based redox-couple compared to that triiodide/iodide one. The computational studies have been carried out to investigate the electronic properties of utilized dye sensitizers which are important to support the cell performances explanation.

Briefly, all ETLs that have been developed in the present work have promising properties to be applied as photoelectrode in DSSC. The carefully study of their properties has revealed not only their advantages but also their limitation. This information will be beneficial as a consideration for the future work.

Keywords: Dye-sensitized solar cell, electron transport layer, photoelectrode, TiO₂, ZnO, graphene, impedance spectroscopy

Table of Contents

ACKNOWLEDGEMENT	i
ABSTRACT	iv
Table of Contents	vii
List of Figures	viii
List of Tables.....	xiix
List of Appendix.....	xiii
List of the Important Abbreviations and Symbols	iv
Chapter I: Introduction	1
I.1. Background	1
I.1.1. Solar Energy as an Alternative of Renewable Energy	1
I.1.2. Dye-sensitized solar cells: towards iodine free devices.....	3
I.2. Objectives	6
I.3. Research Approach	6
1.3.1. TiO ₂ Brookite Based DSSC	6
1.3.2. TiO ₂ /graphene Based DSSC.....	7
1.3.3. ZnO_NR Based DSSC..	7
1.4. Thesis Organization.....	7
References	9
Web References:	10
Chapter II: Literature Review.....	11
II. 1. Fundamental of DSSC	11
II. 1.1. DSSC Component.....	11
II. 1.2. Electron Transport in DSSC	27
II.1.3 Basic Principle in Cell Characterization.....	34
II.2 Theoretical Background in Computational Methods.....	40
II.2.1 Quantum Chemistry	40
II.2.2 Density Functional Theory	42
II.2.3 Models in Computational Chemistry.....	44
II.2.5 TDDFT	50
References	51
Chapter III: Research Methods	60
III.1. Synthesis of particles for the photoanodes	61
III. 2. Cell Preparation.....	63
III.3. Characterizations	68
III.4. Computational Details.....	69

References	70
Chapter IV: TiO ₂ -Based DSSC I: Comparison of Anatase and Brookite-Based Dye-Sensitized Solar Cells.....	72
IV. 1. Introduction	72
IV.2 Characteristics of the particles	72
IV. 3. Cell Performance and Impedance Study	76
IV.3.1. I-V Measurement Result	76
IV.3.2 Analysis of the open circuit voltage.....	78
IV.3.3. Analysis of charge transport and recombination in the photoelectrodes	82
IV.4 Computational Study: Comparison of adsorption of Iodine (I ₂) on Anatase (101) and Brookite (210) planes	86
IV. 5 SUMMARY	93
References	94
Chapter V: TiO ₂ -Based DSSC II: The Effect of Graphene Incorporation in TiO ₂ /graphene for Photoelectrode	96
V. 1. Introduction	96
V.2 Composite TiO ₂ /Graphene (TiO ₂ _Gr) Preparation	99
V.3 The cell performance of TiO ₂ /Gr in iodine based DSSCs: The investigation of graphene's role in TiO ₂ photoelectrode.....	105
V.4 The cell performance of TiO ₂ /Gr in cobalt based DSSC	115
V. 5 SUMMARY	122
References	123
Chapter VI: ZnO Nanorod Based Electron Transport Layer for DSSC.....	127
VI. 1. Introduction	127
VI. 2. Particle Characterization ZnO_NR	129
VI. 3. Utilization ZnO_NR for the comparison of the performance of an organic and an inorganic sensitizer.....	131
IV. 4. Impedance Study D149- and TG6-sensitized ZnO_NR cell.....	133
IV. 5. Computational investigation of the electronic and optical properties in D149 and TG6 dyes	138
VI. 6. Use of photoelectrode ZnO_NR for iodine free DSSC.....	142
VI. 7. Computational investigation of the electronic and optical properties of SD4, JM131 and JM164 dyes.....	150
VI.8 SUMMARY	157
References	157
Chapter VII: General Conclusions and Suggestions for Future Works	160
List of Publications, Seminars and Workshop	164
Appendix.....	166

List of Figures

Figure 1.1:	Consumption of the fossil fuel in the world from 1965 to 2030	1
Figure 1.2:	Average annual global solar radiation.....	2
Figure 1.3:	Some applications of solar cells	3
Figure 1.4:	Total installed PVs capacity in the world.....	4
Figure 1.5:	Number of papers on DSSC published since their discovery.....	5
Figure 1.6:	Two DSSC panels installations in Switzerland.	5
Figure 1.7:	Thesis organization	9
Figure 2.1:	Schematic diagram of DSSC using I_3^-/I redox-couple	12
Figure 2.2:	Molecular structures of the dyes, popular in the DSSC literature.	13
Figure 2.3:	D- π -A systems in organic sensitizer SD1.....	14
Figure 2.4:	Normalized dye absorbance of individual D131, D149 and D205 dyes and of equimolar dye mixtures.....	16
Figure 2.5:	J-V curves and IPCE curves of ZnO DSSCs sensitized with D131, D149 and D131/D149	16
Figure 2.6:	Energy diagram schematic of insulator, semiconductor and metal	20
Figure 2.7:	Energy diagram of several semiconductors together with potential redox of several redox-couples	21
Figure 2.8:	Crystal structure of rutile, anatase and brookite.....	22
Figure 2.9:	Wurtzite ZnO crystal structure, consisting of a (2x2x2) unit cell.	24
Figure 2.10:	Simulation of optical absorption of N749 dye attached on TiO ₂ surface	29
Figure 2.11:	Various traps location in the semiconductor.	30
Figure 2.12:	<i>I-V</i> curves of a cell A with $FF = 0.46$; and a cell B with $FF = 0.67$. <i>P-V</i> curve of cell B	35
Figure 2.13:	Air Mass calculation	36
Figure 2.14:	Typical Nyquist plot of electro impedance spectra	37
Figure 2.15:	Electrical equivalent circuit of typical DSSC.....	38
Figure 2.16:	Examples of a unit cell for calculations using periodic boundary conditions for system x that contains one unit cell, a crystal surface that has a high lattice parameter in one of direction and a supercell	47
Figure 2.17:	All electron (AE) and pseudopotential (PP) wave functions for Au at $l=2$. r_c is the radius cutoff in a. u.....	48
Figure 3.1:	Hydrothermal reactor used for TiO ₂ nanoparticles preparation.	62
Figure 3.2:	Ultrasonic horn to prepare TiO ₂ and ZnO paste.....	63
Figure 3.3:	Scheme of doctor blade technique layer deposition	65
Figure 3.4:	Oxide-layer deposition on FTO glass using doctor-blade technique	65

Figure 3.5:	Scheme of sealed cell cross-section and picture of sealed cell that has been prepared.....	67
Figure 4.1:	TEM images of particle B1 and B2	73
Figure 4.2:	Size distribution of the brookite nanoparticles B1 and B2.....	73
Figure 4.3:	XRD pattern of B1; B2 and Brookite standard	74
Figure 4.4:	XRD patterns of Dyesol and Anatase standard	74
Figure 4.5:	Absorbance spectra of sensitized layer of Dyesol; B1; B2 with immersion time 24 hours and Dyesol with immersion time 4 hours	75
Figure 4.6:	I-V curves of TiO ₂ _B1, TiO ₂ _B2 and TiO ₂ _D under 100 mW.cm ⁻² , AM 1.5G filtered illumination.....	77
Figure 4.7:	IPCE action spectra of brookite TiO ₂ _B1 and TiO ₂ _B2 solar cells and of the TiO ₂ _D reference cell.	77
Figure 4.8:	Typical impedance spectra in the dark of B1 brookite cell polarized at 0.775 and effect of applied voltage on the impedance spectra of TiO ₂ _B1 solar cell in the dark.	79
Figure 4.9:	Variation of C_{μ} with V_{cor} for TiO ₂ _B1 and TiO ₂ _B2 brookite solar cells and TiO ₂ _D anatase solar cells.	79
Figure 4.10:	Variation of R_{ct} with V_{cor} for TiO ₂ _B1, TiO ₂ _B2 and TiO ₂ _D solar cells.....	81
Figure 4.11:	Plot of R_{ct} versus V_{ecb} , TiO ₂ _B1, TiO ₂ _B2 and TiO ₂ _D, the applied voltage corrected of the shift due to different conduction band energy level	82
Figure 4.12:	Effect of the phase and particle size on the charge carrier lifetime τ_n and τ_{tr} versus g	83
Figure 4.13:	Effect of photoelectrode TiO ₂ crystal phase on R_{tr} as a function of the corrected applied voltage, TiO ₂ _B1, TiO ₂ _B2 and TiO ₂ _D	83
Figure 4.14:	Effect of photoelectrode TiO ₂ crystal phase on the charge collection efficiency	84
Figure 4.15:	Effect of photoelectrode TiO ₂ crystal phase on the electronic conductivity as a function of the electron concentration, g	85
Figure 4.16:	Effect of photoelectrode TiO ₂ crystal phase on D_n parameter	85
Figure 4.17:	Mean diffusion length of electrons, L_n , in mesoporous brookite TiO ₂ films measured by IS.	86
Figure 4.18:	Optimized geometry of adsorbed iodine on anatase and brookite surface	88
Figure 4.19:	DOS of bare anatase (101) bare brookite (210)	90
Figure 4.20:	LDOS of Ti-61, Ti-85, Ti-2 and Ti-62 on anatase	90
Figure 4.21:	PDOS of anatase/I ₂ and brookite/I ₂	91
Figure 4.22:	The LDOS of Ti-61 3d and I-97 5p in anatase/I ₂ system, LDOS of Ti-82 Ti 3d and I-97 5p in brookite/I ₂ system	91
Figure 5.1:	The Schemes of the carbon allotrope; Graphene, fullerene carbon nanotube, graphite.....	96
Figure 5.2:	FTIR Spectra of SGO, ethycellulose, TiO ₂ _Gr before heat treatment, TiO ₂ _Gr after heat treatment, TiO ₂ _A after heat treatment	100
Figure 5.3:	Zoom out of FTIR Spectra of TiO ₂ _Gr after heat treatment and TiO ₂ _A after heat treatment from 950 to 1150 cm ⁻¹	100
Figure 5.4:	The raman spectra of TiO ₂ _Gr layer	101
Figure 5.5:	SEM Image of TiO ₂ _A and TiO ₂ _Gr12.	102

Figure 5.6:	X-ray diffractogram of TiO ₂ _A and TiO ₂ _Gr12	103
Figure 5.7:	BET Isotherm curve	103
Figure 5.8:	Transmission spectra of TiO ₂ _A, TiO ₂ _Gr06, TiO ₂ _Gr12 and TiO ₂ _Gr30	104
Figure 5.9:	Absorbance spectra of N719 sensitized on TiO ₂ _A, TiO ₂ _Gr06 and TiO ₂ _Gr12	105
Figure 5.10:	Dark current of FTO without TiCl ₄ treatment, one, two and three preliminary TiCl ₄ treatment	106
Figure 5.11:	IV-curves of various times TiCl ₄ treatment once, twice and three times	106
Figure 5.12:	I-V curves of TiO ₂ _A, TiO ₂ _Gr06, TiO ₂ _Gr12, TiO ₂ _Gr30	107
Figure 5.13:	The I-V parameters plot as function of SGO content: η , J_{sc} , V_{oc} and FF	108
Figure 5.16:	IS Spectra of TiO ₂ _A and TiO ₂ _Gr12 at V_{oc} and TiO ₂ at 0.75 V	109
Figure 5.17:	Variation of R_{ct} and C_{μ} with the corrected applied voltage.	110
Figure 5.18:	DOS distribution of TiO ₂ _A cell and TiO ₂ _Gr12	111
Figure 5.19:	Variation of τ_n and τ_{tr} with the corrected applied voltage of TiO ₂ _A and TiO ₂ _Gr12 cell	112
Figure 5.20:	Effect of graphene on the variation of D_n with the corrected applied voltage	112
Figure 5.21:	Effect of graphene on the variation of L_n with the corrected applied voltage	113
Figure 5.22:	Effect of graphene on layer conductivity as function of g	114
Figure: 5.23	Effect of graphene on η_{coll}	114
Figure 5.24:	IPCE spectra of TiO ₂ _A and TiO ₂ _Gr12	115
Figure 5.25:	Optimized struture of Z907and N719	116
Figure 5.26:	The effect of thickness on cell performance of cells using electrolyte Co-2	118
Figure 5.27:	The effect of TBP concentration on V_{oc} , J_{sc} , FF and η	119
Figure 5.28:	I-V curves of Z907 sensitized solar cells of TiO ₂ _A-iodine, TiO ₂ _Gr12-iodine, TiO ₂ _A-cobalt, TiO ₂ _Gr12-cobalt	120
Figure 5.29:	Absorbance of Z907-sensitized TiO ₂ _A and TiO ₂ _Gr12 layer.....	121
Figure 5.30:	IPCE spectra of Z907 sensitized cell TiO ₂ _A and TiO ₂ _Gr12 coupled with I ₃ ⁻ /I ₂ ⁺ ; and TiO ₂ _A and TiO ₂ _Gr12 couple with Co ^{2+/3+}	122
Figure 6.1:	Various one-dimensional structures of ZnO	128
Figure 6.2:	Structure of (branched-ZnO-NW and ZnO nano-forest	129
Figure 6.3:	TEM image of ZnO_NR nanoparciles and SEM image of ZnO_NR layer	130
Figure 6.4:	Particles size distirbution of ZnO_NR	130
Figure 6.5:	XRD pattern of NR partcile based ZnO layer after heat treatment	131
Figure 6.6:	I-V curves of ZnO_NR sensitized with TG6 and D149.	132
Figure 6.7:	Absorbance spectra of D149 and TG6 sensitized layer of ZnO_NR	133
Figure 6.8:	Typical IS spectra measured in the dark of ZnO_NR_TG6 cell at various appllied potential.....	133
Figure 6.9:	Variation of R_{ct} of ZnO_NR_D149 and ZnO_NR_TG6 with V_{cor}	134
Figure 6.10:	Variation of C_{μ} of ZnO_NR_D149 and ZnO_NR_TG6 with V_{cor}	134
Figure 6.11:	The logarithmic plots of τ_{tr} and τ_n of ZnO_NR_D149 and ZnO_NR_TG6 as a function of g	135

Figure 6.12:	The variation of charge collection efficiency (η_{coll}) of ZnO_D149 and ZnO_TG6 with V_{cor}	136
Figure 6.13:	The variation of σ with g of ZnO_NR_D149, ZnO_NR_TG6, TiO ₂ _D, TiO ₂ _B1, TiO ₂ _B2, TiO ₂ _A and TiO ₂ _Gr12	136
Figure 6.14:	Variation of D_n with g of ZnO_NR_D149, ZnO_NR_TG6 and TiO ₂ _A	137
Figure 6.15:	Variation of L_n with g of ZnO_NR_D149, ZnO_NR_TG6 and TiO ₂ _A	137
Figure 6.16:	Calculation and experimental results of UV-Vis spectra of D149 in DMF and TG6 in CH ₂ Cl ₂	138
Figure 6.17:	HOMO and LUMO orbitals of D149 dye.	140
Figure 6.18:	HOMO and LUMO orbitals of TG6 dye.....	140
Figure 6.19:	Energy diagram of the D149 and TG6 dye orbitals, active in the charge transfer, conduction band (CB) and valence band (VB) of ZnO and I ₃ ⁻ / I ⁻ redox couple	141
Figure 6.20:	Position of anchoring site (carboxylate function) on the dye D149 and TG6	142
Figure 6.21:	Structure of SD4, JM131 and JM164	142
Figure 6.22:	The position of E ⁰ of I ₃ ⁻ /I ⁻ , [Co(bpy) ₃] ^{2+/3+} , [Co(phen) ₃] ^{2+/3+} and [Co(bpy-pz) ₂] ^{2+/3+} redox-couples	144
Figure 6.23:	<i>I</i> - <i>V</i> curve of the best ZnO_NR-based cells using [Co(bpy-pz) ₂] ^{2+/3+} and I ₃ ⁻ /I ⁻ as redox couple with JM164 as sensitizer and has ~ 5 μ m photoelectrode thickness.	147
Figure 6.24:	The ZnO_NR cell stability of <i>I</i> - <i>V</i> parameters (a) J _{SC} (b) V _{oc} (c) <i>FF</i> and (d) η . The cell use [Co(bpy-pz) ₂] ^{2+/3+} as redox-couple and JM164 as sensitizer	148
Figure 6.25:	TEM Image of ZnO_C20	149
Figure 6.26:	Absorbance spectra a of JM164 in UV-Vis range based on experimental measurement and on calculation using TD-DFT method and level theory B3LYP, ω b97XD and CAM-B3LYP.....	151
Figure 6.27:	Calculation and experimental results of absorbance spectra in UV-Vis range of SD4, JM131 and JM164 dyes.	152
Figure 6.28:	LUMO, HOMO-1 and HOMO molecular orbitals of SD4, JM131 and JM164 dyes (positive = green; negative = purple, isovalue = 0.001)	154
Figure 6.29:	Graphical representative of d^{CT} of SD4, JM131 and JM164	155

List of Tables

Table 2.1	The different between ZnO and TiO ₂	24
Table 2.2	Some cobalt-complexes that have been studied	33
Table 3.1	Name and composition of electrolytes used in the thesis	66
Table 4.1	Dye loading and cell characteristics under 100 mW.cm ⁻² , AM 1.5G filtered illumination.	76
Table 4.2	α , T_0 and β parameters extracted from the $C_{\mu}(V_{cor})$ and $R_{ct}(V_{cor})$ curve analysis.	80
Table 4.3	Analysis of the open circuit voltage difference between anatase and brookite cells.....	80
Table 4.4	Calculation of ΔE_{ads} of I ₂ adsorption on anatase (101) and brookite (210) surface	89
Table 5.1:	Effect of composite SGO content on the specific surface area determined by BET (S_{BET}), on the sensitized layer dye concentration and on the maximum of absorbance at 530 nm	104
Table 5.2	I-V curve parameters of TiO ₂ _A and various TiO ₂ _Gr cells	107
Table 5.3	α , β and T_0 value of TiO ₂ _A and TiO ₂ _Gr that is extracted from IS Spectra	110
Table 5.4.	The comparison of Z907 sensitized cell performances using (Co[bpy] ₂) ³⁺ and NOBF ₄ as source of Co ³⁺	117
Table 5.5.	The effect of ligand on cell performances	117
Table 5.6	Effect of Co(II)/NOBF ₄ molar ratio on Z907-sensitized cell performances	118
Table 5.7.	Cell parameters for TiO ₂ _Gr12 cobalt-based DSSC experiment	120
Table 5.8	I-V parameters of Z907 sensitized TiO ₂ _A and TiO ₂ _Gr12 solar cells with iodine (I ₂ -2) and cobalt-based electrolytes (Co-6)	121
Table 6.1	Dye molar extinction coefficient and I-V curve characteristic under 100 mW.cm ⁻² , AM 1.5 G filtered illumination	132
Table 6.2.	Calculated TD-DFT spectra of TG6 and D149 above 350 nm with oscillator strength, $f > 0.1$	139
Table 6.3	I-V characteristics using iodine redox-couple (I ₂ -2)	143
Table 6.4	I-V characteristics of SD4 using various cobalt redox-couples	144
Table 6.5:	I-V characteristics of JM164- and JM131-based cell using [Co(bpy-pz) ₂] ^{2+/3+} and I ₃ ⁻ /I ⁻ redox-couples	145
Table 6.6.	I-V measurement of JM164 cell using [Co(bpy-pz) ₂] ^{2+/3+} and I ₃ ⁻ /I ⁻ as redox couple, without the addition of TBP in electrolyte.	146
Table 6.7	The I-V characteristics of cell with a 5 μ m photoelectrode thickness using JM164 sensitizer.....	147
Table 6.8	The I-V characteristics of JM164 sensitized ZnO_C20 based cells	150
Table 6.9	Calculated TD-DFT spectra of SD4, JM131 and JM164 above 350 nm with oscillator strength, $f > 0.1$	153
Table 6.10	The q^{CT} and d^{CT} of SD4, JM131 and JM164 calculated using CT model	155
Table 6.11	The calculated excited states lifetime of SD4, JM131 and JM164	156
Table 7.1	The summary of I-V cell characteristic in this study.....	162

List of Appendix

APPENDIX A: Crystallites Size Determination.....	164
APPENDIX B: Porosity Determination using Direct Method	168
APPENDIX C: Optical Band-gap Calculation.....	169
APPENDIX D: Dye Loading Calculation	173
APPENDIX E: Molar Extinction Coefficient Calculation	176
APPENDIX F: Photocatalytic Properties of TiO ₂ _Gr layer	179
APPENDIX G: Cobalt Complexes Preparation	185
APPENDIX H: Input File Gaussian Explanation	185
APPENDIX I: Input File CP2K Explanation.....	189
APPENDIX J: The Computational Procedure to Quantify Charge Transfer	191
APPENDIX K: Calculation of Fluorescence Energy.....	192

List of the Important Abbreviations and Symbols

a	Absorbance
B3LYP	Three-parameter hybrid functional
bpy	2,2'-bipyridine
bpy-pz	6-(1H-pyrazol-1-yl)-2,2'-bipyridine
CAM-B3LYP	Three-parameter hybrid functional that involved long-range correction
CB	Conduction band
VB	Valence band
c	Speed of light : 3.108 m.s^{-1}
C_{μ}	Chemical capacitance of semiconductor due to electron trapping in states distributed below the conduction band edge
D_{eff}	Diffusion coefficient of electron in material
DEG	Diethylene Glycol
DFT	Density Functional Theory
DMF	Dimethylformamide
DMPII	1,2-diméthyl-3-propylimidazolium
DSSC	Dye-sensitized solar cell
DOS	Density of state
e or q	Charge of electron : $-1,6.10^{-19} \text{ C}$
EC	Ethylcellulose
ETL	Electron Transport Layer
eV	Electron volt
f	Oscillator strength
FF	Fill Factor
FTIR	Fourier-Transform Infra Red

FTO	Flouride dopped Tin Oxide
h	Planck constance : $6,6.10^{-34}$ J.s
HOMO	Highest Occupied Molecular Orbital
HTL	Hole Transport Layer
IPCE	Incident photon-to-electron conversion efficiency
J_{sc}	Short circuit current
k_B	Boltzman constance : $1,38.10^{-23}$ J.K ⁻¹
KOH	Potassium hydroxide
l_n	Diffusion length
LUMO	Lowest Unoccupied Molecular Orbital
p	Porosity of photoelectrode
phen	1,10-phenanthroline
PCE	Power Conversion Efficiency
R_{ce}	Counter electrode resistance
R_{ct}	Resistance to charge transfer (recombination) across the sensitized oxide-electrolyte interface
R_S	Series resistance
R_{tr}	Transport resistance of the electrons traveling in the mesoporous metal oxide films
R	Light reflectance
SEM	Scanning Electron Microscope
SGO	Single Graphene Oxide
T	Light transmission
TEM	Transmission Electron Microscope
TiO ₂ _A	TiO ₂ particles which have anatase structure and were synthesized in this work

TiO ₂ _B	TiO ₂ particles which have brookite structure and were synthesized in collaboration with the Laboratoire de Chimie de la Matière Condensée de Paris, Collège de France, Paris, France
TiO ₂ _D	TiO ₂ particles which have anatase structure and were buy from DSSC Company, Dyesol® as a paste
TiO ₂ _Gr	Composite of TiO ₂ anatase and graphene
TCO	Transparent Conductiove Oxyde
XRD	X-Ray Diffraction
V_{oc}	Open circuit voltage
Z	Elextrical Impedance
ZnO_NR	ZnO rod-like nanoparticles
α	a parameter that corresponds to the depth of the distribution
β	an empirical estimation of the reaction order
ε	Coefficient extinction molar
ε_0	Vacuum permittivity = $8.85419 \times 10^{-12} \text{ F.m}^{-1}$
\hbar	Reduced planck constant = $1.05 \times 10^{-34} \text{ J.s}$
η	Cell efficiency = PCE
η_{coll}	Charge collection effeciency
λ	Wavelength
ν	Light frequency
σ	Conductivity
τ_{tr}	Transport time of electron in semiconductor
τ_n	Electron lifetime of electron in semiconductor

Chapter I: Introduction

I.1. Background

I.1.1. Solar Energy as an Alternative of Renewable Energy

Energy is one of the primary needs of human life. Nowadays, the consumption of energy is increasing not only because the population increase, but also because many activities are more and more energy dependent. Modern people who live in the high technology era need energy for various purposes including communication and transportation.

The fossil fuels, including coal, liquid fuels (oil/petroleum) and natural gas, are the major energy sources in the world that supplies 80% of the world energy demands (Asif and Muneer, 2007). Figure 1.1 displays the consumption of the fossil fuels from 1965 until 2030. This figure shows that the demand increases with time. As non-renewable energy source, the fossil fuels have disadvantages of a limited availability. In their article, Shafiee and Topal have calculated that the oil, coal and gas stocks are only sufficient for about 40, 200 and 70 years, respectively if assumed that the world-consumption rate is constant as 2006's rate (Shafiee and Topal, 2009).

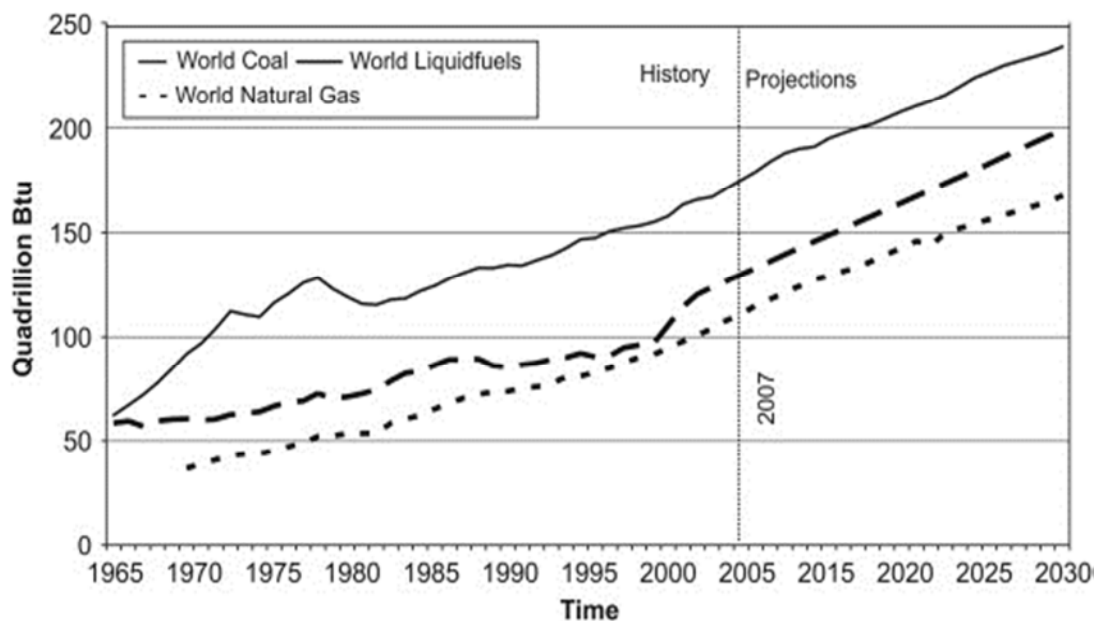


Figure 1.1: Consumption of the fossil fuel in the world from 1965 to 2030 (Shafiee and Topal, 2009)

Another disadvantage of the fossil fuels is their negative effect on the environment. Their combustion releases the greenhouse CO₂ gas in the atmosphere that provokes climate change and global warming (Steinberg, 1999).

The issue of the fossil fuels limited availability and the global warming effect has become a global problem and has been discussed for years. This situation has encouraged many researchers to exploit the renewable energy sources. There are many kinds of renewable energy that have potency to be used, such as: wind, solar, geothermal, hydrogen, hydro-electric or biomass energies (Jacobson and Delucchi, 2011; Salameh, 2003).

One of the potential sources of renewable energy is the solar energy. It meets three criteria as energy source which are sustainability, cleanness and low-risk. These three criteria are important to maintain the energy system for a long term (Jacobson and Delucchi, 2011). The availability of the solar energy depends on geographical area and season/time. Solar irradiance on earth's surface can reach 0.06 kW/m² (at high latitudes) to 0.25 kW/m² (at low latitudes) (Timilsina et al., 2012). Figure 1.2 shows the average annual global solar irradiation. Many areas in the world, especially in the equator area, have high annual solar radiation. As a tropical country, Indonesia which is located between latitudes 6°N -11°N and longitudes 95°E-141°E, receives a solar radiation ranging between 4.6 kWh/m² and 7.2 kWh/m². The highest radiation is received in August and in September (Rumbayan et al., 2012). This makes Indonesia has a promising potential to develop a solar energy system.

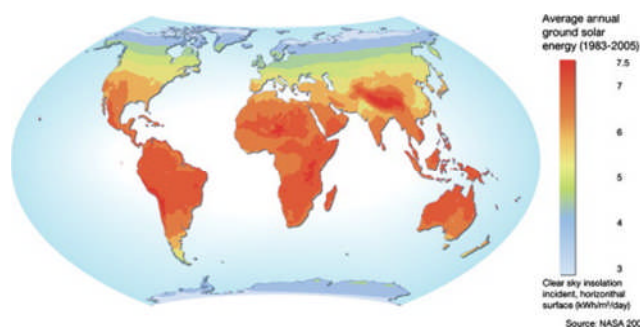


Figure 1.2: Average annual global solar radiation (Devabhaktuni et al., 2013).

The solar energy can be utilized directly as a heat radiation without any changing to another form for instance in traditional drying process. This is a simple and low technology utilization. Since many of household and industrial equipments need electricity source, the solar energy can be more valuable by converting it to electricity. Solar technologies have an

important role to play and it has become a promising competitor for fossil fuels as the energy sources. The pioneer technology to convert the solar energy into a more usable one appeared in 1860. At that time they developed the technology to capture the sun's heat. This heat was used to generate steam for running engines and irrigation pumps. Another typical electricity generating technology from the solar energy is photovoltaic (PV). The photovoltaic effect was discovered by Alexandre Edmond Becquerel in 1839. It is produced in semiconductor that can absorb light in the solar radiation spectrum range. This light absorption generates excitation charges, which are separated, provokes electron/hole flows, produces a voltage difference then finally generates the electricity. Since the first silicon solar cells fabrication in 1954 at the Bell Laboratories in the United States, until now there are many kinds of the PV technologies that have been developed. Figure 1.3 shows some example of the applications of solar cells.

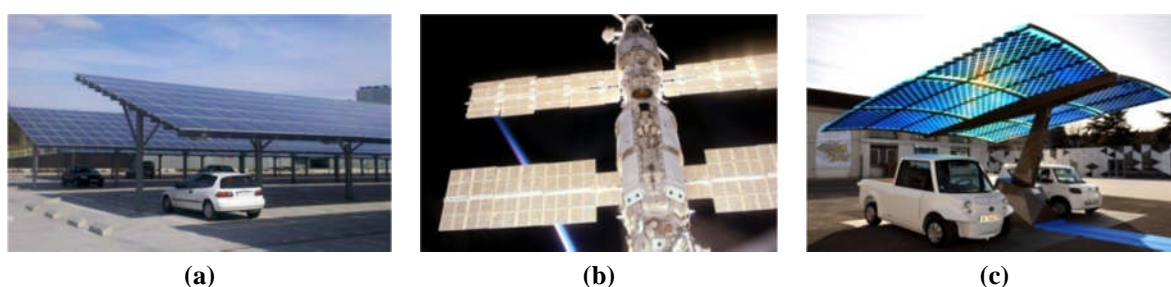


Figure 1.3: Some applications of solar cells: (a) PV Solar parking canopy at the Autonomous University of Madrid, Spain; (b) Solar panels on the International Space Station; (c) Photovoltaic SUDI shade is an autonomous and mobile station in France that provides energy for electric vehicles using solar energy; (<http://en.wikipedia.org>, 2015).

Crystalline silicon-based solar cells are the leading technology in the solar cell market. Novel technologies to find out alternative materials which are less energy demanding to produce an that could replace the silicon one are also developing (Devabhaktuni et al., 2013; Timilsina et al., 2012). Figure 1.4 shows that global installed PVs capacity has increased exponentially from 1.4 GW in 2000 to 40 GW in 2010.

1.1.2. Dye-sensitized solar cells: towards iodine free devices.

Improvements in the solar cell field aim at increasing their efficiency and decreasing their production costs. One emerging technology of solar cells use a dye for sunlight harvesting in devices referred to as Dye Sensitized Solar Cells (DSSCs). They consist of a mesoporous semiconductor layer deposited on a transparent conductive oxide (TCO),

sensitized by a monolayer of dyes, and coupled with an electrolyte and a counter electrode. All components of DSSCs interact each other at molecular level to build a stable and an efficient solar cell device. DSSCs can be small and light, so they can be easily applied to various electronic devices. They are mentioned as a candidate for the third generation of solar cells (Hagfeldt et al., 2010). Despite their advantages, their efficiency is still lower compared to the silicone-based solar cells. The research on improving their performances has been on-going for more than two decades. Figure 1.5 shows that the number of publication on DSSCs has increased exponentially over this period, indicating that the interest on DSSC research is increasing. Moreover, they are emerging on the market of up-scaled energy provision with for instance the installation of large DSSC panels in Switzerland by Soloronix and G2e (Figure 1.5).

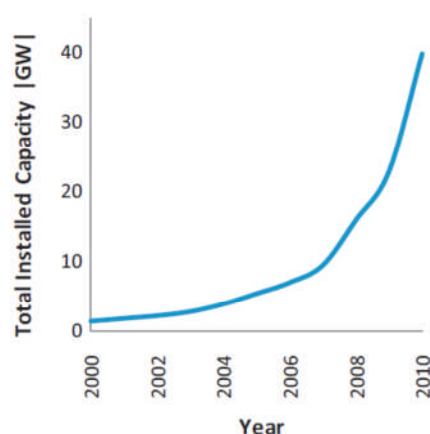


Figure 1.4: Total installed PVs capacity in the world (Timilsina et al., 2012).

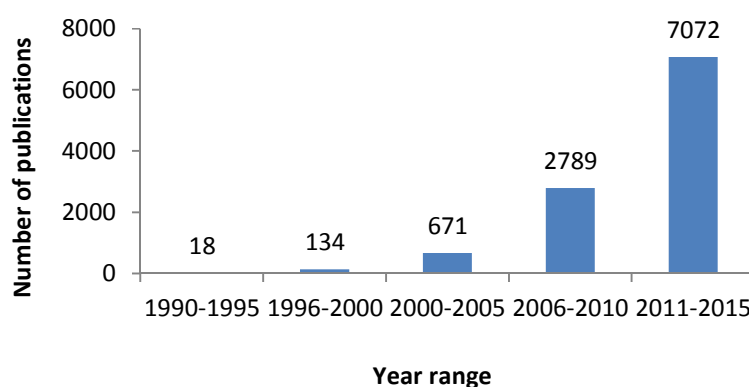


Figure 1.5: Number of papers on DSSC published since their discovery. Data is taken from www.scopus.com with search keywords "dye sensitized" and "solar"

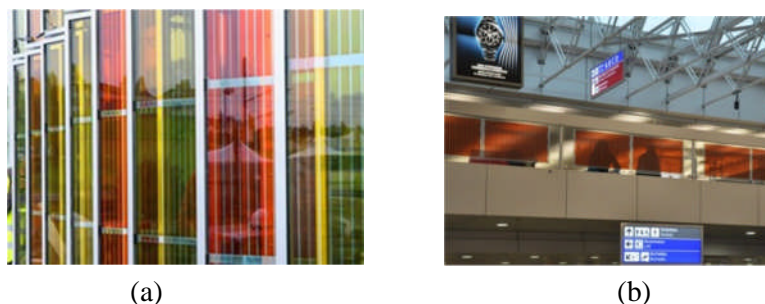


Figure 1.6: Two DSSC panels installations in Switzerland. (a) DSSC panel at EPFL campus, the world's first solar window (<http://actu.epfl.ch>, 2011) (b) DSSC panel at Geneva Airport that is installed by g2e in collaboration with EPFL (<http://g2e.ch>, 2013)

The “classical” DSSC, that was first introduced by Gratzel et. al. (O'Regan and Grätzel, 1991) in 1991 and has been become a standard for years, is composed of a mesoporous TiO_2 electron transport layer sensitized by ruthenium complex dye as the photoelectrode, an electrolyte containing the I_3^-/I^- redox-couple and platinized conducting glass as the counter electrode. In order to increase the cell efficiency, researchers have competed to modify each of the components. The highest efficiency of DSSC was achieved by using the TiO_2 mesoporous as the photoanode, the $[\text{Co}(\text{bpy})_2]^{2+/3+}$ as the redox-couple and a porphyrin-dye, the SM 315 as the sensitizer. A record efficiency of 13% was achieved with this cell developed by Mathew and co-workers in the EPFL laboratory (Mathew et al., 2014). The usage of cobalt as redox-couple to replace the iodide one was based on the observation that employing the I_3^-/I^- as the redox-couple has several limitation because it causes corrosion, absorb the light in the 350-450 nm wavelength region and it has limited open circuit voltage due to its potential reduction value (Feldt et al., 2011, 2010; Hamann et al., 2006). On the other hand, the use of cobalt redox shuttles requires, (1) thinner photoelectrode layer to accommodate transport of bulky cobalt-complex and (2) special structure of sensitizer with long-alkyl chain and D- π -A characteristic to provide better charge separation and avoid the close approach of cobalt-complex to the photoanode surface and then reduce the recombination (Murakami et al., 2014; Yella et al., 2011). Mathew et. al. work focused on modifying the porphyrin sensitizer to improve cobalt based DSSC performance (Mathew et al., 2014). Since the synthesis of organic molecules need special technique and experience, it is important to do modification of others DSSC's component in order to meet a better result when combined with cobalt-based electrolyte. Another strategy that can be applied to increase the DSSC efficiency is to improve the semiconductor as Electron Transfer Layers (ELT) in DSSC to have faster electron transport so it can compete with the charge recombination.

I.2. Objectives

Based on the above consideration and motivation, therefore, the objectives of this work have been set-up as follows: (1) to develop the use of new porous ETLs in DSSC application; (2) to investigate their functioning, for this pupose the cells were investigated in the I_3^-/I^- based electrolyte; and (3) to investigate their use with new redox couples to get iodine-free efficient devices, for this purposes the cell were investigated using $Co^{2+/3+}$ based electrolyte. In order to perform in-depth investigations, there are three kind ETLs were developed in this work, i.e., the TiO_2 -brookite, the composite of TiO_2 /graphene and ZnO nanorods (ZnO_NR) based DSSC. Furthermore, to have a description about the researches in this work, in the next section will be described the research approaches and the specific objectives of this work.

I.3. Research Approaches and Specific Objectives

This section will be devided based on the kinds of ETLs that were developed in this works; the TiO_2 -brookite, the composite of TiO_2 /graphene and ZnO nanorods (ZnO_NR) based DSSC

I. 3.1. TiO_2 Brookite Based DSSC

TiO_2 -anatase has been used widely as semiconductor in DSSC application. Instead of anatase, the other polymorph of TiO_2 , brookite also has promising potential to be used in DSSC application. It has been done in the previous work in our laboratory that the Brookite based DSSC has a higher V_{oc} , unfortunately the J_{sc} of brookite based DSSCs are lower compare to the anatase ones (Magne et al., 2012). Revealing the origin of cell parameters will be beneficial as the material development consideration.

Based on this motivation, therefore, the specific objective of the work on this part is aimed at performing a comprehensive study using impedance spectroscopy to find out the origin of the cell paramteres to the cell functioning.

I. 3.2. TiO_2 /graphene Based DSSC

Graphene incorporation into TiO_2 particle for DSSC photoelectrode is potentially of great interest. Many reports show that graphene can improve the cell efficiency by increasing the current density (J_{sc}) without significantly decrease in the open circuit voltage (V_{oc}) and fill factor (FF) (Cheng et al., 2013; Fang et al., 2014; Tang et al., 2010; J. Wang et al., 2012; Yang et al., 2010). One of factors that makes J_{sc} increasing is because there is an enhancement

in charge transport leading to electron transport increasing in photoelectrode after graphene incorporation (Fan et al., 2012; H. Wang et al., 2012). Although many reports have shown the improvement of DSSC performances by the addition of graphene, the effect of this additive on the cell functioning still needs to be clarified. In the present work, we have prepared anatase TiO₂/graphene composite films using a simple sol-gel technique and graphene oxide single layer sheets (SGO) as the graphene source.

On the basis of the above considerations, the specific objectives of this work are:

- (1) to clarify the role of RGO in cell improvement using comprehensive study of impedance spectroscopy. This study was done using classical DSSCs, in the I₃⁻/I⁻ based electrolyte.
- (2) to apply the TiO₂/graphene composite on the cobalt-based DSSC. To the best of our knowledge, there has been no previous report concerning the application of TiO₂/graphene DSSCs coupled with cobalt-based DSSCs. This work is motivated by the fact that the cobalt-complexes have a bulky structure that restricts their movement in the photoelectrode and provokes a reduction of the J_{sc} . We hope graphene presence in this cell can overcome the J_{sc} reduction.

I. 3.3. ZnO_NR Based DSSC

As an alternative to TiO₂, ZnO can also be used in DSSC. The use of ZnO is promising due to the electronic properties of this oxide. Electron mobility and diffusion coefficient in ZnO is much higher than that in anatase TiO₂. These properties are profitable for DSSCs application because they support fast charge transport and electron recombination reduction (Quintana et al., 2007; Zhang et al., 2009). Moreover, the crystallization and anisotropic growth of ZnO crystal is relatively easy and allows the preparation of structures with various structural shapes.

In order to obtain further understanding, therefore, the specific objectives of the work on ZnO-based DSSCs study are as follows:

- (1) to investigate the cell performances in classical I₃⁻/I⁻ using two kinds of sensitizers (D149 as representative of organic sensitizer and TG6 as representative of organometallic/ruthenium sensitizer);
- (2) to apply the ZnO_NR in the cobalt based DSSC. The used ZnO_NR particles were 35x110 nm in size. The layers presented also quite large pores. Their structural

properties have been shown promising to facilitate cobalt-complexes transport in their porous network.

1.4. Thesis Organization

The heart of this thesis is placed from Chapter IV to Chapter VI which is described about the result of the works. Before reach that part, there is an introduction in Chapter I which is described about the background, the objectives and the research map of this work. Whereas Chapter II explains about the literature review and Chapter III describes the experimental and computational procedure.

The impedance study results of anatase and brookite DSSC are presented in the Chapter IV. The computational study of iodine adsorption on Anatase and Brookite surface that support experimental result is also presented in this Chapter.

The study of TiO_2 /graphene-based DSSC is presented in the Chapter V. This work is divided into two parts: the first work presents the key role of graphene incorporation into the TiO_2 photoelectrode. For this study, we used the I_3^-/I^- as a redox-couple and the N719 as a sensitizer. In a second part we have investigated the TiO_2 /graphene cobalt-based DSSC. Z907 was used as a sensitizer then. Some optimizations have been done to find out the best cell performances.

The Chapter VI presents the result on ZnO_NR based DSSCs. In first part, the ZnO-NR cells were tested in the I_3^-/I^- based electrolyte using D149 and TG6 as sensitizer. The D149 was chosen as representative of organic dye, whereas the TG6 was chosen as representative of ruthenium dye. In a second part of Chapter VI, we discuss the optimization and the performance of the ZnO-NR based cells in the cobalt-based electrolyte system. The TD-DFT computational study of the dye used in this chapter is also discussed. The scheme of thesis organization is showed in Figure 1.7.

The experimental techniques used in the thesis are presented in the Chapter III. The Chapter II presents the literature review on the DSSCs that has attracted our consideration in making a work plans in this thesis. Some supporting experimental procedures are gathered in the Appendix. We have also enclosed in the Appendix the results of photocatalytic degradation of 4-chlorophenol using TiO_2 /graphene layer, a work that has been done in collaboration with the J. Heyrovsky Institute of Physical Chemistry, v.i.i., Academy of Sciences of the Czech Republic.

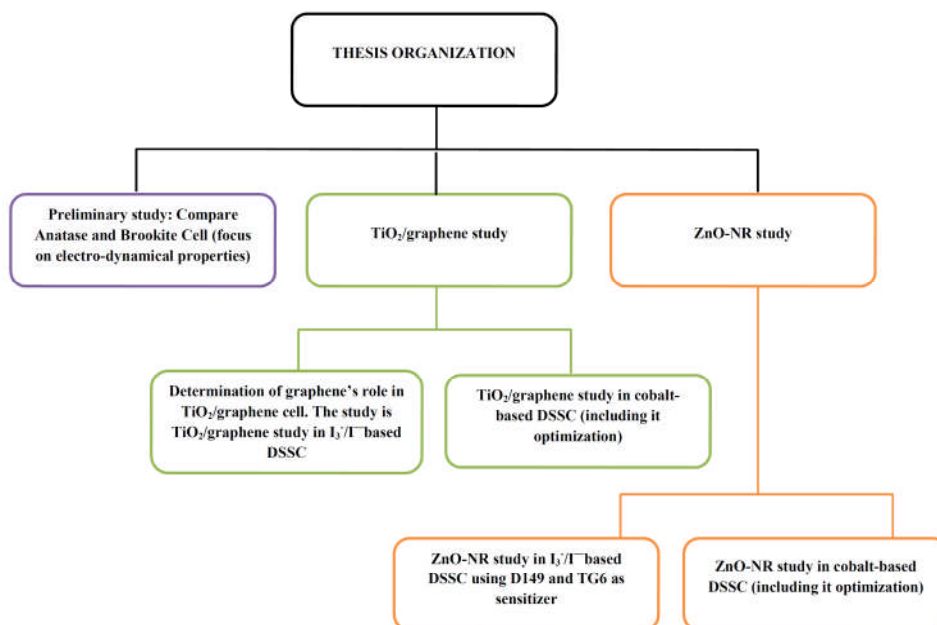


Figure 1.7: Thesis organization. The purple, green and orange box will be discussed in chapter IV, V and VI, respectively.

References

- Asif, M., Muneer, T., 2007. Energy supply, its demand and security issues for developed and emerging economies. *Renew. Sustain. Energy Rev.* 11, 1388–1413. doi:10.1016/j.rser.2005.12.004
- Cheng, G., Akhtar, M.S., Yang, O.-B., Stadler, F.J., 2013. Novel Preparation of Anatase TiO₂@Reduced Graphene Oxide Hybrids for High-Performance Dye-Sensitized Solar Cells. *ACS Appl. Mater. Interfaces* 5, 6635–6642. doi:10.1021/am4013374
- Devabhaktuni, V., Alam, M., Shekara Sreenadh Reddy Depuru, S., Green II, R.C., Nims, D., Near, C., 2013. Solar energy: Trends and enabling technologies. *Renew. Sustain. Energy Rev.* 19, 555–564. doi:10.1016/j.rser.2012.11.024
- Fang, X., Li, M., Guo, K., Liu, X., Zhu, Y., Sebo, B., Zhao, X., 2014. Graphene-compositing optimization of the properties of dye-sensitized solar cells. *Sol. Energy* 101, 176–181. doi:10.1016/j.solener.2013.12.005
- Fan, J., Liu, S., Yu, J., 2012. Enhanced photovoltaic performance of dye-sensitized solar cells based on TiO₂ nanosheets/graphene composite films. *J. Mater. Chem.* 22, 17027–17036. doi:10.1039/C2JM33104G
- Feldt, S.M., Gibson, E.A., Gabrielsson, E., Sun, L., Boschloo, G., Hagfeldt, A., 2010. Design of Organic Dyes and Cobalt Polypyridine Redox Mediators for High-Efficiency Dye-Sensitized Solar Cells. *J. Am. Chem. Soc.* 132, 16714–16724. doi:10.1021/ja1088869
- Feldt, S.M., Wang, G., Boschloo, G., Hagfeldt, A., 2011. Effects of Driving Forces for Recombination and Regeneration on the Photovoltaic Performance of Dye-Sensitized Solar Cells using Cobalt Polypyridine Redox Couples. *J. Phys. Chem. C* 115, 21500–21507. doi:10.1021/jp2061392
- Hagfeldt, A., Boschloo, G., Sun, L., Kloo, L., Pettersson, H., 2010. Dye-Sensitized Solar Cells. *Chem. Rev.* 110, 6595–6663.
- Hamann, T.W., Brunschwig, B.S., Lewis, N.S., 2006. Comparison of the Self-Exchange and Interfacial Charge-Transfer Rate Constants for Methyl- versus tert-Butyl-Substituted Os(III) Polypyridyl Complexes†. *J. Phys. Chem. B* 110, 25514–25520. doi:10.1021/jp0649697
- Jacobson, M.Z., Delucchi, M.A., 2011. Providing all global energy with wind, water, and solar power, Part I: Technologies, energy resources, quantities and areas of infrastructure, and materials. *Energy Policy* 39, 1154–1169. doi:10.1016/j.enpol.2010.11.040

- Magne, C., Dufour, F., Labat, F., Lancel, G., Durupthy, O., Cassaignon, S., Pauporté, T., 2012. Effects of TiO₂ nanoparticle polymorphism on dye-sensitized solar cell photovoltaic properties. *J. Photochem. Photobiol. Chem.* 232, 22–31. doi:10.1016/j.jphotochem.2012.01.015
- Mathew, S., Yella, A., Gao, P., Humphry-Baker, R., Curchod, B.F.E., Ashari-Astani, N., Tavernelli, I., Rothlisberger, U., Nazeeruddin, M.K., Grätzel, M., 2014. Dye-sensitized solar cells with 13% efficiency achieved through the molecular engineering of porphyrin sensitizers. *Nat. Chem.* 6, 242–247. doi:10.1038/nchem.1861
- Murakami, T.N., Koumura, N., Kimura, M., Mori, S., 2014. Structural Effect of Donor in Organic Dye on Recombination in Dye-Sensitized Solar Cells with Cobalt Complex Electrolyte. *Langmuir* 30, 2274–2279. doi:10.1021/la4047808
- O'Regan, B., Grätzel, M., 1991. A low-cost, high-efficiency solar cell based on dye-sensitized colloidal TiO₂ films. *Nature* 353, 737–740. doi:10.1038/353737a0.
- Quintana, M., Edvinsson, T., Hagfeldt, A., Boschloo, G., 2007. Comparison of Dye-Sensitized ZnO and TiO₂ Solar Cells: Studies of Charge Transport and Carrier Lifetime. *J. Phys. Chem. C* 111, 1035–1041. doi:10.1021/jp065948f
- Rumbayan, M., Abudureyimu, A., Nagasaka, K., 2012. Mapping of solar energy potential in Indonesia using artificial neural network and geographical information system. *Renew. Sustain. Energy Rev.* 16, 1437–1449. doi:10.1016/j.rser.2011.11.024
- Salameh, M.G., 2003. Can renewable and unconventional energy sources bridge the global energy gap in the 21st century? *Appl. Energy, Energex 2002 - Oil and Gas - Topic III and Nuclear Energy - Topic IV* 75, 33–42. doi:10.1016/S0306-2619(03)00016-3
- Shafiee, S., Topal, E., 2009. When will fossil fuel reserves be diminished? *Energy Policy* 37, 181–189. doi:10.1016/j.enpol.2008.08.016
- Steinberg, M., 1999. Fossil fuel decarbonization technology for mitigating global warming. *Int. J. Hydrog. Energy* 24, 771–777. doi:10.1016/S0360-3199(98)00128-1
- Tang, Y.-B., Lee, C.-S., Xu, J., Liu, Z.-T., Chen, Z.-H., He, Z., Cao, Y.-L., Yuan, G., Song, H., Chen, L., Luo, L., Cheng, H.-M., Zhang, W.-J., Bello, I., Lee, S.-T., 2010. Incorporation of Graphenes in Nanostructured TiO₂ Films via Molecular Grafting for Dye-Sensitized Solar Cell Application. *ACS Nano* 4, 3482–3488. doi:10.1021/nn100449w
- Timilsina, G.R., Kurdgelashvili, L., Narbel, P.A., 2012. Solar energy: Markets, economics and policies. *Renew. Sustain. Energy Rev.* 16, 449–465. doi:10.1016/j.rser.2011.08.009
- Wang, H., Leonard, S.L., Hu, Y.H., 2012. Promoting Effect of Graphene on Dye-Sensitized Solar Cells. *Ind. Eng. Chem. Res.* 51, 10613–10620. doi:10.1021/ie300563h
- Wang, J., Tsuzuki, T., Tang, B., Hou, X., Sun, L., Wang, X., 2012. Reduced Graphene Oxide/ZnO Composite: Reusable Adsorbent for Pollutant Management. *ACS Appl. Mater. Interfaces* 4, 3084–3090. doi:10.1021/am300445f
- Yang, N., Zhai, J., Wang, D., Chen, Y., Jiang, L., 2010. Two-Dimensional Graphene Bridges Enhanced Photoinduced Charge Transport in Dye-Sensitized Solar Cells. *ACS Nano* 4, 887–894. doi:10.1021/nn901660v
- Yella, A., Lee, H.-W., Tsao, H.N., Yi, C., Chandiran, A.K., Nazeeruddin, M.K., Diau, E.W.-G., Yeh, C.-Y., Zakeeruddin, S.M., Grätzel, M., 2011. Porphyrin-Sensitized Solar Cells with Cobalt (II/III)-Based Redox Electrolyte Exceed 12 Percent Efficiency. *Science* 334, 629–634. doi:10.1126/science.1209688
- Zhang, Q., Dandeneau, C.S., Zhou, X., Cao, G., 2009. ZnO Nanostructures for Dye-Sensitized Solar Cells. *Adv. Mater.* 21, 4087–4108. doi:10.1002/adma.200803827

Web References:

- Photovoltaics. *Wikipedia, the free encyclopedia*, 2015. at <<http://en.wikipedia.org/w/index.php?title=Photovoltaics&oldid=642545739>>, downloaded on January 28th, 2015.
- EPFL's campus has the world's first solar window, 5th November 2011 at <<http://actu.epfl.ch/news/epfl-s-campus-has-the-world-s-first-solar-window/>>, downloaded on January 28th, 2015.
- g2e launches first installation at Geneva International Airport, 9th April 2013 at <http://g2e.ch/views/media_newsletter/g2e_gva-vitre-orange-300dpi.jpg>, downloaded on January 28th, 2015

Chapter II

Literature Review

The important concepts at the background of the present thesis will be explained in this chapter. Dye-sensitized solar cell (DSSC) concepts will be explained in the first section including the device structure, charge transport in the device and the principle of cell characterizations that have been carried out in the present work. Computational investigation has been also carried out in this thesis to support experimental result; therefore the fundamental concepts in computational chemistry will be explained in the second section.

II. 1. Fundamental of DSSC

As defined in Chapter 1 DSSCs are photovoltaic devices that convert solar energy into electricity. For the conversion process to occur, it requires a dye that will act as the sensitizer to harvest the solar light, a semiconductor material which collects the charge generated in the excited dye and transfer it to the transparent front contact. The charge then must reach the counter electrode and oxidized dye is regenerated by a redox-couple dissolved in an electrolytic solution. We can note that chemical additives are added to the sensitizing dye solution and to the electrolyte to improve DSSC performances. Due to the versatility of the system, many different kind of DSSC have been described in the literature. The present thesis will focus on n-type DSSC devices, in which a wide bandgap n-type oxide plays a role as the electron transport layer (ETL) and a liquid electrolyte is used as the hole transport layer (HTL).

II. 1.1. DSSC Component

A Schematic illustration of a DSSC and of its components is presented in the Figure 2.1.

Dye Sensitizer

To achieve good performances, the dye sensitizer has to fulfill several requirements. (i) Ideally, it should be able to absorb all incident solar light below the near-IR wavelength of approximately 920 nm. (ii) Structurally, it must have functional groups that allow the anchoring of the dye onto semiconductor surface, classically a carboxylate or a phosphonate functional group. (iii) It must have the Lowest Unoccupied Molecular Orbital (LUMO) energy localized above the conduction band of the semiconductor to guaranty the electron injection. (iv) The position of the Highest Occupied Molecular Orbital (HOMO) energy must

be localized below the redox potential of electrolyte. (v) At last, it must have good stability. If the dye still has good performance after 10^8 turnovers, it will equal to 20 years stability exposure to sunlight (Hagfeldt et al., 2010; Jena et al., 2012).

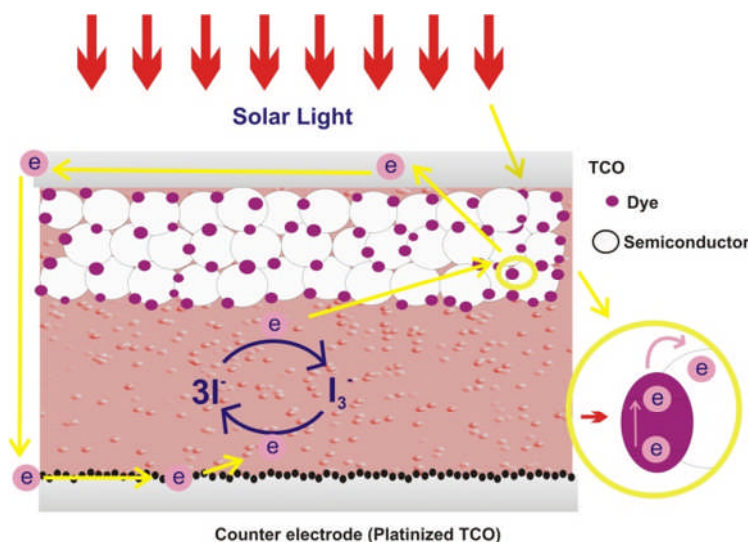


Figure 2.1: Schematic diagram of DSSC using I_3^-/I^- redox-couple

We can distinguish two main families of dyes that have been investigated for use in DSSCs. The first there are the metal complex compounds such as ruthenium, osmium, iron or zinc-based complexes and the second are the organic dyes including the indoline, coumarine or carbazole ones. Recently, Mathew, et. al. have successfully prepared cells with a 13% of efficiency using Zinc-Porphyrin complex dye (Mathew et al., 2014). Examples of dye molecular structure successfully used as sensitizer in DSSC are presented in Figure 2.2

The investigation of the dye electronic properties is very important to find out the electronic excitation behavior of the molecule which is related to its molecular structure. An efficient intramolecular charge transfer is required for a good cell performance. For this purpose, computational calculations are very helpful since they can describe electron density in the molecule. Moreover a first principle-based calculation technique, call TD-DFT (Time Dependent Density Functional Theory; see section II.2.2), it allows to reveal the electron excitation direction in the molecule upon the excitation process (Le Bahers et al., 2009; Marques and Gross, 2004; Runge and Gross, 1984). By comparing the calculated absorption spectrum with the experimental one, one can verify the accuracy of computational procedure.

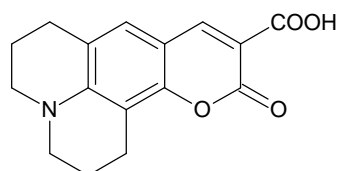
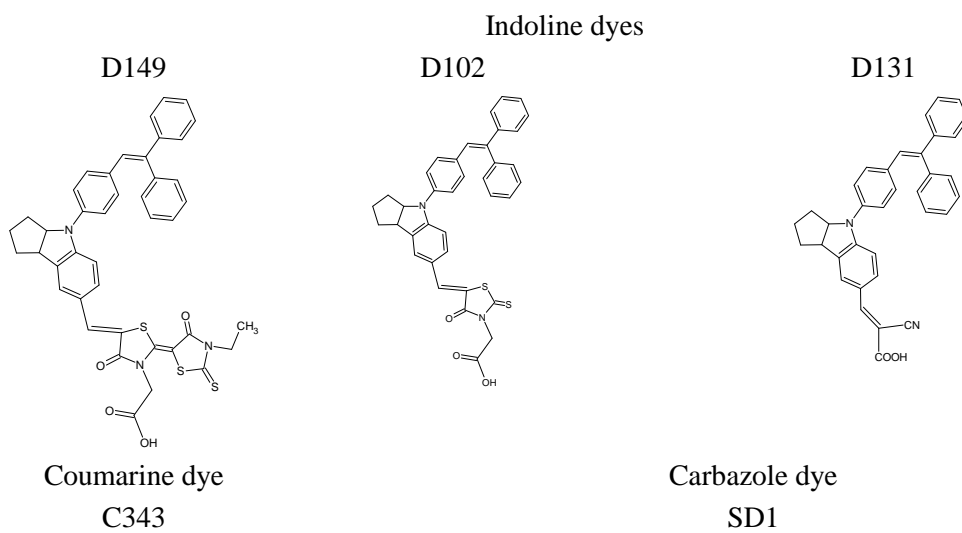
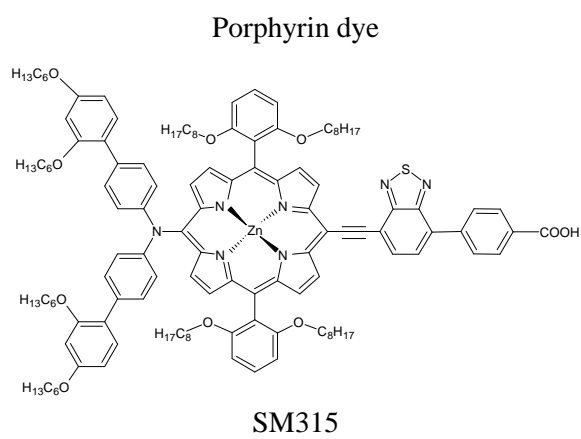
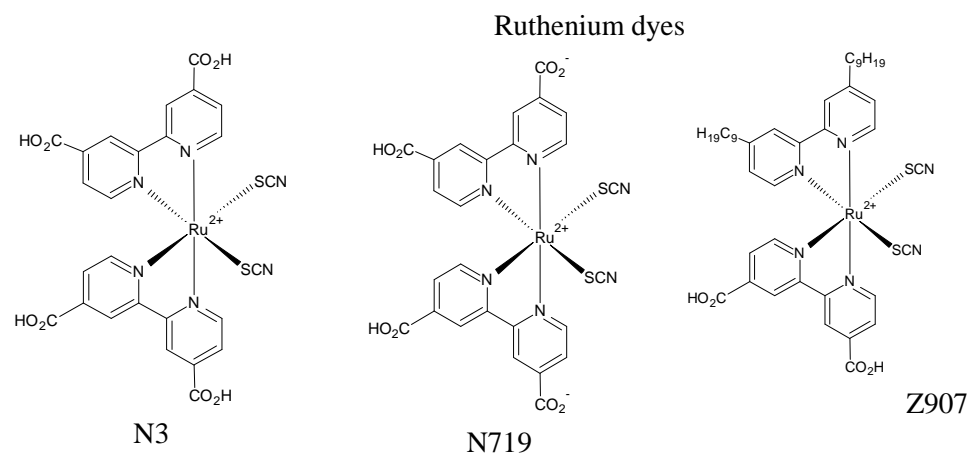


Figure 2.2: Molecular structures of the dyes, popular in the DSSC literature.

The intense charge transfer must be oriented from the donor group in contact with the electrolyte solution towards the acceptor group localized near the semiconductor-surface anchoring group. In the case of ruthenium-complex dyes, the MLLCT (Metal and Ligand to Ligand Charge Transfer) process from ruthenium and thiocyanate groups to the bipyridine ligand carrying the carboxylate group is an efficient charge transfer that contributes to the high cell performances (Le Bahers et al., 2014). The presence of CN or NO group functions, for instance, that can increase the electron density near the carboxylate group are preferable (Funaki et al., 2014). On the contrary, the presence of substitute group that make electron density decrease around carboxylate moiety or shift far from carboxylate group must be avoided. Moreover, it is preferable to avoid the use of a ligand that is able to absorb light in the visible region or can undergo intra-Ligand to Ligand Charge Transfer (LLCT), since this type of charge transfer will not effectively increase electron density near the carboxylate group and the oxide surface (Le Bahers et al., 2014).

For organic dyes, the molecules that have D- π -A (donor- π spacer-acceptor) structure (Figure 2.3) are described to give the highest performances. The π -bridge between D-A systems acts as a light absorber unit. A longer π -bridge extends the absorption towards the longer wavelength region (Kim et al., 2013). The advantages of organic dye compared to metal-complexes are: (i) they are easier and cheaper to produce, (ii) they have a higher molar extinction coefficient that leads to highly efficient light-harvesting properties and (iii) it is possible to tune the desirable properties by inserting suitable substituent (Le Bahers et al., 2014; Ham and Kim, 2010).

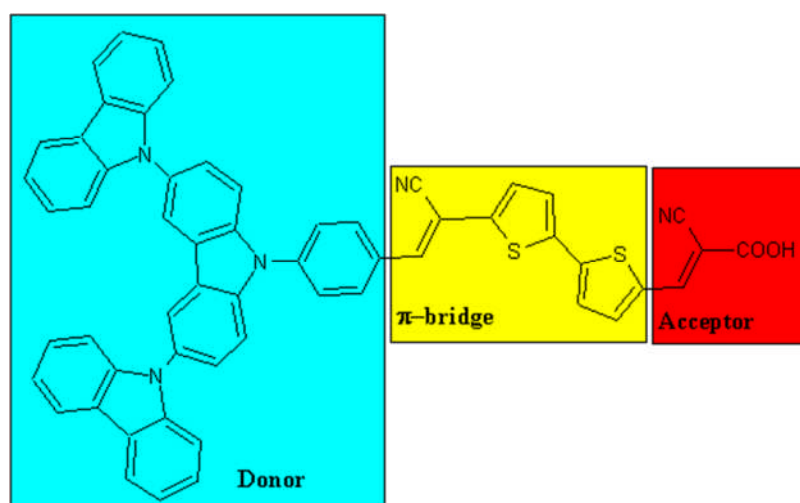


Figure 2.3: D- π -A systems in organic sensitizer SD1

Motivated by these potential advantages of organic dyes, many researchers have developed these sensitizers DSSC application (Alarco et al., 2007; Ganesan et al., 2014; Guérin and Pauporté, 2011; Hara et al., 2005; Ito et al., 2008; Magne et al., 2013b; Marinado et al., 2009). However, unfortunately, these efforts have not been fully successful yet. Based on the records of DSSC, metal complex compounds are still leading compared to the organic ones as a sensitizer in DSSC. As mentioned above, the highest efficiency reported for a DSSC employing an inorganic dye used a zinc-porphyrin complex dye, was coupled with cobalt-based electrolyte and reached 13% of (Mathew et al., 2014) On the other hand, the best performance of a DSSC employing an organic dye is 10.3 % using C219, as sensitizer (Zeng et al., 2010). Both are TiO₂-based DSSCs.

The limitation of organic dyes notably lies on the aggregation of molecules that can happen. To achieve the best light-harvesting spectrum and a good electron intramolecular transfer, it requires a long- π bond and a planar geometry. However, this structure induces π - π stacking, and then causes aggregation of molecules (Kim et al., 2013). To overcome this, the addition of an anti-aggregation agent, for example chenodeoxycholic acid (CDA), is required. This agent will be adsorbed on semiconductor surface, it will make the inter-dyes distance longer and then limit the intermolecular aggregation. Based on their working principle, they are also called “co-adsorbent agent”. Magne, et. al. have investigated a series of fatty acids as co-adsorbents. They have shown that octanoic acid gives rise to better performances than CDA when combined with indoline dyes for ZnO-based DSSCs (Magne et al., 2012).

Another limitation is due to the poor electron to electricity conversion character of the D- π -A organic molecules. The presence of strong electron withdrawing molecule functions near to the anchoring group causes a charge entrapment effect that induces electron recombination. The phenomenon has been overcome by inserting another π -bridge into the molecule, to get the D- π -A π -A structure. This resulted in an increase of the incident-photon-to electron conversion efficiency from 20% to 90% (Haid et al., 2012; Kim et al., 2013).

Co-sensitization by two or more dyes is another strategy to improve the DSSC performances. By using two or more dyes that have different maximum absorption wavelength ranges, the absorption spectrum of the system will be broaden and become panchromatic. They will complement each other and then, finally, the light-harvesting efficiency will be increased. This approach has been used for instance using D131 as the co-sensitization dye of D205 and D149 dyes for ZnO based DSSCs. The absorption spectra of each dye are displayed in Figure 2.4. It can be seen that D131 has the λ_{max} at 450 nm, whereas

the λ_{\max} of D149 and D205 dyes are localized at about 520-530 nm with a little weak absorbance at 450 nm. By combining D131 with D149 and D131 with D205, the light harvesting was gave rise to an increase of the short circuit current J_{sc} (Figure 2.5.a). IPCE spectra of both systems, shown in Figure 2.5.b, confirm this result (Magne et al., 2013b).

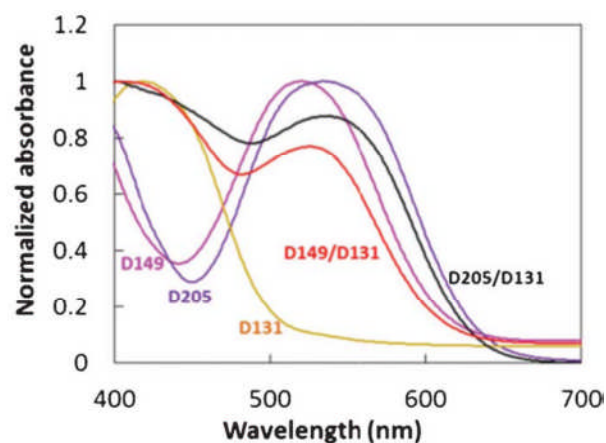


Figure 2.4: Normalized dye absorbance of individual D131, D149 and D205 dyes and of equimolar dye mixtures (Magne et al., 2013b)

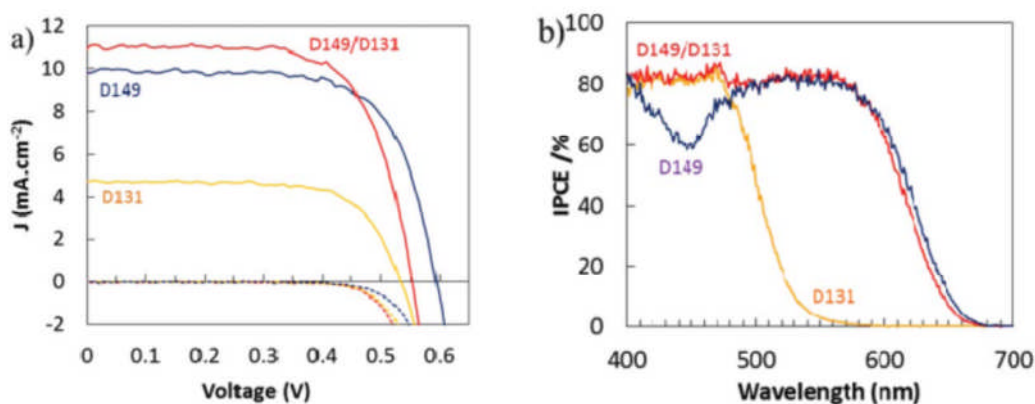


Figure 2.5: (a) J–V curves and (b) IPCE curves of ZnO DSSCs sensitized with D131, D149 and D131/D149 (Magne et al., 2013b)

The porphyrin family of inorganic dyes has attracted a considerable attention during the last few years. Porphyrins have important roles in biological processes, including catalysis, oxygen binding, electron transfer and photosynthesis. Their electronic absorption characteristic are interesting with two kinds of intense bands called Soret band (400-450 nm) and Q-bands (550-600 nm) (Kang et al., 2012). Their characteristics have inspired many researchers to prepare porphyrin derivatives compounds that can be applied as sensitizers in

DSSCs (Griffith et al., 2012; Kang et al., 2012; Lee et al., 2010; Mathew et al., 2014; Yella et al., 2014, 2011). Molecular modifications are needed in order to improve the light-harvesting properties of the basic porphyrin, especially at around 500 nm and beyond 600 nm. Inserting bulky donor moiety and combining with as the transition metal is the best approach up to now to achieve high performance porphyrin-based DSSCs (Griffith et al., 2012; Mathew et al., 2014; Yella et al., 2011). It has been mentioned above that the highest DSSC efficiency up to now is utilize Zinc-porphyrins dye as a sensitizer (Mathew et al., 2014). A non-certified power conversion efficiency of 13% was measured under full sun.

Transparent and Conductive Oxides (TCO)

TCO coated glass sheets are employed as substrates to deposit the photoanodes and the counter-electrodes. For the application, they must be transparent (Transmittance > 80%) and conductive (resistance < $10^{-3} \Omega \text{ cm}$). The two kinds of TCO mostly used in DSSC are ITO (indium tin oxide) composed of 90 wt % In_2O_3 ; 10 wt % SnO_2 and FTO (fluorine doped tin oxide) (Magne, 2012). The effect of TCO on the DSSC performance has been studied by Sima, et. al. and they have shown that the cell that used FTO as substrate had efficiency 9.6 %. This result was very high compared to that of ITO substrate, for which the efficiency just reached 2.24%. Both of cell employed N3 dye sensitizer and AN50 iodolyte electrolyte from Solaronix. The outstanding performance of FTO was due to its resistivity which is smaller than that of ITO (8.5 Ω/sq vs 18 Ω/sq). Moreover, the FTO resistivity is more thermally stable. It did not change after heat treatment at 450°C, whereas ITO resistivity increased to 52 Ω/sq after the same treatment (Sima et al., 2010) .

Unfortunately, FTO is a brittle material. Its mechanical brittleness then limit its usage (Jena et al., 2012). Flexible DSSCs are important for application, to make cells installed easily in building or electronic devices such as computer or mobile phone. Moreover, flexible DSSCs would be important for fabrication issue, to realize roll-to-toll mass production (Weerasinghe et al., 2013). Others materials, such as metal, carbon, plastic or others polymer have been studied to apply in order to make flexible DSSC.

Replacement of rigid substrate must address two issues, first the replacement of the photoelectrode substrate and second of the counter-electrode one. ITO/PEN (indium tin oxide coated polyethylene naphthalate sheets) or ITO/PET (indium tin oxide coated polyethylene terephthalate sheets) has been used widely as plastic substrate for photoelectrode. But, their utilization has limitations since these substrates have poor thermal stability require low

temperature photoelectrode processing. In the classical TiO₂ layer preparation, it will result in the poor necking of TiO₂ nanoparticles and poor connection between TiO₂ and the substrate. Consequently the cell performances will be low due to limited electron transport (Wang et al., 2014; Wu et al., 2014b). Based on this issue, the research on flexible-photoelectrode have focused on finding the best metal-substrate (Kang et al., 2006; J.-Y. Liao et al., 2012; Wu et al., 2014b) or on overcoming electron transport issue in low-heat-treatment preparation (Jin et al., 2014; Jung et al., 2013).

We give now examples of the utilization of metal-based substrates for working electrode. Kang et. al. have prepared flexible working electrodes that consisted of TiO₂ coated on both ITO and SiO_x-sputtered stainless steel foils. Their cell reached an efficiency of 4.2% under 100 mW/cm² illumination (Kang et al., 2006). Liao et.al used Ti-Foil as substrate for the photoelectrode. They deposited hierarchical TiO₂ nanowire arrays on Ti-foils by two steps hydrothermal reaction. Combining this working electrode with transparent PEDOT/ITO-PET (PEDOT poly-(3,4-ethylenedioxythiophene)) resulted in flexible DSSCs with a power conversion efficiency (PCE) of 4.32% (J.-Y. Liao et al., 2012). Ti based materials for flexible photoelectrode is the best choice compared to other metal due to their low corrosion properties but their opaque properties and the possibility of electron to trap in the TiO₂ particle has limited cell performance (Wang et al., 2014; Wu et al., 2014b). Recently, Wu, et. al have prepared flexible photoelectrode that consisted of TiO₂ nanoparticles on Ti-Foil substrates. This photoelectrode had three layers of TiO₂ with different structures, 1-D nanotubes, 3-D hierarchical microsized spheres and 0-D nanoparticles. The three layer design of photoanode TiO₂ could enhance light harvesting and charge collection thus delivering a cell PCE as high as 9.10% (Wu et al., 2014b).

Two main properties guide the research on flexible counter-electrodes: the conductivity and the capability of reducing tri-iodide (Chen et al., 2011; Hashmi et al., 2014; Hou et al., 2011; Yeh et al., 2011). Yeh, et. al have shown that the addition of titanium nitride nano-particles into poly(3,4-ethylene dioxythiophene):poly(styrene sulfonate) (PEDOT:PSS) matrix can increase the conductivity and they obtained flexible counter-electrode of DSSC with 5.82% of efficiency (Yeh et al., 2011). Other materials that have recently been studied as counter-electrode are carbon derivatives, such as activated carbon (Chen et al., 2011), carbon nanotube (Hashmi et al., 2014) and graphene (Roy-Mayhew et al., 2010). Carbon based materials have promising potential due to their inexpensiveness, chemical stability and good conductivity properties especially for carbon nanotubes and graphene allotrope.

Semiconductor

The semiconductor oxide plays an important role in DSSC. It receives electrons from photoexcited dyes attached on the surface and plays the role of the electron transport material ensuring the electron transfer to the front contact of the solar cell. To understand why wide bandgap semiconductors are used in DSSC photoanode, one has to describe the material's electronic properties.

Based on their electric conductivity, solid states materials are divided into three categories, insulators, semiconductors and conductors. Their conductivity properties can be explained by revealing their solid state electronic properties. To start, let us take a look at the atomic scale. Every atom has atomic orbitals fulfilled by electrons and others that are empty. Orbitals filled with electrons have lower energy compare to the empty ones. The filled orbital that has the highest energy is called HOMO (Highest Occupied Molecular Orbital), and that one lowest-empty energy is called LUMO (Lowest Unoccupied Molecular Orbital). In the case of solid materials there are a large amount of atoms. As a consequence, the outermost shell, subshell and orbitals merge, providing a greater number of available energy levels, then finally form a continues energy-bands. Therefore the HOMO in an atom becomes valence band in solids whereas the LUMO becomes conduction band. In some solids, there is a distance between conduction and valence band called band gap. It is also called a forbidden band where there is no possibility to find electrons. Information regarding energy level energy in solid states materials can be presented in energy diagrams.

Figure 2.6 shows energy diagram of insulator, semiconductor and conductor. The bandgap in Insulator is the largest, above 6 eV at room temperature. It indicates that energy above this value must be transferred to excite electron from the valence band to the conduction band. On the contrary, conductor materials do not have a band gap and their conduction band is partially filled. Semiconductors have an intermediate electronic property between insulator and conductor. The most commonly used semiconductors are germanium and silicon which have a bandgap energy of 0.72 eV and 1.1 ev respectively (Sharma, 1996). The bandgap energies for oxide semiconductor are generally quite large, for example $\text{TiO}_2 = 3.2\text{-}3.4\text{ eV}$; $\text{ZnO} = 3.2\text{ eV}$ and $\text{SnO}_2 = 3.8\text{ eV}$ (Gong et al., 2012).

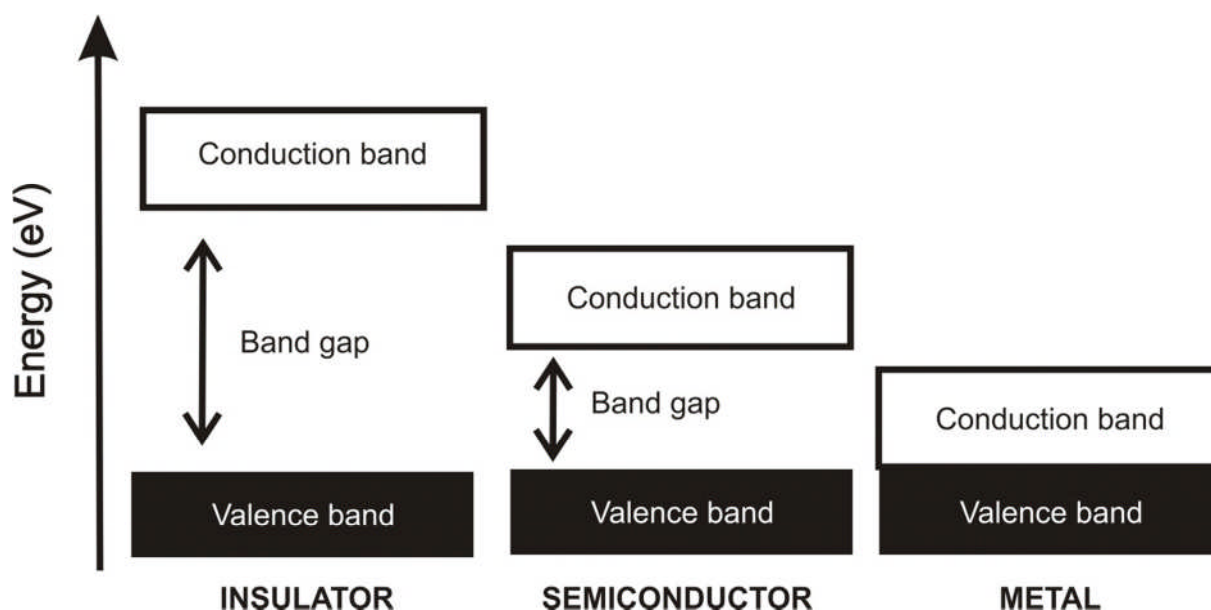


Figure 2.6: Energy diagram schematic of insulator, semiconductor and metal

Due to these unique electronic properties, semiconductors are widely used in electronic devices. Their conductivity can be controlled by applying certain energy which is suitable with the band-gap energy. In the case of photovoltaic solar cell devices, solar light energy is the source to generate electric energy. There are many different kinds of solar cell devices. DSSC development is motivated by replacing the widespread silicon solar cells by low-cost solar cells. Anatase TiO_2 has been chosen as a heart of DSSC due to its lower-cost, availability, chemical stability and adsorption ability. However, the electronic properties of this material limit its application since the TiO_2 -band-gap energy (around 3.2 eV) is only suitable for UV light absorption, which represents only $\sim 5\%$ of the solar spectrum. To broaden their absorbance spectral range towards the solar spectrum, TiO_2 is sensitized with a dye. Their conduction band energy level is suitable too with excited-sites energy level of many dyes. The breakthrough has been founded by Gratzel and O'Regan, who used mesoporous TiO_2 to apply in DSSC (O'Regan and Grätzel, 1991).

Aside from TiO_2 , there are others semiconductor that have promising potential to be used since their electronic properties electronic properties is similar to TiO_2 . Figure 2.7 shows an energy diagram of alternatives semiconductors along with energy level of some of redox-couples (Gong et al., 2012). ZnO is the most-commonly-studied semiconductor after TiO_2 . This section will focus on TiO_2 and ZnO, the two oxide semiconductor used in the present thesis.

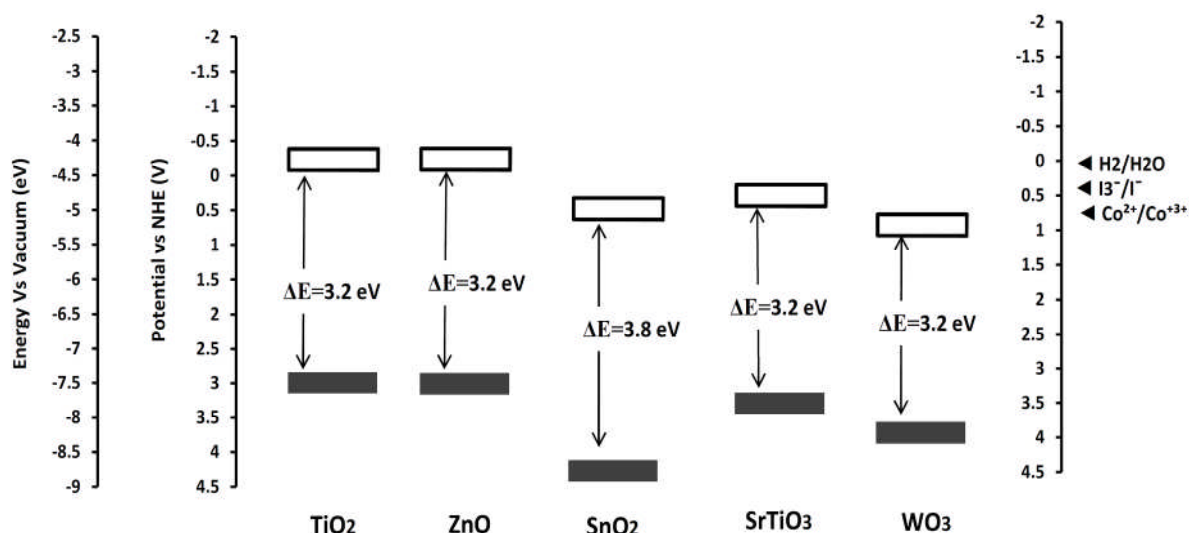


Figure 2.7: Energy diagram of several semiconductors together with potential redox of several redox-couples (Gong et al., 2012)

TiO₂

Titanium dioxide is a wide bandgap semiconductor gifted with many advantageous chemical, structural, optical and electronic properties (Facci and Huguenin, 2010; Fenoglio et al., 2009; Khare et al., 2011; Koziej et al., 2009; Y. Liao et al., 2012; Nussbaumer et al., 2003). The main applications of TiO₂ include pigments (Y. Liao et al., 2012), functional coatings (Parkin and Palgrave, 2005), gas sensors (Karunagaran et al., 2007), batteries (Wang et al., 2009), photocatalysis (Fujishima et al., 2008; Linsebigler et al., 1995) and the energy field through, for instance, hydrogen production (Ni et al., 2007) and solar cells (Burschka et al., 2013; Kim et al., 2012; Liu and Kelly, 2014).

There are three polymorphs of TiO₂ stable under ambient conditions, namely anatase, brookite and rutile. Brookite is stable up to 600°C and anatase up to 836°C (Magne et al., 2012), whereas at higher temperature they transform to the rutile phase. Rutile and anatase are structurally similar, being made of TiO₆ octahedra chains. The difference between their structures lies in the higher distortion in anatase compared to in rutile, so anatase has a lower orthorhombic symmetry (Lancelle-Beltran et al., 2008). On the contrary, brookite adopts an orthorhombic structure in which the octahedra share three edges and also corners, and the dominant structural feature is a chain of edge sharing (Chen and Mao, 2007). Figure 2.8 shows the crystal structures of the three main TiO₂ polymorphs.

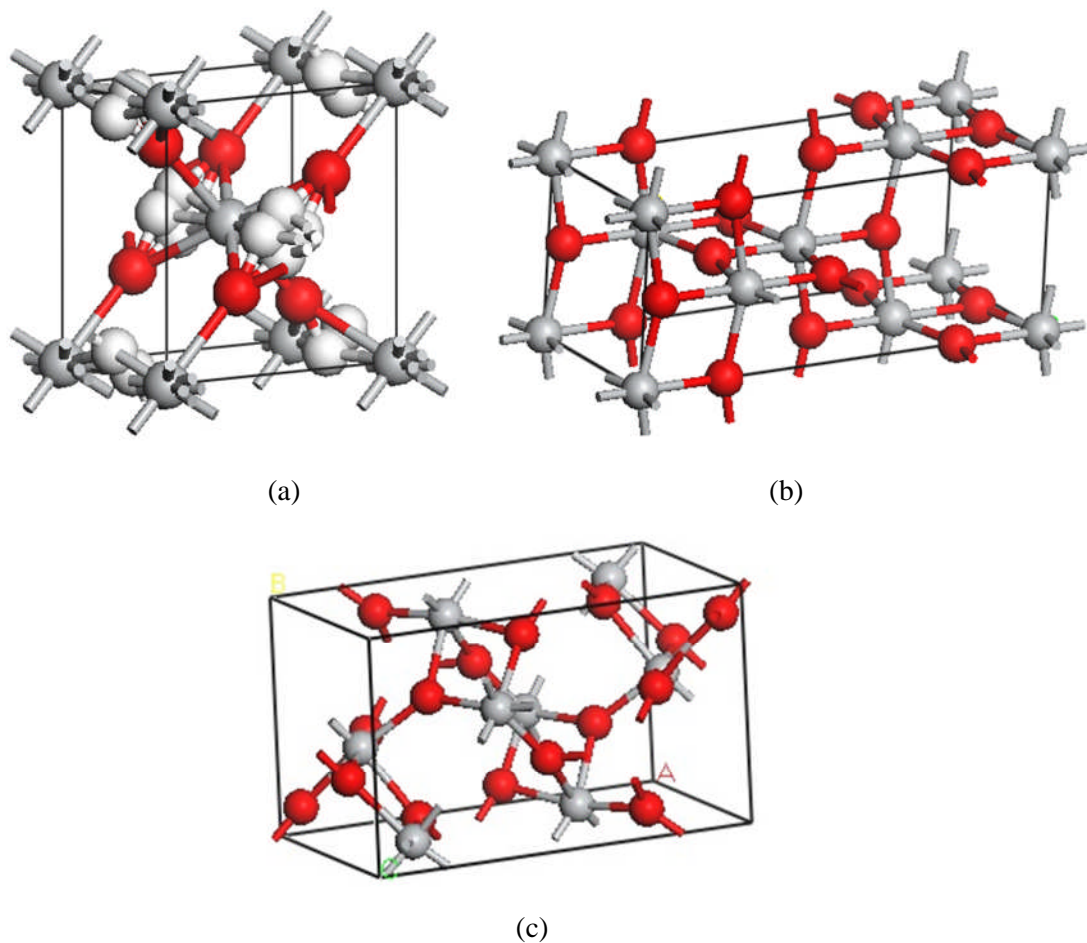


Figure 2.8: Crystal structure of (a) rutile (b) anatase and (c) brookite; White = titanium, red = oxygen.

The difference in term of structure between the TiO_2 polymorphs leads to different properties. For example, in rutile each octahedron is in contact with 10 neighbor octahedra whereas in anatase, each octahedron is in contact with 8 neighbor octahedra. This lattice structure makes rutile denser compared to anatase, furthermore, it makes their electronic band structures different with different bandgaps (Lancelle-Beltran et al., 2008; Reyes-Coronado et al., 2008). Some physical properties of brookite lie between those of rutile and anatase. For example, the refractive index of anatase, brookite, and rutile increases in the order 2.52, 2.63, and 2.72, while their theoretical density are 3.84, 4.11, and 4.26 g/cm^3 , respectively (Chen and Mao, 2007).

Among the three polymorphs of TiO_2 , anatase is the leading phase used in most of the DSSC literature because of its good conductivity (Hagfeldt et al., 2010; Reyes-Coronado et al., 2008). Moreover, the anatase (101) surface has the lowest surface energy, which supports the dye adsorption (Fisher et al., 2000). There are few data on DSSCs using the rutile phase.

DSSC based on this phase has drawn some attention because of its potentially cheaper production cost and its superior light-scattering characteristics that could be useful for solar light harvesting (Bisquert and Vikhrenko, 2004; Magne et al., 2011; Thomas and Syres, 2012). Brookite has been very poorly investigated for DSSC application. Very low conversion efficiency has been reported by Lancelle-Beltran et al. for nano-brookite based solid-state DSSCs (Lancelle-Beltran et al., 2008). Jiang, et al. have studied the use of a 75% brookite and 25% anatase mixture in DSSC photoelectrodes and they have obtained an efficiency of 4.1% (Jiang et al., 2000). Magne, et. al. have shown that brookite has potential for use in DSSC (Magne et al., 2012).

ZnO

ZnO can be used as an alternative material to replace TiO₂ in DSSC. Wurtzite ZnO is the most stable crystal structure of ZnO (Figure 2.10). Actually, it can be noted that ZnO was the first semiconductor that be used in DSSC (Tsubomura et al., 1976). Compared to TiO₂, ZnO has higher electron mobility and diffusion coefficient. This is potentially advantageous for DSSC application because it can provoke fast charge transport and reduce charge recombination (Quintana et al., 2007; Zhang et al., 2009). The comparison of TiO₂ and ZnO properties are summarized in Table 2.1

There are many factors that have been reported to limit the application of ZnO in DSSC and contribute to the lower efficiency of ZnO-based DSSCs compared to the TiO₂ ones. These factors are slow electron injection, low dye regeneration (Quintana et al., 2007) and instability of ZnO in acidic solution of dye (Zhang et al., 2009). The study of the electron injection kinetics from dye (Ru-polypyridyl complexes) to ZnO shows that injection time scales in thermalized and relaxed excited states are 1.5 and 150 ps respectively. These values are one order of magnitude slower than those in TiO₂ (Anderson et al., 2003). The difference in the injection kinetics between ZnO and TiO₂ is explained by the difference in the conduction-band of structures and the mechanism of the electron injection of ZnO which passes through intermediate states (Zhang et al., 2009).

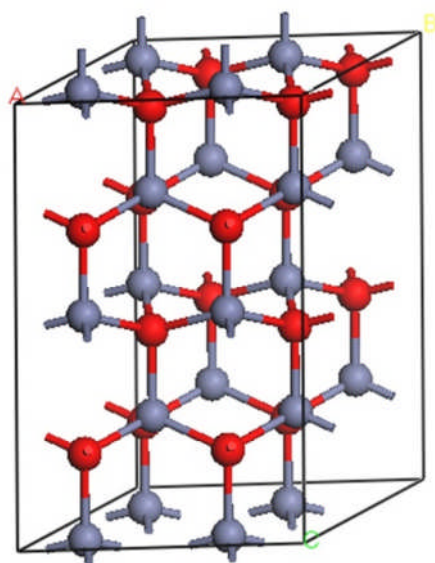


Figure 2.9: Wurtzite ZnO crystal structure, consisting of a (2x2x2) unit cell.

Table 2.1: The different between ZnO and TiO₂ (Zhang et al., 2009).

Properties	ZnO	TiO ₂
Crystal structure	rocksalt, zinc blende, wurtzite	rutile, anatase, brookite
Energy band gap (eV)	3.2-3.3	~ 3.0 eV (rutile), 3.05-3.2 eV (anatase), ~3.4 eV (brookite)
Electron mobility (cm ² Vs ⁻¹)	205-300 (bulk ZnO), 1000 (single nanowire)	0.1-4
Refractive index	2.0	2.52 (anatase), 2.63 (brookite), and 2.72 (rutile)
Electron effective mass (m_e)	0.26	9
Relative dielectric constant	8.5	170
Electron diffusion coefficient (cm ² s ⁻¹)	5.2 (bulk ZnO), 1.7 x 10 ⁻⁴ (nanoparticulate film)	0.5 (bulk TiO ₂), ~ 10 ⁻⁸ - 10 ⁻⁴ (nanoparticulate film)

Dyes that are usually used in DSSC will connect with TiO₂ through the bonding of carboxyl groups of the dye. This bonding is difficult to form in ZnO, because it is not stable in the condition of acidic solution of the dye. Furthermore this condition can provoke the agglomeration of Zn²⁺ with the dye. Some researchers have suggested strategies to overcome this problem. Sakuragi, Y., et. al. used Cholic Acid (CA) to prevent aggregation of indolines dye (D149) (Sakuragi et al., 2010). Whereas Magne, et. al., showed that Octanoic Acid has better performance to prevent this aggregation compared to CA because OA is less steric than CA (Magne et al., 2012).

A major interest of ZnO is that its crystallization and anisotropic growth is relatively easy. Therefore the preparation of ZnO structures with various shapes is quite easy. A one-dimensional nanostructure of ZnO, called nanowire, is important in DSSC because it can reduce the recombination rate (Zhang et al., 2009). Branched ZnO nanowires are also interesting due to their ability to adsorb more dye sensitizer (Omar and Abdullah, 2014). Another interesting material is hexagonal rod-like particles of ZnO that are 35 nm in diameter. These structures are used to prepare porous films by sintering that facilitates electron charge transport. Moreover, they present rather large pores that provide good space for dye sensitization and electrolyte penetration resulting in a better power conversion efficiency compared to other shapes (Hosni, 2014).

Counter Electrode

In DSSCs, the counter electrode catalysis the oxidized shuttle species reduction reaction. As mentioned in a previous section TCO, especially FTO, is classically used as a counter electrode after activation by deposition of a catalyst. The most commonly used catalyst is platinum (Pt) (Jena et al., 2012). Pt is deposited on substrate by thermal annealing of a salt, electrodeposition or vapor deposition. To limit the cost, a small amount of Pt is deposited, usually about $5 \mu\text{g.cm}^{-2}$ (Hagfeldt et al., 2010).

There have been many materials studied to replace Pt such as carbon materials (graphene (Roy-Mayhew et al., 2010) or carbon nano-tubes (Hashmi et al., 2014)), conducting polymers (such as Poly(3,4-ethylenedioxythiophene) (PEDOT)) or cobalt sulfide that have good catalytic properties. Even if their performances are not as good as Pt, but their use seems economically promising (Hagfeldt et al., 2010).

Electrolyte

The electrolyte consists of a redox-couple and additives dissolved in an organic solvent. The most important component of the electrolyte is the redox-couple. The role of the redox-couple is to regenerate the oxidized dye by providing an electron. I_3^-/I^- is the most popular redox couple used in DSSCs since the pioneering work by O'Regan and Gratzel in 1991 (O'Regan and Grätzel, 1991). Its main advantage lies in the slow reduction kinetics of I_3^- and the slow recombination parasitic reaction (Gong et al., 2012). Moreover, I_3^-/I^- almost fulfills the main requirements of component electrolyte which are: a redox potential located below the HOMO level of the dye, an efficient regeneration of the dye, a high conductivity ($\sim 10^{-3} \text{ S.cm}^{-1}$), an easy penetration into photoanode pores, a good contact between photoanode

and counter-electrode. Moreover, it does not cause desorption of the dye from photoanode, does not damage the sealant of the cell and it has a good chemical and thermal stabilities (Boschloo and Hagfeldt, 2009; Jena et al., 2012).

To gain in performance, several chemical additives must be added into the electrolyte. Most of them are added in order to avoid the reduction of redox-couple on the semiconductor surface. For example, the addition of 4-tert-butylpyridine (TBP) leads to a negative shift of the conduction band edge to a higher energy and finally make enlarges of the cell V_{oc} . On the contrary, this effect decreases the J_{sc} due to a reduction of the driving force for electron injection from the excited dye into the conduction band. This mechanism is different to the one described for guanidinium thiocyanate (GuT) additive. The adsorption of GuT on the semiconductor surface shift the conduction band toward lower energy and promotes the J_{sc} as a result of the increase of the driving force for the electron injection from the excited dye into the conduction band. Moreover, V_{oc} is also enlarged because of the blocking effect of the adsorbed cation on semiconductor surface (Jena et al., 2012). Li^+ has been also described as an important additive. Its presence provokes a decrease in the flatband potential that finally enhances the electron injection (Taya et al., 2014).

The progress in DSSC research has revealed that I_3^-/I^- redox-couple is not the best electrolyte shuttle for DSSCs because it has corrosive properties towards metals including Ag, Au and Cu, that makes the material selection for DSSC module very limited. I_3^-/I^- has also two other disadvantages: first, it absorbs the light in the 350-450 nm wavelength region and second, its reduction potential value is quite low and restricts the open circuit voltage in the DSSC (Fan et al., 2013; Feldt et al., 2011; Hamann, 2012; Klahr and Hamann, 2009).

Cobalt (II)/(III) complex redox couples are ones of the major candidates to replace I_3^-/I^- . They have promising properties such as less absorbance in the 350-450 nm region compared to that of I_3^-/I^- , low-corrosive properties, by changing the ligands or by adding certain substituents to the ligand they can be fitted with the dye ground state potential, in favor of dye regeneration with a minimal over-potential loss (Feldt et al., 2011; Hamann, 2012; Yum et al., 2012) On the other hand, cobalt (II)/(III) complexes have a bulky structure that hinder mass transport through photoelectrode and has a quite rapid recombination kinetics with electron from the TiO_2 conduction band (Hamann, 2012).

Some efforts have been made to overcome the limitation of cobalt-based DSSCs. The utilization of thin and more porous photoelectrodes are required to facilitate mass transport of cobalt redox species (Feldt et al., 2010; Hamann, 2012; Pazoki et al., 2014). Some researchers

covered the TiO₂ surface using alumina to passivate it. Alumina can inhibit the recombination of electrons by acting as a barrier between conductive electrons and the redox mediator (Pascoe et al., 2013). Employing dyes that have long alkyl chain or bulky alkoxy groups can restrain the recombination at the semiconductor and electrolyte interface (Bai et al., 2011; Feldt et al., 2011, 2010).

The best of cobalt-based DSSCs until now, which were also the best performing DSSCs, employed a donor- π -bridge-acceptor (D- π -A) porphyrin dye endowing with alkoxy group as sensitizers for TiO₂-based DSSC. The cell efficiency reached 13% under simulated air mass 1.5 global-one sunlight (Mathew et al., 2014) The use of a cobalt redox-couple in ZnO-based DSSC is not well-documented. Fan. J et. al reported the utilization of LEG4 sensitized ZnO nanowires coupled with [Co(bpy)₂]^{2+/3+} (bpy= 2,2'-bipyridine) as redox-couple for DSSC application. A power conversion efficiency of 2.7% was reported (Fan et al., 2013).

The effect of additive on cobalt-based cell performances has been studied. It is reported that increasing of Li⁺ provokes an increase in electron lifetime due to the reduction of charge-transfer rate as a consequences of a decrease of the Co³⁺ local concentration. The addition of 4-*tert*-butylpyridine with the presence of Li⁺ facilitates charge transfer from Co²⁺ to dye cation and then improves the short circuit current (J_{sc}) (Feldt et al., 2010).

II. 1.2. Electron Transport in DSSC

Charge transport, recombination and transfers are the main processes that occur in DSSCs. To gain ideal efficiency it is important to understand their mechanism. This section describes the main electron route in DSSC devices, and the unwanted recombination of electron pathways.

Light Harvesting

Light absorption by the dye provides energy to promote electrons to a higher energy. After photon absorption of accurate energy, electrons from HOMO of the dye are excited into the LUMO. λ_{max} of molecule absorption spectra may correspond to another electronic transition, for example in TG6 λ_{max} at 550 nm corresponds to the transition of electrons from HOMO-2 to LUMO (Matar et al., 2008). Another example, is found for N749 in which the λ_{max} at 610 nm corresponds to electron transition from HOMO to LUMO+6 orbitals (Liu et al., 2012). Techniques to increase light harvesting are not only restricted to the molecular structure modification or dye co-sensitization to broaden absorption in the desired wavelength

region as mentioned in section II.1.1 (page 16) They also include doping of TiO₂ with a rare earth ion to improve the UV-light harvesting through the down-conversion (DC) process (Chuang et al., 2014; Hafez et al., 2011; Klampaftis et al., 2009; Li et al., 2011). For example, Hafez et. al. doped TiO₂ with the lanthanide ions, Sm³⁺ and Eu³⁺. They found that the UV-light capturing was significantly improved and increased the cell efficiency (Hafez et al., 2011). Modifying the TiO₂ structure can also be another alternative to improve the light harvesting, for example cactus-like branched TiO₂ arrays with a large surface area and a good light scattering capability have been reported (Wu et al., 2014a).

Electron injection from the excited dye to semiconductor

Electrons need to be injected into semiconductor conduction band after its activation. Effective transitions which can easily transfer into the semiconductor are needed. The first requirement for this is that the position of LUMO or of another orbital which is the excited electron destination (for example LUMO+1) of dye must be near anchoring group (Le Bahers et al., 2014). Computational studies can investigate how the dye attaches to semiconductor surface, behavior of electron excitation and electron distribution in dye attached semiconductor system (Le Bahers et al., 2011). Figure 2.10 shows an example of computational calculation result that give information about how the N749 dye is attached onto (101) TiO₂ anatase surface. Furthermore, it describes the electron injection process.

There are other factors that influence the effectiveness of the electron injection process, such as the heterogeneity of the semiconductor surface, the binding mode and strength of the dye on the semiconductor surface and also the possible interaction between dyes (Asbury et al., 2000; Hagfeldt et al., 2010). Additives that are dissolved in the electrolyte and have the ability to shift semiconductor conduction band energy will also influence the electron injection (Koops et al., 2009).

Kinetically, the electron injection efficiency is defined with formula (Hagfeldt et al., 2010):

$$\varphi_{inj} = \frac{k_{inj}}{k_{inj} + k_i} \quad [2.1]$$

where, k_{inj} and k_i are the rate constant for electron injection and decay (radiative and nonradiative) of the excited dye, respectively. To obtain an ideal injection, k_{inj} must not be

much higher than k_i , but the good comparison value is more than 100 times (Hagfeldt et al., 2010).

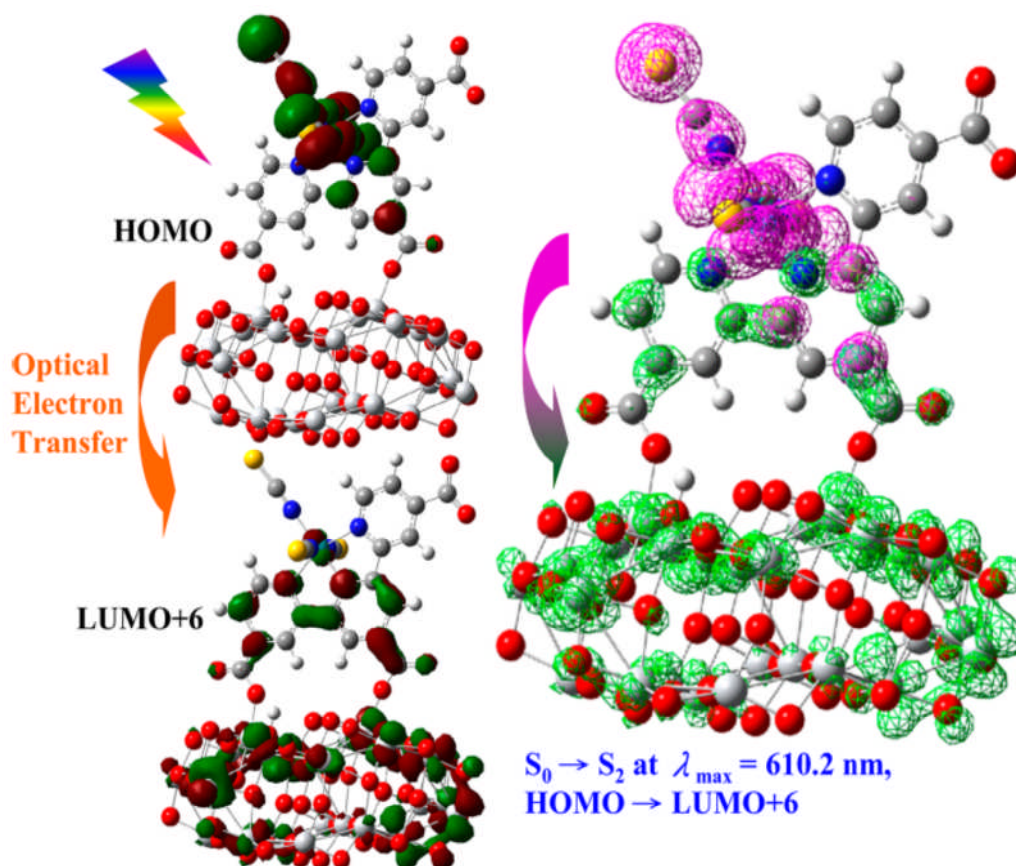


Figure 2.10: Simulation of optical absorption of N749 dye attached on TiO_2 surface along with HOMO and LUMO+6 configurations, the orbitals that correspond to the absorption. Right: Charge density difference between the ground state S_0 and the excited state S_2 . Pink mesh indicates the decrease in charge density, while green mesh indicates the increase in charge density upon photoexcitation. The isovalue for the contours is 0.02(Liu et al., 2012)

Electron transport in semiconductor

To gain electricity, electron must travel inside the semiconductor. As we know that semiconductor consists of nanoparticles, it means that electrons must travel through a lot of particles before they reach the TCO front contact. Electron transport in the mesoporous of TiO_2 is different from that of in ionic compound or single crystal of TiO_2 . It will be influenced by many factors that are mainly due to particles properties such as particle connectivity, geometry of particles and electronic coupling between particles. These make electron transport in particles much slower than that in single crystal (Jose et al., 2009).

Electron transport in mesoporous oxides is explained by Multiple-Trapping (MT) mechanisms. This mechanism consists of electrons trapping-detraping process that reduced the rate of electron transport. Electrons are considered to be mostly trapped in localized states below the conduction band, from which they can escape by thermal activation. The traps involved in electron transport in DSSC are localized in the bulk, at the grain boundaries or at the interface between TiO_2 surface and electrolyte as described in Figure 2.11 (Hagfeldt et al., 2010). Surface traps have greater influence on recombination than bulk traps due to their location that has ability to couple with electrolyte (Pascoe et al., 2013; Zhang et al., 2014). Surface traps can be reduced or eliminated by surface passivation, while bulk traps are difficult to passivate (Zhang et al., 2014). By applying surface passivation it creates a tunneling barrier between the semiconductor and the redox mediator (Pascoe et al., 2013).

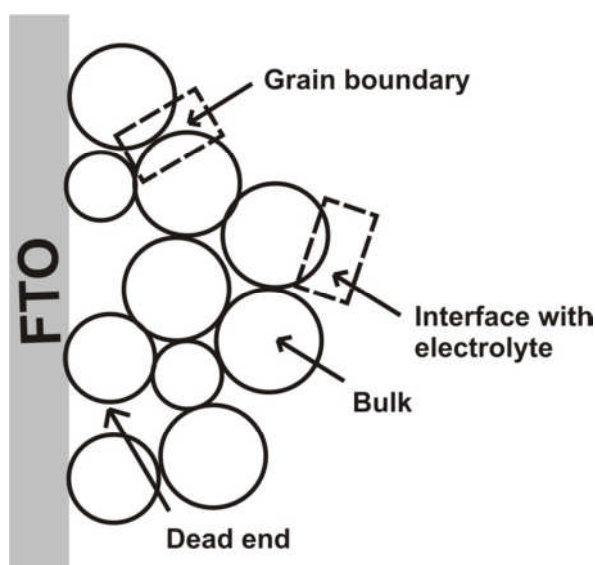


Figure 2.11: Various traps location in the semiconductor.

The influences of the particle geometry on the electron diffusion coefficient has been studied by Villanueva-Cab et.al (Villanueva-Cab et al., 2014). They have investigated electron transport in nanotubes and nanoparticles of TiO_2 . They obtained that a trap-free diffusion coefficient in the nanotubes ($4 \times 10^{-1} \text{ cm}^2 \text{ s}^{-1}$) almost the same as in single crystal (1.4×10^{-1}) and up to two orders of magnitude higher than those observed in nanoparticles (1.4×10^{-3}) (Villanueva-Cab et al., 2014). One- dimensional structures such as nanorods like or nanowires have promising performance in electron transport but they have low surface area that limits the dye loading and sensitization (Sheng et al., 2014; Wijeratne and Bandara, 2014).

Combining one-dimensional with three-dimensional structures has been studied by Sheng et. al. They prepared single-crystal-like 3D TiO₂ branched-nanowire arrays consisting of 1D branches epitaxially grown from the primary trunk. This structure showed 52% improvement in power conversion efficiency due to a 71% increase in surface area compared with 1D nanowire but still had comparable charge transport compare to that of 1D single crystal nano-arrays (Sheng et al., 2014).

The dependence of semiconductor surface area on electron diffusion through TiO₂ has been investigated by Nakade et.al. (Nakade et al., 2003). They found that diffusion coefficient increased with increasing particle size due to decreasing in surface area where the charge trap sites mostly are located. Unfortunately, decreasing surface area means the amount of dye-attached onto the surface will be decreased too, and it results in a lowered light harvesting efficiency (Nakade et al., 2003). Whereas a different trend was observed in TiO₂/graphene photoanode, that showed increasing in electron mobility with decreasing TiO₂ particle size. This phenomenon was explained by the formation of more continuous and intimate conduction network with graphene in smaller TiO₂ particles (He et al., 2013).

Electron transport in Electrolyte

Charge transport in electrolyte occurs through redox-couple species diffusion. The redox shuttle is reduced at the counter-electrode of the device whereas the dye adsorbed on the semiconductor surface is place where the redox-couple is oxidized by the oxidized-dye. The properties of the electrolyte, as medium transport, are the primary factor that influenced electron transport. Electrolyte viscosity, concentration and distance between the two electrodes are the parameters that influence electron diffusion (Boschloo and Hagfeldt, 2009; Hagfeldt et al., 2010). For cobalt-based DSSC, it is important to have larger size of semiconductor pores to facilitate the diffusion of redox species (Hamann, 2012).

Dye Regeneration

After light irradiation and charge transfer, the dye is in an oxidized state. It is reduced by electron donation from the redox-couple species dissolved in electrolyte. It is an important process since it makes the dye ready for the next turnover of electron cycle. Dye regeneration competes with reduction of oxidized species by the electrons present in the semiconductor surface.

Kinetics studies have shown that the dye regeneration by tri-iodide passes through the formation of intermediate species such as I_2^- radical (Hagfeldt et al., 2010). This step requires a high driving force and then induces a limitation of the cell potential output. It was recorded that for the regeneration of the ruthenium dyes series with tri-iodide a driving force of about 0.5 eV is needed that limiting the cell V_{oc} values around 0.7-0.8 V (Feldt et al., 2011; Friedrich et al., 2014)

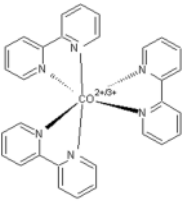
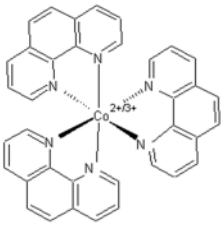
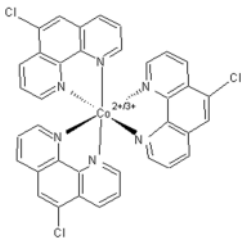
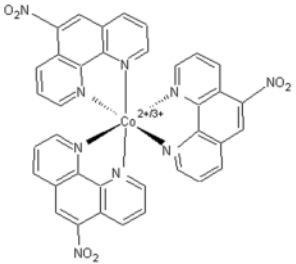
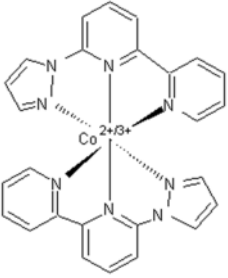
The addition of cations, such as Li^+ or Mg^{2+} into electrolyte that adsorb on the semiconductor surface increases the regeneration rate due to the creation of a higher local iodide concentration near the semiconductor surface (Hagfeldt et al., 2010). Several other redox-couples have been considered due to their similar properties with iodine, such as Br^-/Br_3^- , $SCN^-/(SCN)_3^-$ and $SeCN^-/(SeCN)_3^-$ (Boschloo and Hagfeldt, 2009). Cobalt-complexes redox-couples that have a more positive redox-potential have proven to increase V_{oc} due to a lower driving force of dye regeneration compare to that of iodine (Feldt et al., 2011). The molecular structure and the redox standard potential of some studied cobalt-complexes are gathered in Table 2.2.

Electron recombination

There are two electron recombination pathways described in the literature that reduce the DSSC efficiency due to rather slow electron travelling through semiconductor mesoporous to the photoelectrode front contact. First, the recombination of electron from semiconductor conduction band to an oxidized electrolyte species. Second, the recombination of electron from semiconductor conduction band back to HOMO states of oxidized dye. The former is the first source of cell performance loss, since dye regeneration as the competitive reaction of the second recombination, usually occurs rapidly (Bisquert et al., 2004; Hagfeldt et al., 2010).

The recombination reaction to the redox electrolyte species dominantly occurs at the interface of semiconductor and electrolyte, even if there is a little possibility to occur at the interface of conducting substrate and electrolyte (Boschloo and Hagfeldt, 2009). Recombination with I_3^- is favored under normal light intensity, whereas recombination with I_2^- preferably occurs under high light intensities (Bisquert et al., 2004; Boschloo and Hagfeldt, 2009). The presence of additive such as 4-*tert*-butylpyridine or guanidine thiocyanate can decrease recombination rate due to the blocking effect of cation that avoid electrolyte species to reach the semiconductor surface, as described in the section II.1.1 (page 27) (Boschloo and Hagfeldt, 2009; Taya et al., 2014).

Table 2.2: Some cobalt-complexes that have been studied

Cobalt-complexes	Structure	Standard potential redox (V, NHE)	Reference
$[\text{Co}(\text{bpy})_3]^{2+/3+}$ = cobalt (II/III) tris(2,2'-bipyridine)		0.56	(Feldt et al., 2011)
$[\text{Co}(\text{phen})_3]^{2+/3+}$ = cobalt (II/III) tris(1,10-phenanthroline)		0.62	
$[\text{Co}(\text{Cl-phen})_3]^{2+/3+}$ = cobalt (II/III) tris(5-chloro-1,10-phenanthroline)		0.72	
$[\text{Co}(\text{NO}_2\text{-phen})_3]^{2+/3+}$ = cobalt (II/III) tris(5-nitro-1,10-phenanthroline)		0.85	
$[\text{Co}(\text{bpy-pz})_2]^{2+/3+}$ = cobalt (II/III) bis(6-(1H-pyrazol-1-yl)-2,2'-bipyridine)		0.86	(Yum et al., 2012)

Since the recombination reaction compete with electron transport in semiconductor then the semiconductor electronic properties will also influence the recombination rate. Recombination with oxidized dye usually occurs in a time scale of picoseconds to milliseconds (Hagfeldt et al., 2010; Haque et al., 2000). Haque, et. al found that this recombination is very dependent on the electron occupation in trap/conduction band states of the TiO₂. This electron occupation will be influenced by light intensity, applied electrical potential, electrolyte composition, the oxide and its structure. Variation of the external applied potential by only 600 mV results in a 10⁷-fold acceleration of the recombination kinetics. Similarly, a 500 mV shift in the TiO₂ conduction band/trap density of states induced by variations in electrolyte composition results in a variation in recombination rate by up to 10⁶ (Haque et al., 2000). Study of molecular structure of dye on semiconductor showed that the recombination rate depends on the spatial separation of the dye cation HOMO orbital from the metal oxide surface. This point must be considered to construct new dye for use in DSSC (Clifford et al., 2004; Ganesan et al., 2014).

Employing cobalt-based redox-couples reduces the recombination due to the bulky structure of the molecule. In addition, we know that the cobalt-redox will convert from Co(III) (low spin) into Co(II) (high spin). During this process, a large inner-sphere reorganization energy (~ 1eV) occurs, acts as a barrier for self-exchange kinetics and then finally provokes slow recombination kinetics at the TiO₂ electrode (Hamann, 2012; Nakade et al., 2005; Ondersma and Hamann, 2011).

II.1.3 Basic Principle in Cell Characterization

The basic principles of the main characterization techniques used here for the cell performance and functioning investigations are described in this section. They include current-voltage (*I-V*) curve measurement, Incident-photon-to-electron conversion efficiency (IPCE) and Impedance Spectroscopy (IS).

I-V Measurement

I-V measurements are done by measuring cell current as a function of the applied voltage. With these measurements we can determine the total cell Power Conversion Efficiency (PCE), also noted (η), given by:

$$\eta = \frac{|J_{max} \cdot V_{max}|}{P_{in}} = \frac{J_{sc} V_{oc} FF}{P_{in}} \quad [2.2]$$

$$\text{With, } FF = \frac{|J_{max} \cdot V_{max}|}{J_{sc} V_{oc}} \quad [2.3]$$

where, P_{in} is the power density of the incident light; J_{max} and V_{max} are the value of current and voltage respectively when P cell reach maximum value; J_{sc} is the short circuit current; V_{oc} is the open circuit voltage; FF is the fill factor. The fill factor value ranges between 0 and less than 1. It describes the decreasing of photocurrent with increasing of applied voltage and is related to the I - V curve shape. The squarer of the curve shape the higher the FF value (Hagfeldt et al., 2010; Jose et al., 2009). Typical I - V curves that has $FF = 0.46$ and 0.67 are shown in Figure 2.12. It is shown that an I - V curve with $FF = 0.67$ has a more square curve-shape than that of the cell with $FF = 0.46$. Figure 2.12 also shows a P - V curve which allows the determination of I_{max} and V_{max} .

The standard measurement is done at 25°C , under AM 1.5 G (AM for *air mass*; G for global) solar irradiation. AM is a parameter that is related to the incident solar light defined as:

$$AM = \frac{1}{\cos \theta} \quad [2.4]$$

Where θ is the angle of elevation of the sun (as presented in Figure 2.13). AM 1.5 G occurs for $\theta = 48.2^{\circ}$. The normalized spectrum at this value has a radiance power (integrated irradiance) of 1000 W/m^2 .

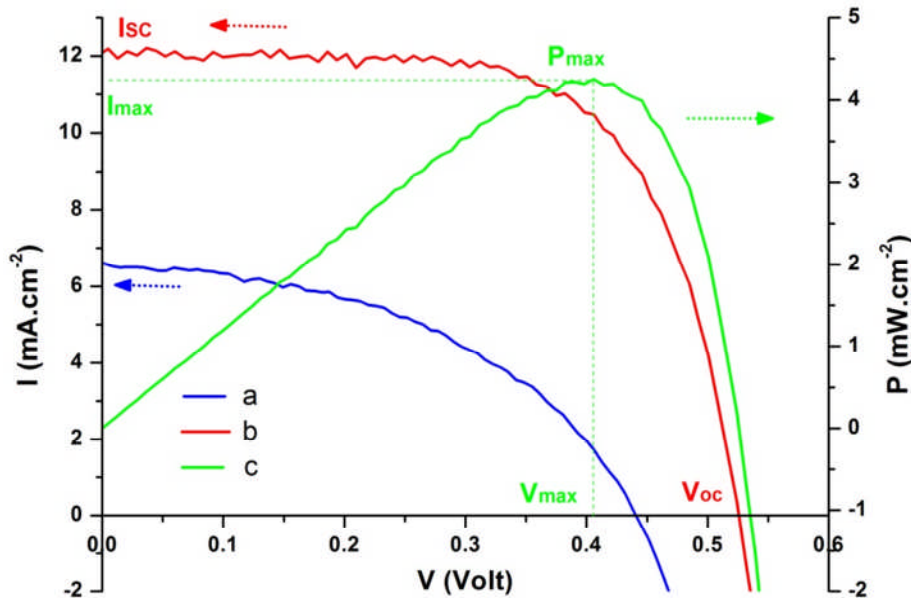


Figure 2.12: I - V curves of (a) a cell A with $FF = 0.46$; and (b) a cell B with $FF = 0.67$. (c) P - V curve of cell B (Data is taken from our experimental data base)

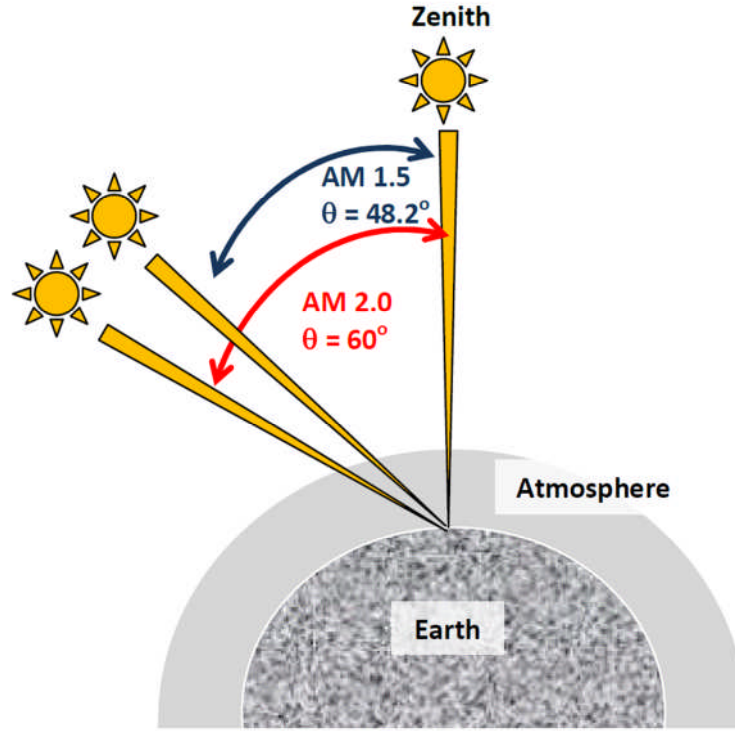


Figure 2.13: Air Mass calculation

Impedance Spectroscopy (IS)

IS is a powerful technique to study the electrical charge transfer and accumulation in the cell upon functioning. IS usually is measured by applying a small (3-20 mV) sinusoidal potential excitation signal (ΔV), at certain potential, V ;

$$V = V_0 + \Delta V = V_0 + v \sin(\omega t) \quad [2.5]$$

With v is amplitude of the signal and (ω) is the angular frequency when a certain voltage is applied.

The response to this potential perturbation is a pseudo-linear AC current signal, ΔI , that will be a sinusoid at the same frequency but phase shifted (φ) and with a different amplitude, i . It is written;

$$I = I_0 + \Delta I = I_0 + i \sin(\omega t + \varphi) \quad [2.6]$$

Electrical impedance (Z) is defined as the measure of the opposition that a circuit presents to a current when a voltage is applied. It can be analogized as resistance (R) in DC circuit. The difference is that Z has both a magnitude and a phase component. It is formulated:

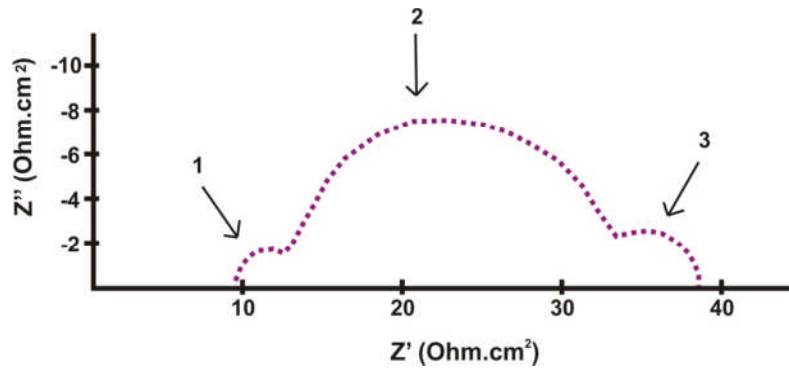
$$Z(\omega) = \frac{\Delta V}{\Delta I} \quad [2.7]$$

$$Z = |Z|e^{j\varphi(\omega)} = Z' + jZ'' \quad [2.8]$$

IS measurement result can be present as two kinds of spectra, Z' vs Z'' and/or phase φ ($^\circ$) vs frequency (Hz). Where;

$$\tan(\varphi) = \frac{Z''}{Z'} \quad [2.9]$$

A typical Nyquist plot of an IS DSSC spectrum is presented in Figure 2.14



Figures 2.14: Typical Nyquist plot of electro impedance spectra (first semi-circle at high frequency; second semi-circle at medium frequency; third semi-circle at low frequency)

To gain interpretation into this spectrum an electrical-circuit model that represents the cell must be constructed. In the DSSC system based on a liquid electrolyte with ionic species, electron diffuses in the mesoporous TiO_2 and also experience the recombination with the oxidized species of the redox shuttle. The best circuit that represents this model is shown in Figure 2.16 (Bisquert, J and Fabregat-Santiago, F 2010). For mesoscopic-oxide layer with a thickness $= L$, R_{ct} ($=r_{ct}/L$) is the charge-transfer resistance (recombination process) that occurs at the interface of the mesoporous metal oxide film and the electrolyte; C_μ ($=c_\mu \cdot L$) is the chemical capacitance of the mesoporous metal oxide film; R_{tr} ($=r_{tr} \cdot L$) is the transport resistance of the electrons traveling in the mesoporous metal oxide films; Z_d is the Warburg element showing the Nernst diffusion of ions in the electrolyte; R_{pt} and C_{pt} are the charge-transfer resistance and double-layer capacitance at the counter electrode; R_{BL} and C_{BL} are the resistance and capacitance due to the contact of TCO and electrolyte; R_s is the series resistance due to electrical contacts and TCOs (Jose et al., 2009; Magne et al., 2013a).

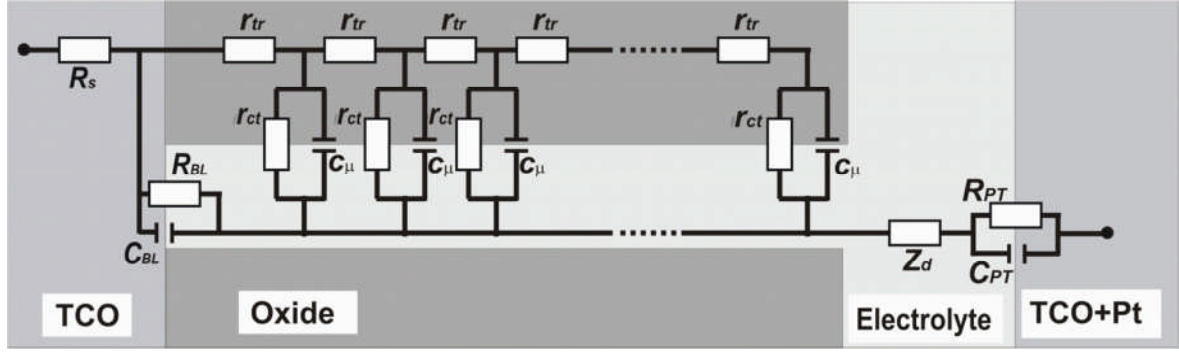


Figure 2.15: Electrical equivalent circuit of typical DSSC (Magne et al., 2013a; Pauporté and Magne, 2014)

We can extract the values of R (resistance) and C (capacitance) from EIS spectra. Each of the arc-of-circles results from a combination of R and C . Using the electrical equivalent circuit model as shown in Figure 2.15, each of arc-of-circle in the IS spectra (Figure 2.15) have a meaning; the first semicircle of spectra that appears at high frequency corresponds to regeneration of redox-couple at counter-electrode; the second arc-of-circle, at the medium frequency, with a segment at more or less 45° in its high frequency parts corresponds to the diffusion and recombination of electrons in the mesoporous semiconductor oxide; the third arc-of-circle with a segment at more or less 45° in its high frequency part that appears at low frequency corresponds to the diffusion of the redox-couple ions in the electrolyte.

Studying IS spectra at various voltages in the dark and under illumination is very powerful to extract many parameters that are related to the electron transport and accumulation in DSSC. First of all, by impedance spectra fitting, we can determine the chemical capacitance C_μ due to electron trapping in states distributed below the conduction band edge. Through semi-logarithmic plot of C_μ to the voltage we can extract α , a parameter that accounts for the depth of the trap energy level (Magne et al., 2013a; Pauporté and Magne, 2014; Wang et al., 2006):

$$C_\mu = C_{0,\mu} \exp \left[\alpha \frac{qV_{cor}}{k_B T} \right] \quad [2.10]$$

In which $k_B T$ is the thermal energy, $\alpha = T/T_0$ with T_0 a parameter with temperature unit that corresponds to the depth of the distribution, V_{cor} is the ohmic drop corrected-value of applied voltage through equation (Magne et al., 2013a; Pauporté and Magne, 2014; Wang et al., 2006):

$$V_{cor} = V_{applied} - V_{drop} \quad [2.11]$$

$$\text{where, } V_{drop} = \int R_{Aseries} dl \quad [2.12]$$

$$R_{Aseries} = R_s + R_{CE} \quad [2.13]$$

R_s is the series resistance and R_{CE} the counter-electrode resistance which are determined from the impedance spectra (Pauporté and Magne, 2014).

Based on the data of C_μ the density of states (DOS) due to the traps (g) can be calculated by the following equation:

$$g = \frac{C_\mu}{qAL(1-p)} \quad [2.14]$$

where A is the geometric area of the cell, L is the oxide layer thickness and p is the film porosity. g versus V_{cor} plot shows increasing value of g by increasing V_{cor} until it reach plateau. This represents the distribution of the trap level density below the conduction band (Magne et al., 2013a; Pauporté and Magne, 2014).

Secondly, we also obtain the R_{ct} as a function of V_{cor} from which we extract an empirical estimation of the reaction order (β) follows the equation:

$$R_{ct} = R_{0,ct} \exp \left[-\beta \frac{qV_{cor}}{k_B T} \right] \quad [2.15]$$

Furthermore, many parameters that are related to dynamics electron transport can be extracted as written bellow:

- The lifetime of electrons in the photoelectrode:

$$\tau_n = R_{ct} \cdot C_\mu , \quad [2.16]$$

- The transport time / collection time:

$$\tau_{tr} = R_{tr} \cdot C_\mu , \quad [2.17]$$

- The charge collection efficiency:

$$\eta_{coll} = \frac{1}{\left(1 + \frac{\tau_{tr}}{\tau_n}\right)} \quad [2.18]$$

- The conductivity of semiconductor in photoelectrode:

$$\sigma_n = \frac{d}{A(1-p)R_{tr}} \quad [2.19]$$

- The charge (electron) chemical diffusion coefficient in semiconductor:

$$D_n = \frac{dL^2}{\tau_{tr}} \quad [2.20]$$

- The electron diffusion length:

$$L_n = \sqrt{D_n \cdot \tau_n} \quad [2.21]$$

Incident Photon to Electron Conversion Efficiency (IPCE)

IPCE spectra represent the number of electron collected in the cell for a give number of incident monochromatic photons.

$$IPCE(\lambda) = \frac{n_{electron}(\lambda)}{n_{photons}(\lambda)} = \frac{I(\lambda)hc}{P_{in}(\lambda)e\lambda} \quad [2.22]$$

where, $I(\lambda)$ is the measured current, $P_{in}(\lambda)$ is the input power and λ is the wavelength of irradiation (nm).

IPCE is also defined as multiplication product of four efficiencies:

$$IPCE(\lambda) = LHE(\lambda) \cdot \phi_{inj} \eta_{coll} \eta_{reg} \quad [2.23]$$

with, $LHE(\lambda)$ is the light harvesting efficiency of sensitizer, ϕ_{inj} is the electron injection efficiency from the excited dye to the semiconductor, η_{coll} is the charge collection efficiency at the contact and η_{reg} is the efficiency of dye regeneration.

II.2 Theoretical Background in Computational Methods

II.2.1 Quantum Chemistry

Quantum chemistry has opened possibility to calculate molecule energy or others properties, such as magnetic, optical or thermal properties of system. The Schrödinger equation can be considered as the heart of quantum chemistry due to its solution that can theoretically fulfill many questions about molecule properties, through the relationship (Schrödinger, 1926):

$$\hat{H}\psi = E\psi \quad [2.24]$$

\hat{H} (Hamiltonian operator) is a differential operator that represents the total energy of molecule. For a system that consists of M atomic nuclei and N electrons, it is expressed in the following form:

$$\hat{H} = -\frac{1}{2} \sum_{i=1}^N \nabla_i^2 - \frac{1}{2} \sum_{A=1}^M \frac{1}{M_A} \nabla_A^2 - \sum_{i=1}^N \sum_{A=1}^M \frac{Z_A}{r_{iA}} + \sum_{i=1}^N \sum_{j>1}^N \frac{1}{r_{ij}} + \sum_{A=1}^M \sum_{B>A}^M \frac{Z_A Z_B}{R_{AB}} \quad [2.25]$$

The terms in equation 2.25 represent; (1) the kinetic energy of electron; (2) the kinetic energy of nuclei; (3) the attractive electrostatic interaction between nuclei and electrons; and (4) the repulsive potential due to the electron-electron and nucleus-nucleus interactions, in order. A and B are the index of the M nuclei; whereas i and j are that of the N electrons. ∇_i^2 is the Laplacian operator, commonly in Cartesian coordinates:

$$\nabla^2 = \frac{\partial^2}{\partial x^2} + \frac{\partial^2}{\partial y^2} + \frac{\partial^2}{\partial z^2} \quad [2.26]$$

E is the energy of the system, ψ is the wave function of the electrons present in systems, containing all information about it. As the mass of the nuclei is much higher mass than that of electron, they move much more slowly compared to them. Therefore, equation 2.25 can be simplified by assuming that the kinetic energy of nuclei is zero and that the potential due to nucleus-nucleus repulsion is almost constant. This approximation was first proposed by Born-Oppenheimer who obtained the following electronic Hamiltonian (Born and Oppenheimer, 1927):

$$\hat{H}_{elec} = -\frac{1}{2} \sum_{i=1}^N \nabla_i^2 - \sum_{i=1}^N \sum_{A=1}^M \frac{Z_A}{r_{iA}} + \sum_{i=1}^N \sum_{j>1}^N \frac{1}{r_{ij}} \quad [2.27]$$

The Schrödinger equation and the Born-Oppenheimer approximation are the two fundamental concepts in quantum chemistry. Unfortunately, up to this date, this equation remains analytical solvable only in a few cases with limited amount of electrons. This fact has encouraged many researchers many researchers to develop new numerical methods in order to calculate the electronic structure of systems of different sizes. The three main types of computational approaches most often used for these calculations:

- (1) *ab-initio* methods, which solve Schrödinger equation using mathematical approximation. The Hartree-Fock (HF) approximation is the first on these methods to simplify the Schrodinger equation by replacing the N-electron wave function with an anti-symmetrized product (namely the Slater determinant) of N one-electron wave function (for fermions), or with a single permanent of N spin orbital (for bosons)

(Koch and Holthausen, 2000). The next approximation has been developed to accomplish the shortcomings of the HF approximation that did not include yet the correlation effect of the motion of electrons of opposite spins. The approximations that try to include this effect are called electron correlation methods. For example, the Møller-Plesset perturbation method is one of them (Møller and Plesset, 1934).

- (2) Semi-empirical methods, which use parameters derived from the experimental data to solve the Schrödinger equation. The first method has been introduced in 1965 by Pople, et al. through the all-valence-electron semi-empirical SCF-MO (Self-Consistent-Field Molecular-Orbital) methods. Since then, three more popular semi-empirical methods have been developed, namely MNDO (*Modified Neglect of Diatomic Overlap*), AM1 (*Austin Model 1*) and PM3 (*Parameterized Model number 3*) (Thiel, 2005). For the same system, semi-empirical methods require less computational sources than *ab-initio* methods.
- (3) Density Functional Theory (DFT), just like *ab-initio* methods, it uses a mathematical approximation. However, DFT derives the electron distribution (electron density function of system). DFT will be helpful for treating large systems that are too expensive to calculate HF methods. This method has been chosen in the calculations of the present work and will be explained separately in the next section.

II.2.2 Density Functional Theory

Density functional theory (DFT) is a computational method for the calculation of the electronic ground-state structure that determines the properties of a system as a function of electron density. That is the primary difference compared to the previous theory, which describes a system or a molecule with many electron wave functions $\Psi(r_1, r_2, \dots, r_N)$. Hohenberg, Kohn and Sham, who had developed the theory of the description of the ground state of an inhomogeneous interacting electron gas, have laid the fundamental concept of DFT (Hohenberg and Kohn, 1964; Kohn and Sham, 1965). Hohenberg and Kohn postulate their first theorem that relate the potential ($v(\mathbf{r})$), the particle density $\rho(\mathbf{r})$ and the ground state wave function (Ψ_0) through one to one mapping:

$$\rho(\mathbf{r}) \leftrightarrow v(\mathbf{r}) \leftrightarrow \Psi_0 \quad [2.28]$$

In other words, this theorem mentions that in order to find out molecule properties, we have to know the ground-state electron-density. But, how could we find that? This question is

answered by the HK-2 theorem that states that the ground-state electron density is the one that correspond to the minimum energy, which has been known as variational principle in mathematics and is formulated:

$$E_v[\rho] = \langle \Psi[\rho] | \hat{T} + \hat{V} + \hat{W} | \Psi[\rho] \rangle \geq E_0 \quad [2.29]$$

Here, \hat{T} , \hat{V} and \hat{W} are operator energies for kinetics energy, external potential that refers to nuclear field in the case for electrons moving in the field of fixed nuclei and electrons interaction energy (Baerends and Gritsenko, 1997; Koch and Holthausen, 2000).

The HK-1 theorem is addressed for systems that contain only one electron. This equation does not include particle interaction between two atoms or more. To overcome this difficulty, Kohn and Sham introduced the concept of the Kohn-Sham orbital. This orbital consists of one electron functions that is not interact each other. From this concept, it was found that in order to handle a system that consists of interacting particles, it is necessary to consider an effective external potential (v_{KS}) that is the sum of the coulomb interaction (v_{ext}); the *hartree classical* potential ($v_{hartree}$) and the *exchange-correlation* potential (v_{xc}) as written in equation 2.30.

$$v_{KS}(\mathbf{r}) = v_{ext}(\mathbf{r}) + v_{hartree}(\mathbf{r}) + v_{xc}(\mathbf{r}) \quad [2.30]$$

The improvement then focused to find out the *exchange-correlation* functional that depend on the observed systems. Globally, it is summarized below (Cohen et al., 2012; Koch and Holthausen, 2000):

- LDA (*Local Density Approximation*), it is developed for the uniform electron gas and is formulated (Dirac, 1930):

$$E_{xc}^{LDA}[\rho] = \int \rho(\vec{r}) \varepsilon_{xc}(\rho(\vec{r})) d\vec{r} \quad [2.31]$$

Here the ε_{xc} part consists of two parts, exchange and correlation as written:

$$\varepsilon_{xc}(\rho(\vec{r})) = \varepsilon_x(\rho(\vec{r})) + \varepsilon_c(\rho(\vec{r})) \quad [2.32]$$

$$\text{Where, } \varepsilon_x = -\frac{3}{4} \sqrt{\frac{3(\rho(\vec{r}))}{\pi}} \quad [2.33]$$

The relation between V_x and E_x is written :

$$V_x \equiv \frac{\delta E_x}{\delta \rho} \quad [2.34]$$

- GEA (*Gradient Expansion Approximation*): it is developed for systems that are characterized by heterogeneous density with very slowly varying (Cohen et al., 2012; Gross and Dreizler, 1981):

$$E_x^{GEA}[\rho, x] = - \int \rho^{4/3} \left[\frac{3}{4} \left(\frac{3}{\pi} \right)^{1/3} + \frac{7}{423\pi(3\pi^2)^{1/3}} x^2 + \dots \right] dr \quad [2.35]$$

- GGA (*Generalized Gradient Approximation*): it was developed to improve the GEA functional that is difficult to apply for any exponentially decaying density $x \rightarrow \infty$. It is formulated as (Cohen et al., 2012):

$$E_x^{GGA}[\rho, x] = \int \rho^{4/3} F(x) dr \quad [2.36]$$

where $F(x)$ is the function that is chosen and obey the gradient expansion in the low x limit (Cohen et al., 2012). The examples of typical GGA functionals for instance B88 and PBE, which are formulated in the equation 2.37 and 2.38 respectively.

$$E_x^{B88} = - \sum_{\sigma=\alpha,\beta} \int \rho_{\sigma}^{4/3} \left[\frac{3}{4} \left(\frac{6}{\pi} \right)^{1/3} + \frac{\beta x_{\sigma}^2}{1+6\beta x_{\sigma} \sinh^{-1} x_{\sigma}} \right] dr \quad (\text{Becke, 1988}) \quad [2.37]$$

$$E_x^{PBE} = - \int \rho^{4/3} \left[\frac{3}{4} \left(\frac{3}{\pi} \right)^{1/3} + \frac{\mu s^2}{1+\mu s^2/\kappa} \right] dr \quad (\text{Perdew et al., 1996}) \quad [2.38]$$

- Hybrid-functionals are functionals that contain including portion of Hartree-Fock exchange (E_x^{HF}). The development of this method was initiated by Axel Becke in 1993 (Becke, 1993). Apart from the *Becke* hybrid-functional, many other hybrid-functionals have been developed such as, B3LYP (Becke, three-parameter, Lee-Yang-Parr) (Becke, 1993; Lee et al., 1988), LYP (Lee et al., 1988) and VWN (Vosko-Wilk-Nusair) (Vosko et al., 1980). Among them, B3LYP the most widely used. It is formulated (Becke, 1993; Cohen et al., 2012; Lee et al., 1988):

$$E_{xc}^{B3LYP} = 0.2E_x^{HF} + 0.8E_x^{LDA} + 0.72\Delta E_x^{B88} + 0.81E_c^{LYP} + 0.19E_c^{VWN} \quad [2.39]$$

II.2.3 Models in Computational Chemistry

Before starting a calculation, the first important step is to build a model of the system. This model must be as close to the real system as possible, but at the same time, should also

be simple enough to run calculations using computational resources. To build a model as an object for computational calculations, we have to consider two aspects. First the geometry model and second the molecular orbital one. Geometrically, the computational calculations model is divided by two systems. (1) The molecular/isolated system which is used to describe a finite atomic model such as a molecular model or solid states cluster. (2) The periodic system which is used to describe infinite solid-state model for instance metal or oxide.

Molecular/Isolated system

The geometry model of molecular systems can be obtained from the information about the chemical bonding (bond and angle length), then we construct in Cartesian coordinate or Z-Matrix. To describe the atomic orbitals model in the molecular systems, we have to make the important choice of the basis set, a set of functions that are linearly combined, and represent the atomic orbitals of the molecules to approximate their electron wave function. Gaussian-type functions are the most functions that are used to represent the atomic orbital functions.

The several kinds of basis sets vary in their accuracy. The simplest basis set is called *minimal basis set*. In this basis set, each orbital is represented by one mathematical Gaussian function. An example of minimal basis set is STO-3G (STO = *Slater type orbital*, 3G = 3 Gaussian functions). It consists of three Gaussian functions to approximate a Slater type orbital.

The next level of accuracy is represented by the *split valence basis sets* that contain two (or more) functions for each of orbital. For instance, 3-21G basis sets. The first number **3** means that the core 1s orbital is the linear combination of **3** Gaussian functions. The next numbers **2** and **1** before the letter **G** mean that the valence shell 2s and 2p orbitals are split into two parts: (1) the inner part is the linear combination of **2** Gaussian functions and the outer part is composed of **1** Gaussian function.

In case of polarized *basis sets*, angular momentum functions are added to the functions that describe atomic orbitals. For example, it is possible to add *p* functions to the functions describing the H atomic orbital, to add *d* orbitals to the functions describing second row atoms, or to add *f* functions to those corresponding to the atomic orbitals of transition metals. This addition allows the angular flexibility of the orbitals. The notation * or ** is used to show that angular momentum functions are added. The 6-31G* basis set, also notated as 6-31G(d), corresponds to a 6-31G basis set with *d* functions added to heavy atoms. Another

example is the 6-31G**, also written as 6-31G(d,p), which corresponds to a 6-31G basis set with a d function added to heavy atoms and a p function to H atoms.

For large systems, in which the distance between electrons and nuclei is relatively large, it is necessary to include *diffuse functions* in the basis set. This modification of the basis set is denoted by the addition of “+”. For instance, 6-31+G(d) is a 6-31G(d) basis set augmented with a diffuse function added to heavy atoms, or 6-31++G(d) stands for a similar basis set with a diffuse function added to hydrogen (or helium) atoms instead of heavy atoms.

For third row atoms, such as transition metals (which have very large nuclei) an (R)ECP (*relativistic effective core potential*) treatment is applied on the electrons near the nuclei. Examples of basis sets for these kinds of atoms are LanL2MB or LanL2DZ (Hay and Wadt, 1985).

Periodic system

The main difficulty of defining a geometrical model of solid state structures (like crystals) is the large number of atoms that the system is constructed of. Due to the high computational cost, it is important to build a model for solid state systems that can approach the infinite system by a suitable finite one. In this section, we will explain a concept that has been developed to build a geometry model of crystal structure: periodic boundary conditions (PBC). The concepts that is important to describe electronic structure in periodic systems, plane-wave and pseudopotential will also be described

Periodic Boundary Condition (PBC)

Crystals are made of periodically repeating unit cells. When using periodic boundary conditions, we first define the lattice parameter of the unit cell. For bulk systems, the lattice parameter is three dimensional, whereas for surfaces, it is two dimensional (or three dimensional, with one of directions having a very high cell parameter, so it is assumed that there is no interaction between the layers). The unit cell of a crystal is defined by the lattice parameters, the position and the composition of atoms. We can either define our crystal by one unit cell or by a supercell that is composed of several unit cells.

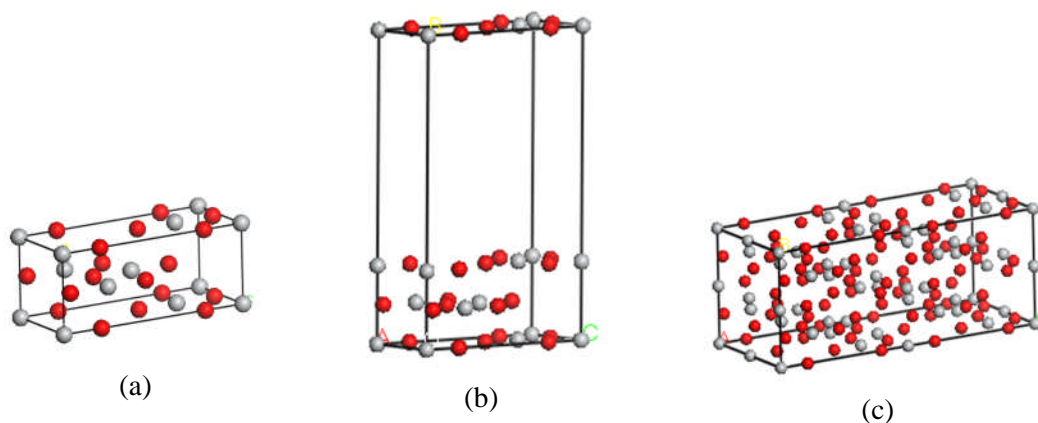


Figure 2.16: Examples of a unit cell for calculations using periodic boundary conditions for system (a) that contains one unit cell, (b) a crystal surface that has a high lattice parameter in one of direction and (c) a supercell that contains eight unit cells of (a)

Plane-wave basis sets

It is already shown that in solid states system there is an infinite number of interacting electrons moving in the static field of an infinite number of ions or atoms. It will be difficult to handle the calculation of this system as the molecular models. Bloch theorem is the answer to overcome the problem, which states that in periodic solid each electronic wave function can be written as the product of the cell-periodic and wavelike parts. The system need to be modeled as periodic boundary condition to conduct the Bloch theorem. Mathematically, the Bloch theorem can be expressed by expanding the electron wave function into a finite number plane-wave whose wave vectors are reciprocal lattice vectors of the crystal. Technically, we need to select the plane wave basis set in the calculation that has small energy kinetic. For this purposes we need to truncate the plane wave at the certain value which is called the cut-off energy.

Pseudopotential

The pseudopotential concept considers the separation between core and valence orbitals. This concept makes an assumption that core orbitals are not involved in chemical bonding and do not change as a consequence of the structural modification. The core electrons and the strong coulomb potential are replaced by the pseudopotential, whereas valence orbitals are involved in the chemical bonding and must be considered to the calculation. The definition of core orbitals and valence ones depend on the necessity of the calculation. For instance, Ti with the electron configurations: $(1s)^2 (2s)^2 (2p)^6 (3s)^2 (3p)^6 (4s)^2 (3d)^2$, the $[(1s)^2$

$(2s)^2 (2p)^6]$ can be considered as the core orbitals or $[(1s)^2 (2s)^2 (2p)^6 (3s)^2 (3p)^6]$ are considered as the core orbitals in the larger core. The pseudopotential matches the all electron beyond the certain value of radius cutoff (r_c). Figure 2.17 shows the comparison of calculations using all electron and pseudopotential.

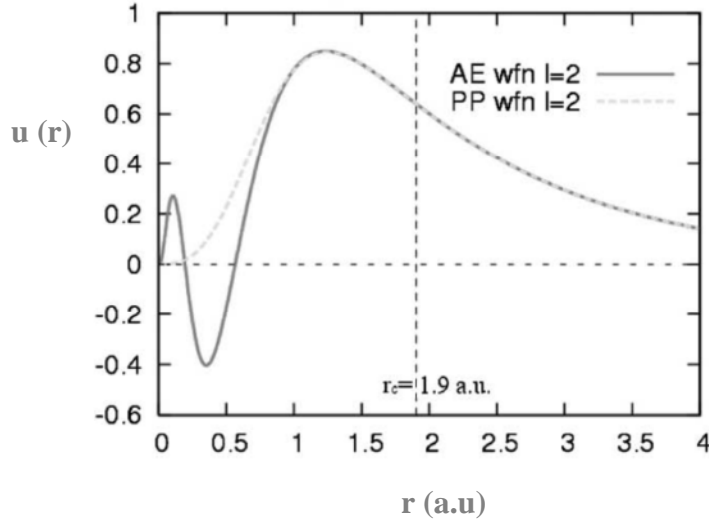


Figure 2.17: All electron (AE) and pseudopotential (PP) wave functions for Au at $l=2$. r_c is the radius cutoff in a. u. (Coquet et al., 2006)

The implementation of pseudopotential concept in the plane wave basis set will be beneficial since an expansion of an atomic all-electron density or wave function is computationally in efficient.

Gaussian and Plane Waves Method (GPW)

Gaussian and Plane Wave (GPW) method is an hybrid method that combine an atom-centered Gaussian-type basis set to describe the wave functions, but uses an auxiliary plane wave basis to describe the density (VandeVondele et al., 2005). The implementation of two representations of the electron density allows for solving the total energy and Kohn-Sham matrix using computational resources that has a linear scaling with system size due to an efficient treatment of the electrostatic interactions.

In the two previous sections, it has been mentioned that it is necessary to replace the core electrons with the pseudopotential to avoid computational inefficient due to an expansion of an atomic all-electron density or wave function in plane waves. In GPW method, the

pseudopotential Goedecker, Teter and Hutte (GTH) (Goedecker et al., 1996) is implemented to replace the core electrons. The GTH pseudopotential consists of (1) a local part that include a long-ranged (LR) and a short-ranged (SR) term and (2) a non-local part with the Gaussian-type projectors. The utilization of this pseudopotential in plane wave method requires relative high cut-off values. On the contrary, in GPW method it is less computationally effort since the kinetic energy and the short range pseudopotential terms are integrals over Gaussians functions which can be calculated analytically (VandeVondele et al., 2005; Krack and Parrinello, 2004).

II.2.4 Solvation Effect

To calculate the solution system, it is important to take the solvation effect into account. One model developed to consider this effect is called *Self-Consistent Reaction Field* (SCRF) method. It considers the solvent as a continuum of uniform dielectric constant (ϵ). The solute is modeled as cavity within the solvent. There are many approaches that differ in defining the cavity and the reaction field (Foresman and Frisch, 1996):

- Onsager Model. It assumes that the solute occupies a fixed spherical cavity radius a_0 within the solvent field. The stabilization of the systems results from interaction of a molecular dipole and a solvent dipole, and vice versa (Onsager, 1936).
- Tomasi's Polarized Continuum Model (PCM). This model considers the effect of the isodensity surface-based SCRF. It uses numerical approximations to represent the polarization effect of solvent and isodensity surface-based SCRF models (Miertuš et al., 1981; Miertuš and Tomasi, 1982).
- Conductor-like PCM (CPCM). This model uses the same cavity parameters as that in PCM. The difference lies the use of conductor-like salvation model (COSMOS) approach for modeling the continuum instead of dielectric polarizable dielectric (Barone and Cossi, 1998; Cossi et al., 2003; Klamt and Schüürmann, 1993).
- Isodensity PCM (IPCM) model. In this model the cavity is modeled as an isodensity surface of the molecule (Foresman et al., 1996).
- Self-consistency Isodensity Polarized Continuum Model (SCI-PCM). This model includes cavity, electron density and coupling terms in the calculation (Foresman et al., 1996).

II.2.5 TDDFT

The main topic of this thesis is about DSSC where the interaction between photons and electrons lead to the formation of excited electrons. This section will explain TDDFT (*Time Dependent Density Functional Theory*), the theory that has been widely used in computational chemistry to investigate the properties of excited electron.

The several methods that have been developed to calculate electron excitation properties are divided into wave-function-based methods and electron-density-based methods. The most commonly used methods due to their applicability to large molecules are CIS (*Configuration Interaction Singles*), TDHF (*Time Dependent Hartree-Fock*) and TDDFT. The first two are wave-function-based-methods whereas the last one is an electron-density-based methods (Dreuw and Head-Gordon, 2005).

TDDFT was introduced for the first time by Runge and Gross (Runge and Gross, 1984). They formulated Theorem I that states:

“the single particle potential $v(\vec{r}, t)$ leading to a given v -representable density $\rho(\vec{r}, t)$ is uniquely determined so that the corresponding map $v \rightarrow \rho$ is invertible”
(Runge and Gross, 1984)

In other words, this theorem is the form of the time-dependent HK-I theorem (see equation 2.28). Since the potential and the wave function are functionals of the density, we can rewrite this statement:

$$\rho(\mathbf{r}, t) \leftrightarrow v[\rho](\mathbf{r}, t) + \mathbf{C}(t) \leftrightarrow \Psi[\rho](\mathbf{r}, t)e^{-iat} \quad [2.40]$$

The additive function $\mathbf{C}(t)$ is needed for TD-system.

The same scheme that has been used to derive DFT as described in section II.2.3 is also applied to derive TDDFT. The difference is that all the equations (2.28, 2.29 and 2.30) become time-dependent in TDDFT. So now, the second step is to determine the exact density which is solved by variational principle in DFT (equation 2.29). Unfortunately, the same procedure cannot be applied in TDDFT. It is not possible to use variational principle to determine the total energy of the system in TDDFT. It is required to define a quantity analogous to the energy (A) (Dreuw and Head-Gordon, 2005; Marques and Gross, 2004; Runge and Gross, 1984):

$$A(\Psi) = \int_{t_0}^{t_1} \left\langle \Psi(t) \left| i \frac{\partial}{\partial t} - \hat{H}(t) \right| \Psi(t) \right\rangle dt \quad [2.41]$$

Thus, the exact electron density can be obtained by solving:

$$\frac{\delta A[\rho]}{\delta \rho(\mathbf{r}, t)} = 0 \quad [2.42]$$

The next scheme is also the same as that in DFT. We need to determine the solution of a problem for a system that contain of more than one atom. The Kohn-Sham formalism has revealed that in order to solve many-body systems, we need to determine the *exchange-correlation* functional. In TDDFT, the time dependent *exchange-correlation* functional, (v_{xc}) can be obtained through the equation 2.43 (Marques and Gross, 2004; Runge and Gross, 1984).

$$v_{xc}(\mathbf{r}, t) = \frac{\delta A_{xc}}{\delta \rho(\mathbf{r}, t)} \quad [2.43]$$

But the solution of the TDDFT problem is not simple as that of DFT, since it involves time-evolving density, $\rho(\mathbf{r}, t)$. Here, we need to define another parameter, $f_{xc}(\mathbf{r}t, \mathbf{r}'t')$, named xc-kernel, which is related to v_{xc} through the equation:

$$f_{xc}(\mathbf{r}t, \mathbf{r}'t') = \frac{\delta v_{xc}(\mathbf{r}, t)}{\delta \rho(\mathbf{r}, t)} \quad [2.44]$$

The last, to solve the TDDFT problem, it need to make an approximation of the xc-kernel. The simplest approximation that has been formulated is the Adiabatic Local Density Approximation (ALDA) (Gross, E. K. U and Maitra, N. P, 2012):

$$f_{xc}^{ALDA}[\rho](\mathbf{r}, \mathbf{r}') = \delta(\mathbf{r} - \mathbf{r}') \frac{d^2 \rho e_{xc}^{hom}(\rho)}{d\rho^2} \Big|_{\rho=\rho(\mathbf{r})} \quad [2.45]$$

where, $e_{xc}^{hom}(\rho)$ is the xc energy per electron of the homogeneous electron gas of density ρ .

The accuracy key of TDDFT lies in finding of the xc-kernel that can approach the investigated systems (Casida, 2009; Dreuw and Head-Gordon, 2005; Marques and Gross, 2004).

References

- Alarco, H., Hedlund, M., Johansson, E.M.J., Rensmo, H., Hagfeldt, A., Boschloo, G., 2007. Modification of Nanostructured TiO₂ Electrodes by Electrochemical Al³⁺ Insertion : Effects on Dye-Sensitized Solar Cell Performance 13267–13274.
- Anderson, N.A., Ai, X., Lian, T., 2003. Electron Injection Dynamics from Ru Polypyridyl Complexes to ZnO Nanocrystalline Thin Films. J. Phys. Chem. B 107, 14414–14421. doi:10.1021/jp036201h

- Asbury, J.B., Hao, E., Wang, Y., Lian, T., 2000. Bridge Length-Dependent Ultrafast Electron Transfer from Re Polypyridyl Complexes to Nanocrystalline TiO₂ Thin Films Studied by Femtosecond Infrared Spectroscopy. *J. Phys. Chem. B* 104, 11957–11964. doi:10.1021/jp002541g
- Baerends, E.J., Gritsenko, O.V., 1997. A Quantum Chemical View of Density Functional Theory. *J. Phys. Chem. A* 101, 5383–5403. doi:10.1021/jp9703768
- Le Bahers, T., Brémond, E., Ciofini, I., Adamo, C., 2014. The nature of vertical excited states of dyes containing metals for DSSC applications: insights from TD-DFT and density based indexes. *Phys. Chem. Chem. Phys.* 16, 14435–14444. doi:10.1039/C3CP55032J
- Le Bahers, T., Pauporté, T., Scalmani, G., Adamo, C., Ciofini, I., 2009. A TD-DFT investigation of ground and excited state properties in indoline dyes used for dye-sensitized solar cells. *Phys. Chem. Chem. Phys.* 11, 11276–11284. doi:10.1039/B914626A
- Bai, Y., Zhang, J., Zhou, D., Wang, Y., Zhang, M., Wang, P., 2011. Engineering Organic Sensitizers for Iodine-Free Dye-Sensitized Solar Cells: Red-Shifted Current Response Concomitant with Attenuated Charge Recombination. *J. Am. Chem. Soc.* 133, 11442–11445. doi:10.1021/ja203708k
- Barone, V., Cossi, M., 1998. Quantum Calculation of Molecular Energies and Energy Gradients in Solution by a Conductor Solvent Model. *J. Phys. Chem. A* 102, 1995–2001. doi:10.1021/jp9716997
- Becke, A.D., 1988. Density-functional exchange-energy approximation with correct asymptotic behavior. *Phys. Rev. A* 38, 3098–3100. doi:10.1103/PhysRevA.38.3098
- Becke, A.D., 1993. A new mixing of Hartree–Fock and local density-functional theories. *J. Chem. Phys.* 98, 1372–1377. doi:10.1063/1.464304
- Bisquert, J., Cahen, D., Hodes, G., Rühle, S., Zaban, A., 2004. Physical Chemical Principles of Photovoltaic Conversion with Nanoparticulate, Mesoporous Dye-Sensitized Solar Cells. *J. Phys. Chem. B* 108, 8106–8118. doi:10.1021/jp0359283
- Bisquert, J., Vikhrenko, V.S., 2004. Interpretation of the Time Constants Measured by Kinetic Techniques in Nanostructured Semiconductor Electrodes and Dye-Sensitized Solar Cells. *J. Phys. Chem. B* 108, 2313–2322. doi:10.1021/jp035395y
- Bisquert, J. and Fabregat-Santiago, F. (2010). *Impedance Spectroscopy: A General Introduction and Application to Dye-Sensitized Solar Cells* in Kalyanasundaram, K. *Dye-sensitized Solar Cells*. EPFL Press. p. 523
- Born, M., Oppenheimer, R., 1927. Zur Quantentheorie der Molekeln. *Ann. Phys.* 389, 457–484. doi:10.1002/andp.19273892002
- Boschloo, G., Hagfeldt, A., 2009. Characteristics of the Iodide/Triiodide Redox Mediator in Dye-Sensitized Solar Cells. *Acc. Chem. Res.* 42, 1819–1826. doi:10.1021/ar900138m
- Burschka, J., Pellet, N., Moon, S.-J., Humphry-Baker, R., Gao, P., Nazeeruddin, M.K., Grätzel, M., 2013. Sequential deposition as a route to high-performance perovskite-sensitized solar cells. *Nature* 499, 316–319. doi:10.1038/nature12340
- Casida, M.E., 2009. Time-dependent density-functional theory for molecules and molecular solids. *J. Mol. Struct. THEOCHEM*, Time-dependent density-functional theory for molecules and molecular solids 914, 3–18. doi:10.1016/j.theochem.2009.08.018
- Chen, J., Li, B., Zheng, J., Zhao, J., Jing, H., Zhu, Z., 2011. Polyaniline nanofiber/carbon film as flexible counter electrodes in platinum-free dye-sensitized solar cells. *Electrochimica Acta* 56, 4624–4630. doi:10.1016/j.electacta.2011.02.097
- Chen, X., Mao, S.S., 2007. Titanium Dioxide Nanomaterials: Synthesis, Properties, Modifications, and Applications. *Chem. Rev.* 107, 2891–2959. doi:10.1021/cr0500535
- Chuang, P.-K., Lin, Y.-J., Chen, C.-M., Chang, C.-C., 2014. Improved Power Conversion Efficiency of Dye-Sensitized Solar Cells by Fluorophore-Assisted Spectrum Down-Conversion. *J. Electrochem. Soc.* 161, H404–H409. doi:10.1149/2.092406jes
- Clifford, J.N., Palomares, E., Nazeeruddin, M.K., Grätzel, M., Nelson, J., Li, X., Long, N.J., Durrant, J.R., 2004. Molecular Control of Recombination Dynamics in Dye-Sensitized Nanocrystalline TiO₂ Films: Free Energy vs Distance Dependence. *J. Am. Chem. Soc.* 126, 5225–5233. doi:10.1021/ja039924n
- Cohen, A.J., Mori-Sánchez, P., Yang, W., 2012. Challenges for Density Functional Theory. *Chem. Rev.* 112, 289–320. doi:10.1021/cr200107z
- Coquet, R., Hutchings, G.J., Taylor, S.H., Willock, D.J., 2006. Calculations on the adsorption of Au to MgO surfaces using SIESTA. *J. Mater. Chem.* 16, 1978–1988. doi:10.1039/B601213B
- Cossi, M., Rega, N., Scalmani, G., Barone, V., 2003. Energies, structures, and electronic properties of molecules in solution with the C-PCM solvation model. *J. Comput. Chem.* 24, 669–681. doi:10.1002/jcc.10189

- Dirac, P. a. M., 1930. Note on Exchange Phenomena in the Thomas Atom. *Math. Proc. Camb. Philos. Soc.* 26, 376–385. doi:10.1017/S0305004100016108
- Dreuw, A., Head-Gordon, M., 2005. Single-Reference ab Initio Methods for the Calculation of Excited States of Large Molecules. *Chem. Rev.* 105, 4009–4037. doi:10.1021/cr0505627
- Facci, T., Huguenin, F., 2010. Spectroelectrochemical Properties and Lithium Ion Storage in Self-Assembled Nanocomposites from TiO₂. *Langmuir* 26, 4489–4496. doi:10.1021/la903301c
- Fan, J., Hao, Y., Cabot, A., Johansson, E.M.J., Boschloo, G., Hagfeldt, A., 2013. Cobalt(II/III) Redox Electrolyte in ZnO Nanowire-Based Dye-Sensitized Solar Cells. *ACS Appl. Mater. Interfaces* 5, 1902–1906. doi:10.1021/am400042s
- Feldt, S.M., Gibson, E.A., Gabrielsson, E., Sun, L., Boschloo, G., Hagfeldt, A., 2010. Design of Organic Dyes and Cobalt Polypyridine Redox Mediators for High-Efficiency Dye-Sensitized Solar Cells. *J. Am. Chem. Soc.* 132, 16714–16724. doi:10.1021/ja1088869
- Feldt, S.M., Wang, G., Boschloo, G., Hagfeldt, A., 2011. Effects of Driving Forces for Recombination and Regeneration on the Photovoltaic Performance of Dye-Sensitized Solar Cells using Cobalt Polypyridine Redox Couples. *J. Phys. Chem. C* 115, 21500–21507. doi:10.1021/jp2061392
- Fenoglio, I., Greco, G., Livraghi, S., Fubini, B., 2009. Non-UV-Induced Radical Reactions at the Surface of TiO₂ Nanoparticles That May Trigger Toxic Responses. *Chem. – Eur. J.* 15, 4614–4621. doi:10.1002/chem.200802542
- Fisher, A.C., Peter, L.M., Ponomarev, E.A., Walker, A.B., Wijayantha, K.G.U., 2000. Intensity Dependence of the Back Reaction and Transport of Electrons in Dye-Sensitized Nanocrystalline TiO₂ Solar Cells. *J. Phys. Chem. B* 104, 949–958. doi:10.1021/jp993220b
- Foresman, J.B., Frisch, Ae., 1996. Exploring Chemistry with Electronic Structure Methods. Gaussian, Incorporated.
- Foresman, J.B., Keith, T.A., Wiberg, K.B., Snoonian, J., Frisch, M.J., 1996. Solvent Effects. 5. Influence of Cavity Shape, Truncation of Electrostatics, and Electron Correlation on ab Initio Reaction Field Calculations. *J. Phys. Chem.* 100, 16098–16104. doi:10.1021/jp960488j
- Friedrich, D., Valldecabres, L., Kunst, M., Moehl, T., Zakeeruddin, S.M., Grätzel, M., 2014. Dye Regeneration Dynamics by Electron Donors on Mesoscopic TiO₂ Films. *J. Phys. Chem. C* 118, 3420–3425. doi:10.1021/jp4113206
- Fujishima, A., Zhang, X., Tryk, D.A., 2008. TiO₂ photocatalysis and related surface phenomena. *Surf. Sci. Rep.* 63, 515–582. doi:10.1016/j.surfrep.2008.10.001
- Funaki, T., Otsuka, H., Onozawa-Komatsuzaki, N., Kasuga, K., Sayama, K., Sugihara, H., 2014. Systematic evaluation of HOMO energy levels for efficient dye regeneration in dye-sensitized solar cells. *J. Mater. Chem. A* 2, 15945–15951. doi:10.1039/C4TA00613E
- Ganesan, P., Chandiran, A., Gao, P., Rajalingam, R., Grätzel, M., Nazeeruddin, M.K., 2014a. Molecular Engineering of 2-Quinolinone Based Anchoring Groups for Dye-Sensitized Solar Cells. *J. Phys. Chem. C* 118, 16896–16903. doi:10.1021/jp5004352
- Ganesan, P., Chandiran, A., Gao, P., Rajalingam, R., Grätzel, M., Nazeeruddin, M.K., 2014b. Molecular Engineering of 2-Quinolinone Based Anchoring Groups for Dye-Sensitized Solar Cells. *J. Phys. Chem. C* 118, 16896–16903. doi:10.1021/jp5004352
- Goedecker, S., Teter, M., Hutter, J., 1996. Separable dual-space Gaussian pseudopotentials. *Phys. Rev. B* 54, 1703–1710. doi:10.1103/PhysRevB.54.1703
- Gong, J., Liang, J., Sumathy, K., 2012a. Review on dye-sensitized solar cells (DSSCs): Fundamental concepts and novel materials. *Renew. Sustain. Energy Rev.* 16, 5848–5860. doi:10.1016/j.rser.2012.04.044
- Gong, J., Liang, J., Sumathy, K., 2012b. Review on dye-sensitized solar cells (DSSCs): Fundamental concepts and novel materials. *Renew. Sustain. Energy Rev.* 16, 5848–5860. doi:10.1016/j.rser.2012.04.044
- Griffith, M.J., Sunahara, K., Wagner, P., Wagner, K., Wallace, G.G., Officer, D.L., Furube, A., Katoh, R., Mori, S., Mozer, A.J., 2012. Porphyrins for dye-sensitized solar cells: new insights into efficiency-determining electron transfer steps. *Chem. Commun.* 48, 4145–4162. doi:10.1039/C2CC30677H
- Gross, E.K.U., Dreizler, R.M., 1981. Gradient expansion of the Coulomb exchange energy. *Z. Für Phys. At. Nucl.* 302, 103–106. doi:10.1007/BF01413038
- Gross, E. K. U., Maitra, N. P. 2012. Introduction to TDDFT in Rubio, A. Fundamentals of Time-Dependent Density Functional Theory, Springer-Verlag :Berlin. p. 82

- Guérin, V.-M., Pauporté, T., 2011. From nanowires to hierarchical structures of template-free electrodeposited ZnO for efficient dye-sensitized solar cells. *Energy Environ. Sci.* 4, 2971–2971. doi:10.1039/c1ee01218e
- Hafez, H., Saif, M., Abdel-Mottaleb, M.S.A., 2011. Down-converting lanthanide doped TiO₂ photoelectrodes for efficiency enhancement of dye-sensitized solar cells. *J. Power Sources* 196, 5792–5796. doi:10.1016/j.jpowsour.2011.02.031
- Hagfeldt, A., Boschloo, G., Sun, L., Kloo, L., Pettersson, H., 2010. Dye-Sensitized Solar Cells. *Chem. Rev.* 110, 6595–6663.
- Haid, S., Marszalek, M., Mishra, A., Wielopolski, M., Teuscher, J., Moser, J.-E., Humphry-Baker, R., Zakeeruddin, S.M., Grätzel, M., Bäuerle, P., 2012. Significant Improvement of Dye-Sensitized Solar Cell Performance by Small Structural Modification in π -Conjugated Donor–Acceptor Dyes. *Adv. Funct. Mater.* 22, 1291–1302. doi:10.1002/adfm.201102519
- Hamann, T.W., 2012. The end of iodide? Cobalt complex redox shuttles in DSSCs. *Dalton Trans.* 41, 3111. doi:10.1039/c2dt12362b
- Ham, H.W., Kim, Y.S., 2010. Theoretical study of indoline dyes for dye-sensitized solar cells. *Thin Solid Films, Proceedings of the 2nd International Conference on Microelectronics and Plasma Technology – ICMAP 2009* 518, 6558–6563. doi:10.1016/j.tsf.2010.03.048
- Haque, S.A., Tachibana, Y., Willis, R.L., Moser, J.E., Grätzel, M., Klug, D.R., Durrant, J.R., 2000. Parameters Influencing Charge Recombination Kinetics in Dye-Sensitized Nanocrystalline Titanium Dioxide Films. *J. Phys. Chem. B* 104, 538–547. doi:10.1021/jp991085x
- Hara, K., Wang, Z.-S., Sato, T., Furube, A., Katoh, R., Sugihara, H., Dan-oh Yasufumi, Kasada, C., Shinpo, A., Suga, S., 2005. Oligothiophene-Containing Coumarin Dyes for Efficient Dye-Sensitized Solar Cells. *J. Phys. Chem. B* 109, 15476–15482. doi:10.1021/jp0518557
- Hashmi, S.G., Moehl, T., Halme, J., Ma, Y., Saukkonen, T., Yella, A., Giordano, F., Decoppet, J.-D., Zakeeruddin, S.M., Lund, P., Grätzel, M., 2014. A durable metal free SWCNT/PET polymer foil based counter electrode for flexible dye sensitized solar cells. *J. Mater. Chem. A*. doi:10.1039/C4TA03730H
- Hay, P.J., Wadt, W.R., 1985. Ab initio effective core potentials for molecular calculations. Potentials for the transition metal atoms Sc to Hg. *J. Chem. Phys.* 82, 270–283. doi:10.1063/1.448799
- He, Z., Phan, H., Liu, J., Nguyen, T.-Q., Tan, T.T.Y., 2013. Understanding TiO₂ Size-Dependent Electron Transport Properties of a Graphene-TiO₂ Photoanode in Dye-Sensitized Solar Cells Using Conducting Atomic Force Microscopy. *Adv. Mater.* 25, 6900–6904. doi:10.1002/adma.201303327
- Hohenberg, P., Kohn, W., 1964. Inhomogeneous Electron Gas. *Phys. Rev.* 136, B864–B871. doi:10.1103/PhysRev.136.B864
- Hosni, M., 2014. *Optimisation du Procédé Polyol pour la Synthèse de Nanoparticules d'Oxyde de Zinc : Mise à l'échelle du Procédé et Applications Photovoltaïques*. Doctoral Thesis UNIVERSITE PARIS 13 - Sorbonne Paris Cité-Institut Galilée and UNIVERSITE DE TUNIS EL MANAR-Faculté des Sciences de Tunis. Chapter IV, page 181-234
- Hou, S., Cai, X., Fu, Y., Lv, Z., Wang, D., Wu, H., Zhang, C., Chu, Z., Zou, D., 2011. Transparent conductive oxide-less, flexible, and highly efficient dye-sensitized solar cells with commercialized carbon fiber as the counter electrode. *J. Mater. Chem.* 21, 13776–13779. doi:10.1039/C1JM12056E
- Ito, S., Miura, H., Uchida, S., Takata, M., Sumioka, K., Liska, P., Comte, P., Péchy, P., Grätzel, M., 2008. High-conversion-efficiency organic dye-sensitized solar cells with a novel indoline dye. *Chem. Commun.* 5194–5196. doi:10.1039/B809093A
- Jena, A., Mohanty, S.P., Kumar, P., Naduvath, J., Gondane, V., Lekha, P., Das, J., Narula, H.K., Mallick, S., Bhargava, P., 2012. Dye Sensitized Solar Cells: A Review. *Trans. Indian Ceram. Soc.* 71, 1–16. doi:10.1080/0371750X.2012.689503
- Jin, H.-Y., Kim, J.-Y., Lee, J.A., Lee, K., Yoo, K., Lee, D.-K., Kim, B., Kim, J.Y., Kim, H., Son, H.J., Kim, J., Lim, J.A., Ko, M.J., 2014. Rapid sintering of TiO₂ photoelectrodes using intense pulsed white light for flexible dye-sensitized solar cells. *Appl. Phys. Lett.* 104, 143902. doi:10.1063/1.4871370
- Jose, R., Thavasi, V., Ramakrishna, S., 2009. Metal Oxides for Dye-Sensitized Solar Cells. *J. Am. Ceram. Soc.* 92, 289–301. doi:10.1111/j.1551-2916.2008.02870.x
- Jung, H., Park, J., Yoo, E.S., Han, G.-S., Jung, H.S., Ko, M.J., Park, S., Choe, W., 2013. Functionalization of nanomaterials by non-thermal large area atmospheric pressure plasmas: application to flexible dye-sensitized solar cells. *Nanoscale* 5, 7825–7830. doi:10.1039/C3NR01889J.

- Kang, M.G., Park, N.-G., Ryu, K.S., Chang, S.H., Kim, K.-J., 2006. A 4.2% efficient flexible dye-sensitized TiO₂ solar cells using stainless steel substrate. *Sol. Energy Mater. Sol. Cells* 90, 574–581. doi:10.1016/j.solmat.2005.04.025
- Kang, M.S., Kang, S.H., Kim, S.G., Choi, I.T., Ryu, J.H., Ju, M.J., Cho, D., Lee, J.Y., Kim, H.K., 2012. Novel D- π -A structured Zn(II)-porphyrin dyes containing a bis(3,3-dimethylfluorenyl)amine moiety for dye-sensitized solar cells. *Chem. Commun.* 48, 9349–9351. doi:10.1039/C2CC31384G
- Karunakaran, B., Uthirakumar, P., Chung, S.J., Velumani, S., Suh, E.-K., 2007. TiO₂ thin film gas sensor for monitoring ammonia. *Mater. Charact.*, XIV International Materials Research Congress: Symposium 7 XIV International Materials Research Congress 58, 680–684. doi:10.1016/j.matchar.2006.11.007
- Khare, P., Sonane, M., Pandey, R., Ali, S., Gupta, K.C., Satish, A., 2011. Adverse Effects of TiO₂ and ZnO Nanoparticles in Soil Nematode, *Caenorhabditis elegans*. *J. Biomed. Nanotechnol.* 7, 116–117. doi:10.1166/jbn.2011.1229
- Kim, B.-G., Chung, K., Kim, J., 2013. Molecular Design Principle of All-organic Dyes for Dye-Sensitized Solar Cells. *Chem. – Eur. J.* 19, 5220–5230. doi:10.1002/chem.201204343
- Kim, H.-S., Lee, C.-R., Im, J.-H., Lee, K.-B., Moehl, T., Marchioro, A., Moon, S.-J., Humphry-Baker, R., Yum, J.-H., Moser, J.E., Grätzel, M., Park, N.-G., 2012. Lead Iodide Perovskite Sensitized All-Solid-State Submicron Thin Film Mesoscopic Solar Cell with Efficiency Exceeding 9%. *Sci. Rep.* 2. doi:10.1038/srep00591
- Klahr, B.M., Hamann, T.W., 2009. Performance Enhancement and Limitations of Cobalt Bipyridyl Redox Shuttles in Dye-Sensitized Solar Cells. *J. Phys. Chem. C* 113, 14040–14045. doi:10.1021/jp903431s
- Klampaftis, E., Ross, D., McIntosh, K.R., Richards, B.S., 2009. Enhancing the performance of solar cells via luminescent down-shifting of the incident spectrum: A review. *Sol. Energy Mater. Sol. Cells* 93, 1182–1194. doi:10.1016/j.solmat.2009.02.020
- Klamt, A., Schüürmann, G., 1993. COSMO: a new approach to dielectric screening in solvents with explicit expressions for the screening energy and its gradient. *J. Chem. Soc. Perkin Trans. 2* 799–805. doi:10.1039/P29930000799
- Koch, W., Holthausen, M.C., 2000. A chemist's guide to density functional theory. Wiley-VCH.
- Kohn, W., Sham, L.J., 1965. Self-Consistent Equations Including Exchange and Correlation Effects. *Phys. Rev.* 140, A1133–A1138. doi:10.1103/PhysRev.140.A1133
- Koops, S.E., O'Regan, B.C., Barnes, P.R.F., Durrant, J.R., 2009. Parameters Influencing the Efficiency of Electron Injection in Dye-Sensitized Solar Cells. *J. Am. Chem. Soc.* 131, 4808–4818. doi:10.1021/ja8091278
- Koziej, D., Fischer, F., Kränzlin, N., Caseri, W.R., Niederberger, M., 2009. Nonaqueous TiO₂ Nanoparticle Synthesis: a Versatile Basis for the Fabrication of Self-Supporting, Transparent, and UV-Absorbing Composite Films. *ACS Appl. Mater. Interfaces* 1, 1097–1104. doi:10.1021/am9000584
- Lancelle-Beltran, E., Prené, P., Boscher, C., Belleville, P., Buvat, P., Lambert, S., Guillet, F., Marcel, C., Sanchez, C., 2008a. Solid-State Organic/Inorganic Hybrid Solar Cells Based on Poly(octylthiophene) and Dye-Sensitized Nanobrookite and Nanoanatase TiO₂ Electrodes. *Eur. J. Inorg. Chem.* 2008, 903–910. doi:10.1002/ejic.200701033
- Lancelle-Beltran, E., Prené, P., Boscher, C., Belleville, P., Buvat, P., Lambert, S., Guillet, F., Marcel, C., Sanchez, C., 2008b. Solid-State Organic/Inorganic Hybrid Solar Cells Based on Poly(octylthiophene) and Dye-Sensitized Nanobrookite and Nanoanatase TiO₂ Electrodes. *Eur. J. Inorg. Chem.* 2008, 903–910. doi:10.1002/ejic.200701033
- Le Bahers, T., Labat, F., Pauporté, T., Lainé, P.P., Ciofini, I., 2011. Theoretical Procedure for Optimizing Dye-Sensitized Solar Cells: From Electronic Structure to Photovoltaic Efficiency. *J. Am. Chem. Soc.* 133, 8005–8013. doi:10.1021/ja201944g
- Lee, C., Yang, W., Parr, R.G., 1988. Development of the Colle-Salvetti correlation-energy formula into a functional of the electron density. *Phys. Rev. B* 37, 785–789. doi:10.1103/PhysRevB.37.785
- Lee, C.Y., She, C., Jeong, N.C., Hupp, J.T., 2010. Porphyrin sensitized solar cells: TiO₂ sensitization with a π -extended porphyrin possessing two anchoring groups. *Chem. Commun.* 46, 6090–6092. doi:10.1039/C0CC00257G
- Liao, J.-Y., Lei, B.-X., Chen, H.-Y., Kuang, D.-B., Su, C.-Y., 2012. Oriented hierarchical single crystalline anatase TiO₂ nanowire arrays on Ti-foil substrate for efficient flexible dye-sensitized solar cells. *Energy Environ. Sci.* 5, 5750–5757. doi:10.1039/C1EE02766B

- Liao, Y., Que, W., Jia, Q., He, Y., Zhang, J., Zhong, P., 2012. Controllable synthesis of brookite/anatase/rutile TiO₂ nanocomposites and single-crystalline rutile nanorods array. *J. Mater. Chem.* 22, 7937–7944. doi:10.1039/C2JM16628C
- Linsebigler, A.L., Lu, G., Yates, J.T., 1995. Photocatalysis on TiO₂ Surfaces: Principles, Mechanisms, and Selected Results. *Chem. Rev.* 95, 735–758. doi:10.1021/cr00035a013
- Li, Q., Lin, J., Wu, J., Lan, Z., Wang, Y., Peng, F., Huang, M., 2011. Enhancing photovoltaic performance of dye-sensitized solar cell by rare-earth doped oxide of Lu₂O₃:(Tm³⁺, Yb³⁺). *Electrochimica Acta* 56, 4980–4984. doi:10.1016/j.electacta.2011.03.125
- Liu, D., Kelly, T.L., 2014. Perovskite solar cells with a planar heterojunction structure prepared using room-temperature solution processing techniques. *Nat. Photonics* 8, 133–138. doi:10.1038/nphoton.2013.342
- Liu, S.-H., Fu, H., Cheng, Y.-M., Wu, K.-L., Ho, S.-T., Chi, Y., Chou, P.-T., 2012. Theoretical Study of N749 Dyes Anchoring on the (TiO₂)₂₈ Surface in DSSCs and Their Electronic Absorption Properties. *J. Phys. Chem. C* 116, 16338–16345. doi:10.1021/jp3006074
- Magne, C. 2012. *Optimisation de Couches D'oxyde Nano-structurees pour Applications Aux Cellules Solaires A Colorant*. Doctoral Thesis. Universite Pierre et Marie Curie, p. 21
- Magne, C., Cassaignon, S., Lancel, G., Pauporté, T., 2011. Brookite TiO₂ Nanoparticle Films for Dye-Sensitized Solar Cells. *ChemPhysChem* 12, 2461–2467. doi:10.1002/cphc.201100194
- Magne, C., Dufour, F., Labat, F., Lancel, G., Durupthy, O., Cassaignon, S., Pauporté, T., 2012. Effects of TiO₂ nanoparticle polymorphism on dye-sensitized solar cell photovoltaic properties. *J. Photochem. Photobiol. Chem.* 232, 22–31. doi:10.1016/j.jphotochem.2012.01.015
- Magne, C., Moehl, T., Urien, M., Grätzel, M., Pauporté, T., 2013a. Effects of ZnO film growth route and nanostructure on electron transport and recombination in dye-sensitized solar cells. *J. Mater. Chem. A* 1, 2079. doi:10.1039/c2ta00674j
- Magne, C., Moehl, T., Urien, M., Grätzel, M., Pauporté, T., 2013b. Effects of ZnO film growth route and nanostructure on electron transport and recombination in dye-sensitized solar cells. *J. Mater. Chem. A* 1, 2079–2088. doi:10.1039/C2TA00674J
- Magne, C., Urien, M., Ciofini, I., Tugsuz, T., Pauporté, T., 2012. Amphiphilic acids as co-adsorbents of metal-free organic dyes for the efficient sensitization of nanostructured photoelectrode. *RSC Adv.* 2, 11836–11842. doi:10.1039/C2RA22121G
- Magne, C., Urien, M., Pauporté, T., 2013c. Enhancement of photovoltaic performances in dye-sensitized solar cells by co-sensitization with metal-free organic dyes. *RSC Adv.* 3, 6315–6318. doi:10.1039/C3RA41170B
- Marinado, T., Hagberg, D.P., Hedlund, M., Edvinsson, T., Johansson, E.M.J., Boschloo, G., Rensmo, H., Brinck, T., Sun, L., Hagfeldt, A., 2009. Rhodanine dyes for dye-sensitized solar cells: spectroscopy, energy levels and photovoltaic performance. *Phys. Chem. Chem. Phys.* 11, 133. doi:10.1039/b812154k
- Marques, M.A.L., Gross, E.K.U., 2004. Time-Dependent Density Functional Theory. *Annu. Rev. Phys. Chem.* 55, 427–455. doi:10.1146/annurev.physchem.55.091602.094449
- Matar, F., Ghaddar, T.H., Walley, K., DosSantos, T., Durrant, J.R., O'Regan, B., 2008. A new ruthenium polypyridyl dye, TG6, whose performance in dye-sensitized solar cells is surprisingly close to that of N719, the “dye to beat” for 17 years. *J. Mater. Chem.* 18, 4246–4253. doi:10.1039/B808255C
- Mathew, S., Yella, A., Gao, P., Humphry-Baker, R., Curchod, B.F.E., Ashari-Astani, N., Tavernelli, I., Rothlisberger, U., Nazeeruddin, M.K., Grätzel, M., 2014. Dye-sensitized solar cells with 13% efficiency achieved through the molecular engineering of porphyrin sensitizers. *Nat. Chem.* 6, 242–247. doi:10.1038/nchem.1861
- Miertuš, S., Scrocco, E., Tomasi, J., 1981. Electrostatic interaction of a solute with a continuum. A direct utilization of AB initio molecular potentials for the prevision of solvent effects. *Chem. Phys.* 55, 117–129. doi:10.1016/0301-0104(81)85090-2
- Miertuš, S., Tomasi, J., 1982. Approximate evaluations of the electrostatic free energy and internal energy changes in solution processes. *Chem. Phys.* 65, 239–245. doi:10.1016/0301-0104(82)85072-6
- Møller, C., Plesset, M.S., 1934. Note on an Approximation Treatment for Many-Electron Systems. *Phys. Rev.* 46, 618–622. doi:10.1103/PhysRev.46.618
- Nakade, S., Makimoto, Y., Kubo, W., Kitamura, T., Wada, Y., Yanagida, S., 2005. Roles of Electrolytes on Charge Recombination in Dye-Sensitized TiO₂ Solar Cells (2): The Case of Solar Cells Using Cobalt Complex Redox Couples. *J. Phys. Chem. B* 109, 3488–3493. doi:10.1021/jp046002d

- Nakade, S., Saito, Y., Kubo, W., Kitamura, T., Wada, Y., Yanagida, S., 2003. Influence of TiO₂ Nanoparticle Size on Electron Diffusion and Recombination in Dye-Sensitized TiO₂ Solar Cells. *J. Phys. Chem. B* 107, 8607–8611. doi:10.1021/jp034773w
- Ni, M., Leung, M.K.H., Leung, D.Y.C., Sumathy, K., 2007. A review and recent developments in photocatalytic water-splitting using for hydrogen production. *Renew. Sustain. Energy Rev.* 11, 401–425. doi:10.1016/j.rser.2005.01.009
- Nussbaumer, R.J., Caseri, W.R., Smith, P., Tervoort, T., 2003. Polymer- TiO₂ Nanocomposites: A Route Towards Visually Transparent Broadband UV Filters and High Refractive Index Materials. *Macromol. Mater. Eng.* 288, 44–49. doi:10.1002/mame.200290032
- Omar, A., Abdullah, H., 2014. Electron transport analysis in zinc oxide-based dye-sensitized solar cells: A review. *Renew. Sustain. Energy Rev.* 31, 149–157. doi:10.1016/j.rser.2013.11.031
- Ondersma, J.W., Hamann, T.W., 2011. Measurements and Modeling of Recombination from Nanoparticle TiO₂ Electrodes. *J. Am. Chem. Soc.* 133, 8264–8271. doi:10.1021/ja201333u
- Onsager, L., 1936. Electric Moments of Molecules in Liquids. *J. Am. Chem. Soc.* 58, 1486–1493. doi:10.1021/ja01299a050
- O'Regan, B., Grätzel, M., 1991a. A low-cost, high-efficiency solar cell based on dye-sensitized colloidal TiO₂ films. *Nature* 353, 737–740. doi:10.1038/353737a0
- O'Regan, B., Grätzel, M., 1991b. A low-cost, high-efficiency solar cell based on dye-sensitized colloidal TiO₂ films. *Nature* 353, 737–740. doi:10.1038/353737a0
- Parkin, I.P., Palgrave, R.G., 2005. Self-cleaning coatings. *J. Mater. Chem.* 15, 1689–1695. doi:10.1039/B412803F
- Park, N.-G., van de Lagemaat, J., Frank, A.J., 2000. Comparison of Dye-Sensitized Rutile- and Anatase-Based TiO₂ Solar Cells. *J. Phys. Chem. B* 104, 8989–8994. doi:10.1021/jp9943651
- Pascoe, A.R., Bourgeois, L., Duffy, N.W., Xiang, W., Cheng, Y.-B., 2013a. Surface State Recombination and Passivation in Nanocrystalline TiO₂ Dye-Sensitized Solar Cells. *J. Phys. Chem. C* 117, 25118–25126. doi:10.1021/jp408055g
- Pascoe, A.R., Bourgeois, L., Duffy, N.W., Xiang, W., Cheng, Y.-B., 2013b. Surface State Recombination and Passivation in Nanocrystalline TiO₂ Dye-Sensitized Solar Cells. *J. Phys. Chem. C* 117, 25118–25126. doi:10.1021/jp408055g
- Pauporté, T., Magne, C., 2014. Impedance spectroscopy study of N719-sensitized ZnO-based solar cells. *Thin Solid Films*. doi:10.1016/j.tsf.2013.11.121
- Pazoki, M., Taghavinia, N., Hagfeldt, A., Boschloo, G., 2014. Mesoporous TiO₂ Microbead Electrodes for Cobalt-Mediator-Based Dye-Sensitized Solar Cells. *J. Phys. Chem. C* 118, 16472–16478. doi:10.1021/jp4113574
- Perdew, J.P., Burke, K., Ernzerhof, M., 1996. Generalized Gradient Approximation Made Simple. *Phys. Rev. Lett.* 77, 3865–3868. doi:10.1103/PhysRevLett.77.3865
- Quintana, M., Edvinsson, T., Hagfeldt, A., Boschloo, G., 2007. Comparison of Dye-Sensitized ZnO and TiO₂ Solar Cells: Studies of Charge Transport and Carrier Lifetime. *J. Phys. Chem. C* 111, 1035–1041. doi:10.1021/jp065948f
- Reyes-Coronado, D., Rodríguez-Gattorno, G., Espinosa-Pesqueira, M.E., Cab, C., Coss, R. de, Oskam, G., 2008. Phase-pure TiO₂ nanoparticles: anatase, brookite and rutile. *Nanotechnology* 19, 145605. doi:10.1088/0957-4484/19/14/145605
- Roy-Mayhew, J.D., Bozym, D.J., Punckt, C., Aksay, I.A., 2010. Functionalized Graphene as a Catalytic Counter Electrode in Dye-Sensitized Solar Cells. *ACS Nano* 4, 6203–6211. doi:10.1021/nn1016428
- Runge, E., Gross, E.K.U., 1984. Density-Functional Theory for Time-Dependent Systems. *Phys. Rev. Lett.* 52, 997–1000. doi:10.1103/PhysRevLett.52.997
- Sakuragi, Y., Wang, X.-F., Miura, H., Matsui, M., Yoshida, T., 2010. Aggregation of indoline dyes as sensitizers for ZnO solar cells. *J. Photochem. Photobiol. Chem.* 216, 1–7. doi:10.1016/j.jphotochem.2010.08.015
- Schrödinger, E., 1926. An Undulatory Theory of the Mechanics of Atoms and Molecules. *Phys. Rev.* 28, 1049–1070. doi:10.1103/PhysRev.28.1049
- Sharma, A.K., 1996. *Semiconductor Electronics*. New Age International, p 6-7.
- Sheng, X., He, D., Yang, J., Zhu, K., Feng, X., 2014. Oriented Assembled TiO₂ Hierarchical Nanowire Arrays with Fast Electron Transport Properties. *Nano Lett.* 14, 1848–1852. doi:10.1021/nl4046262

- Sima, C., Grigoriu, C., Antohe, S., 2010. Comparison of the dye-sensitized solar cells performances based on transparent conductive ITO and FTO. *Thin Solid Films, Special Section: Romanian Conference on Advanced Materials 2009* 519, 595–597. doi:10.1016/j.tsf.2010.07.002
- Taya, S., Kuwahara, S., Shen, Q., Toyoda, T., Katayama, K., 2014. Role of lithium and co-existing cations in electrolyte to improve performance of dye-sensitized solar cells. *RSC Adv.* 4, 21517–21520. doi:10.1039/C4RA02309A
- Thiel, W., 2005. Chapter 21 - Semiempirical quantum-chemical methods in computational chemistry, in: Scuseria, C.E.D.F.S.K.E. (Ed.), *Theory and Applications of Computational Chemistry*. Elsevier, Amsterdam, pp. 559–580.
- Thomas, A.G., Syres, K.L., 2012. Adsorption of organic molecules on rutile TiO₂ and anatase TiO₂ single crystal surfaces. *Chem. Soc. Rev.* 41, 4207–4217. doi:10.1039/C2CS35057B
- Tsubomura, H., Matsumura, M., Nomura, Y., Amamiya, T., 1976. Dye sensitised zinc oxide: aqueous electrolyte: platinum photocell. *Nature* 261, 402–403. doi:10.1038/261402a0
- VandeVondele, J., Krack, M., Mohamed, F., Parrinello, M., Chassaing, T., Hutter, J., 2005. Quickstep: Fast and accurate density functional calculations using a mixed Gaussian and plane waves approach. *Comput. Phys. Commun.* 167, 103–128. doi:10.1016/j.cpc.2004.12.014
- Villanueva-Cab, J., Jang, S.-R., Halverson, A.F., Zhu, K., Frank, A.J., 2014. Trap-Free Transport in Ordered and Disordered TiO₂ Nanostructures. *Nano Lett.* 14, 2305–2309. doi:10.1021/nl4046087
- Vosko, S.H., Wilk, L., Nusair, M., 1980. Accurate spin-dependent electron liquid correlation energies for local spin density calculations: a critical analysis. *Can. J. Phys.* 58, 1200–1211. doi:10.1139/p80-159
- Wang, D., Choi, D., Li, J., Yang, Z., Nie, Z., Kou, R., Hu, D., Wang, C., Saraf, L.V., Zhang, J., Aksay, I.A., Liu, J., 2009. Self-Assembled TiO₂–Graphene Hybrid Nanostructures for Enhanced Li-Ion Insertion. *ACS Nano* 3, 907–914. doi:10.1021/nn900150y
- Wang, Q., Ito, S., Grätzel, M., Fabregat-Santiago, F., Mora-Seró, I., Bisquert, J., Bessho, T., Imai, H., 2006. Characteristics of High Efficiency Dye-Sensitized Solar Cells†. *J. Phys. Chem. B* 110, 25210–25221. doi:10.1021/jp064256o
- Wang, X., Xi, M., Fong, H., Zhu, Z., 2014. Flexible, Transferable, and Thermal-Durable Dye-Sensitized Solar Cell Photoanode Consisting of TiO₂ Nanoparticles and Electrospun TiO₂/SiO₂ Nanofibers. *ACS Appl. Mater. Interfaces* 6, 15925–15932. doi:10.1021/am503542g
- Weerasinghe, H.C., Huang, F., Cheng, Y.-B., 2013. Fabrication of flexible dye sensitized solar cells on plastic substrates. *Nano Energy* 2, 174–189. doi:10.1016/j.nanoen.2012.10.004
- Wijeratne, K., Bandara, J., 2014. Aspect-Ratio Dependent Electron Transport and Recombination in Dye-Sensitized Solar Cells fabricated with one-dimensional ZnO nanostructures. *Electrochimica Acta* 148, 302–309. doi:10.1016/j.electacta.2014.10.046
- Wu, W.-Q., Rao, H.-S., Feng, H.-L., Guo, X.-D., Su, C.-Y., Kuang, D.-B., 2014a. Morphology-controlled cactus-like branched anatase TiO₂ arrays with high light-harvesting efficiency for dye-sensitized solar cells. *J. Power Sources* 260, 6–11. doi:10.1016/j.jpowsour.2014.02.107
- Wu, W.-Q., Xu, Y.-F., Rao, H.-S., Su, C.-Y., Kuang, D.-B., 2014b. Trilayered Photoanode of TiO₂ Nanoparticles on a 1D–3D Nanostructured TiO₂-Grown Flexible Ti Substrate for High-Efficiency (9.1%) Dye-Sensitized Solar Cells with Unprecedentedly High Photocurrent Density. *J. Phys. Chem. C* 118, 16426–16432. doi:10.1021/jp4116782
- Yeh, M.-H., Lin, L.-Y., Lee, C.-P., Wei, H.-Y., Chen, C.-Y., Wu, C.-G., Vittal, R., Ho, K.-C., 2011. A composite catalytic film of PEDOT:PSS/TiN-NPs on a flexible counter-electrode substrate for a dye-sensitized solar cell. *J. Mater. Chem.* 21, 19021–19029. doi:10.1039/C1JM12428E
- Yella, A., Lee, H.-W., Tsao, H.N., Yi, C., Chandiran, A.K., Nazeeruddin, M.K., Diao, E.W.-G., Yeh, C.-Y., Zakeeruddin, S.M., Grätzel, M., 2011. Porphyrin-Sensitized Solar Cells with Cobalt (II/III)-Based Redox Electrolyte Exceed 12 Percent Efficiency. *Science* 334, 629–634. doi:10.1126/science.1209688
- Yella, A., Mai, C.-L., Zakeeruddin, S.M., Chang, S.-N., Hsieh, C.-H., Yeh, C.-Y., Grätzel, M., 2014. Molecular Engineering of Push–Pull Porphyrin Dyes for Highly Efficient Dye-Sensitized Solar Cells: The Role of Benzene Spacers. *Angew. Chem.* 126, 3017–3021. doi:10.1002/ange.201309343
- Yum, J.-H., Baranoff, E., Kessler, F., Moehl, T., Ahmad, S., Bessho, T., Marchioro, A., Ghadiri, E., Moser, J.-E., Yi, C., Nazeeruddin, M.K., Grätzel, M., 2012a. A cobalt complex redox shuttle for dye-sensitized solar cells with high open-circuit potentials. *Nat. Commun.* 3, 631. doi:10.1038/ncomms1655

- Yum, J.-H., Baranoff, E., Kessler, F., Moehl, T., Ahmad, S., Bessho, T., Marchioro, A., Ghadiri, E., Moser, J.-E., Yi, C., Nazeeruddin, M.K., Grätzel, M., 2012b. A cobalt complex redox shuttle for dye-sensitized solar cells with high open-circuit potentials. *Nat. Commun.* 3, 631. doi:10.1038/ncomms1655
- Zeng, W., Cao, Y., Bai, Y., Wang, Y., Shi, Y., Zhang, M., Wang, F., Pan, C., Wang, P., 2010. Efficient Dye-Sensitized Solar Cells with an Organic Photosensitizer Featuring Orderly Conjugated Ethylenedioxythiophene and Dithienosilole Blocks. *Chem. Mater.* 22, 1915–1925. doi:10.1021/cm9036988
- Zhang, J., Feng, J., Hong, Y., Zhu, Y., Han, L., 2014. Effect of different trap states on the electron transport of photoanodes in dye sensitized solar cells. *J. Power Sources* 257, 264–271. doi:10.1016/j.jpowsour.2014.01.086
- Zhang, Q., Dandeneau, C.S., Zhou, X., Cao, G., 2009. ZnO Nanostructures for Dye-Sensitized Solar Cells. *Adv. Mater.* 21, 4087–4108. doi:10.1002/adma.200803827

Chapter III

Research Methods

The research in the present work has been carried out both experimentally and computationally. The experimental part has been done at the *Institut de Recherche Chimie-Paristech*, IRCP-ENSCP, Paris, France; whereas the computational part has been done at the Inorganic and Physical Chemistry Laboratory, Faculty of Mathematics and Natural Sciences, *Institut Teknologi Bandung* (ITB), Bandung, Indonesia. The computational study was implemented to support some experimental results.

The heart of experimental aspect in this research was to measure the cell performance and to achieve an in-deep understanding of the cell functioning. The former was obtained by doing I-V curve measurement of the cell functioning and the later by using the impedance spectroscopy (IS) technique. The other characterizations were also implemented to support the cell performance measurements, such as optical spectroscopies, X-ray diffraction (XRD), Scanning Electron Microscopy (SEM), BET (Brunauer, Emmett and Teller) specific internal surface area measurement, Fourier-Transform Infra-Red (FTIR) spectroscopy and Raman measurements. All photoelectrodes in this thesis were prepared by doctor-blading technique with pastes prepared at the laboratory, except the anatase nanoparticle paste Dyesol® 18NR-T. We have prepared some of the investigated nanoparticles, others were commercial available or prepared by collaboration partners.

The classification of the investigated cells is based on the photoelectrode composition and their nomenclature is written as follows:

- TiO_2 brookite cells: composed on TiO_2 with the brookite structure. We have investigated two kinds of brookite cells with two different brookite nanoparticles. The first one was synthesized by hydrolysis (named $\text{TiO}_2\text{_B1}$) and second one was synthesized by co-hydrolysis (named $\text{TiO}_2\text{_B2}$). Both particles were prepared using acidic conditions.
- Dyesol-anatase cell (named $\text{TiO}_2\text{_D}$): composed on TiO_2 that has anatase structure. We prepared the cell using the commercial paste Dyesol® 18NR-T.
- TiO_2 anatase cell (named $\text{TiO}_2\text{_A}$): composed on TiO_2 that has anatase structure. The particles were prepared at the laboratory by hydrothermal reaction.

- TiO₂/graphene composite cell (named TiO₂_Gr): composed on TiO₂_A and graphene particle that were combined in the upon the paste preparation (see section III.2.1)
- ZnO commercial cell (named ZnO_C20): composed on the nanoparticles ZnO commercial VP-AdNano-ZnO 20 that has more or less a spherical structure with a mean diameter of around 20 nm.
- ZnO nanorod-like cell (named ZnO_NR): composed on the ZnO nanoparticles that have rod-like structure. The particles were prepared by hydrolysis using polyol technique.

The computational study was carried out to explain the electronic properties of sensitizer dyes. It has been done to calculate the electronic mapping of the molecular orbitals, to calculate the UV-Visible spectra and determine which electronic transition is the most favorable in the molecule for the solar light absorption.

To explain all procedures, this chapter is divided into four general parts: the nanoparticle synthesis, the preparation of cells, their characterization and the computational procedure.

III.1. Synthesis of particles for the photoanodes

The section below explains the preparation of TiO₂ anatase particles, brookite nanoparticles and ZnO nanorods.

Synthesis Particle TiO₂ Anatase (TiO₂_A)

TiO₂_A nanoparticles were prepared by using modifications of previously reported methods (Ito et al., 2008). 15.3 mL of titanium iso-propoxide (TIP) was poured in to 50 mL Erlenmeyer under argon. The TIP was obtained from Aldrich. 2.857 mL of glacial acetic acid (Merck) was then added into the TIP to modify it. The mixture was stirred for 15 minutes at room temperature. 72.5 mL water demineralization was poured in a 100 mL round-flask. The modified TIP was then poured into the water as soon as possible under vigorously stirring to produce a white precipitate. The stirring process was continued for 1 hour to complete the hydrolysis reaction. 1 mL HNO₃ 68 % (Merck) was added into the mixture, then the temperature was increased gradually from room temperature to 80°C for 40 minutes under reflux conditions. The mixture was left at this temperature for 75 minutes to get a good dispersion. After that, 2 mL of water was added into the dispersion to adjust the volume at 92.5 mL. It was then allowed to cool at room temperature. The synthesis was continued by putting the dispersion into a teflon-lined hydrothermal reactor. The hydrothermal reaction was done in an oven at 225°C for 12 hours. After cooling a white precipitate was formed in the

reactor. After addition of 0.6 mL of HNO₃ 68%, the mixture was re-dispersed by ultrasonication for 5 minutes, twice. To make the dispersion separation easier, it need to be concentrated. It has been done by removing 50 gram of water using rotary evaporator at 45°C and 70 mbar. The nanoparticles were then washed in water to remove nitric acid. They were centrifugated at 12000 rpm for 15 minutes. The supernatant was removed and the particles were redissolved in water. This step was done three times then the particles were treated in the same manner three times in ethanol to eliminate water. The resulting powder was dried for 1-3 days at 40°C in an oven. They were used without any further purification.



Figure 3.1: Hydrothermal reactor used for TiO₂ nanopartciles preparation.

Synthesis of brookite TiO₂ nanopartciles (TiO₂_B1 and TiO₂_B2)

The brookite particles B1 and B2 were synthesized in collaboration with the *Laboratoire de Chimie de la Matière Condensée de Paris, Collège de France*, Paris, France. The brookite particles B1 were synthesized by adding pure TiCl₄ (Aldrich) in a 3 M HCl (Merck) solution to form a colorless solution with a Ti concentration of 0.15 M (Pottier et al., 2001a). The solution was heated and aged at 95°C during 3 days and was then after peptized to eliminate the rutile phase. The brookite particles B2 were synthesized by co-hydrolysis of the aqueous precursors TiCl₃ and TiCl₄ with a total Ti concentration of 0.04 M (Pottier et al., 2001b) The pH of an equimolar solution of Ti³⁺ and Ti⁴⁺ was adjusted to 4.5 and the suspension was aged one week at 60°C.

Synthesis ZnO nanoparticles (ZnO_NR)

ZnO_NR were prepared in collaboration with the *Laboratoire des Sciences des Procédés et des Matériaux, Université Paris 13, Villetaneuse, France*. Zinc acetate dihydrate ($\text{Zn}(\text{OAc})_2 \cdot 2\text{H}_2\text{O}$), and an appropriate volume of distilled water were successively added to diethylene glycol DEG ($\text{O}(\text{CH}_2\text{CH}_2\text{OH})_2$) at 161°C . The size and morphology of the particles were controlled by adjusting the zinc concentration (z), $z = 0.5 \text{ M}$, and the hydrolysis ratio, defined as $h = n_{\text{H}_2\text{O}}/n_{\text{Zn}^{2+}}$, $h = 5$. The mixture was then heated under reflux at a specified temperature for 1 hour. After hydrolysis, the white precipitate of zinc oxide nanoparticles was centrifuged, washed several times with ethanol and acetone, and dried at 60°C .

III. 2. Cell Preparation

Photoelectrode

TiO₂ paste preparation

1 g of TiO_2 , 4.06 g of terpineol (Aldrich), 5 mL of ethanol were mixed together under vigorous agitation. Ethylcellulose solution in ethanol then was added into TiO_2 solution. For TiO_2 paste, ethylcellulose solution composed by 281 mg of ethyl cellulose (EC) powder (5–15 mPas) (Fluka), 219 mg of EC (30–50m Pa.s) (Fluka) and 4.5 mL of ethanol. The two solutions were then mixed and sonicated several times using an ultrasonic horn (Figure 3.2). Ethanol and water were subsequently removed from the solution in a rotary-evaporator at an initial temperature of 58°C in order to create a viscous paste (Magne et al., 2013; Magne et al., 2012).



Figure 3.2: Ultrasonic horn to prepare TiO_2 and ZnO paste

In the case for TiO₂_Gr cell, the composite was prepared by adding various amount of single layer graphene oxide (SGO) into TiO₂ nanoparticles in the step paste preparation. The SGO was obtained from Cheap Tubes Inc. The initial SGO weight to the total SGO plus TiO₂ weight ratio was varied at 0.6, 1.2, and 3%, namely TiO₂_Gr6, TiO₂_12, and TiO₂_30, respectively. For Dyesol-based cell, Dyesol(® 18NR-T paste was used directly without any treatment.

ZnO paste preparation

We also investigated the ZnO-based DSSCs in this present work. For preparing the ZnO-based DSSCs, the ZnO paste was prepared as the TiO₂ one except that the ZnO paste, was composed by 281 mg of ethyl cellulose (EC) powder (5–15 mPas), 109 mg of EC (30–50 m Pa.s) and 4.5 mL of ethanol.

Porous layer preparation by doctor blading

The photoelectrodes were prepared by spreading the paste on FTO glass substrate. The FTO glass substrates (TEC15, Pilkington) were cleaned with soap and rinsed with distilled water. They were then treated in acetone in an ultrasonic bath in acetone for 5 min and in ethanol for 5 min. The substrates were dried and placed in furnace at 450°C for 30 min.

In the case of TiO₂ layers, after cooling down, the substrates were immersed in a 40 mmol.L⁻¹ aqueous solution of TiCl₄ at 70°C for 30 min and rinsed with water and ethanol. The substrates were then dried and p at 500°C for 30 min. This process was repeated once.

A layer of oxide paste was spread on the FTO glass substrates by the doctor blading technique (Figure 3.3 and 3.4), relaxed under an ethanol atmosphere for at least 5 minutes and dried at 125°C for 5 min. The step was repeated several times in order to achieve the desired film thickness. No scattering layer was used for all the investigated cells. The films were then annealed at 500°C for 15 min, for TiO₂ layer and 410°C for 30 min, for ZnO layer. In the case of TiO₂ layers, a final TiCl₄ treatment was finally done by immersing the TiO₂ films in a 40 mmol.L⁻¹ TiCl₄ solution at 70°C for 30 min and annealing again at 500°C.

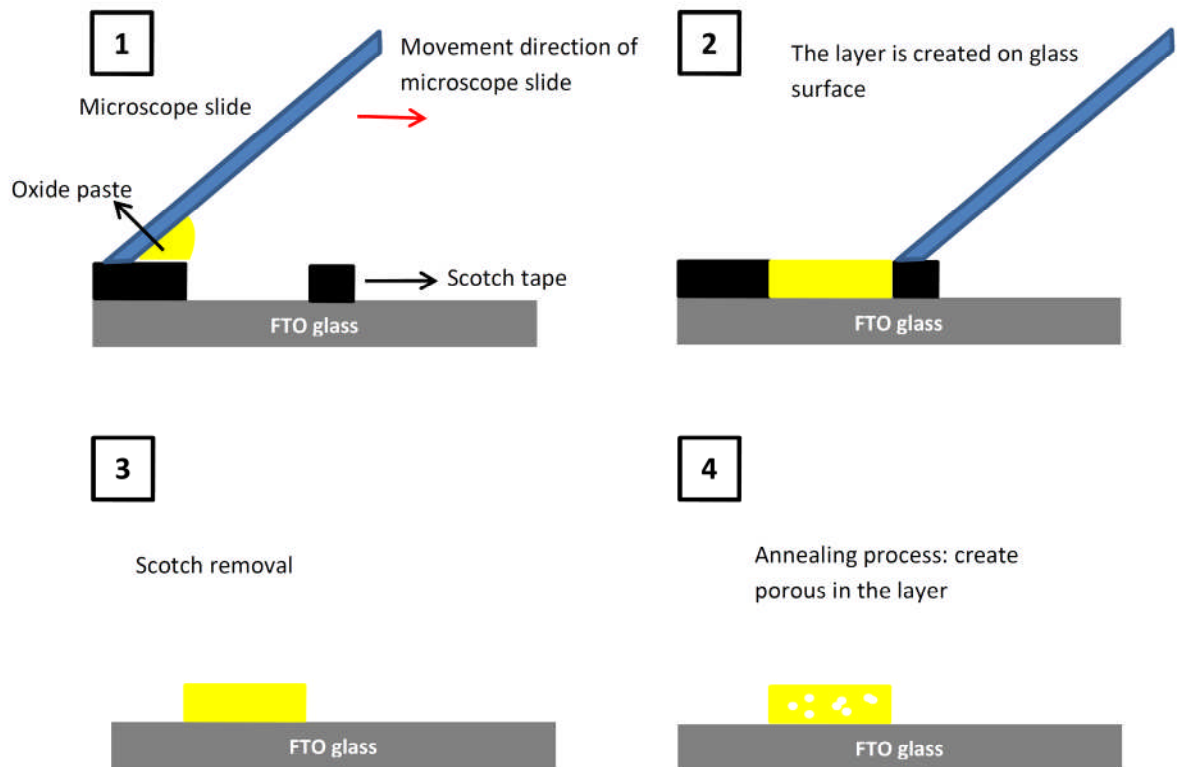


Figure 3.3: Scheme of doctor blade technique layer deposition (not a real colour)

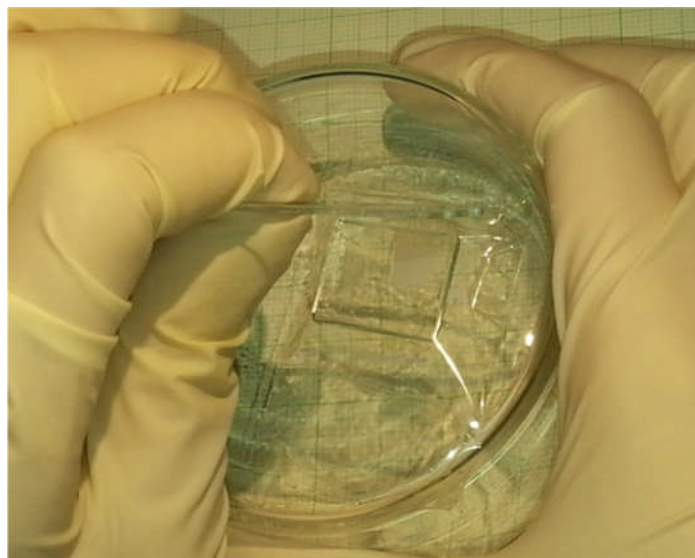


Figure 3.4: Oxide-layer deposition on FTO glass using doctor-blade technique

Electrolyte

The composition of the various electrolytes used in the present work is listed in the Table 3.1.

Table 3.1 Name and composition of electrolytes used in the thesis

Name	Iodine	DMPII	Co ²⁺	Co ³⁺	NOBF ₄	Li ⁺	GuA	TBP	Solvent
I ₂ -1	0.05 M	0.6 M	-	-	-	0.1 M	0.1 M	0.5 mM	Acetonitrile/Valeoronitrile (85:15)
I ₂ -2	0.05 M	0.6 M	-	-	-	0.1 M	0.1 M	0.2 mM	Acetonitrile/Valeoronitrile (85:15)
I ₂ -3	0.05 M	0.6 M	-	-	-	-	-	-	Acetonitrile
Co-1	-	-	0.11 M	0.01 M	-	0.1 M	-	0.2 mM	Acetonitrile
Co-2	-	-	0.11 M	-	0.01 M	0.1 M	-	0.2 mM	Acetonitrile
Co-3	-	-	0.11 M	-	0.01 M	0.1 M	-	0.1 mM	Acetonitrile
Co-4	-	-	0.11 M	-	0.01 M	0.1 M	-	0.5 mM	Acetonitrile
Co-5	-	-	0.22 M	-	0.02 M	0.1 M	-	0.2 mM	Acetonitrile
Co-6	-	-	0.11M	-	0.02 M	0.1 M	-	0.2 mM	Acetonitrile
Co-7	-	-	0.11M	-	0.02 M	0.1 M	-	-	Acetonitrile

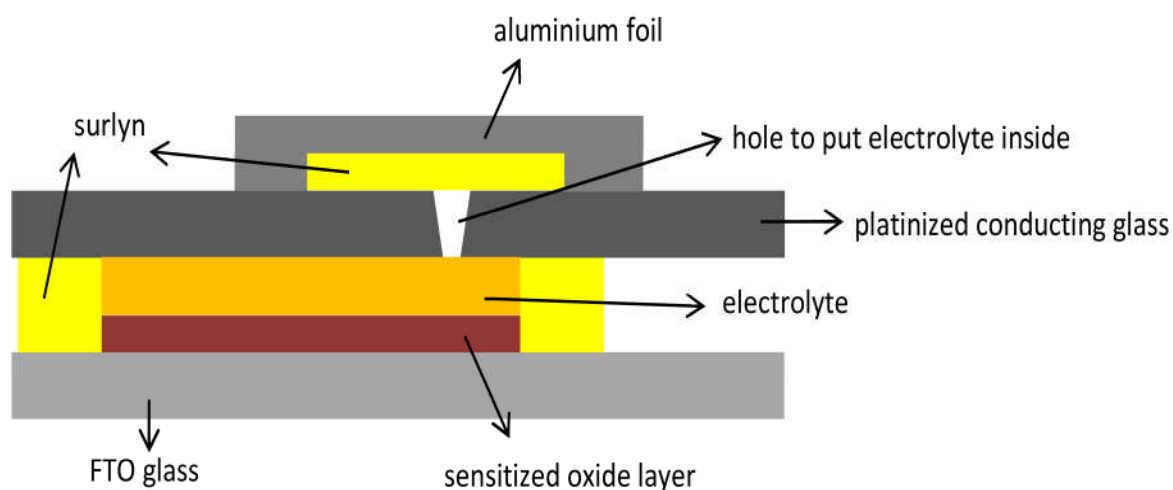
Counter electrode

The counter electrodes were prepared by depositing Platinum (Pt) on FTO glass. FTO glass substrates were first cleaned by ultrasound in acetone and ethanol for 5 min each. They were then treated in a furnace for 30 min at 450°C to remove organic contaminants. The Pt catalyst was deposited on the FTO glass by coating with a droplet of H₂PtCl₆ solution (6 mg in 1 mL ethanol) and subsequently heated at 400°C for 20 min. This step was repeated once or two to get the ad-hoc black color (Magne, 2012).

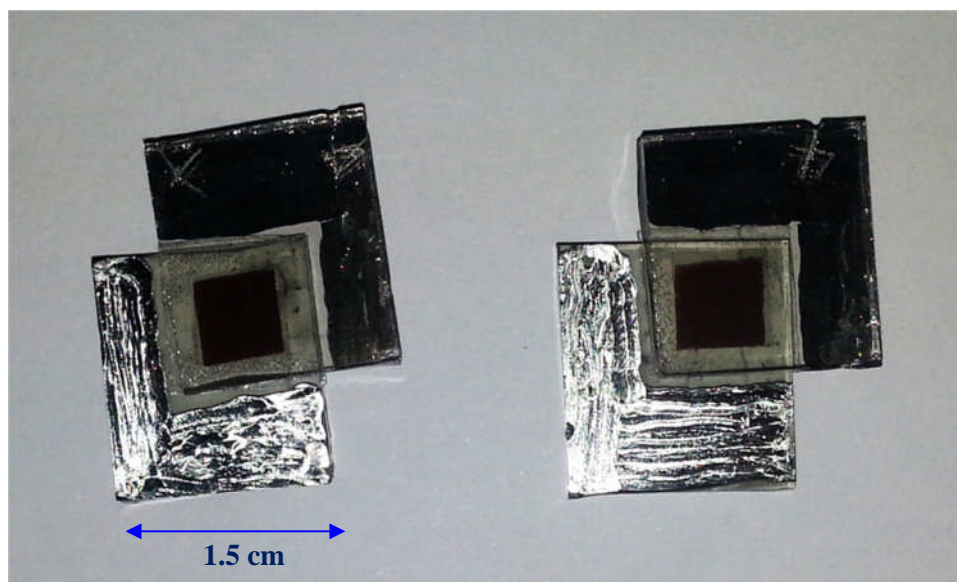
Cell Assembly

The photoanodes were sensitized by immersion in a dye solution. The immersion time depended on the photoelectrode. For TiO₂-based photoelectrode, sensitization time was 24 hours, whereas for the ZnO-based ones the immersion time was reduced to 2 hours to avoid the formation of dye aggregates. The photoelectrodes were then carefully rinsed with

acetonitrile. Then the photoelectrode and the counter-electrode were sealed together using a 50 μm hot melt spacer (Surlyn, DuPont). The internal space was filled with the electrolyte in vacuum through a hole drilled in the counter electrode (Figure 3.5.a). The hole was finally sealed by a piece of Surlyn and aluminium foil. Metal contact was then made on FTO using an ultrasonic solder. (Figure 3.5.b)



(a)



(b)

Figure 3.5: (a) Scheme of sealed cell cross-section (not a real colour) (b) Picture of sealed cell that has been prepared

III.3. Characterizations

Morphology and structure

The film morphologies were examined with a high-resolution Ultra 55 Zeiss FEG scanning electron microscope (SEM) at an acceleration voltage of 10 kV. Their thicknesses were measured with a Dektak 6 M stylus profiler. For the film structural characterizations, by a Phillips X'pert high-resolution X-ray diffractometer operated at 40 kV and 45 mA using the Cu K α radiation with $\lambda = 1.5406 \text{ \AA}$ was used. The crystallite size was determined from the XRD peak FWHM-data using the Scherrer formula (Appendix A) (Patterson, 1939).

The film porosities were estimated by mass measurements. The optical film properties (total transmission and total reflection) were recorded with a Carry 5000 UV-vis-NIR spectrophotometer equipped with an integrating sphere. The absorbance spectra of bare-layer and sensitized-layer were determined from the total transmission and total reflection data. The absorbance spectra of the bare-layer was used to calculate the semiconductor oxide bandgap (Appendix C) (Hagfeldt and Graetzel, 1995).

BET (Brunauer, Emmett and Teller)

The BET specific internal surface area measurements were done to see the effect of graphene on the specific surface area of the TiO₂ composite (see chapter IV). It was determined from the adsorption isotherms of Kr at the boiling point of liquid nitrogen ($\sim 77 \text{ K}$) using a Micromeritics ASAP 2010 apparatus (Pauporte and Rathousky, 2009; Pauporté and Rathouský, 2007).

FTIR (Fourier Transform Infra-Red) spectroscopy

FTIR analysis was carried out to confirm the convert of the graphene-oxide into reduced graphene and to control the kind of bound that happened in the composite of TiO₂/graphene (see Chapter IV). The FTIR curves were measured with a Tensor 27 apparatus from Bruker. The investigated samples were mixed with dry KBr, pressed as a pellet, and measured in a transmission mode.

Raman Spectroscopy

Micro-Raman spectroscopy was done to verify the graphene existence in TiO₂_Gr composite. The micro-Raman spectra of the films were measured using a Horiba Jobin-Yvon

LabRam IR system with backscattering geometry, using a 514.5 nm Ar⁺ laser as an excitation source.

Solar cell performance characterizations

The I - V curves were recorded by a Keithley 2400 digital sourcemeter, using a 0.01 V·s⁻¹ voltage sweep rate. The solar cells were illuminated with a solar simulator (Abet Technology Sun 2000) filtered to mimic air mass AM 1.5G conditions. The power density was calibrated to 100 mW·cm⁻² by the use of a reference silicon solar cell. The illuminated surface was delimited by a black mask. The incident-photon-to-electron conversion-efficiency (IPCE) spectra were measured at a short circuit with a homemade Jobin-Yvon system.

The spectra measurement of electrical impedance spectra (IS) were measured in the dark (except when mentioned), over a large potential range, by a Solartron FRA1255 frequency response analyzer coupled with a PAR273 EGG potentiostat. The AC signal was 10 mV and the frequency range was 100 kHz to 0.05 Hz. The reproducibility of the impedance data was checked on several cells prepared from different batches. The spectra were fitted and analyzed using the Zview modeling software (Scribner). The impedance spectroscopy results were corrected for IR-Drop over the sum of all series resistances. The real potential (V_{cor}) applied was determined by the subtraction of the voltage drop (V_{Drop}) from the applied potential ($V_{applied}$). The voltage drop was calculated by the integration of the sum of all series resistances, $R_{series} = R_s + R_{ce}$ with R_s being the series resistance, and R_{ce} the resistance due to the counter electrode (the diffusion resistance was negligible) over the current passed.

III.4. Computational Details

Investigation electronic properties of the dyes

The calculation to study the nature of the dye was carried out using the Gaussian 09 program package (Frisch, M. J. et. al., 2009). The B3LYP exchange-correlation functional (Becke, 1993a, 1993b; Lee et al., 1988) was used for small molecules, whereas the CAM-B3LYP one. for the longer molecule ones (Yanai et al., 2004). The dye geometries were optimized using the 6-311G* or 6-311G** basis set for C, H, O, N and S atoms (Krishnan et al., 1980; McLean and Chandler, 1980) together with the Los Alamos effective core potential LanL2DZ for Ruthenium and Cobalt [45-47].(Hay and Wadt, 1985; Wadt and Hay, 1985) Solvation effects were evaluated by the conductor-like polarizable continuum model (C-PCM) (Cossi et

al., 2003; Cossi and Barone, 2001), using DMF as a solvent for D149; acetonitrile for N719 and Z907; and dichloromethane for SD4, JM131, JM164 and TG6. The single point TD-DFT calculation (Runge and Gross, 1984) was carried out then to gain insight the electronic properties and the detailed excited states behavior that contribute to the UV/VIS spectra.

Investigation the adsorption of redox-couple species on anatase and brookite surface

The DFT calculation has been carried out using CP2K/Quickstep code which employs a hybrid Gaussian and plane-wave basis set (VandeVondele et al., 2005). The Perdew, Burke and Ernzerhof exchange-correlation functional has been used (Perdew et al., 1996). Goedecker, Teter and Hutter pseudopotentials (Goedecker et al., 1996) were used for describing the core electrons, and the wave functions of the valence electrons are expanded in terms of Gaussians function with a double- ζ (zeta) polarized basis set (DZVP) (Godbout et al., 1992; VandeVondele and Hutter, 2007). The details about this procedure is explained in section IV.4.

References

- Becke, A.D., 1993a. Density-functional thermochemistry. III. The role of exact exchange. *J. Chem. Phys.* 98, 5648–5652. doi:10.1063/1.464913
- Becke, A.D., 1993b. A new mixing of Hartree–Fock and local density-functional theories. *J. Chem. Phys.* 98, 1372–1377. doi:10.1063/1.464304
- Cossi, M., Barone, V., 2001. Time-dependent density functional theory for molecules in liquid solutions. *J. Chem. Phys.* 115, 4708–4717. doi:10.1063/1.1394921
- Cossi, M., Rega, N., Scalmani, G., Barone, V., 2003. Energies, structures, and electronic properties of molecules in solution with the C-PCM solvation model. *J. Comput. Chem.* 24, 669–681. doi:10.1002/jcc.10189
- Frisch, M. J.; Trucks, G. W.; Schlegel, H. B.; Scuseria, G. E.; Robb, M. A.; Cheeseman, J. R.; Scalmani, G.; Barone, V.; Mennucci, B.; Petersson, G. A.; Nakatsuji, H.; Caricato, M.; Li, X.; Hratchian, H. P.; Izmaylov, A. F.; Bloino, J.; Zheng, G.; Sonnenberg, J. L.; Hada, M.; Ehara, M.; Toyota, K.; Fukuda, R.; Hasegawa, J.; Ishida, M.; Nakajima, T.; Honda, Y.; Kitao, O.; Nakai, H.; Vreven, T.; Montgomery, J. A., Jr.; Peralta, J. E.; Ogliaro, F.; Bearpark, M.; Heyd, J. J.; Brothers, E.; Kudin, K. N.; Staroverov, V. N.; Kobayashi, R.; Normand, J.; Raghavachari, K.; Rendell, A.; Burant, J. C.; Iyengar, S. S.; Tomasi, J.; Cossi, M.; Rega, N.; Millam, M. J.; Klene, M.; Knox, J. E.; Cross, J. B.; Bakken, V.; Adamo, C.; Jaramillo, J.; Gomperts, R.; Stratmann, R. E.; Yazyev, O.; Austin, A. J.; Cammi, R.; Pomelli, C.; Ochterski, J. W.; Martin, R. L.; Morokuma, K.; Zakrzewski, V. G.; Voth, G. A.; Salvador, P.; Dannenberg, J. J.; Dapprich, S.; Daniels, A. D.; Farkas, Ö.; Foresman, J. B.; Ortiz, J. V.; Cioslowski, J.; Fox, D. J. (2009) Gaussian 09, Revision D.01, Gaussian, Inc., Wallingford CT, 2009
- Hagfeldt, A., Graetzel, M., 1995. Light-Induced Redox Reactions in Nanocrystalline Systems. *Chem. Rev.* 95, 49–68. doi:10.1021/cr00033a003
- Hay, P.J., Wadt, W.R., 1985. Ab initio effective core potentials for molecular calculations. Potentials for the transition metal atoms Sc to Hg. *J. Chem. Phys.* 82, 270–283. doi:10.1063/1.448799

- Godbout, N., Salahub, D.R., Andzelm, J., Wimmer, E., 1992. Optimization of Gaussian-type basis sets for local spin density functional calculations. Part I. Boron through neon, optimization technique and validation. *Can. J. Chem.* 70, 560–571. doi:10.1139/v92-079
- Goedecker, S., Teter, M., Hutter, J., 1996. Separable dual-space Gaussian pseudopotentials. *Phys. Rev. B* 54, 1703–1710. doi:10.1103/PhysRevB.54.1703
- Ito, S., Murakami, T.N., Comte, P., Liska, P., Grätzel, C., Nazeeruddin, M.K., Grätzel, M., 2008. Fabrication of thin film dye sensitized solar cells with solar to electric power conversion efficiency over 10%. *Thin Solid Films* 516, 4613–4619. doi:10.1016/j.tsf.2007.05.090
- Krishnan, R., Binkley, J.S., Seeger, R., Pople, J.A., 1980. Self-consistent molecular orbital methods. XX. A basis set for correlated wave functions. *J. Chem. Phys.* 72, 650–654. doi:10.1063/1.438955
- Lee, C., Yang, W., Parr, R.G., 1988. Development of the Colle-Salvetti correlation-energy formula into a functional of the electron density. *Phys. Rev. B* 37, 785–789. doi:10.1103/PhysRevB.37.785
- Magne, C. 2012. Optimisation de Couches D'oxyde Nano-structurees pour Applications aux Cellules Solaires a Colorant. Doctoral Thesis. Universite Pierre et Marie Curie, p. 208
- Magne, C., Dufour, F., Labat, F., Lancel, G., Durupthy, O., Cassaignon, S., Pauporté, T., 2012. Effects of TiO₂ nanoparticle polymorphism on dye-sensitized solar cell photovoltaic properties. *J. Photochem. Photobiol. Chem.* 232, 22–31. doi:10.1016/j.jphotochem.2012.01.015
- Magne, C., Moehl, T., Urien, M., Grätzel, M., Pauporté, T., 2013. Effects of ZnO film growth route and nanostructure on electron transport and recombination in dye-sensitized solar cells. *J. Mater. Chem. A* 1, 2079. doi:10.1039/c2ta00674j
- McLean, A.D., Chandler, G.S., 1980. Contracted Gaussian basis sets for molecular calculations. I. Second row atoms, Z=11–18. *J. Chem. Phys.* 72, 5639–5648. doi:10.1063/1.438980
- Patterson, A.L., 1939. The Scherrer Formula for X-Ray Particle Size Determination. *Phys. Rev.* 56, 978–982. doi:10.1103/PhysRev.56.978
- Pauporté, T., Rathouský, J., 2007. Electrodeposited Mesoporous ZnO Thin Films as Efficient Photocatalysts for the Degradation of Dye Pollutants. *J. Phys. Chem. C* 111, 7639–7644. doi:10.1021/jp071465f
- Pauporte, T., Rathousky, J., 2009. Growth mechanism and photocatalytic properties for dye degradation of hydrophobic mesoporous ZnO/SDS films prepared by electrodeposition. *Microporous Mesoporous Mater.* 117, 380–385. doi:10.1016/j.micromeso.2008.07.016
- Perdew, J.P., Burke, K., Ernzerhof, M., 1996. Generalized Gradient Approximation Made Simple. *Phys. Rev. Lett.* 77, 3865–3868. doi:10.1103/PhysRevLett.77.3865
- Pottier, A., Chanéac, C., Tronc, E., Mazerolles, L., Jolivet, J.-P., 2001a. Synthesis of brookite TiO₂ nanoparticles by thermolysis of TiCl₄ in strongly acidic aqueous media. *J. Mater. Chem.* 11, 1116–1121. doi:10.1039/B100435M
- Pottier, A., Chanéac, C., Tronc, E., Mazerolles, L., Jolivet, J.-P., 2001b. Synthesis of brookite TiO₂ nanoparticles by thermolysis of TiCl₄ in strongly acidic aqueous media. *J. Mater. Chem.* 11, 1116–1121. doi:10.1039/B100435M
- Runge, E., Gross, E.K.U., 1984. Density-Functional Theory for Time-Dependent Systems. *Phys. Rev. Lett.* 52, 997–1000. doi:10.1103/PhysRevLett.52.997
- Wadt, W.R., Hay, P.J., 1985. Ab initio effective core potentials for molecular calculations. Potentials for main group elements Na to Bi. *J. Chem. Phys.* 82, 284–298. doi:10.1063/1.448800
- Yanai, T., Tew, D.P., Handy, N.C., 2004. A new hybrid exchange–correlation functional using the Coulomb-attenuating method (CAM-B3LYP). *Chem. Phys. Lett.* 393, 51–57. doi:10.1016/j.cplett.2004.06.011
- VandeVondele, J., Hutter, J., 2007. Gaussian basis sets for accurate calculations on molecular systems in gas and condensed phases. *J. Chem. Phys.* 127, 114105. doi:10.1063/1.2770708
- VandeVondele, J., Krack, M., Mohamed, F., Parrinello, M., Chassaing, T., Hutter, J., 2005. Quickstep: Fast and accurate density functional calculations using a mixed Gaussian and plane waves approach

Chapter IV

TiO₂-Based DSSC I: Comparison of Anatase and Brookite-Based Dye-Sensitized Solar Cells

IV. 1. Introduction

Brookite is one of the crystal polymorph of TiO₂ which use in DSSC is potentially interesting. As explained in the section II.1.1, page 23, brookite has a wider band gap compared to that of anatase, due to this property a higher V_{oc} can be expected when brookite is used in DSSC photoelectrode compared to anatase. On contrary the J_{sc} of DSSCs based on brookite have been reported with a lower value compare to that of anatase. It strongly suggest because anatase has the lowest surface energy, which supports the dye adsorption (Thomas and Syres, 2012).

This section will discuss the comparison of the anatase and the brookite photoelectrode performance in the DSSC. This study is the continuation of preliminary work carried out at Chimie-paristech in Dr. Pauporté's group. That previous study has shown that the highest power conversion efficiency of brookite based cell reached 5.97% compare to anatase-standard one that reached 7.97% (Magne et al., 2012). To improve the brookite-based DSSCs, it is necessary to do an in-deep study to reveal the origin of the brookite cell characteristic. In this thesis, we have investigated these cells by impedance spectroscopy (IS). We have compared the performance of three kinds of cells, TiO₂_D; TiO₂_B1 and TiO₂_B2. The TiO₂_D is composed on the TiO₂ anatase photoanode, whereas both the TiO₂_B1 and the TiO₂_B2 are based on two different kind of brookite nanoparticles (see Chapter III for details). The key-point of IS results are (1) brookite surfaces are less active for I₃⁻ recombination on the TiO₂ surface compare to anatase and (2) their charge transfer is much slower due to a lower conductive. A computational study has also been done to support the first IS results, we have investigated the adsorption of iodine on the anatase and the brookite surface.

IV.2 Characteristics of the particles

The morphology and size of the B1 and B2 particles have been investigated by TEM observations and the results are displayed in the Figure 4.1 and 4.2.

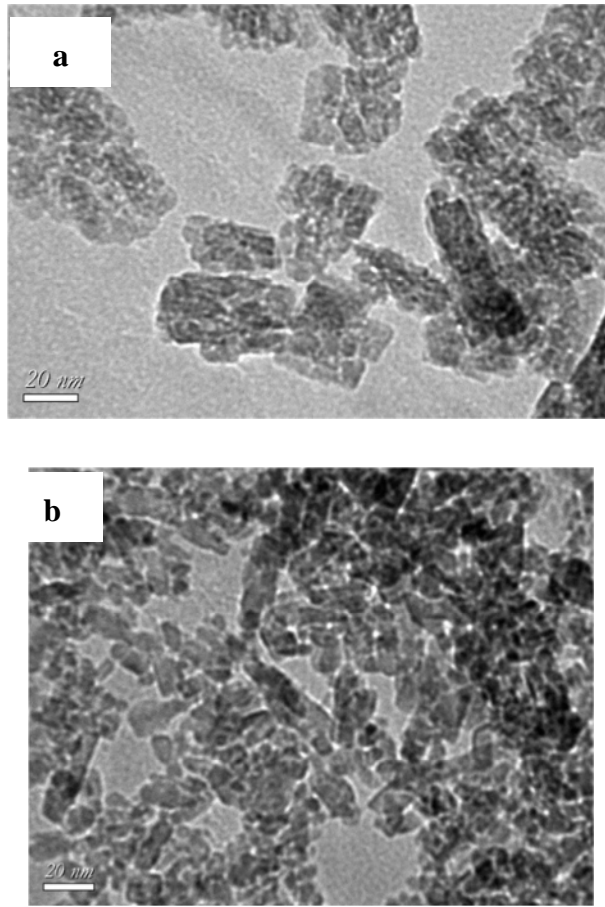


Figure 4.1: TEM images of particle (a) B1 and (b) B2

The B1 particles are aggregated, whereas the B2 particles are more anisotropic and elongated (Figure 4.1). Their size distribution analysis gives a mean diameter of 13 nm for the B1 particles, and 17x10 nm mean size for the B2 particles.

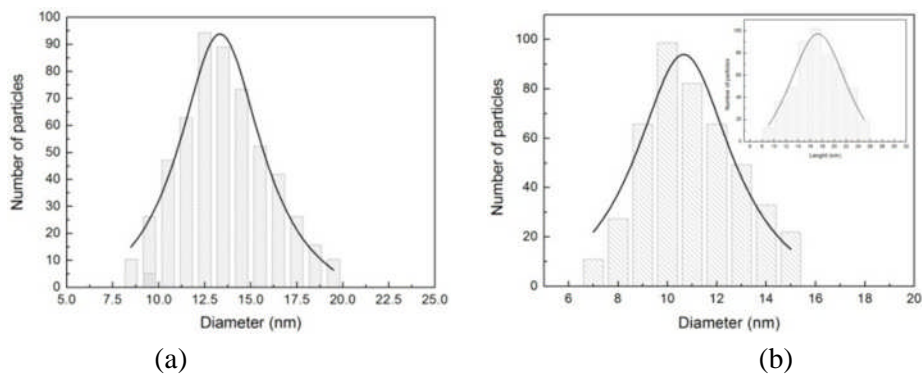


Figure 4.2: Size distribution of the brookite nanoparticles (a) B1 and (b) B2.

Porous layers have been prepared from the Dyesol and pastes based on anatase standard, B1 and B2 particles. The crystal structure of these samples has been checked by XRD measurements (Figure 4.3 and 4.4).

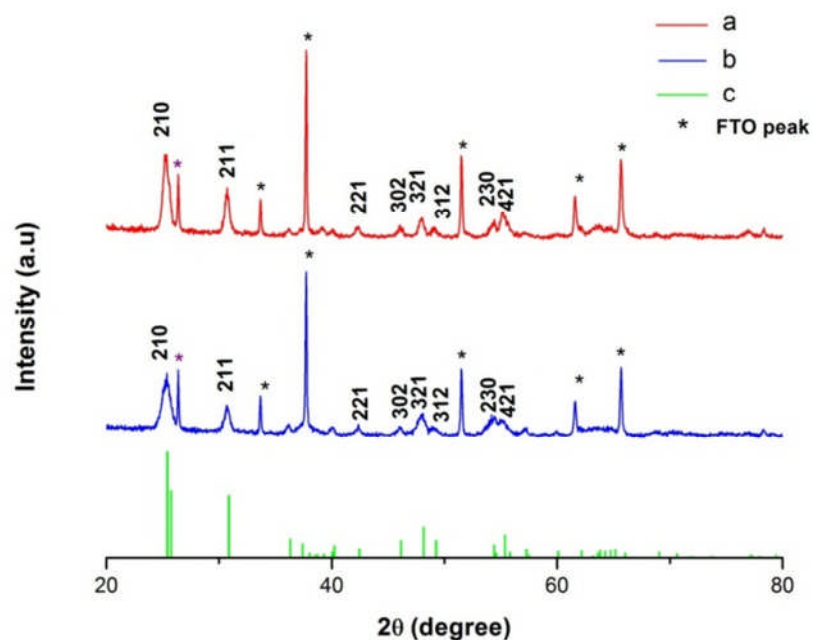


Figure 4.3: XRD pattern of (a) B1; (b) B2 and (c) Brookite standard

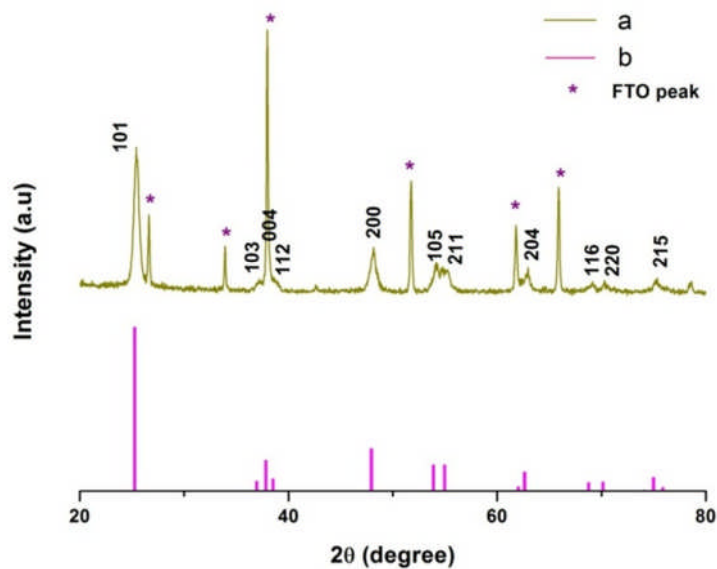


Figure 4.4: XRD patterns of (a) Dyesol and (b) Anatase standard

Figure 4.3 confirms that no phase change to rutile occurred upon the annealing process. XRD patterns of the Dyesol (Figure 4.4) are indexed with the anatase structure (standard JCPDS card no. 01-076-7109). The XRD patterns of the B1 and B2 (Figure 4.3) that also get in line with the brookite standard (No. 01-071-6410). The average crystallite size was estimated from the FWHM of the X-ray diffraction peaks using the Scherrer equation at 17 nm and 20 nm for B1 and B2 films, respectively (see Appendix A).

The optical properties of the layers have been measured by spectrophotometry. From the absorption edge in the near UV, the bandgap of the TiO_2 layers has been calculated. Band-gap calculation using the data from optical measurement affirm that band gap of Dyesol anatase is indirect with a value of 3.25 eV. On the other hand, B1 and B2 layers have a direct bandgap measured at 3.35 and 3.39, respectively (Appendix B). Absorption spectra of the Dyesol, B1 and B2 layers, sensitized by the N719 dye for 24h are shown in Figure 4.5 curves (a), (b) and (c), respectively. The figure also presents the absorbance curve of a dyesol porous layer sensitized for 4h (Figure 4.5, curve (d)).

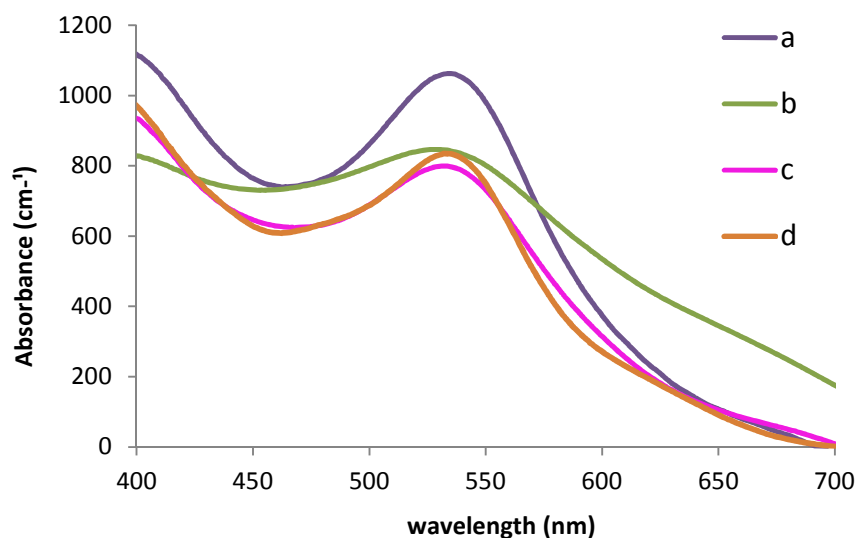


Figure 4.5: Absorbance spectra of sensitized layer of (a) Dyesol; (b) B1; (c) B2 with immersion time 24 hours and (d) Dyesol with immersion time 4 hours

IV. 3. Cell Performance and Impedance Study

IV.3.1. I-V Measurement Result

The I-V curve characteristics of Dyesol, B1 and B2 based DSSCs employing the N719 dye as the sensitizer and the I_3^-/I^- as the redox-couple (electrolyte I₂-1) gathered as well as the dye loading measurement are gathered in the Table 4.1. The sensitization time was 24 hours.

Table 4.1 Dye loading and cell characteristics under 100 mW.cm⁻², AM 1.5G filtered illumination.

Sample	Crystal phase	Thickness / μm	p^b	Dye concentration /mM	V_{oc} / V	J_{sc} /mA.cm ⁻²	FF	η /%
TiO ₂ _B1	Brookite	13.4	0.60	80	0.74	9.76	0.79	5.71
TiO ₂ _B2	Brookite	13.5	0.65	86	0.72	10.2	0.79	5.79
TiO ₂ _D	Anatase	13.4	0.65	122	0.69	14.5	0.79	7.42

^a Initial nanoparticle size; ^b Film porosity.

The B1 films made of the smallest brookite particles and with the smallest porosity exhibit a slightly lower dye loading compared to the B2 films. It can be explained by the surface reduction by necking upon the annealing process (Bisquert, 2002; Pauporté et al., 2005). We note that the dye loading for brookite is significantly lower than that of the reference anatase photoelectrode (Table 4.1) as evidenced by B2 and Dyesol films which have similar porosity and crystallite size. It suggests a lower density of anchoring sites for the dye on the brookite surface.

The sensitized films have been used for the preparation of DSSCs. Typical I-V curves are presented in Figure 4.5 and the photovoltaic curve parameters are gathered in Table 4.1. The efficiency of brookite cells is lower than that of the reference anatase cell. The fill factors (FF) are similar for the three cells. However, J_{sc} is significantly smaller for brookite. On the other hand, the brookite cells show higher V_{oc} than the anatase reference one. J_{sc} of the anatase cells is much larger than that of the brookite cells that is in agreement with a much larger dye loading (Table 4.1). As well, J_{sc} of B2 cells is slightly larger than B1 cells due to a better dye loading (Table 4.1). The B2 photoelectrodes have a higher amount of dye that

ensures a better sunlight harvesting which leads to a larger J_{sc} . However, the B1 cells have a higher V_{oc} due to a lower dark current (Figure 4.6).

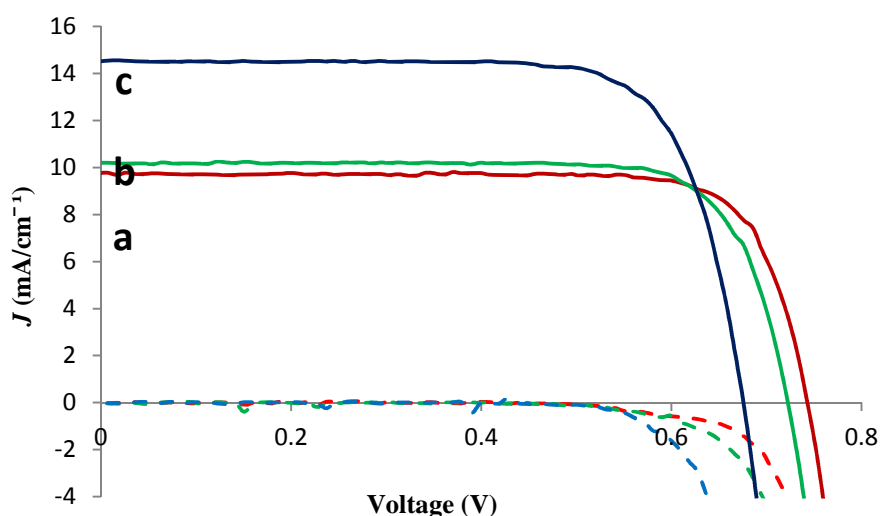


Figure 4.6: I-V curves of (a) TiO₂_B1, (b) TiO₂_B2 and (c) TiO₂_D under 100 mW.cm⁻², AM 1.5G filtered illumination. The dashed lines are the dark currents.

Overall, both brookite DSSCs have similar external conversion efficiency close to 6%. The IPCE curves of the investigated DSSCs are presented in Figure 4.7. They are in good agreement with the J_{sc} data with lower IPCE in the case of the brookite cells.

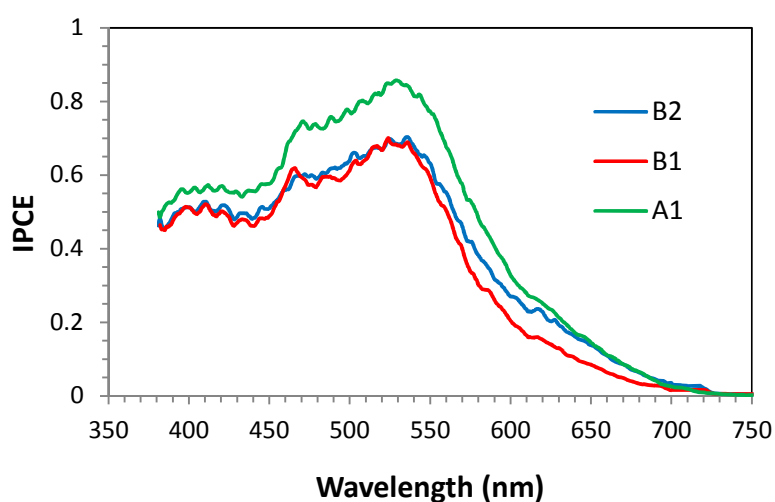


Figure 4.7: IPCE action spectra of brookite TiO₂_B1 and TiO₂_B2 solar cells and of the TiO₂_D reference cell.

IV.3.2 Analysis of the open circuit voltage

Impedance spectroscopy (IS) is a powerful technique that has been employed in a large extent to investigate the kinetic of electrochemical and photoelectrochemical reactions occurring in many functional systems, including DSSCs, in which coupled processes are involved (Bisquert and Vikhrenko, 2004; Wang et al., 2005). The impedance spectra of brookite and reference anatase cells were measured in the dark over a large applied voltage range in order to extract the kinetic data of the photoelectrodes at variable concentrations of trapped electrons (noted g , see chapter II, section II. 1. 3, page 39). Examples of spectra are presented in Figure 4.8. They have been analyzed according to the multiple trapping (MT) model (described in section II.1.2, page 30) (Kalyanasundaram, 2010). They all showed a characteristic low-middle frequency semicircle due to the resistance to charge transfer (recombination) (R_{ct}) across the sensitized oxide-electrolyte interface coupled to the total electrode capacitance, denoted as C_{μ} , which is a chemical capacitance due to filled trap states localized below the conduction band minimum. At high frequency, a second semicircle was found due to the resistance (R_{Pt}) and capacitance (C_{Pt}) of the charged counter-electrode/electrolyte interface. In the intermediate frequency range, a $\sim 45^\circ$ straight-line segment could be clearly observed for both B1 and B2 cells polarized at not too high applied voltage, which is characteristic of the electron transport by diffusion and is modeled by a transport resistance, noted R_{tr} . The high frequency series resistance, R_s , is due to the electrical contacts. The full equivalent circuit used to fit the spectra is presented in Figure 2.16. We noted that for all the investigated cells based on brookite or anatase, the IS spectra did not exhibit a clear Warburg loop at low frequency, even at a high applied voltage (Figure 4.8). This clearly excludes a performance limitation due to the diffusion of the I/I_3^- redox shuttle.

C_{μ} is a chemical capacitance due to filled trap states localized below the conduction band minimum (sub-band gap state). In the MT model of the DSSC functioning, these states are usually described as mainly located near the particle surface and/or at the necks between adjacent particles (Park et al., 2013; Zhu et al., 2006). C_{μ} is plotted as a function of V_{cor} in Figure 4.9 and it varies more or less exponentially as expected for the model used. The experimental data have been fitted by the equation 2.10 (Chapter 2).

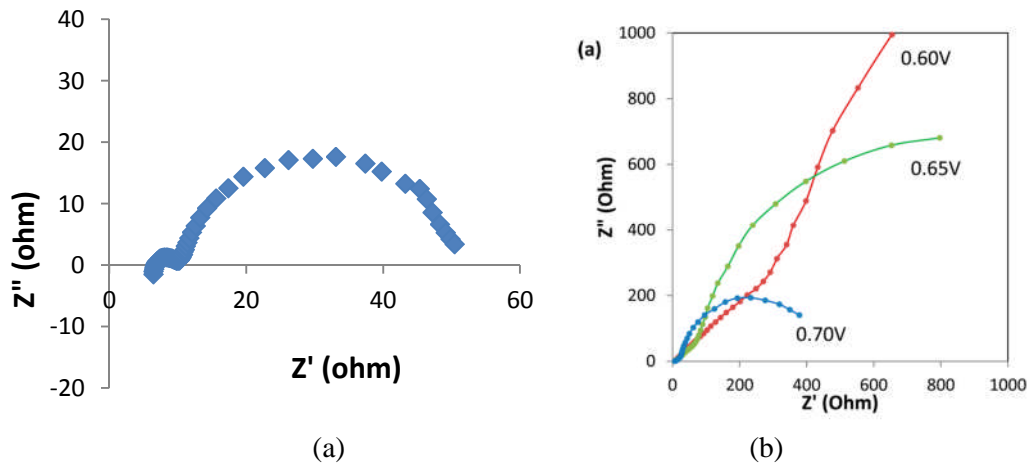


Figure 4.8: (a) Typical impedance spectra in the dark of B1 brookite cell polarized at 0.775 V (b) Effect of applied voltage on the impedance spectra of TiO₂_B1 solar cell in the dark.

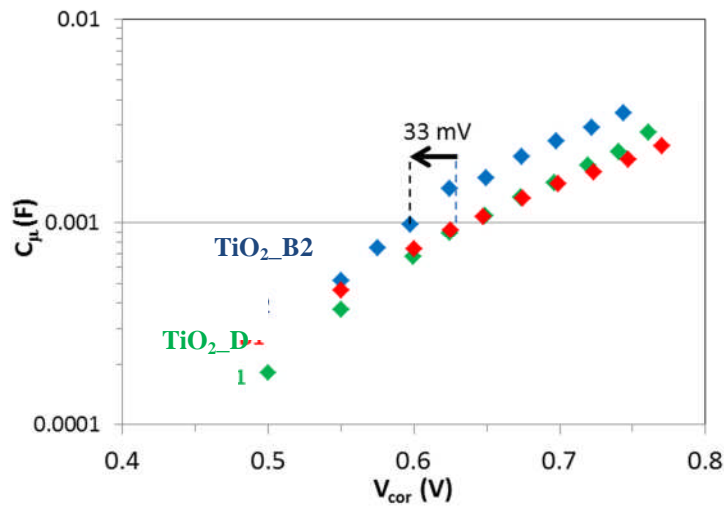


Figure 4.9: Variation of C_{μ} with V_{cor} for TiO₂_B1 (red) and TiO₂_B2 (blue) brookite solar cells and TiO₂_D (green) anatase solar cells.

α value for B1 and B2 is equal to 0.18 and 0.22, respectively (Table 3). For the reference anatase TiO₂ solar cell (TiO₂_D) this parameter is found at 0.23. α of anatase is classically reported in the literature to range between 0.2 and 0.4 (Peter, 2007; Wang et al., 2006). According to Equation 2.10 (page 38), the trap state depth can also be expressed as a temperature, T_0 , found to be 1330K and 1600K for the investigated brookite cells (Table 4.2).

Table 4.2 α , T_0 and β parameters extracted from the $C_\mu(V_{cor})$ and $R_{ct}(V_{cor})$ curve analysis.

Sample	α	T_0 (K)	β
TiO ₂ _B1	0.18	1600	0.60
TiO ₂ _B2	0.22	1330	0.57
TiO ₂ _D	0.23	1280	0.61

In Figure 4.9, the TiO₂_B1 curve has a lower slope than the TiO₂_D one but both curves more or less overlap. Therefore it can be concluded that the conduction band edge for these two compounds is located at about the same energy level. On the other hand, C_μ of TiO₂_B2 are higher and shifted by 33 mV ($-\Delta E_c/q$, with q the elementary charge) compared to TiO₂_D (Figure 4.9 and Table 4.3). It suggests that the conduction band edge of TiO₂_B2 is located 33 mV below the conduction band edge of TiO₂_B1 and TiO₂_D. This result confirms that the better J_{sc} of anatase cells is due to the higher dye loading and not to a poor efficiency of electron injection between the excited dye and the oxide matrix.

Table 4.3 Analysis of the open circuit voltage difference between anatase (taken as a reference) and brookite cells. ΔV_{cal} is a calculated value from the impedance data analysis and ΔV_{oc} is calculated from the I-V curve experimental data.

Sample	TiO ₂ _D	TiO ₂ _B1	TiO ₂ _B2
V_{oc} (mV)	690	740	720
$\Delta E_c/q$ (mV) ^a	/	0	-33
ΔV_k (mV) ^b	/	57	57
ΔV_{cal} (mV) ^c	/	57	24
ΔV_{oc} (mV) ^d	/	50	30

^a $\Delta E_c/q$ is the voltage shift needed to compare all the cells at the same conduction band level obtained after displacing the capacitances in Figure 4a. ^b ΔV_k is the voltage difference in R_{ct} due to the differences in recombination rates. ^c ΔV_{cal} is the voltage shift due to $\Delta E_c/q$ and ΔV_k (sum of both). ^d ΔV_{oc} is the open circuit voltage shift compared to the TiO₂_D cell used as a reference.

In Figure 4.10, R_{ct} is presented versus V_{cor} . Less recombination are found for the brookite cells compared to the anatase cell. Moreover, as expected, the cell with the highest R_{ct} values (TiO₂_B1) has the smallest dark current in Figure 4.6. R_{ct} of the TiO₂ cells show an

exponential variation, in agreement with the trapping-detrapping model, that follows the equation 2.15 (Chapter II, section II. 1. 3, page 39).

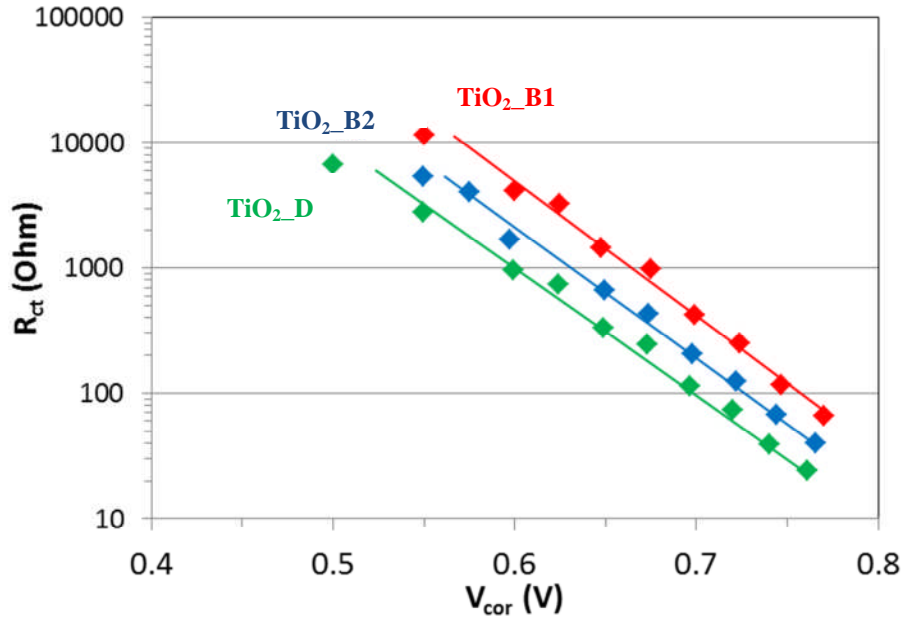


Figure 4.10: Variation of R_{ct} with V_{cor} for TiO₂_B1 (red), TiO₂_B2 (blue) and TiO₂_D (green) solar cells

β can be considered an estimation of the reaction order. β values for TiO₂_B1 and TiO₂_B2 cells are 0.60 and 0.57, respectively (Table 4.2). β lower than 1 is an empirical way to describe sublinear recombination kinetics that takes into account that electrons may be transferred from occupied levels located in the energy gap (Bisquert and Mora-Seró, 2010; Villanueva-Cab et al., 2010). The higher recombination rate in the TiO₂_D photoelectrode can explain the lower V_{oc} of these cells. We have quantified the effect of recombination on V_{oc} by analyzing the IS data according to the procedure described by Fabregat-Santiago et al in the Ref (Raga et al., 2012). In the Figure 4.11, R_{ct} is plotted versus the applied voltage corrected of the ohmic drop and of the -33 mV shift due to the different conduction band energy level (CBEL) in the case of B2 cells. This potential is noted V_{ecb} with $V_{ecb} = V_{cor} - \Delta E_c/q$. The CBEL of the TiO₂_D photoelectrode has been taken as the reference. We can see that after correction, TiO₂_B1 and TiO₂_B2 cells have the same R_{ct} values which are higher than that of TiO₂_D cells. The potential shift between the two curves, noted ΔV_k , is 57mV. It is the contribution of R_{ct} on the improvement of the V_{oc} in the brookite DSSCs. ΔV_{cal} is the voltage shift due to $\Delta E_c/q$ and ΔV_k . We found 57 mV for B1 and 24 mV for B2 (Table 4.3). These

values are close to the recorded V_{oc} shifts that are 50 mV and 30 mV for the B1 and B2 cells, respectively (Table 4.3). Therefore, we can conclude that the V_{oc} improvement in brookite DSSCs is due to a reduced recombination phenomenon.

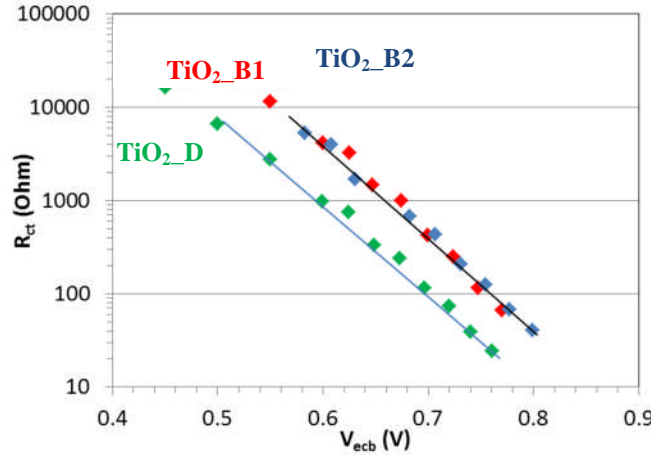


Figure 4.11: Plot of R_{ct} versus V_{ecb} , TiO₂_B1 (red), TiO₂_B2 (blue) and TiO₂_D (green), the applied voltage corrected of the shift due to different conduction band energy level.

IV.3.3. Analysis of charge transport and recombination in the photoelectrodes

The electron lifetime, τ_n , is the mean time before the charge recombination with the tri-iodine species in solution. It has been calculated according to: $\tau_n = R_{ct}C_{\mu}$ (Kalyanasundaram, 2010). Due to the different trap state distribution and conduction band level for the various electrodes, these parameters have been compared as a function of the trapped electron concentration, g . From C_{μ} , g has been calculated according to the equation 2.14 (Chapter 2, section II. 1. 3, page 39). τ_n and τ_{tr} are displayed in the Figure 4.12. τ_n decreases with the applied potential (and then g) because the electron interception increases with the driving force. τ_n for the two different brookite kinds of cells are longer than for the anatase reference cell in spite of a lower dye loading. The transport properties of the films are described by the R_{tr} parameter (Figure 4.13). The transport time is the mean time for the photogenerated electrons to reach the back contact. It has been calculated as $\tau_{tr} = R_{tr}C_{\mu}$ (Kalyanasundaram, 2010) and is plotted as a function of g in the Figure 4.12. We observe that the TiO₂ crystal phase has a strong influence on this parameter since much

shorter transport time is found for anatase compared to brookite. Figure 4.12 clearly illustrates that the ratio between the electron lifetime and transport time strongly depends on the crystal phase. τ_n is about two orders of magnitude higher than τ_{tr} in the case of anatase. On the other hand, it is only one order of magnitude higher for the two types of investigated brookite cells.

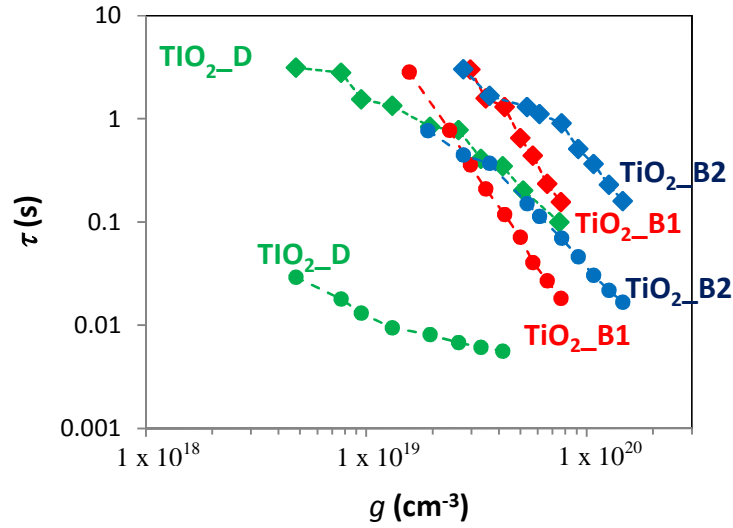


Figure 4.12: Effect of the phase and particle size on the charge carrier lifetime τ_n (diamond symbol) and τ_{tr} (dot symbols) versus g .

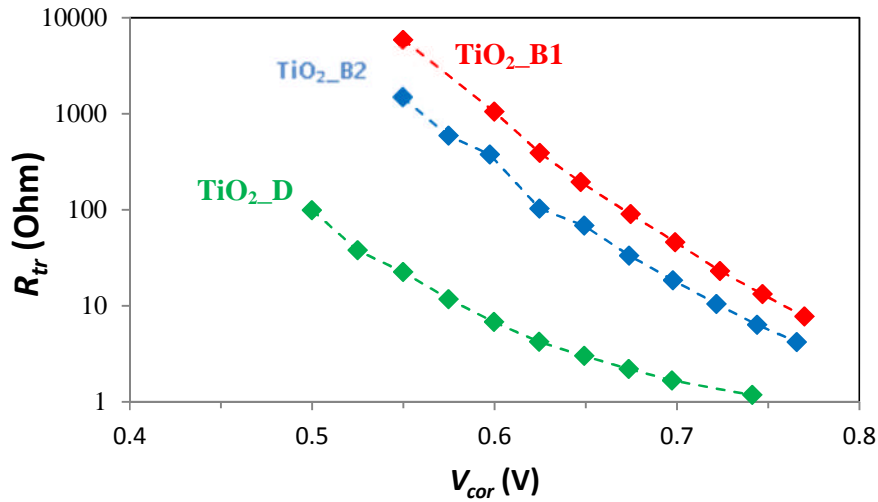


Figure 4.13: Effect of photoelectrode TiO₂ crystal phase on R_{tr} as a function of the corrected applied voltage, TiO₂-B1 (red), TiO₂-B2 (blue) and TiO₂-D (green)

This phenomenon has a consequence on the charge collection efficiency, η_{coll} , in the photoelectrodes. η_{coll} has been calculated using the following classical relationship as written

in equation 2.18 (Chapter II, section II. 1. 3, page 40) (Hagfeldt et al., 2010). The results are displayed in Figure 4.14. The collection efficiency is very high, higher than 95%, in the case of anatase cell, whereas significantly lower values are found in the case of the brookite cells. Therefore a cell performance loss is expected for the latter phase due to a poorer collection of charge.

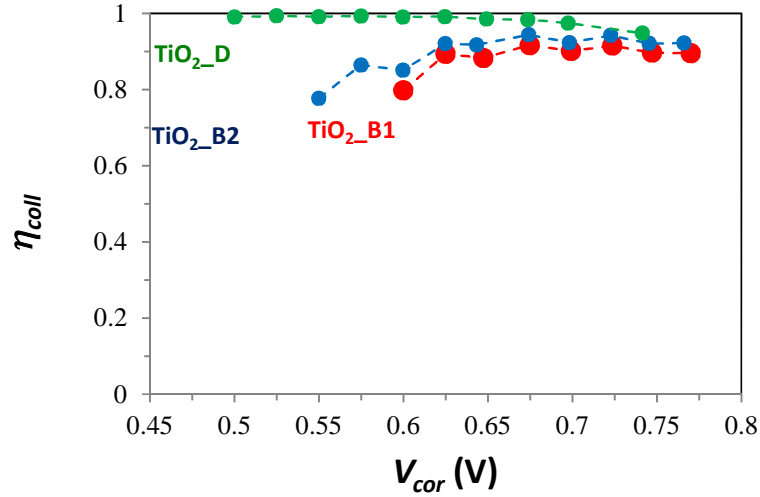


Figure 4.14: Effect of photoelectrode TiO₂ crystal phase on the charge collection efficiency

The lower η_{coll} can be explained by the conductivity behavior. The conductivity of TiO₂ was determined from the charge transport resistance as written in equation 2.19. Figure 4.15 shows the conductivity of brookite and anatase layers as a function of g . σ increases rapidly with this parameter due to the trap filling. Moreover, the conductivity measurements by IS show that brookite is less conductive than anatase by more than one order of magnitude.

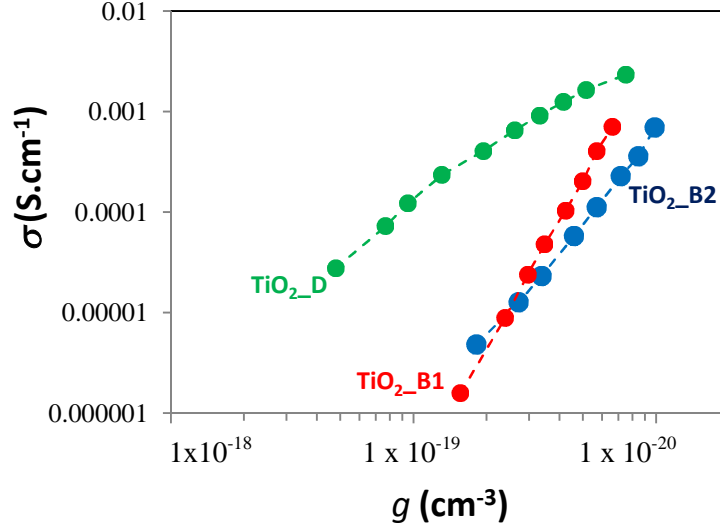


Figure 4.15: Effect of photoelectrode TiO₂ crystal phase on the electronic conductivity as a function of the electron concentration, g

From τ_n and τ_{tr} measured by IS, we have also estimated the effect of the crystal phase on the chemical diffusion coefficient of electrons in TiO₂, noted D_n (equation 2.20, chapter II, section II. 1. 3, page 40). In Figure 4.16, D_n is plotted as a function of g . As expected, the behavior is similar to that found for σ_n and D_n is much larger for anatase compared to brookite.

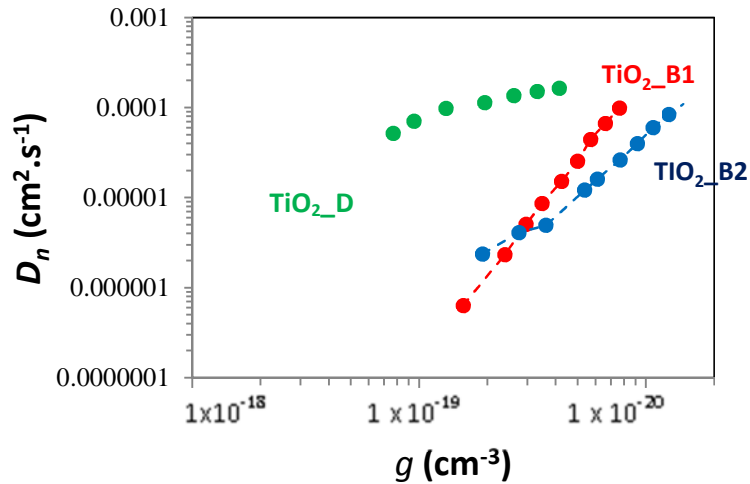


Figure 4.16: Effect of photoelectrode TiO₂ crystal phase on D_n parameter

Using the IS data, we have also determined the electron diffusion length (L_n) defined as the average distance traveled by the electrons in TiO₂ before recombination. This

parameter is given by equation 2.21 (Chapter II, section II. 1. 3, page 40) (Magne et al., 2013). The results are displayed in Figure 4.17. The electron diffusion lengths in the brookite films measured in the dark are found to be larger than the photoelectrode thickness (about 14 μm) in all cases, in agreement with the η_{coll} determined above. L_n has also been estimated by measuring the IS spectra of the cells at various applied voltages under one sun illumination. τ_n and τ_{ir} parameters have been extracted and the resulting L_n are plotted as star symbols in Figure 4.17. Similar L_n are found either in the dark or under illumination once plotted as a function of the electron concentration. Therefore, η_{coll} can be estimated using any of these measurement conditions.

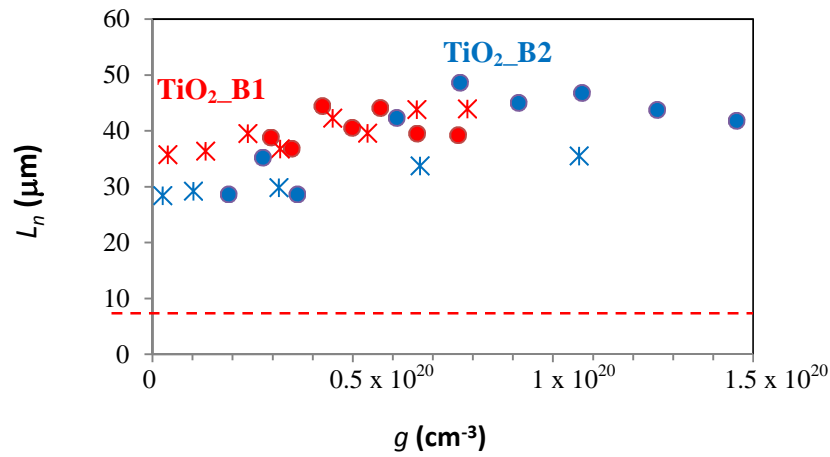


Figure 4.17: Mean diffusion length of electrons, L_n , in mesoporous brookite TiO_2 films measured by IS. Dot symbols : measurements in the dark. Star symbols : measurements under 1 sun illumination. Red : B1 cells; Blue: B2 cells. The dashed line is the photoelectrode thickness.

IV.4 Computational Study: Comparison of adsorption of Iodine (I_2) on Anatase (101) and Brookite (210) planes

The IS results and analysis have shown that the recombination on brookite surface is less promoted than that on anatase surface. These facts encouraged us to investigate the adsorption and interaction properties of redox species on both surfaces. In the case electron recombination at TiO_2 surface with redox species there are two most probable routes, (1) recombination with I_3^- and (2) recombination with free iodine (I_2). Richards et. al. have shown that for N719 sensitized DSSC coupled with I_3^-/I redox-couple, the recombination at TiO_2 surface mainly occurs through the reduction of I_2 due to the fact that the electron lifetime depends on the concentration of free-iodine and has no relation with the I_3^- concentration

(Richards, et. al., 2012). Based on their results, we simplify our investigation by comparing the adsorption properties of I_2 on anatase and brookite with (101) and (210) surface respectively. Brookite (210) is one of the most stable surfaces of brookite which has surface energy about 0.7 J.m^{-2} , is about the same with the other stable surface, (010), which has surface energy 0.77 J.m^{-2} and is higher about 0.08 J.m^{-2} than another one, (001), which has surface energy 0.62 J.m^{-2} (Gong, X-Q., et. al., 2007).

The DFT calculations have been carried out using the CP2K/Quickstep code which employs a hybrid Gaussian and plane-wave basis set (Vande Vondele, et. al., 2005). The Perdew, Burke and Ernzerhof exchange-correlation functional has been employed (Perdew, et. al., 1996). Goedecker, Teter and Hutter pseudopotentials (Goedecker, et. al., 1996) were used for describing the core electrons. The wave functions of the valence electrons are expanded in terms of Gaussians function with a double- ζ (zeta) polarized basis set (DZVP) (Godbout et al., 1992; VandeVondele and Hutter, 2007). A plane wave cutoff of 400 Ry was used in the plane wave expansion of the electron density. Both surface models supercell contained 96 atoms, which represent a $(\text{TiO}_2)_{32}$. To have a rectangular surface instead of a parallelogram one, the anatase TiO_2 unit cell was expanded to a $1 \times 2 \times 1$ super cell and then it was cleaved to form the (101) plane. TiO_2 anatase (101) model has a (2×1) surface cell which consists of 6 atomic layers with a 20 \AA thickness of vacuum layer above each slab. To have a TiO_2 brookite (210) surface model which surface area is about the same as TiO_2 anatase model, the same procedure was implemented. The brookite surface model consisted of 4 atomic layers.

The first step of the DFT calculation was to obtain optimized structures. The geometry optimization was implemented by putting the I atoms as close as possible to Ti atom based on the assumption that I is negatively charged and will then be favorably attached to Ti. The optimized geometry of I_2 adsorption on anatase and brookite are shown in Figure 4.18. It shows that both I atoms of iodine were attached to Ti atoms of anatase surface and that only one of them was attached to Ti atom of brookite surface. It can be explained by the structural characteristics of both surfaces, where the distance of free Ti on the brookite surface ($\sim 5 \text{ \AA}$) is longer than on the anatase one ($\sim 3\text{-}4 \text{ \AA}$). The distance between I atoms in the I_2 molecule that attached to anatase changed from 2.836 \AA (optimized gas phase of I_2) to 4.09 \AA (on anatase surface). This indicates that I_2 tends to dissociate and adsorb as iodide on the anatase surface. However, the I-I bond length on brookite surface was found similar to those in gas phase (2.74 \AA). The Ti-I bond length range on both surface are in agreement with previous

calculation reported by Assaduzaman and Schreckenbach, whose investigated the I^- and I_3^- interaction on the rutile surface (Assaduzaman and Schreckenbach, 2011). The fact that the Ti-I bond length on anatase surface is shorter than that on brookite one, indicates that I atoms are attached stronger on anatase surface compared to brookite one.

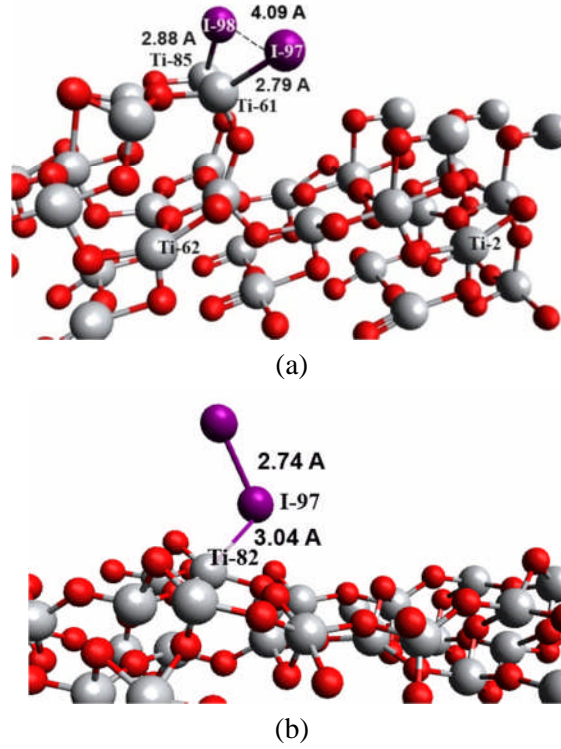


Figure 4.18: Optimized geometry of adsorbed iodine on (a) anatase and (b) brookite surface

Adsorption energies are calculated through the following formulae (Zeng, et. al., 2010):

$$\Delta E_{ads} = E_{ads} - E_{surf} - E_{I_2} \quad [4.1]$$

where,

ΔE_{ads} = the adsorption energy, negative value indicates that the molecule adsorption is exothermic and thus the adsorption is energetically stable

E_{ads} = total energy of optimized I_2 on anatase or brookite systems

E_{surf} = total energy of optimized clean surface

E_{I_2} = total energy of optimized gas-phase of iodine.

The calculation results of adsorption energy are given in Table 4.4. This calculation verifies that I_2 is adsorbed stronger on anatase surface as reflected by a more negative ΔE_{ads} value.

Table 4.4 Calculation of ΔE_{ads} of I_2 adsorption on anatase (101) and brookite (210) surface

	The value observed on anatase (101)	The value observed on brookite (210)
E_{ads} (eV)	-79 333.23	-79 367.38
E_{surf} (eV)	-78 698.65	-78743.43
E_{I_2} (eV)	-623.53	-623.55
ΔE_{ads} (eV)	-11.05	-0.40
ΔE_{ads} (eV) for each Ti-I bond	-5.53	-0.40

The PDOS (Projected Density of States) of bare-anatase and bare-brookite are presented in Figure 4.19. The calculation revealed that the anatase and the brookite band-gap are 2.2 eV and 3.0 eV, respectively. Those results have the similar values to that obtained from theoretical calculation of the both bulk-phases (Zhang, et. al., 2014) and smaller than the experimental results (~3.2 eV for anatase and ~3.4 eV for brookite) (Magne et al., 2012). This difference is due to the discontinuity of exchange-correlation energy and is typical in DFT (Zhang, et. al., 2014; Lu, et. al., 2011).

The interaction between Ti and O in TiO_2 is achieved by the existence of Ti 3d orbital character in 2p orbital of O and vice versa which indicates the overlap of these two orbitals. Figure 4.19 (a) shows that there are two localized states at about 0.04 eV and -1 eV. These states appear because the anatase surface has a terrace-like top. The atomic orbitals which are located in the edge of terraces do not overlap with the others and then contribute to this localized state (Singh and Shimakawa, 2003). On the other hand, this localized state does not appear in the PDOS of brookite, because it has flat surface that conditioning the surface energy band formation due to the overlap of atomic orbital at the top layer of surface. To confirm this, we have already investigated the LDOS (Local Density of States) of two Ti atoms on the top layer surface, namely Ti-85 and Ti-61 (see Figure 4.18 (a)) as well as two Ti

atoms which are located in the three layers (middle layer), namely Ti-2 and Ti-62 (see also Figure 4.18 (a)). These results are presented in Figure 4.20

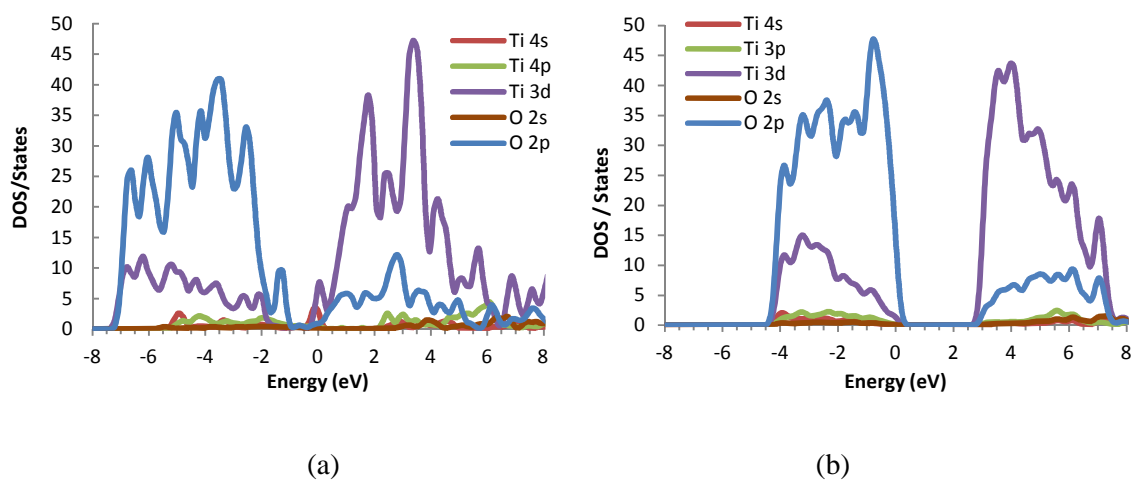


Figure 4.19. DOS of (a) bare anatase (101) (b) bare brookite (210)

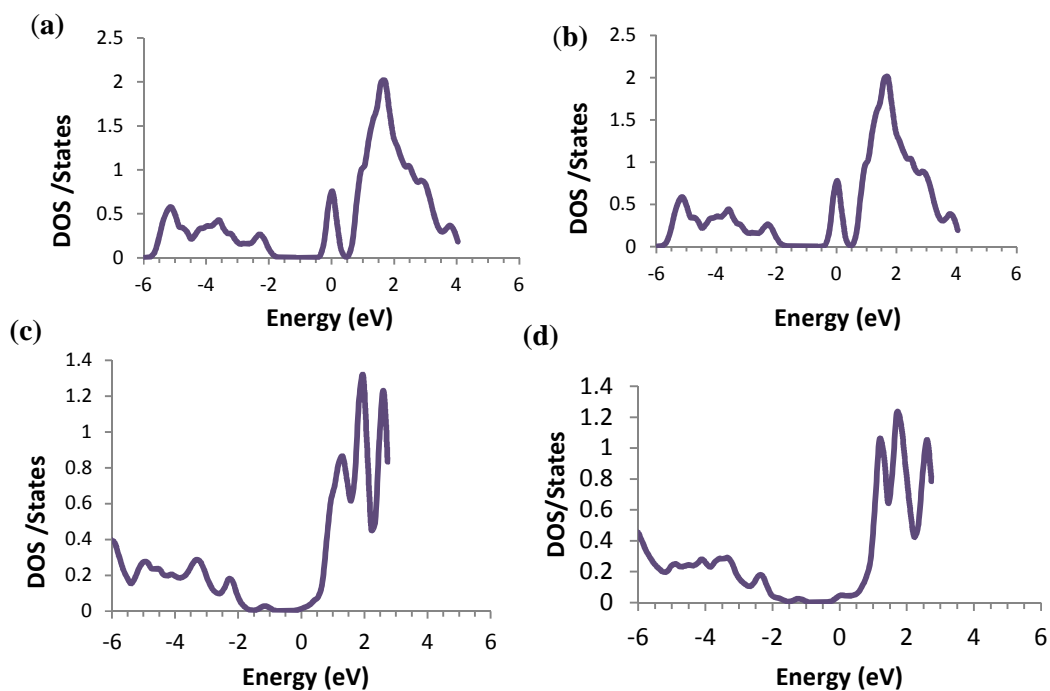


Figure 4.20 LDOS of (a) Ti-61 (b) Ti-85 (c) Ti-2 and (d) Ti-62 on anatase

The PDOS of anatase/I₂ and brookite/I₂ systems are shown in Figure 4.21. It shows that the bandgap of these surfaces before and after I₂ adsorption are similar, but we observed new localized states that strongly suggest the occurrence of Ti-I interactions on the surface.

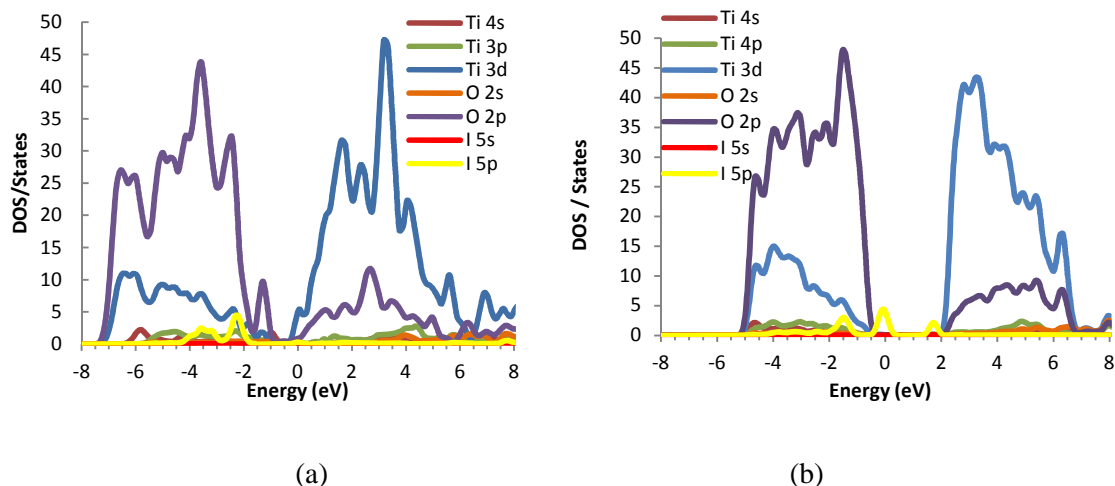


Figure 4.21 PDOS of (a) anatase/I₂ and (b) brookite/I₂

The Ti and I interaction is achieved by the interaction between 3d orbital of Ti and 5p orbital of I. To confirm this, we present the LDOS of Ti on the surface and adsorbed I in Figure 4.22. It shows the overlap of Ti 3d orbital and of the 5p orbital of adsorbed I.

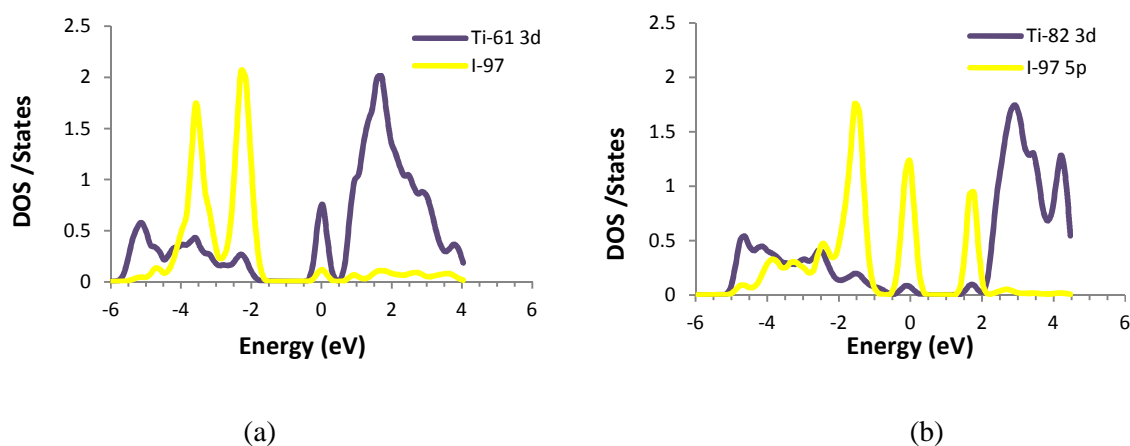
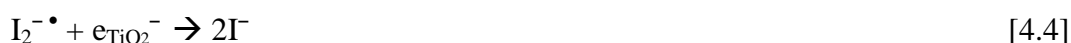


Figure 4.22 (a) The LDOS of Ti-61 3d and I-97 5p in anatase/I₂ system (b) LDOS of Ti-82 Ti 3d and I-97 5p in brookite/I₂ system

The oxide which is less favorable for redox species to adsorb on its surface will be beneficial for DSSCs that employ I_3^-/I^- as the redox-couple. The easier the redox species adsorb on the surface, the larger chance the electron recombination of redox species and one on the surface will occur. However, we need to confirm that this recombination is more difficult on brookite surface. To confirm this, let us present the mechanism reaction of I_3^- reduction on the TiO_2 surface that is proposed by Peter (Peter, 2007). The first step, I_3^- will dissociate become I_2 and I^- , followed by the adsorption of I_2 on the TiO_2 surface (equation 4.2). The second step, I_2 receipt the electron that come from the dye through the TiO_2 conduction band lead to the reduction of I_2 become species radical $I_2^{\bullet -}$ (equation 4.3), which further reduce to I^- (equation 4.4). The mechanism is written as follow:



According to those mechanisms and also supported by the data of electron lifetime that in order of the ionic transfer (section IV.3.3), desorption of I_2 from TiO_2 as I^- will determine the occurrence reduction reaction. Thus, the more stable $(TiO_2/I_2)^-$ system, the more difficult reaction will occur. We have calculated the energy of system (anatase/ I_2)⁻ and (brookite/ I_2)⁻ and obtained the result that the energies of (anatase/ I_2)⁻ and (brookite/ I_2)⁻ systems are -7933.83 eV and -7937.19 eV, respectively. It indicates that I_2 will more difficult to desorb from the brookite surface than the anatase one. As a consequence, the reduction of I_3^- on brookite surface will be more inhibited.

This analysis is also supported with the result of optimized geometry of adsorbed iodine on anatase and brookite surface (Figure 4.18). As it is previously mentioned that on anatase, iodine tend to dissociate and is adsorbed as iodide with presence of the bond elongation between I atoms. This give evidence that if TiO_2 receive an electron from dye, desorption of iodide would probably occur easier from anatase surface compare to brookite one. These explain that the R_{ct} (the resistance to charge transfer (recombination) across the sensitized oxide-electrolyte interface) of brookite is higher than anatase, at the same time these show that our calculation and experimental results are in excellent agreement.

IV. 5 SUMMARY

We have investigated DSSCs prepared using (i) brookite nanoparticles with two different sizes and shapes and (ii) a reference anatase commercial paste. The photoelectrodes with the same thickness have been thoroughly characterized, especially for their dye loading. Moreover, the cell performances have been measured and their functioning has been examined by impedance spectroscopy. We show that layers with the same porosity and particle size have a significantly higher dye loading in the case of anatase TiO_2 compared to brookite TiO_2 . This is due to a lower density of anchoring sites for the dye on the brookite surface. The analysis of C_μ has shown that the conduction band edge in brookite is similar or below that of the anatase photoelectrode. We have also found higher R_{ct} for brookite cells due to a lower recombination reaction rate and therefore to the lower reactivity of the brookite surface. We have explained quantitatively the higher V_{oc} of brookite cells by the reduced recombination side reaction. The transport time of electrons is much slower in brookite films compared to the anatase one. Therefore, in spite of larger electron lifetimes in brookite cells, the collection efficiency is significantly lower compared to anatase. The transport is slowed by the poor conductivity of brookite since we have measured σ_n lower by much than one order of magnitude compared to anatase. In summary, the brookite cell efficiency is mainly limited by two parameters, the dye loading and the charge collection efficiency. The latter limits the optimized photoelectrode thickness and makes it not possible to compensate the lower dye loading by the use of thicker films. Further improvements should then require the doping of brookite TiO_2 in order to circumvent the electrical limitations.

The computational result of the adsorption of one of the electrolyte species that play a role in recombination electron of I_3^-/I^- -based DSSC, I_2 , has been carried out on anatase and brookite with surface plans (101) and (210), respectively. The calculation results show that I_2 adsorb on anatase stronger than on brookite one, with an adsorption energy of each iodine bond of -5.53 eV and 0.4 eV, respectively. All I atoms in I_2 molecule attached to Ti atom of anatase surface and tend to dissociate, whereas only one of the two I atom is attached to Ti atom on brookite surface. Moreover, the calculation reveals that $(\text{brookite}/\text{I}_2)^-$ system is more stable than the $(\text{anatase}/\text{I}_2)^-$ one, which indicates the I_2 will more difficult to desorb as I^- from brookite than from anatase. These calculation results are in excellent agreement with the experimental results that showed the recombination of electrons of brookite conduction band with electrolyte redox species is less preferable than in anatase case.

References

- Asaduzzaman, A.M., Schreckenbach, G., 2011. Computational studies of the interactions of I⁻ and I₃⁻ with TiO₂ clusters: implications for dye-sensitized solar cells. *Theor. Chem. Acc.* 129, 199–208. doi:10.1007/s00214-011-0920-1
- Bisquert, J., 2002. Theory of the Impedance of Electron Diffusion and Recombination in a Thin Layer. *J. Phys. Chem. B* 106, 325–333. doi:10.1021/jp011941g
- Bisquert, J., Mora-Seró, I., 2010. Simulation of Steady-State Characteristics of Dye-Sensitized Solar Cells and the Interpretation of the Diffusion Length. *J. Phys. Chem. Lett.* 1, 450–456. doi:10.1021/jz900297b
- Bisquert, J., Vikhrenko, V.S., 2004. Interpretation of the Time Constants Measured by Kinetic Techniques in Nanostructured Semiconductor Electrodes and Dye-Sensitized Solar Cells. *J. Phys. Chem. B* 108, 2313–2322. doi:10.1021/jp035395y
- Godbout, N., Salahub, D.R., Andzelm, J., Wimmer, E., 1992. Optimization of Gaussian-type basis sets for local spin density functional calculations. Part I. Boron through neon, optimization technique and validation. *Can. J. Chem.* 70, 560–571. doi:10.1139/v92-079
- Gong, X.-Q., Selloni, A., 2007. First-principles study of the structures and energetics of stoichiometric brookite TiO₂ surfaces. *Phys. Rev. B* 76, 235307. doi:10.1103/PhysRevB.76.235307
- Goedecker, S., Teter, M., Hutter, J., 1996. Separable dual-space Gaussian pseudopotentials. *Phys. Rev. B* 54, 1703–1710. doi:10.1103/PhysRevB.54.1703
- Grinter, D.C., Nicotra, M., Thornton, G., 2012. Acetic Acid Adsorption on Anatase TiO₂(101). *J. Phys. Chem. C* 116, 11643–11651. doi:10.1021/jp303514g
- Hagfeldt, A., Boschloo, G., Sun, L., Kloo, L., Pettersson, H., 2010. Dye-Sensitized Solar Cells. *Chem. Rev.* 110, 6595–6663.
- Jena, A., Mohanty, S.P., Kumar, P., Naduvath, J., Gondane, V., Lekha, P., Das, J., Narula, H.K., Mallick, S., Bhargava, P., 2012. Dye Sensitized Solar Cells: A Review. *Trans. Indian Ceram. Soc.* 71, 1–16. doi:10.1080/0371750X.2012.689503
- Kalyanasundaram, K., 2010. *Dye-sensitized Solar Cells*. EPFL Press.
- Liu, G., Yu, J.C., Lu, G.Q. (Max), Cheng, H.-M., 2011. Crystal facet engineering of semiconductor photocatalysts: motivations, advances and unique properties. *Chem. Commun.* 47, 6763–6783. doi:10.1039/C1CC10665A
- Lu, J., Dai, Y., Jin, H., Huang, B., 2011. Effective increasing of optical absorption and energy conversion efficiency of anatase TiO₂ nanocrystals by hydrogenation. *Phys. Chem. Chem. Phys.* 13, 18063–18068. doi:10.1039/C1CP22726B
- Magne, C., Dufour, F., Labat, F., Lancel, G., Durupthy, O., Cassaignon, S., Pauporté, T., 2012. Effects of TiO₂ nanoparticle polymorphism on dye-sensitized solar cell photovoltaic properties. *J. Photochem. Photobiol. Chem.* 232, 22–31. doi:10.1016/j.jphotochem.2012.01.015
- Magne, C., Moehl, T., Urien, M., Grätzel, M., Pauporté, T., 2013. Effects of ZnO film growth route and nanostructure on electron transport and recombination in dye-sensitized solar cells. *J. Mater. Chem. A* 1, 2079. doi:10.1039/c2ta00674j
- Park, K., Zhang, Q., Myers, D., Cao, G., 2013. Charge Transport Properties in TiO₂ Network with Different Particle Sizes for Dye Sensitized Solar Cells. *ACS Appl. Mater. Interfaces* 5, 1044–1052. doi:10.1021/am302781b
- Pauporté, T., Finne, J., Kahn-Harari, A., Lincot, D., 2005. Growth by plasma electrolysis of zirconium oxide films in the micrometer range. *Surf. Coat. Technol., Plasma Electrolysis Plasma Electrolysis* 199, 213–219. doi:10.1016/j.surfcoat.2005.03.003
- Perdew, J.P., Burke, K., Ernzerhof, M., 1996. Generalized Gradient Approximation Made Simple. *Phys. Rev. Lett.* 77, 3865–3868. doi:10.1103/PhysRevLett.77.3865
- Peter, L.M., 2007. Characterization and Modeling of Dye-Sensitized Solar Cells. *J. Phys. Chem. C* 111, 6601–6612. doi:10.1021/jp069058b
- Raga, S.R., Barea, E.M., Fabregat-Santiago, F., 2012. Analysis of the Origin of Open Circuit Voltage in Dye Solar Cells. *J. Phys. Chem. Lett.* 3, 1629–1634. doi:10.1021/jz3005464
- Richards, C.E., Anderson, A.Y., Martiniani, S., Law, C., O'Regan, B.C., 2012. The Mechanism of Iodine Reduction by TiO₂ Electrons and the Kinetics of Recombination in Dye-Sensitized Solar Cells. *J. Phys. Chem. Lett.* 3, 1980–1984. doi:10.1021/jz3006755
- Singh, J., Shimakawa, K., 2003. *Advances in Amorphous Semiconductors*. CRC Press. p.10.

- Taya, S., Kuwahara, S., Shen, Q., Toyoda, T., Katayama, K., 2014. Role of lithium and co-existing cations in electrolyte to improve performance of dye-sensitized solar cells. *RSC Adv.* 4, 21517–21520. doi:10.1039/C4RA02309A
- Thomas, A.G., Syres, K.L., 2012. Adsorption of organic molecules on rutile TiO₂ and anatase TiO₂ single crystal surfaces. *Chem. Soc. Rev.* 41, 4207–4217. doi:10.1039/C2CS35057B
- VandeVondele, J., Hutter, J., 2007. Gaussian basis sets for accurate calculations on molecular systems in gas and condensed phases. *J. Chem. Phys.* 127, 114105. doi:10.1063/1.2770708
- VandeVondele, J., Krack, M., Mohamed, F., Parrinello, M., Chassaing, T., Hutter, J., 2005. Quickstep: Fast and accurate density functional calculations using a mixed Gaussian and plane waves approach. *Comput. Phys. Commun.* 167, 103–128. doi:10.1016/j.cpc.2004.12.014
- Villanueva-Cab, J., Wang, H., Oskam, G., Peter, L.M., 2010. Electron Diffusion and Back Reaction in Dye-Sensitized Solar Cells: The Effect of Nonlinear Recombination Kinetics. *J. Phys. Chem. Lett.* 1, 748–751. doi:10.1021/jz1000243
- Wang, Q., Ito, S., Grätzel, M., Fabregat-Santiago, F., Mora-Seró, I., Bisquert, J., Bessho, T., Imai, H., 2006. Characteristics of High Efficiency Dye-Sensitized Solar Cells†. *J. Phys. Chem. B* 110, 25210–25221. doi:10.1021/jp064256o
- Wang, Q., Moser, J.-E., Grätzel, M., 2005. Electrochemical Impedance Spectroscopic Analysis of Dye-Sensitized Solar Cells. *J. Phys. Chem. B* 109, 14945–14953. doi:10.1021/jp052768h
- Zeng, W., Liu, T., Wang, Z., Tsukimoto, S., Saito, M., Ikuhara, Y., 2010. Oxygen Adsorption on Anatase TiO₂ (101) and (001) Surfaces from First Principles. *Mater. Trans.* 51, 171–175. doi:10.2320/matertrans.M2009317
- Zhang, J., Zhou, P., Liu, J., Yu, J., 2014. New understanding of the difference of photocatalytic activity among anatase, rutile and brookite TiO₂. *Phys. Chem. Chem. Phys.* 16, 20382–20386. doi:10.1039/C4CP02201G
- Zhu, K., Kopidakis, N., Neale, N.R., van de Lagemaat, J., Frank, A.J., 2006. Influence of Surface Area on Charge Transport and Recombination in Dye-Sensitized TiO₂ Solar Cells†. *J. Phys. Chem. B* 110, 25174–25180. doi:10.1021/jp065284+

Chapter V

TiO₂-Based DSSC II: The Effect of Graphene Incorporation in TiO₂/graphene for Photoelectrode

V. 1. Introduction

Carbon is known to present many different allotropes, four of them, namely fullerene, carbon nanotubes, graphene and graphite. These allotropes have a dimension of 0, 1, 2 and 3, respectively. The structures of these carbon allotropes are shown in Figure 5.1. The graphene, which can be prepared with a single atomic layer thickness, is built as a real two-dimensional layer, which is the basics framework of the other allotrope. It can be rolled up to become the carbon nanotube, stacked layers give rise to graphite and wrapped graphene sheets produce the spherical fullerene molecules (Allen et al., 2010; Choi et al., 2010; Geim and Novoselov, 2007; Neto, 2009).

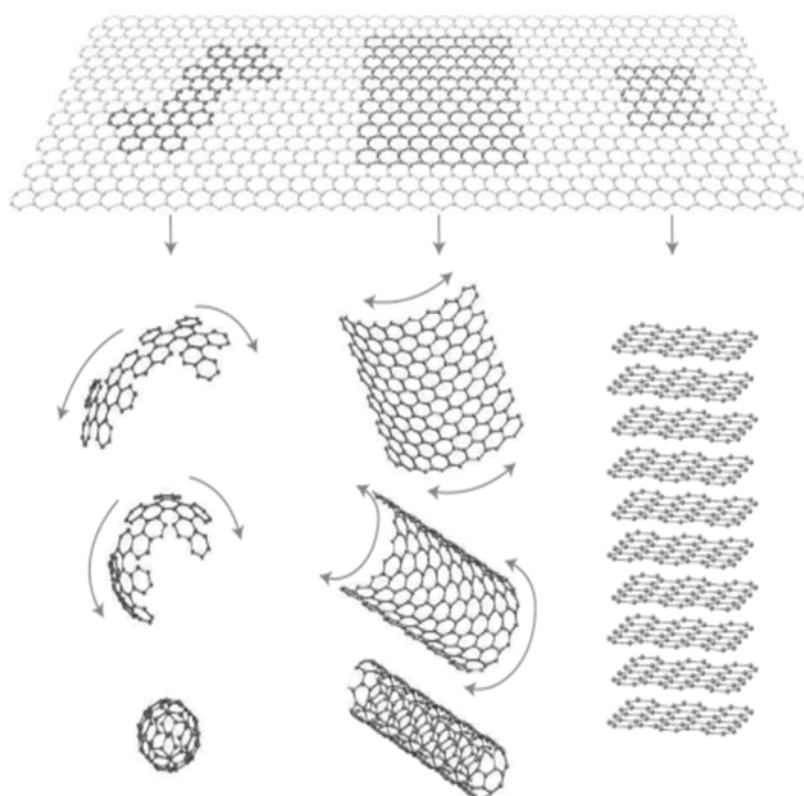


Figure 5.1 The Schemes of the carbon allotrope; Graphene (top), fullerene (left-bottom), carbon nanotube (center-bottom), graphite (right-bottom) (Geim and Novoselov, 2007).

Since the graphene discovery in 2004 (Novoselov, 2009), the research about preparation, characterizations and applications of graphene sheets have growth rapidly and has given rise to a tremendous amount of literature (Bai and Huang, 2010; Bonaccorso et al., 2010; Geim and Novoselov, 2007; Hamann et al., 2006; Liang et al., 2009; Nair et al., 2008; Novoselov, 2011; Robinson et al., 2010; Stankovich et al., 2007; Yoo et al., 2008; Zhang et al., 2013). Graphene sheets can be prepared by various techniques including mechanical exfoliation (Novoselov, 2009), epitaxial growth (Huang et al., 2008; Robinson et al., 2010), chemical vapor deposition (K. S. Kim et al., 2009; Park et al., 2010) and chemical exfoliation (Liang et al., 2009; Stankovich et al., 2007). As a zero band gap material with electrons which are just like massless relativistic particles, this material exhibits excellent electrical conduction properties in two dimensions. The graphene sheet which was prepared by arc discharge exfoliation technique, was reported had electrical conductivity of $\sim 2 \times 10^3 \text{ S.cm}^{-1}$ (Wu et al., 2009). It has also high thermal conductivity of $\sim 5 \times 10^3 \text{ W/mK}$ for suspended single-layer graphene (Balandin et al., 2008). Mechanically, It is a strong compound with a breaking strength of 42 N.m^{-1} (Lee et al., 2008). Graphene can also be produced as very thin sheets with low visible light absorption properties and used as conducting transparent layers (Nair et al., 2008; Zhang et al., 2013). It has also an extremely high theoretical specific surface area of $2600 \text{ m}^2.\text{g}^{-1}$ (Yoo et al., 2008) and is described to have a lattice structure stable up to 1500°C (Bai and Huang, 2010).

Adding graphene into the porous TiO_2 nanoparticle DSSC photoanode network has been shown of great interest with the significant improvement of the cell efficiency by increasing the current density (J_{sc}) of the solar cell without significant decrease of the open circuit voltage (V_{oc}) and fill factor (FF) (Fang et al., 2014a, 2014b; Fan et al., 2012; He et al., 2011; S. R. Kim et al., 2009; Peining et al., 2012; Shen et al., 2011; Song et al., 2011; Sun et al., 2010; Tang et al., 2010; Wang et al., 2012; Xiang et al., 2011; Yang et al., 2010). Various techniques have been developed to prepare TiO_2 /graphene composite such as sol-gel or dispersion techniques (Fan et al., 2012; Tang et al., 2010; Yang et al., 2010), solvothermal approaches (He et al., 2011), hydrothermal technique (Cheng et al., 2013; Fang et al., 2014a; Shen et al., 2011) or electrospinning (Peining et al., 2012). It has been shown that graphene oxide is the best starting material to prepare the composite. By using graphene oxide it is possible to ensure the intimate attachment between graphene and TiO_2 (Shen et al., 2011; Wang et al., 2012). A second step is the reduction of graphene oxide in graphene. Various techniques have been reported including chemical (Yang et al., 2010), UV-assisted

photocatalytic processes (S. R. Kim et al., 2009) and thermal reduction treatments (Jung et al., 2008; Wang et al., 2012). The latter is of special interest in the case of the photoanode preparation since the nanoparticle TiO_2 film requires a final annealing heat treatment (Wang et al., 2012).

The origin of the beneficial effect of graphene on solar cell J_{sc} remains unclear. Graphene has been reported (i) to increase the photoelectrode surface area (Fang et al., 2014a; Tang et al., 2010) and to improve their dye loading (Fang et al., 2014a; Fan et al., 2012; Sun et al., 2010; Tang et al., 2010). Increasing the surface area causes more dye attached to the surface of TiO_2 /graphene composite compared to pure TiO_2 and increases the dye loading. (ii) The work function of graphene (-4.4-4.5 eV) is localized below the conduction band of TiO_2 (-4.2 eV) and may favor the charge extraction from TiO_2 (Sun et al., 2010; Tang et al., 2010). (iii) Graphene is also reported to give higher conductive layers (Tang et al., 2010) and then to enhance the charge transport properties of the photoanode (Fang et al., 2014a; Fan et al., 2012; Wang et al., 2012). It has also been described (iv) to act as a structuring agent that facilitates the production of larger pores that improve the redox shuttle transport by diffusion (Fan et al., 2012).

In this Chapter, we will describe the preparation of DSSC based on TiO_2 -graphene composite photoelectrodes. It will be divided by three sections, the first describe the composite preparation, the second section discusses the graphene role in DSSC efficiency improvement and the third one presents the application of TiO_2 -graphene composite photoelectrode in DSSC with cobalt-based electrolyte. The first investigation was carried out for the classical DSSC system using N719 as dye sensitizer, I_3^-/I^- as redox-couple and platinized counter-electrode. The results show that the addition of an optimized concentration of 1.2% (wt) of graphene into the TiO_2 photoelectrode can increase the layer conductivity up to 60% compared to pure TiO_2 . Graphene induces a faster transport of the electrons in the photoelectrode. This result has encouraged us to couple a cobalt-based shuttle with the TiO_2 /graphene photoelectrode. The improvement of the electron transport in the photoelectrode due to the addition of graphene is promising to reduce the efficiency loss related to the competing with the electron recombination reaction at photoelectrode and electrolyte interface has had and which is a known a problem in cobalt-based DSSC.

V.2 Composite TiO₂/Graphene (TiO₂_Gr) Preparation

The TiO₂/graphene (TiO₂_Gr) composite layers were prepared using a sol gel technique. Single graphene oxide (SGO) (from Cheap Tubes Inc.) has been chosen as a precursor to provide graphene. SGO was added into TiO₂_A in the paste preparation (see chapter 3). Pure TiO₂ layers used as a reference in this experiment are noted TiO₂_A. The presence of carbonyl groups on SGO surface can facilitate the attachment on TiO₂ in composite formation. The interaction between TiO₂ nanoparticles and SGO has been described to occur through physisorption, electrostatic binding, or charge transfer interaction (Cheng et al., 2013) In the present work, the coupling of SGO and TiO₂ has been achieved by a long and vigorous mixing of SGO and TiO₂ in solution including an ultrasonic treatment and subsequent thermal annealing of the mixture to get a composite film.

In addition to the layer annealing, the heat treatment plays also a role to help the reaction process of SGO with TiO₂. Various techniques have been used in the literature to reduce graphene oxide such as using chemical agent (Tang et al., 2010), hydrazine is the most chemical agent that is used; UV-treatment (S. R. Kim et al., 2009), solvothermal (He et al., 2011) and heat treatment (Wang et al., 2012). The later has been chosen in this experiment because in the photoanode preparation, TiO₂ layer heat treatment is implemented.

A final treatment in a TiCl₄ solution, as a part of the photoanode preparation, has a role to cover the structures by small TiO₂ particle that improve the cell performances (more explanation is given in the section IV.3). In the case of composite preparation, it also improves the intimate mixing of the two components, enhances the nanoparticle necking and fully covers the graphene sheets.

FTIR measurements were carried out to verify the reaction of SGO in graphene with TiO₂. Figure 5.2 shows the transmission spectra of SGO, TiO₂_Gr before and after the heat treatment, TiO₂_A after heat treatment and ethylcellulose. FTIR measurement of the ethylcellulose is needed because it was present in the TiO₂ paste. Both FTIR-spectra of the TiO₂_A and the TiO₂_Gr after heat treatment show TiO₂ crystalline characteristic absorptions between 600 to 900 cm⁻¹ (peak 1), that is assigned to Ti-O-Ti vibration mode (Jiang et al., 2011). The reduction of SGO is verified by the disappearance of peak 3 at ~1720 cm⁻¹ that represent the C=O (carbonyl) stretching contribution of COOH groups (Jiang et al., 2011; Shen et al., 2011). Actually there is another peak that can be used to verify; it is a peak at ~1650 cm⁻¹ (peak 2) that can be assigned to the skeletal vibration C=C in graphene. But it is difficult to see since it is overlap with absorption peak of bending vibration Ti-OH bonding

(Ding et al., 2000; Sánchez et al., 1996). To see clearly the existence of TiO₂ and graphene interaction it is needed to zoom out the spectra (Figure 5.3). Figure 5.3 shows there are peaks at about 1125 and 1070 cm⁻¹ in TiO₂_Gr after heat treatment spectra that is not appear in the TiO₂_A-after-heat-treatment one. Those peaks are assigned to Ti-O-C (Vasconcelos, 2011).

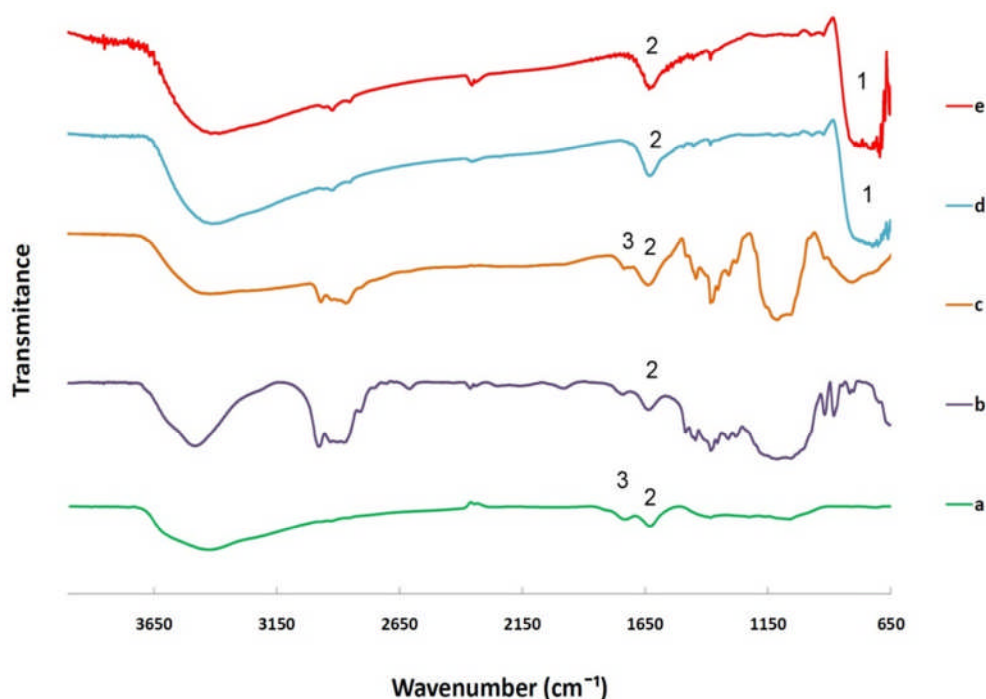


Figure 5.2: FTIR Spectra of (a) SGO (b) ethcellulose (c) TiO₂_Gr before heat treatment (d) TiO₂_Gr after heat treatment (e) TiO₂_A after heat treatment

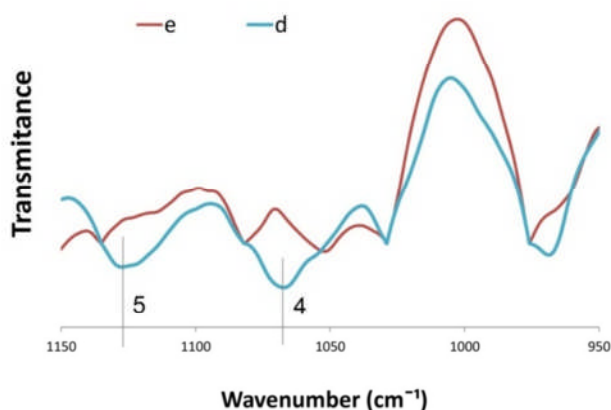


Figure 5.3: Zoom out of FTIR Spectra of (d) TiO₂_Gr after heat treatment and (e) TiO₂_A after heat treatment from 950 to 1150 cm⁻¹

Raman spectroscopy measurements of TiO₂_Gr layers have been performed to support the FTIR analysis. The result is shown in Figure 5.4. Anatase is characterized by six Raman active modes A_{1g} + 2B_{1g} + 3E_g (Chaves et al., 1974). Two typical Raman feature peaks are observed as the presence of graphene. The D band at 1270 cm⁻¹ is assigned to sp³ defect. The peak at around 1660 cm⁻¹ (G band) is close to that for well-ordered graphite, which is assigned to in-plane vibration of sp² bonded carbon atoms (Chen et al., 2010).

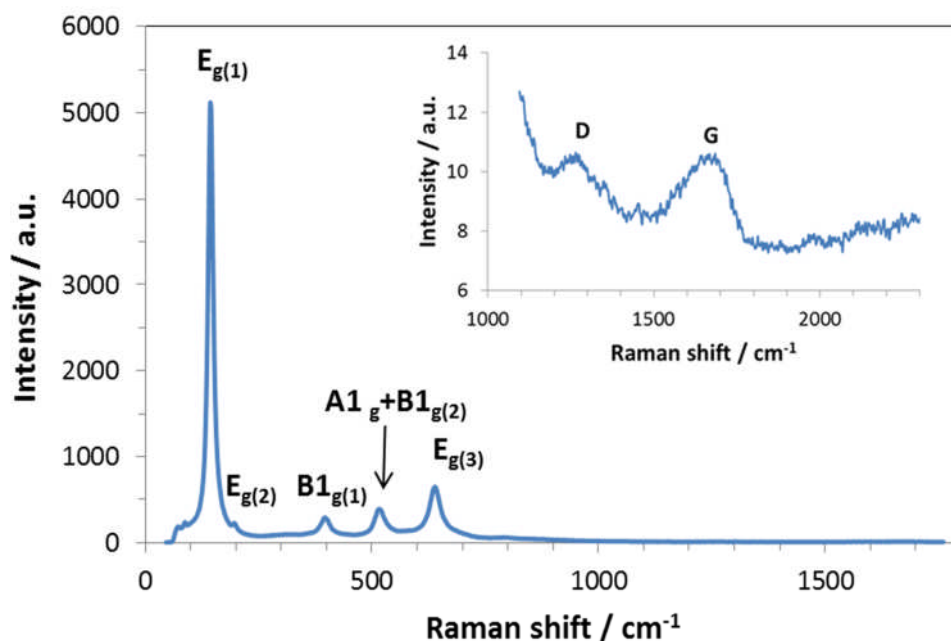
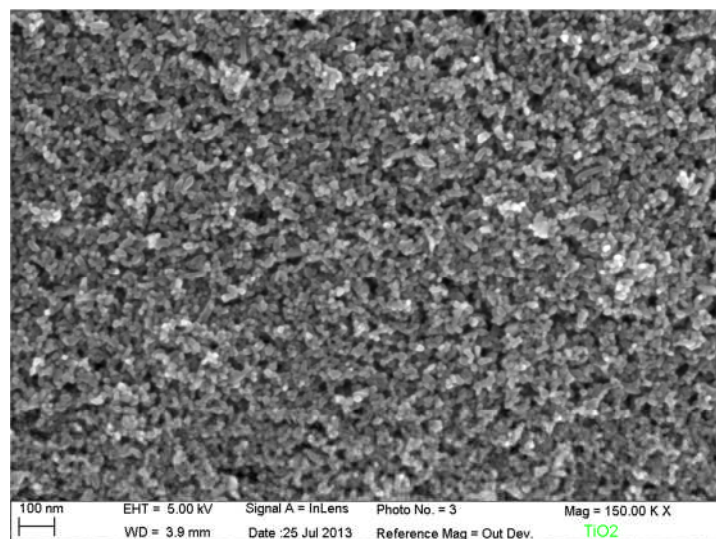
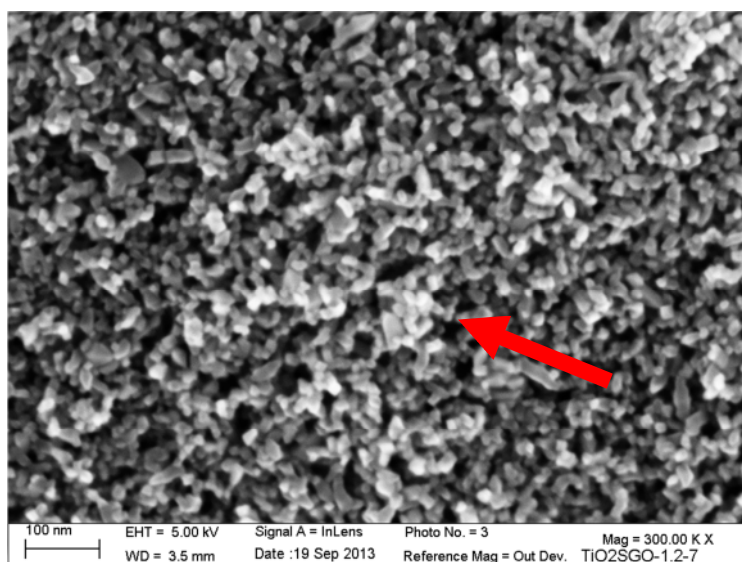


Figure 5.4: The raman spectra of TiO₂_Gr layer

The layers with and without GO have been observed by SEM (Figure 5.5 a and b). The films are porous and made of interconnected nanoparticles. Figure 5.4 shows the presence of graphene sheets in the composite. XRD results are shown in Figure 5.6. Both XRD patterns of TiO₂_A and TiO₂_Gr are indexed by the Anatase phase (Magne et al., 2012). No diffraction peak at 26.1° assigned to the graphite phase (Liu et al., 2010) could be observed in the Figure 5.6 because GO is present at low concentration in the composite layer.



(a)



(b)

Figure 5.5: SEM Image of (a) $\text{TiO}_2\text{-A}$ and (b) $\text{TiO}_2\text{-Gr12}$. The presence of graphene is pointed out by red arrow.

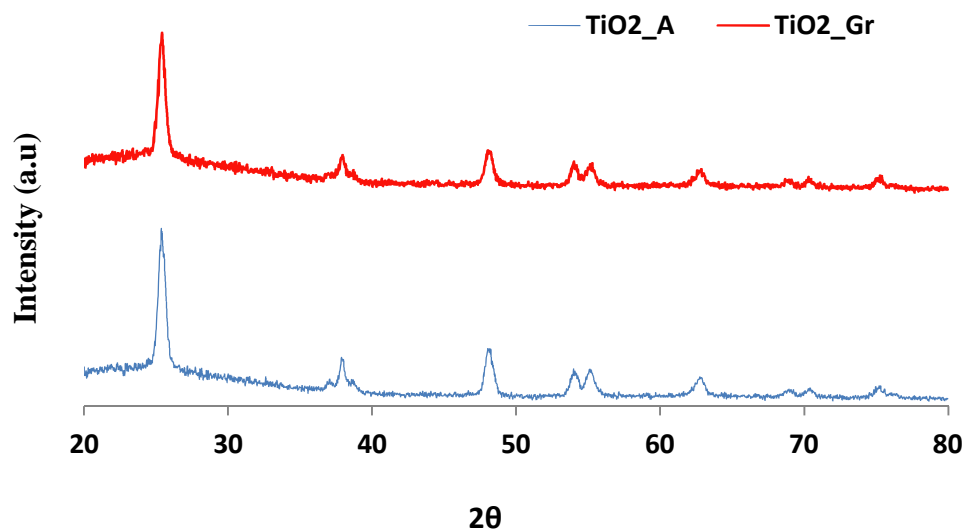


Figure 5.6 X-ray diffractogram of TiO₂_A and TiO₂_Gr12

The porosity and the specific surface areas (SSA) of films containing various graphene concentrations have been studied by krypton adsorption measurements (Pauporte and Rathousky, 2009). The BET isotherm curves are shown in Figure 5.7 and the SSA calculation is gathered in Table 1. The SSA maximum is found for 1.2 wt % of initial SGO (TiO₂_Gr12). A higher SGO concentration provokes an aggregation effect that induces the lower SSA parameter (Cheng et al., 2013).

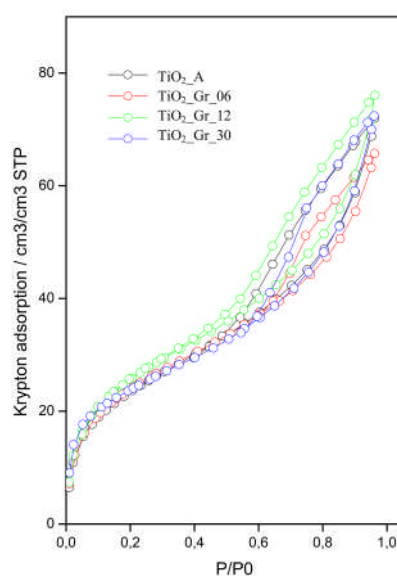


Figure 5.7 BET Isotherm curve

The results of optical measurement are shown in Figure 5.8 and 5.9. Figure 5.8 shows the transmittance spectra of ZnO films with various SGO contents. Graphene has a detrimental effect on the film transparency in the near-IR and visible region, the higher the graphene loading, the lower the optical transmission. Figure 5.9 shows the absorbance spectra of N719-sensitized layer of the higher SSA, TiO₂_Gr12, is higher compared to the TiO₂_A sensitized layer. The N719 dye concentrations in TiO₂_A and TiO₂_Gr12 films after sensitization have been titrated by spectrophotometry. They are reported in Table 5.1 and show a significantly higher dye loading in the presence of RGO.

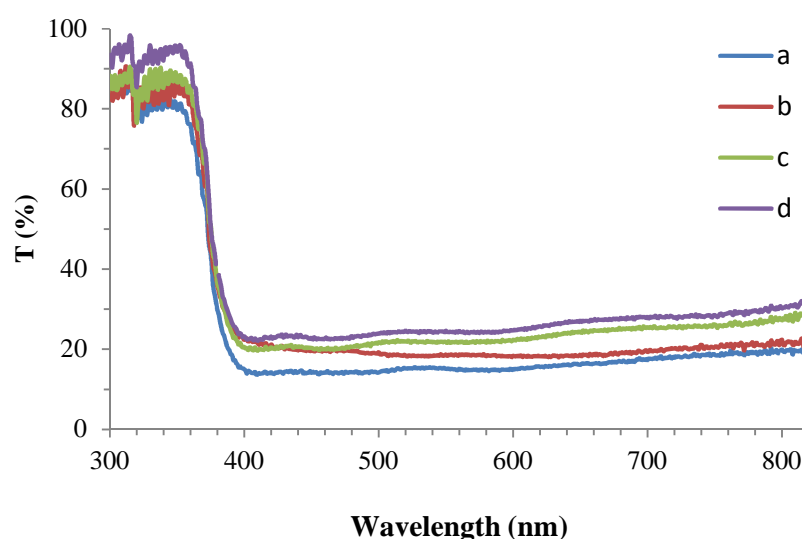


Figure 5.8 Transmission spectra of (a) TiO₂_A (b) TiO₂_Gr06 (c) TiO₂_Gr12 and (d) TiO₂_Gr30

Table 5.1: Effect of composite SGO content on the specific surface area determined by BET (S_{BET}), on the sensitized layer dye concentration and on the maximum of absorbance at 530 nm.

Sample	Graphene content (wt%)	S_{BET} (m ² /cm ³)	Dye concentration (mM)	Absorbance at 530 nm (cm ⁻¹)
TiO ₂ _A	0	114	95	926
TiO ₂ _Gr06	0.6	115	-	992
TiO ₂ _Gr12	1.2	124	111	1285
TiO ₂ _Gr30	3	110	-	-

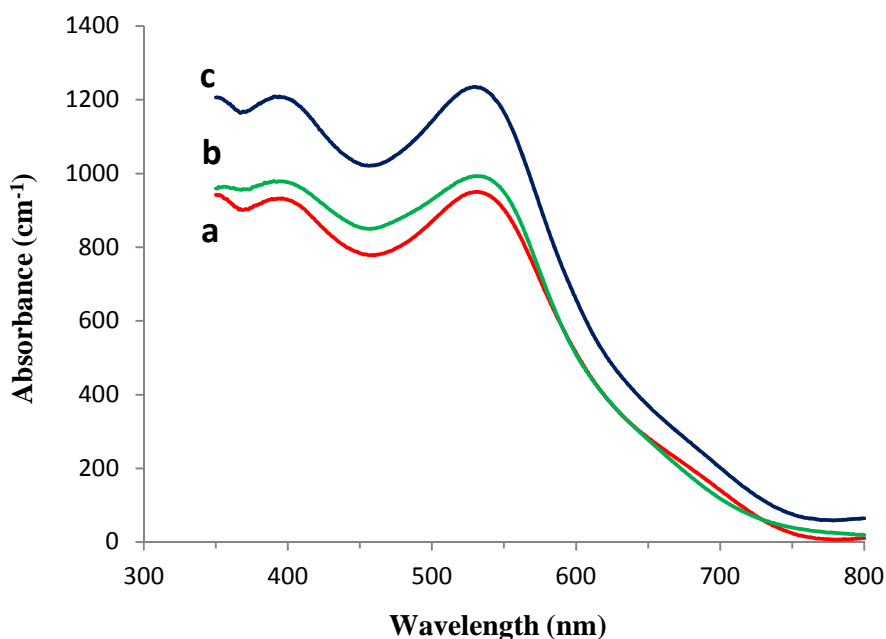


Figure 5.9 Absorbance spectra of N719 sensitized on (a) TiO₂_A (b) TiO₂_Gr06 and (c) TiO₂_Gr12

V.3 The cell performance of TiO₂/Gr in iodine based DSSCs: The investigation of graphene's role in TiO₂ photoelectrode

In a first part we show the results obtained on DSSCs prepared using TiO₂_Gr and an iodine-based electrolyte. The cells were sensitized with the N719 dye and the I-1 electrolyte was used (see Chapter III section III.2, page 66). The TiCl₄ treatment for under-layer deposition has been optimized on the TiO₂_A cell. Actually we have performed two TiCl₄ treatments, before the nanoparticle TiO₂ layer deposition (preliminary-treatment) and after the layer deposition (post-treatment) on FTO. The preliminary treatment has two advantages, first it favors the good interaction between the nanoparticle porous TiO₂ layer and the FTO substrate and second it reduces the electron recombination with I₃⁻ on the FTO surface. On the other hand, the post treatment has the advantage to cover the mesoporous TiO₂ and give a higher roughness and necking that increases the dye adsorption and favor the electron transport (Ito et al., 2008).

The role of the preliminary TiCl₄ treatment is clearly observed on dark current measurements (Figure 5.10). In this experiment, a cell has been built using the treated substrate as an electrode, a platinized FTO/glass as a counter electrode and the I-1 electrolyte.

The three-times treatment gives the largest effect to reduce the dark current. But, technically a three-times treatment did not give the best DSSC performance (Figure 5.11). The best efficiency is achieved for two TiCl_4 treatments and the dark current is similar for one or two treatment and falls after three treatments.

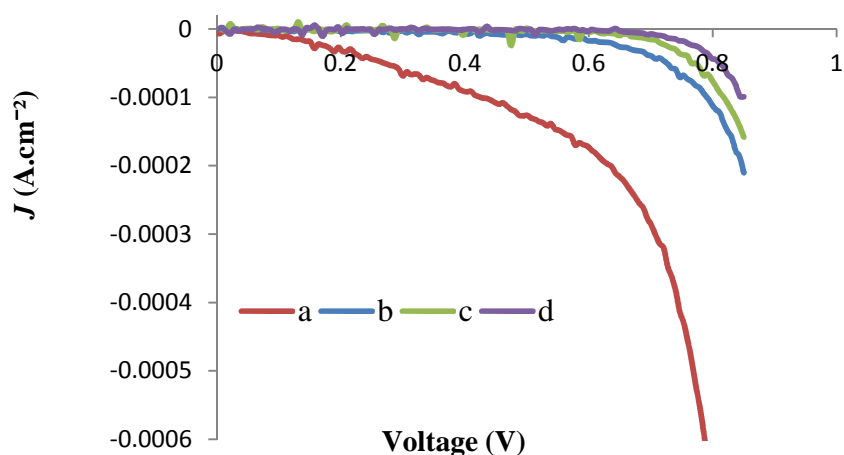


Figure 5.10: Dark current of FTO (a) without TiCl_4 treatment (b) one (c) two (d) three preliminary TiCl_4 treatment

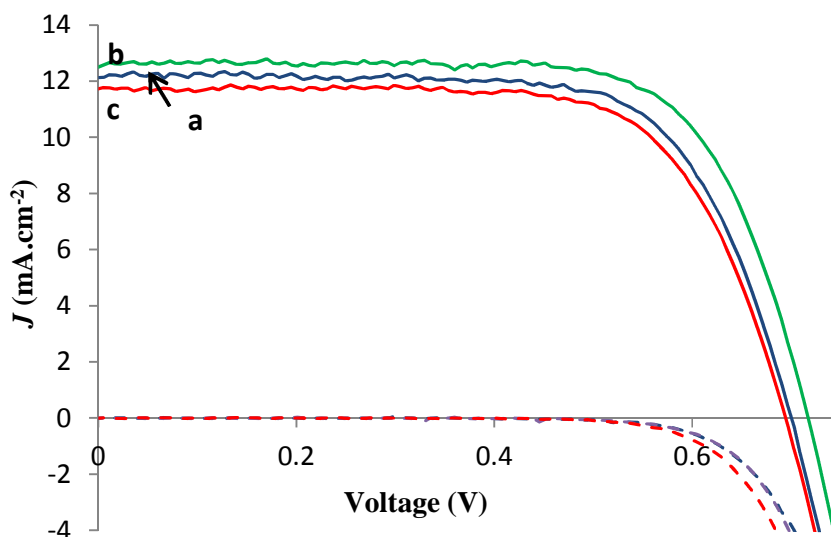


Figure 5.11 IV-curves of various times TiCl_4 treatment (a) once (b) twice (c) three times

The I-V curves of cells containing various amounts of graphene are shown in Figure 5.12 and the I-V curves characteristics are presented in Table 5.2. The best efficiency is found for TGr12 cells with a reproducible overall conversion efficiency increase of 12% compared to the TiO_2 _A reference one.

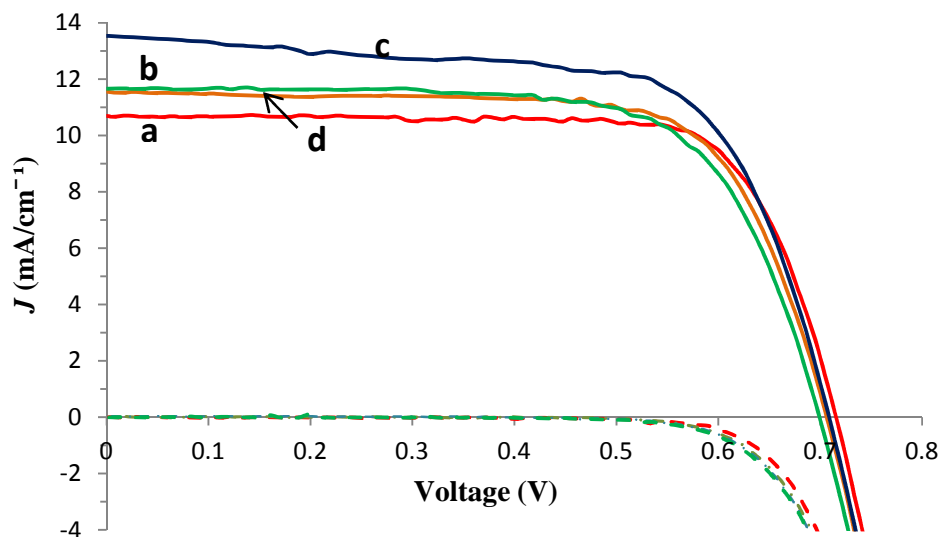


Figure 5.12: I-V curves of (a) TiO₂_A (b) TiO₂_Gr06 (c) TiO₂_Gr12 (d) TiO₂_Gr30

Table 5.2 I-V curve parameters of TiO₂_A and various TiO₂_Gr cells

Sample	Graphene content (wt %)	V_{oc} (V)	J_{sc} (mA.cm ⁻²)	FF (%)	η (%)
TiO ₂ _A	0	0.71	11.0	74.1	5.78
		0.69 ^a	13.0 ^a	74.8 ^a	6.70 ^a
TiO ₂ _Gr06	0.6	0.71	11.5	71.6	5.83
TiO ₂ _Gr12	1.2	0.71	13.6	66.6	6.42
		0.68	14.4 ^a	76.8 ^a	7.49 ^a
TiO ₂ _Gr30	3.0	0.70	11.6	69.4	5.65

^a Cells investigated by impedance spectroscopy

The I-V curve parameters are plotted as function of SGO content in Figure 5.13. The efficiency curve presents a volcano shape which follows the variation of J_{sc} with the graphene content (Figure 5.13a). On the other hand, the V_{oc} is almost constant and the FF slightly decreases with SGO content (Figure 5.13b). The volcano shape is in good agreement with previous reports (Wang et al., 2012). η and J_{sc} decrease at high graphene content is due to visible/near-infrared light absorption by RGO that shields light absorption by the dye and

reduces the number of photogenerated electrons (Wang et al., 2012). The light absorption by graphene is confirmed in Figure 5.9, in the wavelength region above 750 nm where light is no more absorbed by the N719 dye.

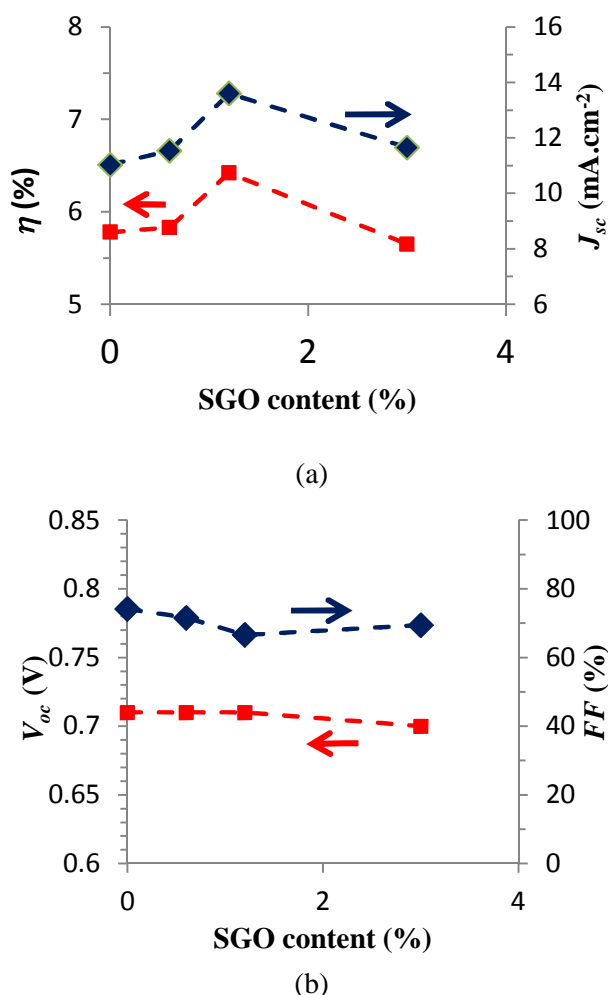
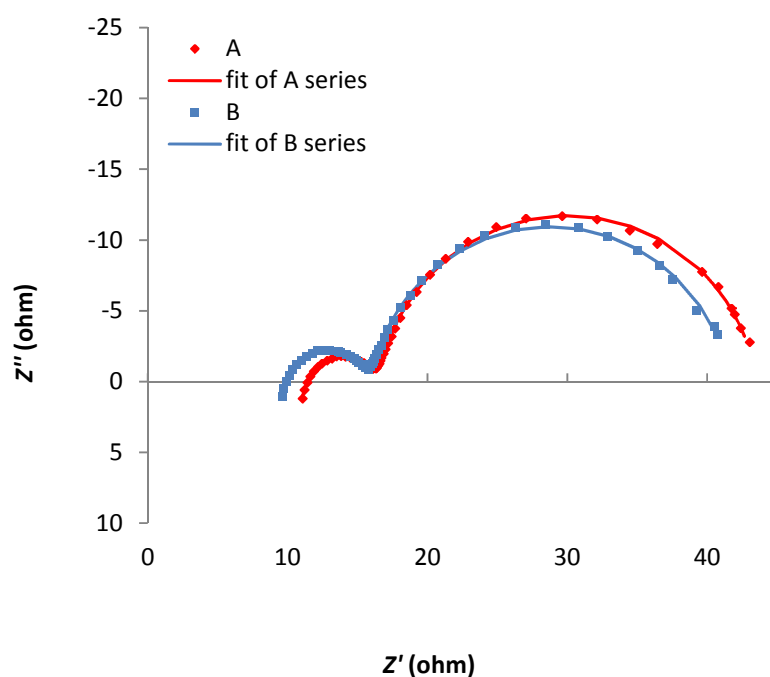


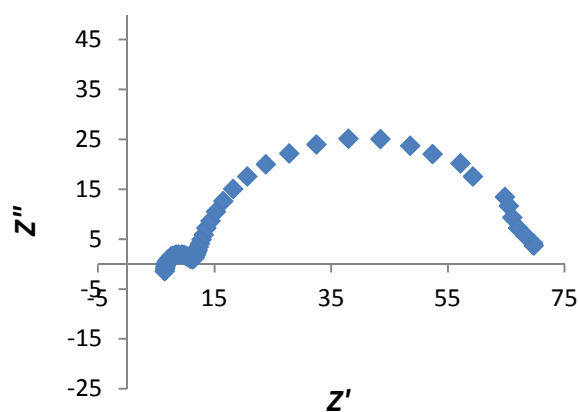
Figure 5.13 The I-V parameters plot as function of SGO content (a) η and J_{sc} (b) V_{oc} and (d) FF

To investigate the kinetic of electrochemical and photoelectrochemical processes occurring in the DSSCs, IS measurements were performed. IS is a powerful technique that has been employed in a large extent in many functional systems, including DSSCs, in which coupled processes are involved (Adachi et al., 2006; Bisquert, 2002; Bisquert and Vikhrenko, 2004; Fabregat-Santiago et al., 2007; Park et al., 2013; Pauporté et al., 2005; Peter, 2007; Wang et al., 2005). The impedance spectra of TiO_2 -A reference cell and TiO_2 -Gr12 cell (which showed the best performances) at V_{oc} are presented in Figure 5.16 (a). They all showed a characteristic low-middle frequency semicircle due to the resistance to charge

transfer (recombination) (R_{ct}) across the sensitized oxide-electrolyte interface coupled to the total electrode capacitance (denoted as C_{μ}). At high frequency, a second semicircle was found due to the resistance (R_{Pt}) and capacitance (C_{Pt}) of the charged counter-electrode/electrolyte interface. We note that for TiO₂_A and TiO₂_Gr12 cells, the IS spectra did not exhibit a clear Warburg loop at low frequency, even at high applied voltage (Figure 5.16 (b)). This fact disproves a performance limitation due to diffusion of the I₃⁻/I redox shuttle. Therefore the point (iv) in the introduction cannot explain the solar cell improvement in the TiO₂/graphene composite photoelectrode.



(a)



(b)

Figure 5.16: IS Spectra of (a) TiO₂_A and TiO₂_Gr12 at V_{oc} and (b) TiO₂ at 0.75 V

To gain insight about the kinetics of electron transport, the IS were measured in the dark over a large voltage range. The spectra were fitted using the ZView® software to extract the electrical parameters C_μ , R_{ct} and R_{tr} . Logarithmic plot of C_μ and R_{CT} are shown in Figure 5.17 as function of V_{cor} . It is shown that the R_{ct} values are very similar and then the rate of the charge transfer (recombination) parasitic reaction is unchanged with the presence of graphene. The final TiCl_4 treatment aims at covering graphene with a thin layer of TiO_2 and then avoids the recombination parasitic reaction.

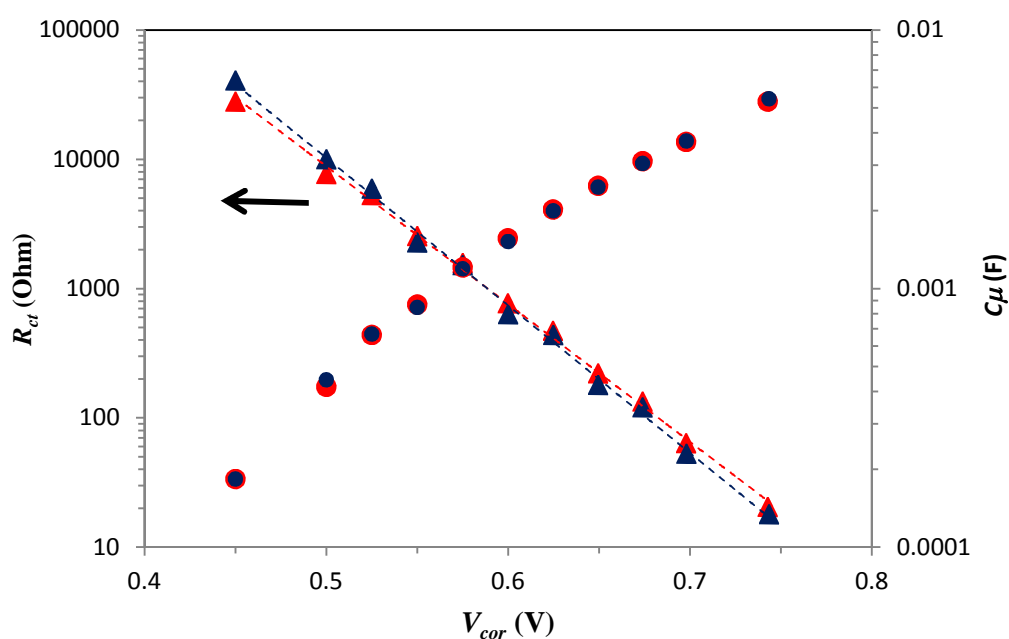


Figure 5.17: Variation of R_{ct} (triangles) and C_μ (dots) with the corrected applied voltage. The red symbols are for the TiO_2_A cell and the blue ones for the TiO_2_Gr12 cell.

As written in equation 2.10 and 2.15 (Chapter II, section II. 1. 3, page 39), the curve slope represents α and β for C_μ vs V_{corr} and R_{ct} vs V_{corr} , respectively. It is obtained that α values are similar with and without RGO in the photoelectrode and equal to 0.28 (Table 5.3).

Table 5.3 α , β and T_0 value of TiO_2_A and TiO_2_Gr that is extracted from IS Spectra

Sample	α	T_0 (K)	β
TiO_2_A	0.28 ^a	1046 ^a	0.62 ^a
TiO_2_Gr12	0.28 ^a	1046 ^a	0.66 ^a

The α value for anatase TiO₂ solar cells is classically reported in the literature in the range between 0.2 and 0.4. (Bisquert and Mora-Seró, 2010; Villanueva-Cab et al., 2010) According to Equation (2.10), the trap state depth can also be expressed as a temperature, T_0 , of 1046 K (Table 5.3). β values determined from the fits are gathered in Table 5.3 and are 0.62 and 0.66 with and without graphene, respectively. The β value which is lower than 1 is an empirical way and it is believed to describe sub-linear recombination kinetics that takes into account that electrons may be transferred from occupied levels located in the energy gap (Guerin et al., 2010; Hagfeldt et al., 2010).

From C_μ , the density of states (DOS) due to the traps, g , has been calculated according to equation 2.15. The g function is presented as energy diagram (Figure 5.18). The curve extrapolation lead to a bottom of the TiO₂ conduction band localized at about 0.75-0.80 V above the redox potential iodine (Magne et al., 2013). TiO₂_A and TiO₂_Gr12 show the similar trend of g it means that there is no clear effect of SGO on the DOS in the layer.

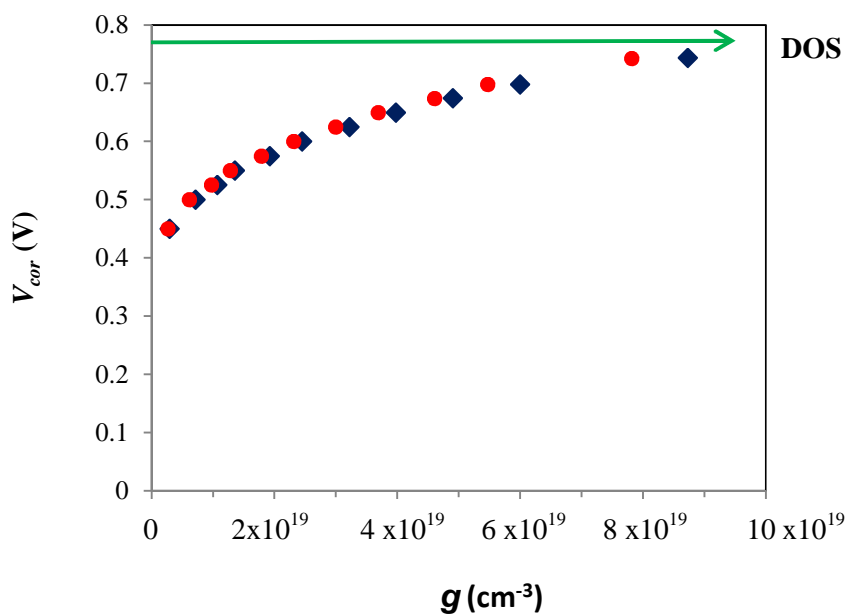


Figure 5.18: DOS distribution, Red symbols: TiO₂_A cell; Blue symbols TiO₂_Gr12 cell

The life time of electrons in the photoelectrode (τ_n), transport time/collection time (τ_n), chemical diffusion coefficient in semiconductor (D_n) and electron diffusion (L_n) length

have been calculated according to the equations 2.17, 2.18, 2.20 and 2.21 (Chapter II, section II. 1. 3, page 40), respectively. The results are presented in Figure 5.19, 5.20 and 5.21.

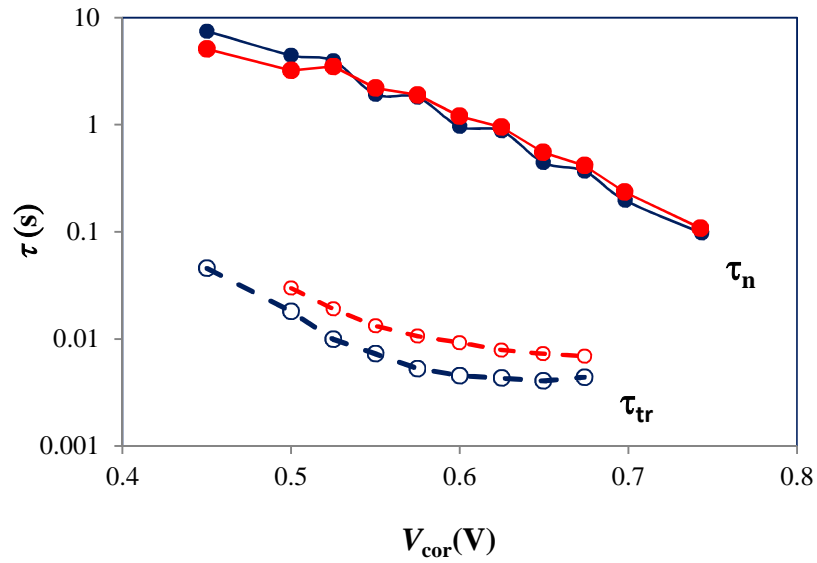


Figure 5.19: Variation of τ_n (full symbols) and τ_{tr} (open symbols) with the corrected applied voltage. Red symbols and lines: TiO₂_A cell; Blue symbols and lines: TiO₂_Gr12 cell

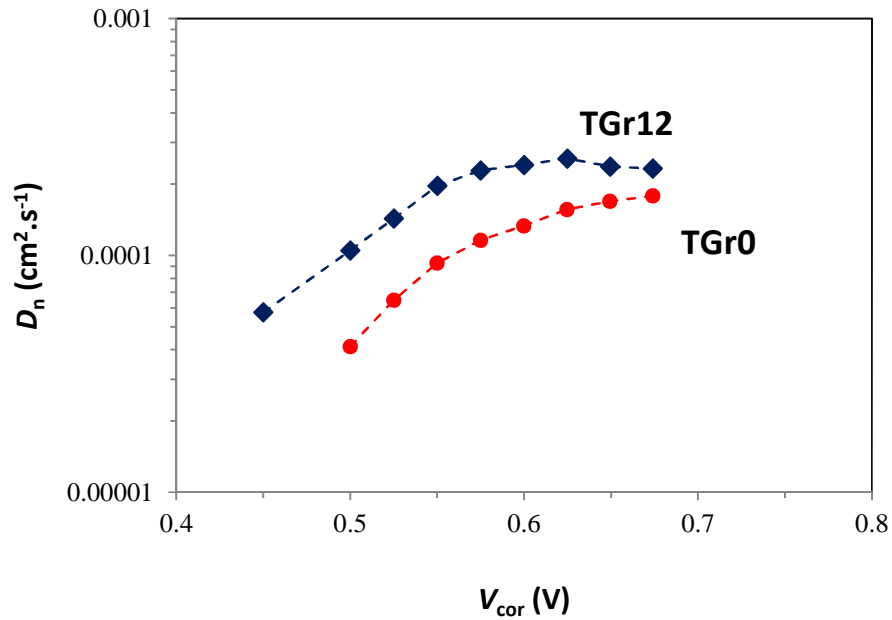


Figure 5.20: Effect of graphene on the variation of D_n with the corrected applied voltage

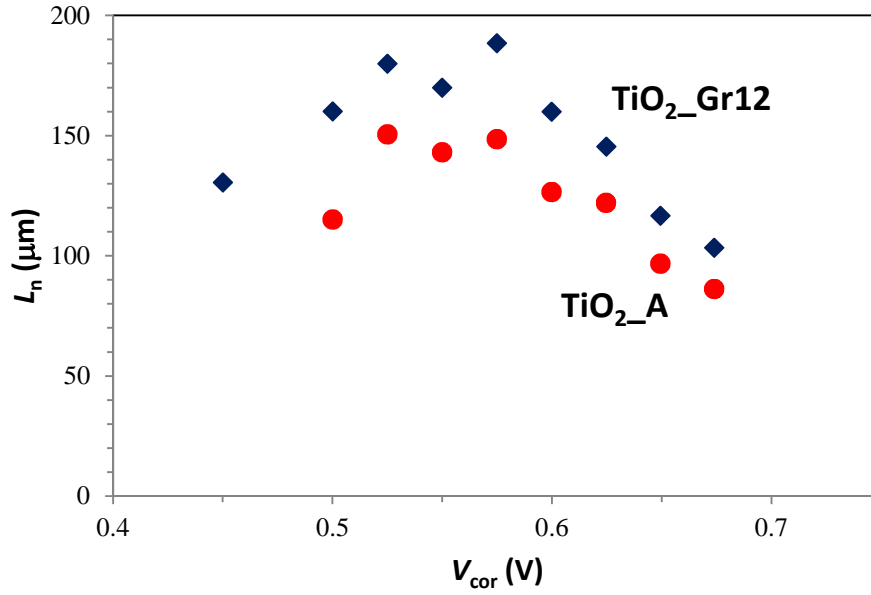


Figure 5.21: Effect of graphene on the variation of L_n with the corrected applied voltage

The same trend and value of τ_n is found for TiO_2_A and TiO_2_Gr12 cell. These results are obtained due to the $TiCl_4$ final treatment. It is hypothesized that the SGO sheets are covered by TiO_2 and are not involved in recombination processes. In addition, the band positions between TiO_2 and graphene facilitate electron transfer between these two components (point (ii) in the introduction) (Sun et al., 2010; Tang et al., 2010). A reduction of the recombination parasitic reaction may be then expected if the SGO is isolated from the electrolyte layer by TiO_2 . However, the IS data do not show such an effect.

The transport time has been calculated according to: $\tau_{tr} = R_{tr}C_{\mu}$ and is plotted as a function of the g in the Figure 5.19. It shows that graphene incorporation causes transport times shorter. Figure 5.20 and 5.21 present the effect of graphene on the diffusion coefficient of the electrons (D_n) and the mean diffusion length of the charge carriers (L_n). As expected, D_n is enlarged in the presence of graphene. L_n values also show longer values in the presence of graphene than that of TiO_2_A .

The conductivity of TiO_2 and composites material in the photoelectrodes was determined from the charge transport resistance according to equation 2.19 (Chapter II, section II. 1. 3, page 40) and the results are presented in Figure 5.22 as function of g . The conductivity increases rapidly with this parameter. Based on data on Figure 5.22, it is calculated that graphene incorporation into composite provokes conductivity increasing by 60% due to the high 2D conductivity of reduced graphene sheets.

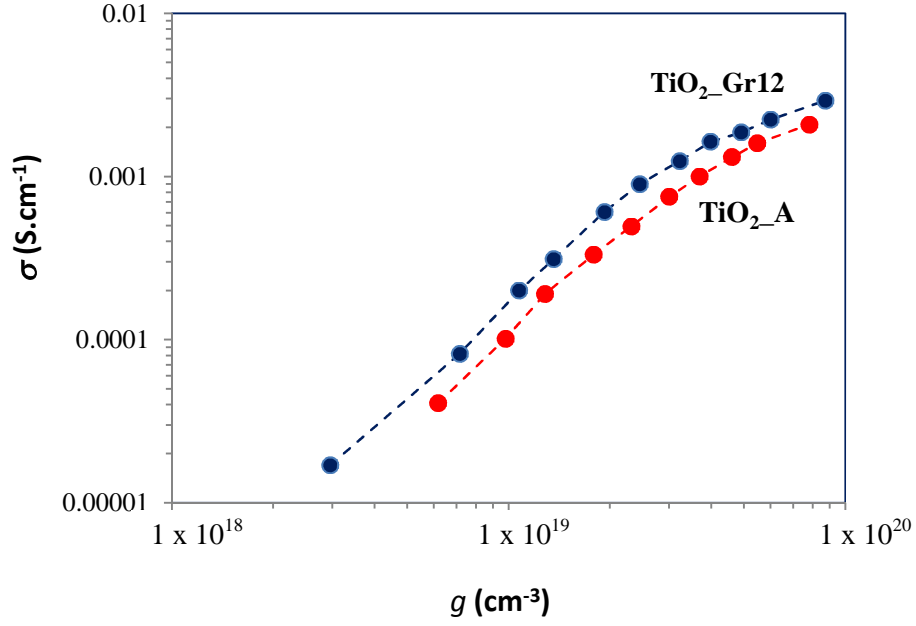


Figure 5.22: Effect of graphene on layer conductivity as function of g

The last parameter that was extracted from IS spectra is the charge collection efficiency (η_{coll}), that has been calculated using equation 2.18 (Chapter II, section II. 1. 3, page 40). Both samples show high η_{coll} . L_n values, are always much larger than the photoelectrode film thickness which is in the order of eleven micrometers. They explain this very high η_{coll} . The shorter τ_{tr} on TiO₂-Gr compare to that of TiO₂-A induce the higher η_{coll} as displayed in Figure 5.23.

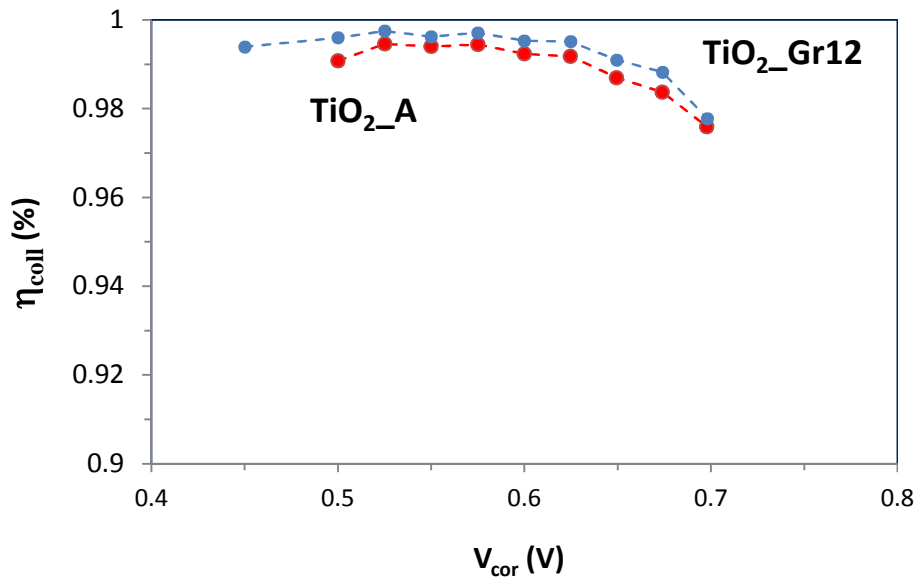


Figure: 5.23 Effect of graphene on η_{coll}

The conductivity improvement of composite photoelectrode due to graphene facilitates the charge transport and the photoelectrode charge collection efficiency (point (iii) in the introduction). However, this parameter is very high both in the presence and in the absence of graphene. This result gives the implication that when I_3^-/I^- redox shuttle is used, the cell J_{sc} and η improvement cannot be explained by the higher electrical conductivity of the photoelectrode. On the other hand, it is explained by the larger SSA and higher dye loading shown above. Using TiO_2/RGO composite photoelectrode enlarges the visible-Near-infrared light absorption by the sensitizer.

IPCE measurement has been done to complete cell performance measurement. The IPCE spectra of TiO_2_A and TiO_2_Gr12 are displayed in Figure 5.24. It shows that IPCE values of TiO_2_Gr12 are higher than that of TiO_2_A at 400-700 nm, especially at their maximum wavelength (530nm).

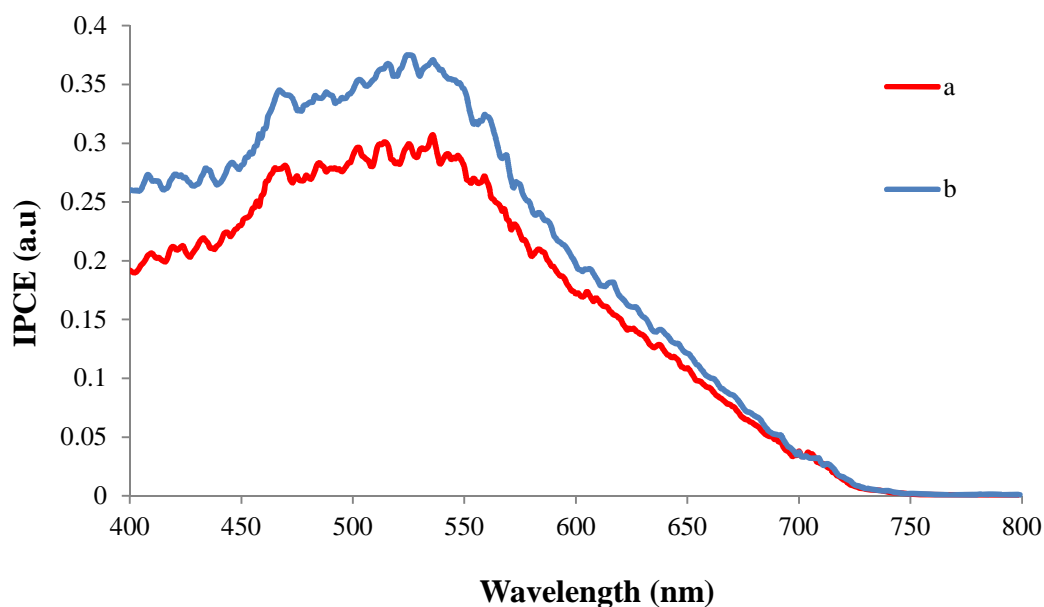


Figure 5.24: IPCE spectra of (a) TiO_2_A (b) TiO_2_Gr12

V.4 The cell performance of TiO_2/Gr in cobalt based DSSC

In this section on cobalt-based DSSC, Z907 was employed as the sensitizer. Alkyl chains on Z907 make it bulky so it hinders cobalt species to approach the TiO_2 surface. Then it reduces the unwanted electron recombination between electron in TiO_2 surface and Co^{3+} (Murakami et al., 2014; Yella et al., 2011). Figure 5.25 displays the optimized geometry of

the Z907 and N719 dyes that is conducted using Gaussian 09 package (Frisch et al., 2009) with B3LYP theory and basis set 6-311G* for all of atoms (Becke, 1993; Krishnan et al., 1980; McLean and Chandler, 1980) except Ruthenium that use LANL2DZ basis set (Hay and Wadt, 1985; Wadt and Hay, 1985). The CPC-M (Conductor-like Polarized Continuum Model) was applied to model solvation effect of acetonitrile (Cossi et al., 2003; Cossi and Barone, 2001). It clearly shows how bulky are the alkyl chains on Z907 compare to the N719 structure.

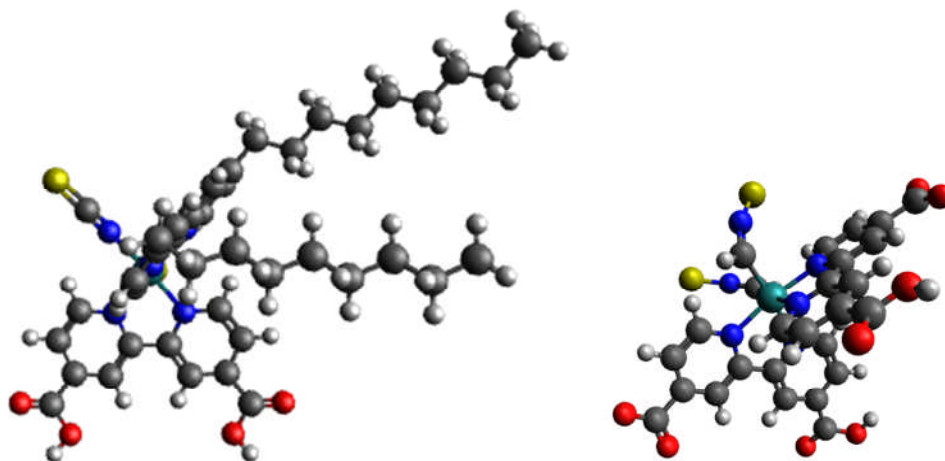


Figure 5.25: Optimized structure of Z907(left) and N719 (right)

Cobalt-based DSSC's components have been optimized using Z907 sensitized TiO_2 _A cell before it was applied into the TiO_2 _Gr based DSSC. The first optimization was about the Co^{3+} source. We compared the performance of DSSC that used Co^{3+} complex-compound as a source of Co^{3+} and another one that use Nitrosonium tetrafluoroborate (NOBF_4). Here, the NOBF_4 plays the role of oxidizing agent to convert the Co^{2+} into the Co^{3+} . In this experiment we used bipyridine as a ligand in the cobalt complex, and $(\text{PF}_6)^-$ as an anion. The concentration of the Co^{2+} was 0.11 M and the concentration of the Co^{3+} or the NOBF_4 was 0.011 M (electrolyte Co-1 and Co-2, see Chapter III, section III. 2, page 66. The preparation of $[\text{Co}(\text{bpy})_3]^{2+}$ and $[\text{Co}(\text{phen})_3]^{2+}$ are explained in Appendix G. $[\text{Co}(\text{bpy})_3]^{3+}$ was obtained from the Université de Bordeaux, Institut des Sciences moléculaires, France). It shows that employing NOBF_4 gives a better result in V_{oc} and FF (Table 5.4). The utilization of NOBF_4 in the electrolyte preparation can eliminate the step in the synthesis of Co^{3+} complex compound.

Table 5.4. The comparison of Z907 sensitized cell performances using $(\text{Co}[\text{bpy}]_2)^{3+}$ and NOBF_4 as source of Co^{3+}

Source of Co^{3+}	Photoelectrode thickness (μm)	V_{oc} (V)	J_{sc} (mA.cm^{-2})	FF (%)	η (%)
$(\text{Co}[\text{bpy}]_3)^{3+}$ (electrolyte Co-1)*	16.3	0.60	3.91	65.38	1.61
NOBF_4 (electrolyte Co-2)*	15.6	0.63	3.99	73.82	1.85

* see chapter III section III.2, page 66.

In a second step, the ligand of cobalt in the complex has been optimized. Here we compared the use of $[\text{Co}(\text{bpy})_3]^{2+/3+}$ and $[\text{Co}(\text{phen})_3]^{2+/3+}$. The result shows that the V_{oc} of $[\text{Co}(\text{phen})_3]^{2+/3+}$ -based cell is higher than that of $[\text{Co}(\text{bpy})_3]^{2+/3+}$ -one (Table 5.5). This trend results are in line with previous result (Feldt et al., 2011). This can be explained by the redox standard potential of $[\text{Co}(\text{phen})_3]^{2+/3+}$ (0.62 V) which is located below the redox potential of $[\text{Co}(\text{bpy})_3]^{2+/3+}$ (0.56 V). However, the value of both V_{oc} are lower than previous results (Feldt et al., 2011), it strongly suggest due to layer thickness of TiO_2 that is used in the experiment ($\sim 20 \mu\text{m}$), which is too thick for cobalt species to diffuse through oxide layer. But this experiment still reliable to compare the performance of $[\text{Co}(\text{bpy})_3]^{2+/3+}$ and $[\text{Co}(\text{phen})_3]^{2+/3+}$.

Table 5.5. The effect of ligand on cell performances

Cobalt-complex compound	Photoelectrode thickness (μm)	V_{oc} (V)	J_{sc} (mA.cm^{-2})	FF (%)	η (%)
$[\text{Co}(\text{bpy})_3]^{2+/3+(*)}$	21.8	0.641	1.669	69.4	0.74
$[\text{Co}(\text{phen})_3]^{2+/3+(*)}$	20.5	0.715	1.984	75.4	1.068

(*) both using electrolyte composition Co-2

We have also optimized the molar ratio of Co^{2+} to NOBF_4 . We have compared the performance of the cell employing electrolyte with a molar ratio of Co^{2+} to $\text{NOBF}_4 = 10:1$ and $= 5:1$. The addition of more the NOBF_4 was not tested, because based on the literature it can attack the ligand and cause the degradation of the complex (Nusbaumer et al., 2003). The results showed that the ratio of Co^{2+} to $\text{NOBF}_4 = 5:1$ gives a better performance than of the

10:1 ratio (Table 5.6). However, the overall conversion efficiency of the cells and the J_{sc} are low because the photoelectrodes used were too thick.

Table 5.6 Effect of Co(II)/NOBF₄ molar ratio on Z907-sensitized cell performances

Molar ratio of Co(II)/NOBF ₄	Photoelectrode thickness (μm)	V_{oc} (V)	J_{sc} (mA.cm ⁻²)	FF (%)	η (%)
1/10 (*)	15.6	0.70	3.58	72.26	1.80
1/5 (**)	14.8	0.70	4.51	72.92	2.29

* using electrolyte composition Co-2 ** using electrolyte composition Co-6

The optimization of the photoelectrode thickness and of the TBP concentration showed that the best performance of the cobalt-based cell was achieved using 10 μm thick photoelectrodes and 0.2 M TBP (Figure 5.26 and 5.27). Too thick photoelectrodes induce a performance limitation due to the bulky cobalt redox molecule diffusion limitation through the pores (Hamann, 2012). On the other hand, a too thin oxide layer causes a decrease in dye loading. Figure 5.26 displays all I - V curve parameters have a volcano shape. The best performance was achieved for cells that had a photoelectrode thickness of about 10 μm.

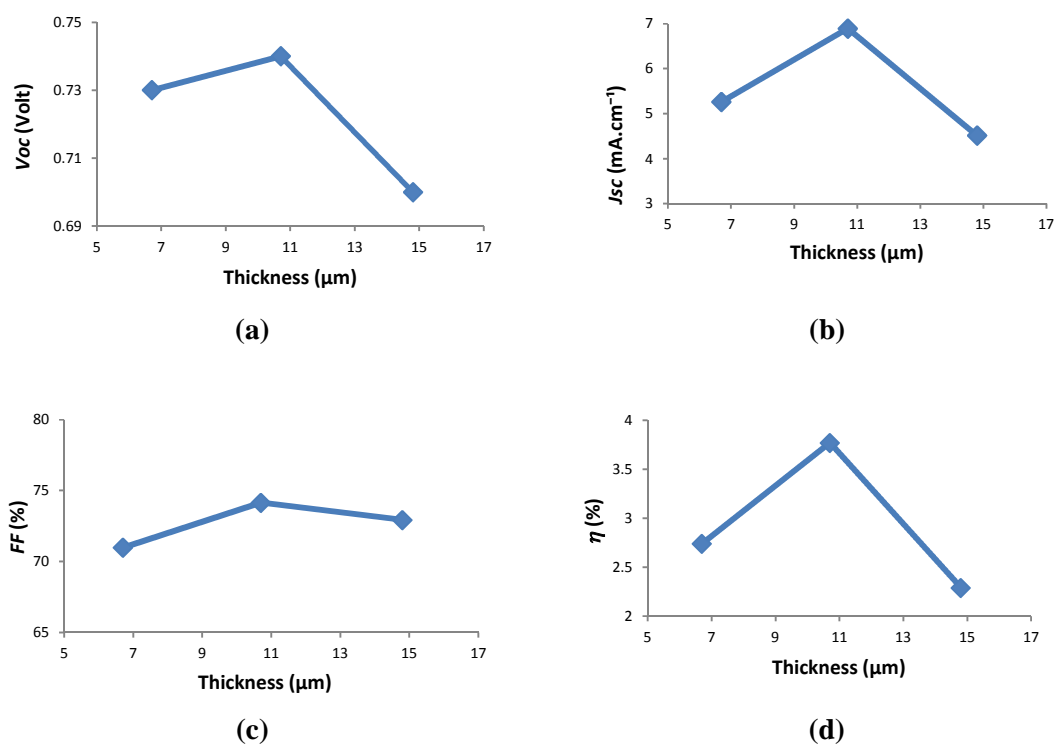


Figure 5.26: The effect of thickness on cell performance (a) V_{oc} (b) J_{sc} (c) FF (d) η . All of cells using electrolyte Co-2

For the optimization of the TBP-concentration in an electrolyte, Figure 5.27(d) shows 0.2 M TBP in the electrolyte yielded to the best power conversion efficiency. The efficiency increase is mainly due to the V_{oc} and J_{sc} enlargement. It is explained by the adsorption of TBP on the oxide surface that reduces the recombination between electron on oxide surface and Co(III). More TBP does not improve the performance because the presence more TBP increases the electrolyte viscosity and then provokes transport limitation of cobalt redox-couple (Koh et al., 2013).

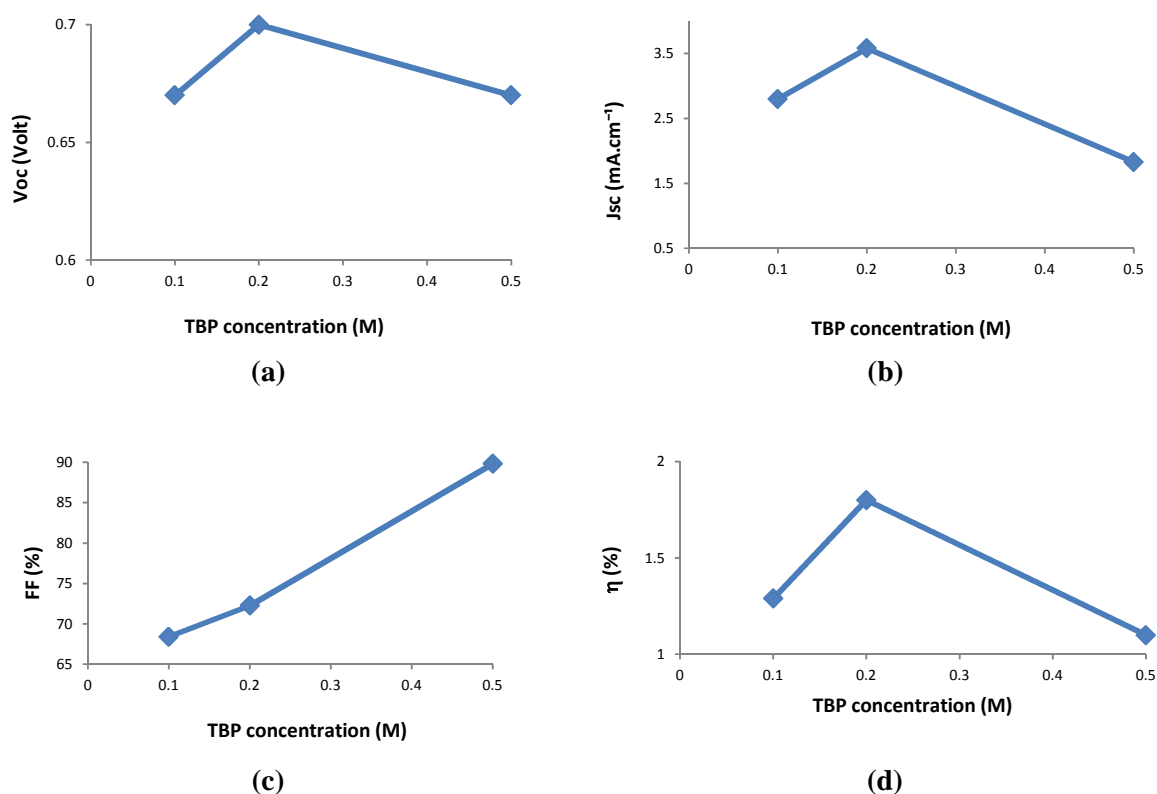


Figure 5.27: The effect of TBP concentration on (a) V_{oc} (b) J_{sc} (c) FF (d) η

(The test was done employing 15-17 μm photoelectrode; the cells use electrolyte Co-3, Co-2 and Co-4 for 0.1 M, 0.2 M and 0.5 M TBP respectively).

Based on the above optimization results, the cell parameters adopted for the $\text{TiO}_2\text{-Gr}$ application are gathered in Table 5.7.

Table 5.7. Cell parameters for TiO₂_Gr12 cobalt-based DSSC experiment

NO	Cell parameters	Optimized result
1	Source of Co(III)	NOBF ₄
2	Ligand of cobalt complex	1,10-phenanthroline
3	Molar ratio of Co(II)/NOBF ₄	1:5
4	TBP concentration	0.2 M
5	Photoelectrode thickness	10-11 μm

Figure 5.28 and Table 5.8 shows the cell performance of TiO₂_A and TiO₂_Gr12 in the cobalt based cells (electrolyte Co-6). They also show the results for the iodine based cells (electrolyte I₂-2) for the sake of comparison. I-V results show an increase in J_{sc} after the addition of graphene in both DSSC systems. In addition, as expected, there is an increase of the cell V_{oc} for cobalt based cells compared to the iodide electrolyte. Back to the purposes to provide iodine free DSSC, based on these results TiO₂_Gr12 is promising since these cells with the cobalt redox have an efficiency close to that of TiO₂_A combined with the Γ^-/I_3^- electrolyte.

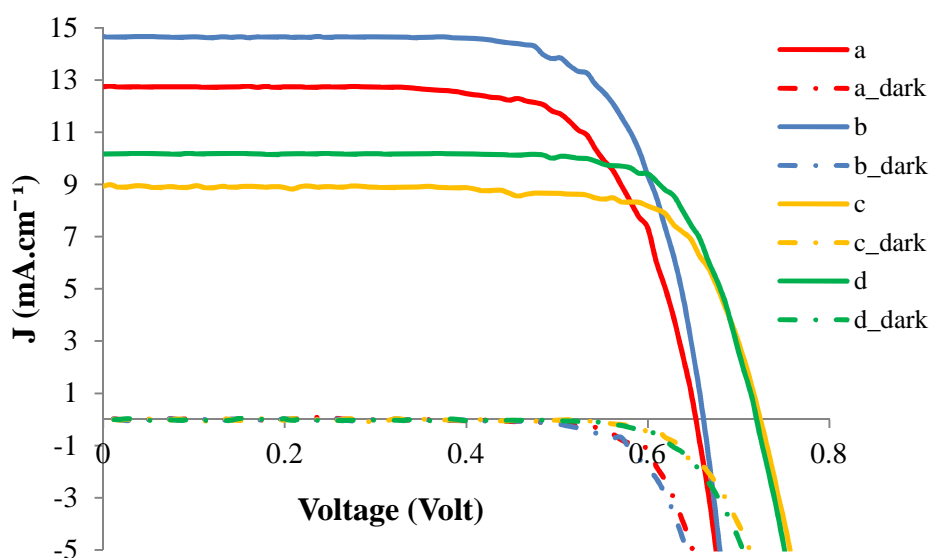


Figure 5.28: I-V curves of Z907 sensitized solar cells of (a) TiO₂_A-iodine (b) TiO₂_Gr12-iodine (c) TiO₂_A-cobalt (d) TiO₂_Gr12-cobalt

Table 5.8 I-V parameters of Z907 sensitized TiO₂_A and TiO₂_Gr12 solar cells with iodine (I₂-2) and cobalt-based electrolytes (Co-6)

Sample	Electrolyte	V_{OC} (V)	J_{SC} (mA.cm ⁻²)	FF (%)	η (%)
TiO ₂ _A	I ₂ -2	0.65	12.73	70.93	5.89
TiO ₂ _Gr12	I ₂ -2	0.66	14.64	73.02	7.06
TiO ₂ _A	Co-6	0.72	8.94	75.06	4.91
TiO ₂ _Gr12	Co-6	0.72	10.17	77.06	5.64

To complete the investigation of cell performance, we measured the absorbance of Z907-sensitized TiO₂_A and TiO₂_Gr12 layers. Figure 5.29 shows that over the 350-700 nm wavelength range, TiO₂_Gr/Z907 has a higher absorbance compared to that of TiO₂_A/Z907. As for the N719 sensitized solar cells (section V.2) J_{sc} increase in TiO₂_Gr is dominantly due to the increase in the light harvesting agent. The IPCE-spectra also confirm the same trend (Figure 5.30). Moreover, because the cobalt species do not absorb the light in the 400-450 nm range, unlike iodine, the IPCE is better for this redox system (Figure 5.30).

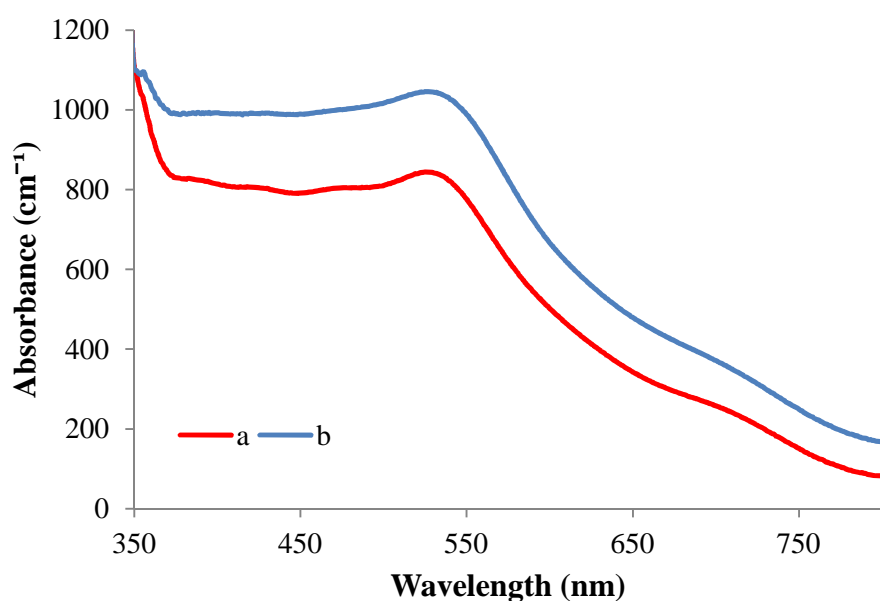


Figure 5.29. Absorbance of Z907-sensitized (a) TiO₂_A and (b) TiO₂_Gr12 layer

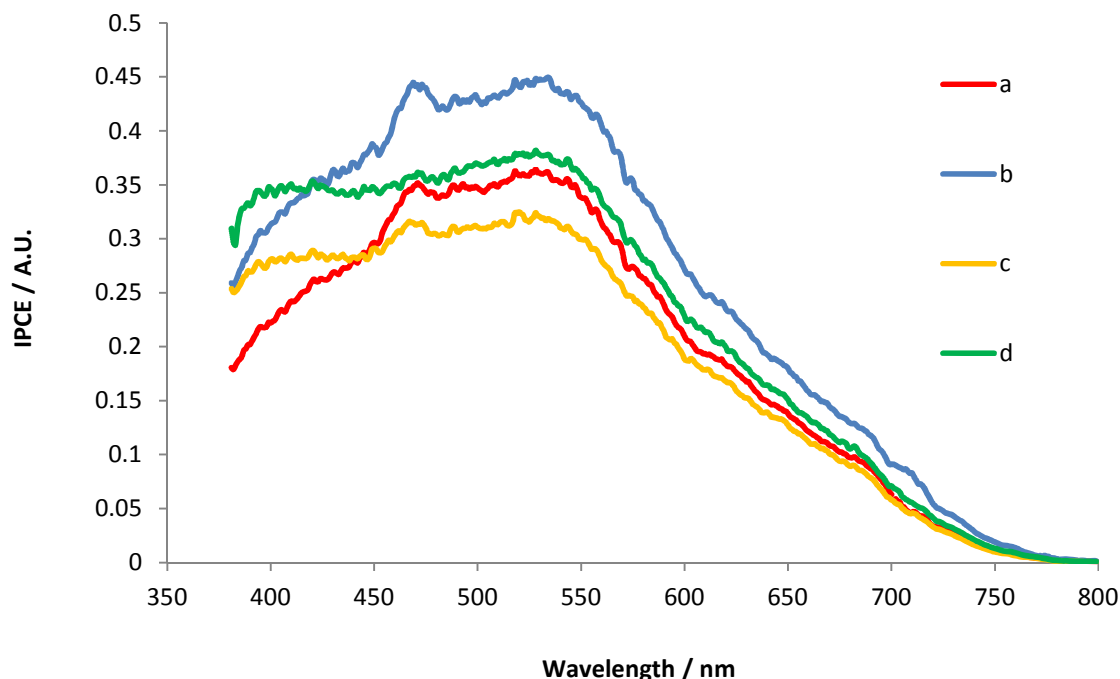


Figure 5.30: IPCE spectra of Z907 sensitized cell. (a) $\text{TiO}_2\text{-A}$ and (b) $\text{TiO}_2\text{-Gr12}$ coupled with I_3^-/I^- ; and (c) $\text{TiO}_2\text{-A}$ and (d) $\text{TiO}_2\text{-Gr12}$ couple with $\text{Co}^{2+/3+}$

V. 5 SUMMARY

We have developed a simple and effective technique for the preparation of mesoporous TiO_2/RGO composite films and integrated the layers in DSSCs. The effect of RGO content on the cell performances has been investigated and we have shown that the use of 1.2 wt% of graphene reproducibly enhances the solar cell overall conversion efficiency by 10-12%. The interaction between TiO_2 and graphene and the thermal reduction of SGO to RGO have been shown. The impedance spectroscopy technique has been used to closely examine the effect of RGO on the cell functioning. The photoelectrodes with and without graphene show no limitation due to the transport of the I_3^-/I^- redox shuttle. The rate of the charge transfer (recombination), a parasitic reaction, is unchanged with the presence of graphene. On the other hand, the electron transport in the photoelectrodes is significantly faster for the composite film, due to a quantified 60% increase of the layer conductivity in the presence of 1.2wt% RGO. However, we have also shown that the charge collection efficiency is very high even without RGO, and that this parameter is not the key to explain the cell performance enhancement.

On the other hand RGO increases the film SSA. Therefore, a higher dye loading occurs in the presence of graphene, gives rise to a better solar light absorption and to the enlargement of J_{sc} . However, we have noted that for RGO content above 1.2 wt%, light absorption by graphene becomes detrimental and shields the light absorption by the dye.

The application of TiO₂/graphene composite to Z907 sensitized as photoelectrode in the cobalt-based DSSCs showed promising results. The PCE of TiO₂_Gr 12 coupled with [Co(Phen)₃]^{2+/3+} reached 5.64% that is a comparable result compare to the TiO₂_A coupled with I₃⁻/I⁻ that reached 5.89%.

References

- Adachi, M., Sakamoto, M., Jiu, J., Ogata, Y., Isoda, S., 2006. Determination of Parameters of Electron Transport in Dye-Sensitized Solar Cells Using Electrochemical Impedance Spectroscopy. *J. Phys. Chem. B* 110, 13872–13880. doi:10.1021/jp061693u
- Allen, M.J., Tung, V.C., Kaner, R.B., 2010. Honeycomb Carbon : A Review of Graphene 132–145.
- Bai, J., Huang, Y., 2010. Fabrication and electrical properties of graphene nanoribbons. *Mater. Sci. Eng. R Rep.*, 3rd IEEE International NanoElectronics Conference (INEC) 70, 341–353. doi:10.1016/j.mser.2010.06.019
- Balandin, A.A., Ghosh, S., Bao, W., Calizo, I., Teweldebrhan, D., Miao, F., Lau, C.N., 2008. Superior Thermal Conductivity of Single-Layer Graphene. *Nano Lett.* 8, 902–907. doi:10.1021/nl0731872
- Becke, A.D., 1993. Density-functional thermochemistry. III. The role of exact exchange. *J. Chem. Phys.* 98, 5648–5652. doi:10.1063/1.464913
- Bisquert, J., 2002. Theory of the Impedance of Electron Diffusion and Recombination in a Thin Layer. *J. Phys. Chem. B* 106, 325–333. doi:10.1021/jp011941g
- Bisquert, J., Mora-Seró, I., 2010. Simulation of Steady-State Characteristics of Dye-Sensitized Solar Cells and the Interpretation of the Diffusion Length. *J. Phys. Chem. Lett.* 1, 450–456. doi:10.1021/jz900297b
- Bisquert, J., Vikhrenko, V.S., 2004. Interpretation of the Time Constants Measured by Kinetic Techniques in Nanostructured Semiconductor Electrodes and Dye-Sensitized Solar Cells. *J. Phys. Chem. B* 108, 2313–2322. doi:10.1021/jp035395y
- Bonaccorso, F., Sun, Z., Hasan, T., Ferrari, A.C., 2010. Graphene photonics and optoelectronics 4, 611–622. doi:10.1038/nphoton.2010.186
- Chaves, A., Katiyar, R.S., Porto, S.P.S., 1974. Coupled modes with A₁ symmetry in tetragonal BaTiO₃. *Phys. Rev. B* 10, 3522–3533. doi:10.1103/PhysRevB.10.3522
- Chen, C., Cai, W., Long, M., Zhou, B., Wu, Y., Wu, D., Feng, Y., 2010. Synthesis of Visible-Light Responsive Graphene Oxide/TiO₂ Composites with p/n Heterojunction. *ACS Nano* 4, 6425–6432. doi:10.1021/nn102130m
- Cheng, G., Akhtar, M.S., Yang, O.-B., Stadler, F.J., 2013. Novel Preparation of Anatase TiO₂-Reduced Graphene Oxide Hybrids for High-Performance Dye-Sensitized Solar Cells. *ACS Appl. Mater. Interfaces* 5, 6635–6642. doi:10.1021/am4013374
- Choi, W., Lahiri, I., Seelaboyina, R., Kang, Y.S., 2010. Synthesis of Graphene and Its Applications: A Review. *Crit. Rev. Solid State Mater. Sci.* 35, 52–71. doi:10.1080/10408430903505036
- Cossi, M., Barone, V., 2001. Time-dependent density functional theory for molecules in liquid solutions. *J. Chem. Phys.* 115, 4708–4717. doi:10.1063/1.1394921
- Cossi, M., Rega, N., Scalmani, G., Barone, V., 2003. Energies, structures, and electronic properties of molecules in solution with the C-PCM solvation model. *J. Comput. Chem.* 24, 669–681. doi:10.1002/jcc.10189
- Ding, Z., Lu, G.Q., Greenfield, P.F., 2000. Role of the Crystallite Phase of TiO₂ in Heterogeneous Photocatalysis for Phenol Oxidation in Water. *J. Phys. Chem. B* 104, 4815–4820. doi:10.1021/jp993819b

- Fabregat-Santiago, F., Bisquert, J., Palomares, E., Otero, L., Kuang, D., Zakeeruddin, S.M., Grätzel, M., 2007. Correlation between Photovoltaic Performance and Impedance Spectroscopy of Dye-Sensitized Solar Cells Based on Ionic Liquids. *J. Phys. Chem. C* 111, 6550–6560. doi:10.1021/jp066178a
- Fang, X., Li, M., Guo, K., Liu, X., Zhu, Y., Sebo, B., Zhao, X., 2014a. Graphene-compositing optimization of the properties of dye-sensitized solar cells. *Sol. Energy* 101, 176–181. doi:10.1016/j.solener.2013.12.005
- Fang, X., Li, M., Guo, K., Liu, X., Zhu, Y., Sebo, B., Zhao, X., 2014b. Graphene-compositing optimization of the properties of dye-sensitized solar cells. *Sol. Energy* 101, 176–181. doi:10.1016/j.solener.2013.12.005
- Fan, J., Liu, S., Yu, J., 2012. Enhanced photovoltaic performance of dye-sensitized solar cells based on TiO₂ nanosheets/graphene composite films. *J. Mater. Chem.* 22, 17027–17036. doi:10.1039/C2JM33104G
- Feldt, S.M., Wang, G., Boschloo, G., Hagfeldt, A., 2011. Effects of Driving Forces for Recombination and Regeneration on the Photovoltaic Performance of Dye-Sensitized Solar Cells using Cobalt Polypyridine Redox Couples. *J. Phys. Chem. C* 115, 21500–21507. doi:10.1021/jp2061392
- Frisch, M.J., Trucks, G.W., Schlegel, H.B., Scuseria, G.E., Robb, M.A., Cheeseman, J.R., Scalmani, G., Barone, V., Mennucci, B., Petersson, G.A., others, 2009. Gaussian 09, Revision A. 1. Wallingford CT: Gaussian, Inc.
- Geim, A.K., Novoselov, K.S., 2007. The rise of graphene. *Nat. Mater.* 6, 183–191. doi:10.1038/nmat1849
- Guerin, V.M., Magne, C., Pauporté, T., Le Bahers, T., Rathousky, J., 2010. Electrodeposited Nanoporous versus Nanoparticulate ZnO Films of Similar Roughness for Dye-Sensitized Solar Cell Applications. *ACS Appl. Mater. Interfaces* 2, 3677–3685. doi:10.1021/am1008248
- Hagfeldt, A., Boschloo, G., Sun, L., Kloo, L., Pettersson, H., 2010. Dye-Sensitized Solar Cells. *Chem. Rev.* 110, 6595–6663.
- Hamann, T.W., 2012. The end of iodide? Cobalt complex redox shuttles in DSSCs. *Dalton Trans.* 41, 3111. doi:10.1039/c2dt12362b
- Hamann, T.W., Gstrein, F., Brunschwig, B.S., Lewis, N.S., 2006. Measurement of the driving force dependence of interfacial charge-transfer rate constants in response to pH changes at n-ZnO/H₂O interfaces. *Chem. Phys.* 326, 15–23. doi:10.1016/j.chemphys.2006.02.027
- Hay, P.J., Wadt, W.R., 1985. Ab initio effective core potentials for molecular calculations. Potentials for the transition metal atoms Sc to Hg. *J. Chem. Phys.* 82, 270–283. doi:10.1063/1.448799
- He, Z., Guai, G., Liu, J., Guo, C., Loo, J.S.C., Li, C.M., Tan, T.T.Y., 2011. Nanostructure control of graphene-composited TiO₂ by a one-step solvothermal approach for high performance dye-sensitized solar cells. *Nanoscale* 3, 4613–4616. doi:10.1039/C1NR11300C
- Huang, H., Chen, W., Chen, S., Wee, A.T.S., 2008. Bottom-up Growth of Epitaxial Graphene on 6H-SiC(0001). *ACS Nano* 2, 2513–2518. doi:10.1021/nn800711v
- Ito, S., Miura, H., Uchida, S., Takata, M., Sumioka, K., Liska, P., Comte, P., Péchy, P., Grätzel, M., 2008. High-conversion-efficiency organic dye-sensitized solar cells with a novel indoline dye. *Chem. Commun.* 5194–5196. doi:10.1039/B809093A
- Jiang, B., Tian, C., Zhou, W., Wang, J., Xie, Y., Pan, Q., Ren, Z., Dong, Y., Fu, D., Han, J., Fu, H., 2011. In Situ Growth of TiO₂ in Interlayers of Expanded Graphite for the Fabrication of TiO₂-Graphene with Enhanced Photocatalytic Activity. *Chem. – Eur. J.* 17, 8379–8387. doi:10.1002/chem.201100250
- Jung, I., Dikin, D.A., Piner, R.D., Ruoff, R.S., 2008. Tunable Electrical Conductivity of Individual Graphene Oxide Sheets Reduced at “Low” Temperatures. *Nano Lett.* 8, 4283–4287. doi:10.1021/nl8019938
- Kim, K.S., Zhao, Y., Jang, H., Lee, S.Y., Kim, J.M., Kim, K.S., Ahn, J.-H., Kim, P., Choi, J.-Y., Hong, B.H., 2009. Large-scale pattern growth of graphene films for stretchable transparent electrodes. *Nature* 457, 706–710. doi:10.1038/nature07719
- Kim, S.R., Parvez, M.K., Chhowalla, M., 2009. UV-reduction of graphene oxide and its application as an interfacial layer to reduce the back-transport reactions in dye-sensitized solar cells. *Chem. Phys. Lett.* 483, 124–127. doi:10.1016/j.cplett.2009.10.066
- Koh, T.M., Nonomura, K., Mathews, N., Hagfeldt, A., Grätzel, M., Mhaisalkar, S.G., Grimsdale, A.C., 2013. Influence of 4-tert-Butylpyridine in DSCs with CoII/III Redox Mediator. *J. Phys. Chem. C* 117, 15515–15522. doi:10.1021/jp403918q
- Krishnan, R., Binkley, J.S., Seeger, R., Pople, J.A., 1980. Self-consistent molecular orbital methods. A basis set for correlated wave functions. *J. Chem. Phys.* 72, 650–654. doi:10.1063/1.438955

- Lee, C., Wei, X., Kysar, J.W., Hone, J., 2008. Measurement of the Elastic Properties and Intrinsic Strength of Monolayer Graphene. *Science* 321, 385–388. doi:10.1126/science.1157996
- Liang, Y., Frisch, J., Zhi, L., Norouzi-Arasi, H., Feng, X., Rabe, J.P., Koch, N., Müllen, K., 2009. Transparent, highly conductive graphene electrodes from acetylene-assisted thermolysis of graphite oxide sheets and nanographene molecules. *Nanotechnology* 20, 434007. doi:10.1088/0957-4484/20/43/434007
- Liu, J., Jeong, H., Liu, J., Lee, K., Park, J.-Y., Ahn, Y.H., Lee, S., 2010. Reduction of functionalized graphite oxides by trioctylphosphine in non-polar organic solvents. *Carbon* 48, 2282–2289. doi:10.1016/j.carbon.2010.03.002
- Magne, C., Dufour, F., Labat, F., Lancel, G., Durupthy, O., Cassaignon, S., Pauporté, T., 2012. Effects of TiO₂ nanoparticle polymorphism on dye-sensitized solar cell photovoltaic properties. *J. Photochem. Photobiol. Chem.* 232, 22–31. doi:10.1016/j.jphotochem.2012.01.015
- Magne, C., Moehl, T., Urien, M., Grätzel, M., Pauporté, T., 2013. Effects of ZnO film growth route and nanostructure on electron transport and recombination in dye-sensitized solar cells. *J. Mater. Chem. A* 1, 2079. doi:10.1039/c2ta00674j
- McLean, A.D., Chandler, G.S., 1980. Contracted Gaussian basis sets for molecular calculations. I. Second row atoms, Z=11–18. *J. Chem. Phys.* 72, 5639–5648. doi:10.1063/1.438980
- Murakami, T.N., Koumura, N., Kimura, M., Mori, S., 2014. Structural Effect of Donor in Organic Dye on Recombination in Dye-Sensitized Solar Cells with Cobalt Complex Electrolyte. *Langmuir* 30, 2274–2279. doi:10.1021/la4047808
- Nair, R.R., Blake, P., Grigorenko, A.N., Novoselov, K.S., Booth, T.J., Stauber, T., Peres, N.M.R., Geim, A.K., 2008. Fine Structure Constant Defines Visual Transparency of Graphene. *Science* 320, 1308–1308. doi:10.1126/science.1156965
- Neto, A.H.C., 2009. The electronic properties of graphene 81. doi:10.1103/RevModPhys.81.109
- Novoselov, K.S., 2009. Electric Field Effect in Atomically Thin Carbon Films 666. doi:10.1126/science.1102896
- Novoselov, K.S., 2011. Nobel Lecture: Graphene: Materials in the Flatland * 83, 837–849. doi:10.1103/RevModPhys.83.837
- Nusbaumer, H., Zakeeruddin, S.M., Moser, J.-E., Grätzel, M., 2003. An Alternative Efficient Redox Couple for the Dye-Sensitized Solar Cell System. *Chem. – Eur. J.* 9, 3756–3763. doi:10.1002/chem.200204577
- Park, H.J., Meyer, J., Roth, S., Skákalová, V., 2010. Growth and properties of few-layer graphene prepared by chemical vapor deposition. *Carbon* 48, 1088–1094. doi:10.1016/j.carbon.2009.11.030
- Park, K., Zhang, Q., Myers, D., Cao, G., 2013. Charge Transport Properties in TiO₂ Network with Different Particle Sizes for Dye Sensitized Solar Cells. *ACS Appl. Mater. Interfaces* 5, 1044–1052. doi:10.1021/am302781b
- Pauporté, T., Finne, J., Kahn-Harari, A., Lincot, D., 2005. Growth by plasma electrolysis of zirconium oxide films in the micrometer range. *Surf. Coat. Technol., Plasma Electrolysis* 199, 213–219. doi:10.1016/j.surfcoat.2005.03.003
- Pauporte, T., Rathousky, J., 2009. Growth mechanism and photocatalytic properties for dye degradation of hydrophobic mesoporous ZnO/SDS films prepared by electrodeposition. *Microporous Mesoporous Mater.* 117, 380–385. doi:10.1016/j.micromeso.2008.07.016
- Peining, Z., Nair, A.S., Shengjie, P., Shengyuan, Y., Ramakrishna, S., 2012. Facile Fabrication of TiO₂–Graphene Composite with Enhanced Photovoltaic and Photocatalytic Properties by Electrospinning 39.
- Peter, L.M., 2007. Characterization and Modeling of Dye-Sensitized Solar Cells. *J. Phys. Chem. C* 111, 6601–6612. doi:10.1021/jp069058b
- Robinson, J., Weng, X., Trumbull, K., Cavalero, R., Wetherington, M., Frantz, E., LaBella, M., Hughes, Z., Fanton, M., Snyder, D., 2010. Nucleation of Epitaxial Graphene on SiC(0001). *ACS Nano* 4, 153–158. doi:10.1021/nn901248j
- Sánchez, E., López, T., Gómez, R., Bokhimi, Morales, A., Novaro, O., 1996. Synthesis and Characterization of Sol–Gel Pt/TiO₂ Catalyst. *J. Solid State Chem.* 122, 309–314. doi:10.1006/jssc.1996.0118
- Shen, J., Yan, B., Shi, M., Ma, H., Li, N., Ye, M., 2011. One step hydrothermal synthesis of TiO₂-reduced graphene oxide sheets. *J. Mater. Chem.* 21, 3415–3421. doi:10.1039/C0JM03542D
- Song, J., Yin, Z., Yang, Z., Amaladass, P., Wu, S., Ye, J., Zhao, Y., Deng, W.-Q., Zhang, H., Liu, X.-W., 2011. Enhancement of Photogenerated Electron Transport in Dye-Sensitized Solar Cells with Introduction of

- a Reduced Graphene Oxide–TiO₂ Junction. *Chem. – Eur. J.* 17, 10832–10837. doi:10.1002/chem.201101263
- Stankovich, S., Dikin, D.A., Piner, R.D., Kohlhaas, K.A., Kleinhammes, A., Jia, Y., Wu, Y., Nguyen, S.T., Ruoff, R.S., 2007. Synthesis of graphene-based nanosheets via chemical reduction of exfoliated graphite oxide. *Carbon* 45, 1558–1565. doi:10.1016/j.carbon.2007.02.034
- Sun, S., Gao, L., Liu, Y., 2010. Enhanced dye-sensitized solar cell using graphene-TiO₂ photoanode prepared by heterogeneous coagulation. *Appl. Phys. Lett.* 96, 083113–083113–3. doi:10.1063/1.3318466
- Tang, Y.-B., Lee, C.-S., Xu, J., Liu, Z.-T., Chen, Z.-H., He, Z., Cao, Y.-L., Yuan, G., Song, H., Chen, L., Luo, L., Cheng, H.-M., Zhang, W.-J., Bello, I., Lee, S.-T., 2010. Incorporation of Graphenes in Nanostructured TiO₂ Films via Molecular Grafting for Dye-Sensitized Solar Cell Application. *ACS Nano* 4, 3482–3488. doi:10.1021/nn100449w
- Vasconcelos, D.C.L., 2011. Infrared Spectroscopy of Titania Sol-Gel Coatings on 316L Stainless Steel. *Mater. Sci. Appl.* 02, 1375–1382. doi:10.4236/msa.2011.210186
- Villanueva-Cab, J., Wang, H., Oskam, G., Peter, L.M., 2010. Electron Diffusion and Back Reaction in Dye-Sensitized Solar Cells: The Effect of Nonlinear Recombination Kinetics. *J. Phys. Chem. Lett.* 1, 748–751. doi:10.1021/jz1000243
- Wadt, W.R., Hay, P.J., 1985. Ab initio effective core potentials for molecular calculations. Potentials for main group elements Na to Bi. *J. Chem. Phys.* 82, 284–298. doi:10.1063/1.448800
- Wang, H., Leonard, S.L., Hu, Y.H., 2012. Promoting Effect of Graphene on Dye-Sensitized Solar Cells. *Ind. Eng. Chem. Res.* 51, 10613–10620. doi:10.1021/ie300563h
- Wang, Q., Moser, J.-E., Grätzel, M., 2005. Electrochemical Impedance Spectroscopic Analysis of Dye-Sensitized Solar Cells. *J. Phys. Chem. B* 109, 14945–14953. doi:10.1021/jp052768h
- Wu, Z.-S., Ren, W., Gao, L., Zhao, J., Chen, Z., Liu, B., Tang, D., Yu, B., Jiang, C., Cheng, H.-M., 2009. Synthesis of Graphene Sheets with High Electrical Conductivity and Good Thermal Stability by Hydrogen Arc Discharge Exfoliation. *ACS Nano* 3, 411–417. doi:10.1021/nn900020u
- Xiang, Q., Yu, J., Jaroniec, M., 2011. Enhanced photocatalytic H₂-production activity of graphene-modified titania nanosheets. *Nanoscale* 3, 3670–3678. doi:10.1039/C1NR10610D
- Yang, N., Zhai, J., Wang, D., Chen, Y., Jiang, L., 2010. Two-Dimensional Graphene Bridges Enhanced Photoinduced Charge Transport in Dye-Sensitized Solar Cells. *ACS Nano* 4, 887–894. doi:10.1021/nn901660v
- Yella, A., Lee, H.-W., Tsao, H.N., Yi, C., Chandiran, A.K., Nazeeruddin, M.K., Diao, E.W.-G., Yeh, C.-Y., Zakeeruddin, S.M., Grätzel, M., 2011. Porphyrin-Sensitized Solar Cells with Cobalt (II/III)-Based Redox Electrolyte Exceed 12 Percent Efficiency. *Science* 334, 629–634. doi:10.1126/science.1209688
- Yoo, E., Kim, J., Hosono, E., Zhou, H., Kudo, T., Honma, I., 2008. Large Reversible Li Storage of Graphene Nanosheet Families for Use in Rechargeable Lithium Ion Batteries. *Nano Lett.* 8, 2277–2282. doi:10.1021/nl800957b
- Zhang, H., Babichev, A.V., Jacopin, G., Lavenus, P., Julien, F.H., Egorov, A.Y., Zhang, J., Pauporté, T., Tchernycheva, M., 2013. Characterization and modeling of a ZnO nanowire ultraviolet photodetector with graphene transparent contact. *J. Appl. Phys.* 114, 234505. doi:10.1063/1.4854455

Chapter VI

ZnO Nanorod Based Electron Transport Layer for DSSC

VI. 1. Introduction

ZnO has been studied as an alternative to TiO₂ photoelectrode in DSSC applications. In the section II.1.1, page 24, the main differences between TiO₂ and ZnO have been presented as well as the important properties of ZnO that make it a good candidate to replace TiO₂. The higher electron mobility in ZnO compared to that in TiO₂ and the ease of its crystallization and anisotropic growth are the strong reason that make ZnO still can compete with TiO₂ (Ko et al., 2011). Moreover, many reports show cell performance improvement due to photoelectrode-oxide structure strategy (Gao et al., 2014; Ko et al., 2011; Lai et al., 2010; Lu et al., 2014; Pan et al., 2009; Suh et al., 2007; Wang et al., 2010; Xu et al., 2010; Zhang et al., 2008, 2007; Zhao et al., 2013).

One-dimensional-like structures (Figure 6.1), such as nanowires (NW), nanorods (NR), nanotubes (NT) or nanobelts (NB) can facilitate the electron transfer (Gao et al., 2014; Lu et al., 2014; Martinson et al., 2007; Xu et al., 2010). This structure accommodates direct conduction pathway for a rapid electrons collection. Moreover, they have lower trap density that induces a faster electron transport. Electron diffusion coefficient in ZnO NW is reported about 0.05-0.5 cm²s⁻¹, which is much larger than in nanoparticle ZnO layers under DSSC operation condition (10⁻⁵-10⁻³ cm²s⁻¹) (Magne et al., 2013; Zhang et al., 2009). The limited performance of ZnO nanowires is due to their insufficient surface area that provokes low dye adsorption. The other one-dimensional-like structures such as NT or NR can become an alternative. Different from NW, these structures have cavity and pores that provide a larger surface area for dye adsorption. Xi et.al have compared the cell performance of ZnO-NT and ZnO-NW. They prepared ZnO NT using hydrothermal reaction and they observed there is significant improvement in short circuit current (J_{sc}), that increase from 0.12 mA.cm⁻² (ZnO-NW) to 0.41 mA.cm⁻² (ZnO-NT). The J_{sc} improvement was clearly due to the increase in surface area that provided more sites for dye adsorption (Xi et al., 2012).

The limitation of ZnO-NW has motivated building of hierarchical structure made of branched NW or combining two or more structures. Suh et. al. have prepared branched ZnO-NW (Figure 6.2.a) by two-step seeding with zinc acetate dehydrate nanoparticles. They observed a 35% efficiency improvement on cell performance of branched-ZnO-NW (PCE =

0.46% with $J_{sc} = 1.84 \text{ mA.cm}^{-2}$) compared to the pillar one (PCE = 0.34% with $J_{sc} = 1.26 \text{ mA.cm}^{-2}$) (Suh et al., 2007). ZnO nanoforest with more branched structure (Figure 6.2.b) was prepared by Ko et. al showed much improvement compared to the pillar one, the power conversion efficiency was greatly improved from 0.45% to 2.63% that is accompanied by an increase in J_{sc} from 1.52 mA.cm^{-2} to 8.78 mA.cm^{-2} (Ko et al., 2011).

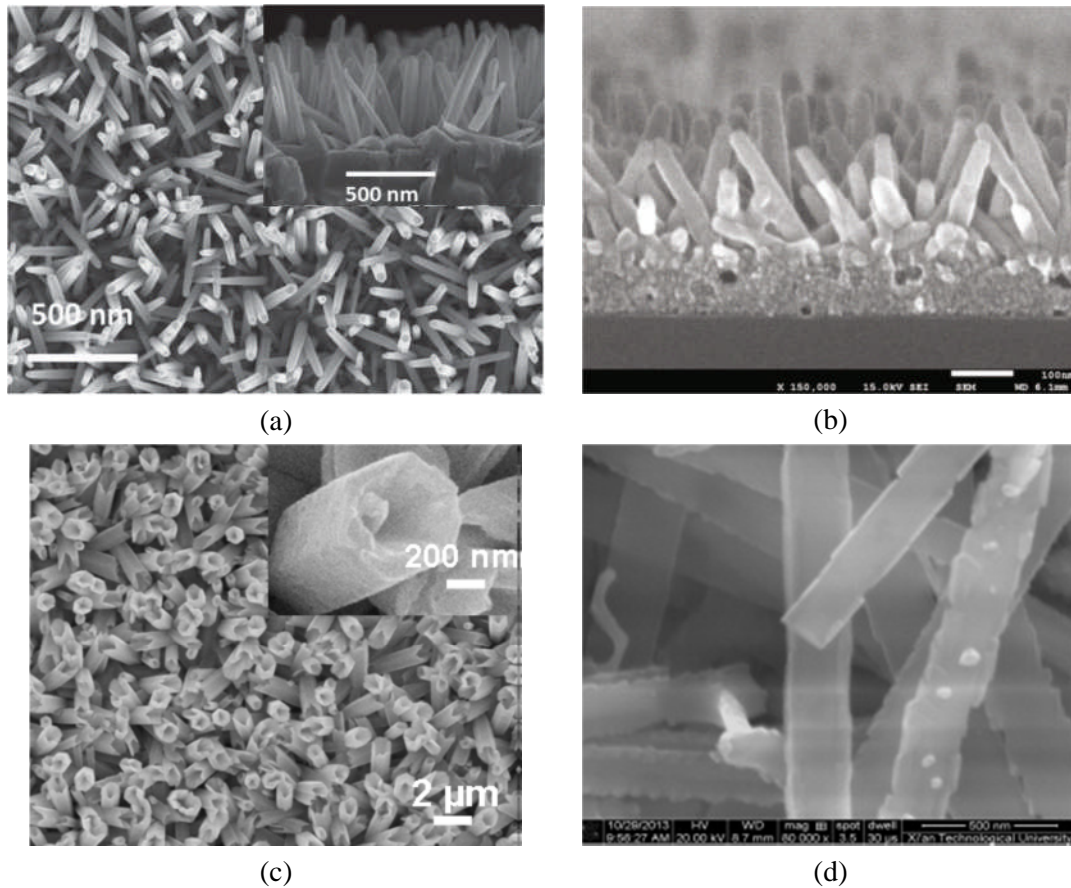


Figure 6.1: Various one-dimensional structures of ZnO (a) Nanowires (Zhang et al., 2014) (b) Nanorods (Lee et al., 2011) (c) Nanotubes (Han et al., 2010) (d) Nanobelts (Yu et al., 2015)

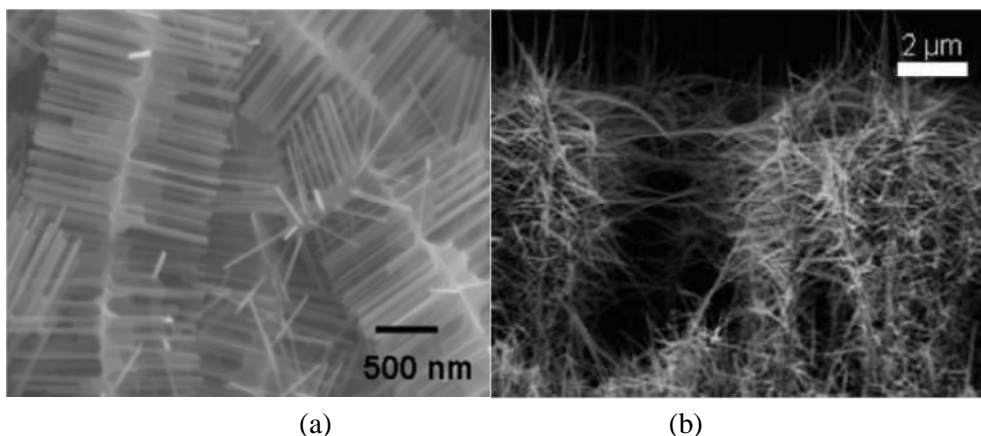


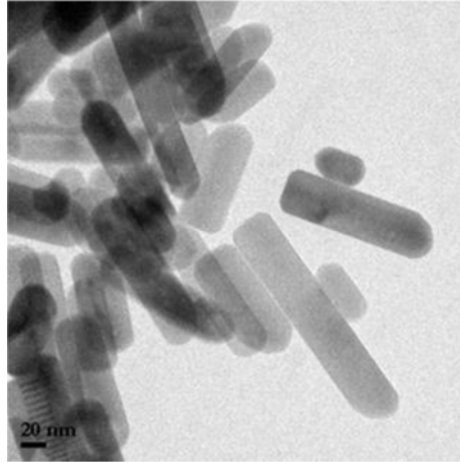
Figure 6.2: Structure of (a) branched-ZnO-NW(Suh et al., 2007) and (b) ZnO nano-forest (Ko et al., 2011)

We have studied the utilization of nanorod-like nanoparticles as building blocks for the preparation of porous photoelectrode for DSSC. ZnO_NR powders have been prepared by the hydrolysis in polyol medium technique in collaboration with *Laboratoire des Sciences des Procédés et des Matériaux*, LSPM UPR 3407, Université Paris 13, Villetaneuse, France.

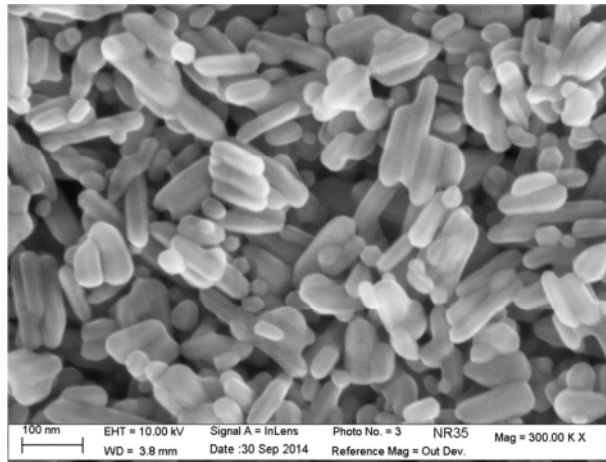
The first study was conducted using iodine as redox-couple with D149 (as organic dye-model) and TG6 (as inorganic dye-model) sensitizers (The molecular structures are shown in Figure 6.17.c, page 140 and 6.18.c, page 141). This study showed that these particles are promising to use as photoelectrode in cobalt-based DSSC due to their large pores that facilitate good diffusion of cobalt redox-shuttle in photoelectrode. Then, we studied cobalt-complex as redox couple combined with carbazole derivative dyes provided by the Université de Bordeaux, Institut des Sciences moléculaires, France as sensitizers.

VI. 2. Particle Characterization ZnO_NR

ZnO_NR particles have been characterized by: XRD characterization, SEM and TEM. Figure 6.3 shows the TEM images of the ZNO_NR particles and SEM images of the ZnO_NR layer with their clear rod-like structure. The particles size distribution shows that they have 110 nm mean length and 35 nm mean diameter (Figure 6.4). XRD pattern of the ZNO_NR layer after heat treatment is presented in Figure 6.5. It has the similar pattern with the standard JCPDS card No. 01-078-3326.



(a)



(b)

Figure 6.3: (a) TEM image of ZnO_NR nanoparticles and (b) SEM image of ZnO_NR layer

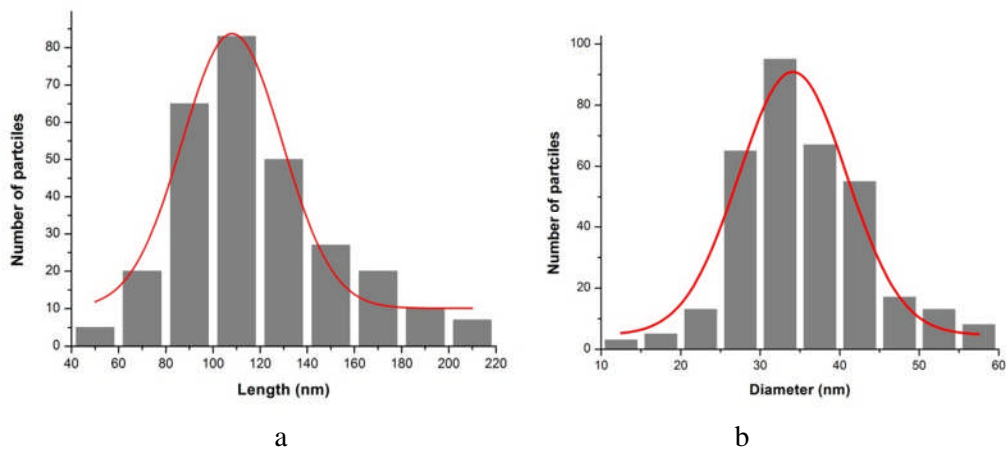


Figure 6.4: Particles size distirbution of ZnO_NR that is obtained from TEM images result analysis, (a) particles length (b) partciles diameter. The red-line is gaussian function fitting.

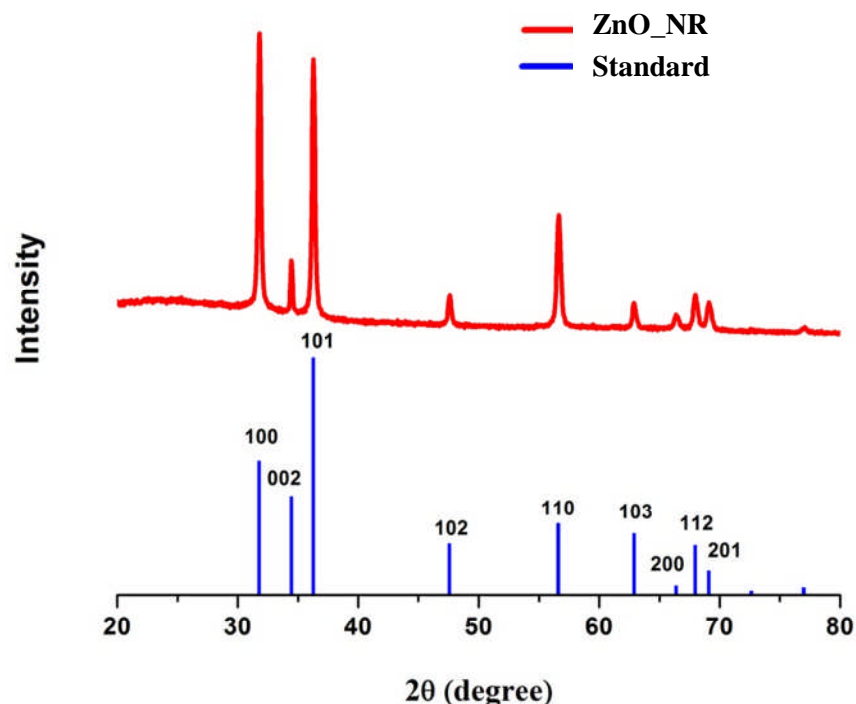


Figure 6.5: XRD pattern of ZnO_NR layer after heat treatment

VI. 3. Utilization ZnO_NR for the comparison of the performance of an organic and an inorganic sensitizer

In this study we compare the performance of ZnO_NR using two different types of sensitizer. The D149 indoline sensitizer was chosen as an organic sensitizer and TG6 as a ruthenium organometallic sensitizer. D149 has been proven to be a good sensitizer when coupled with ZnO photoelectrode, the efficiency can reach 3.5 – 4.74 %. It is good value compared to that of N719 sensitizer which reaches 2.1 – 3.2% in ZnO DSSC (Magne et al., 2013) Whereas, TG6 has higher molar extinction coefficient molar compared to the commonly used N719 ruthenium. When coupled with TiO₂, TG6 has proven more efficient compared to N719 (Matar et al., 2008), For those reasons we investigated ZnO_NR sensitized by D149 and TG6 for DSSC.

I-V measurement results are shown in Figure 6.6. Table 6.1 shows the dye molar extinction coefficient and *I-V* parameters. *I-V* measurement results show that employing TG6 gives rise to a higher power conversion efficiency compared to D149. Absorption spectra of D149 and TG6 sensitized layer of ZnO_NR are presented in Figure 6.7. It shows that TG6-sensitized-layer of ZnO_NR has a boarder spectrum compared to D149. This fact explains the

higher J_{sc} of TG6-cell compared to D149. The IS measurement results of TG6-and D149-sensitized ZnO_NR cells are presented and analyzed in the next section. Whereas, to gain insight into the nature of the dyes that make they lead to different cell performances, we computationally investigated the optical transition in D149 and TG6. The result will be described in the section IV.5.

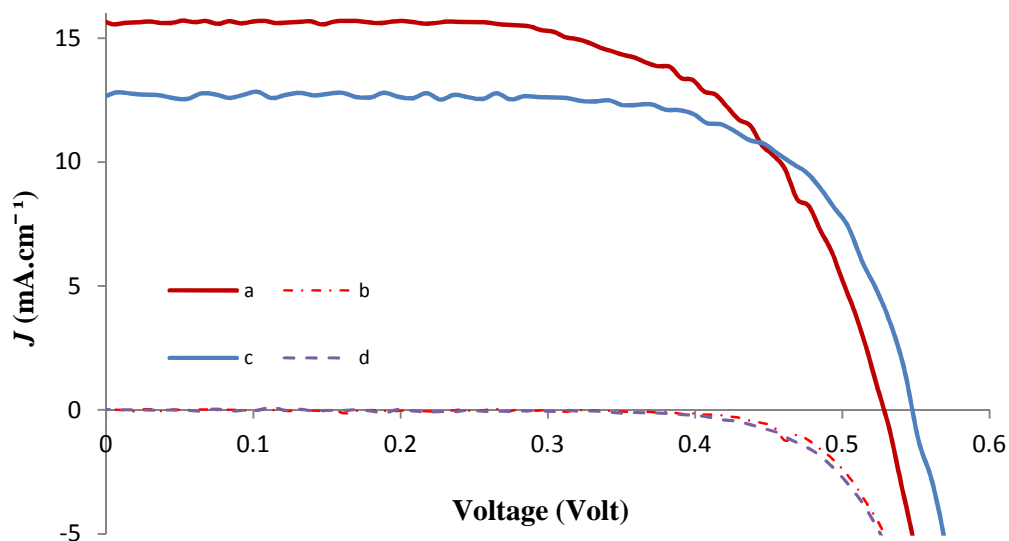


Figure 6.6: I - V curves of ZnO_NR sensitized with (a) TG6 and (b) D149. The dashed line is the dark current.

Table 6.1 Dye molar extinction coefficient and I - V curve characteristic under 100 mW.cm^{-2} , AM 1.5 G filtered illumination

Dye	ϵ ($\text{mol}^{-1}.\text{L.cm}^{-1}$) ^a	Film Thickness (μm)	Voc (Volt)	J_{sc} (mA.cm^{-2})	FF (%)	η (%)
D149	72.350 (530nm)	19.4	0.548	12.68	69.3	4.82
TG6	22.450 (550 nm)	16.6	0.532	15.70	64.2	5.30

^a Dye molar extinction coefficient measured in DMF for D149; and in CH_2Cl_2 for TG6.

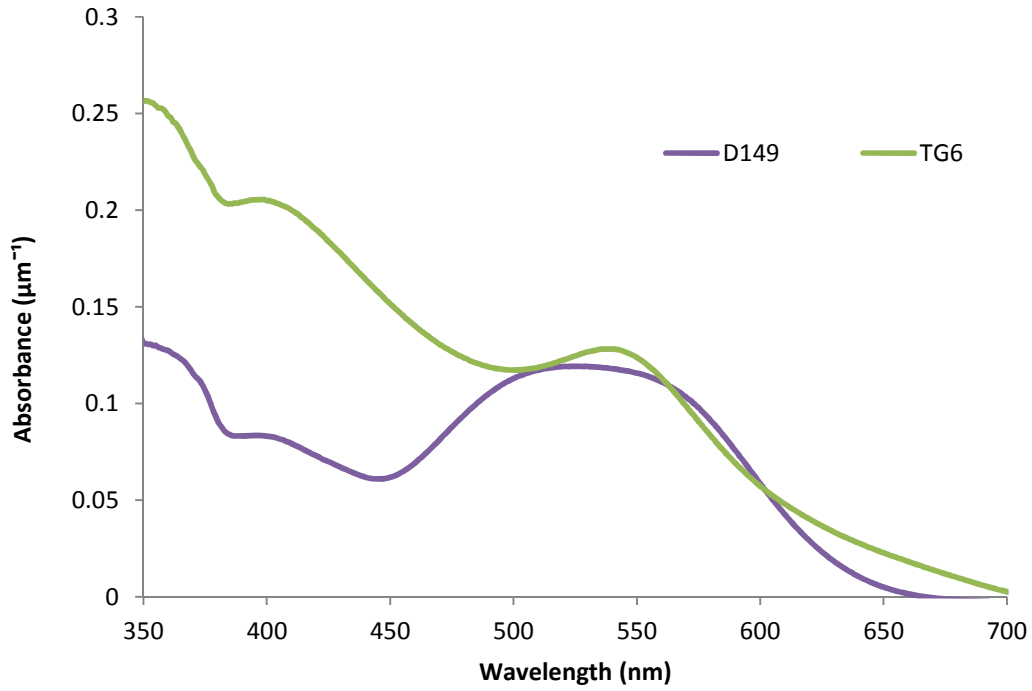


Figure 6.7: Absorbance spectra of (a) D149 and (b) TG6 sensitized layer of ZnO_NR

IV. 4. Impedance Study D149- and TG6-sensitized ZnO_NR cell

The impedance study of D149- and TG6-sensitized ZnO_NR (ZnO_NR_D149 and ZnO_NR_TG6) solar cell has been carried out and will be discussed in this section. The typical of IS spectra measured in the dark is shown in Figure 6.8. This figure shows that the IS spectra of ZnO_NR_TG6 cell did not exhibit a clear Warburg loop at low frequency, even at a high applied voltage. Logarithmic plot of C_μ and R_{ct} of ZnO_NR_D149 and ZnO_NR_TG6 are shown in Figure 6.9 and 6.10 as function of V_{corr} .

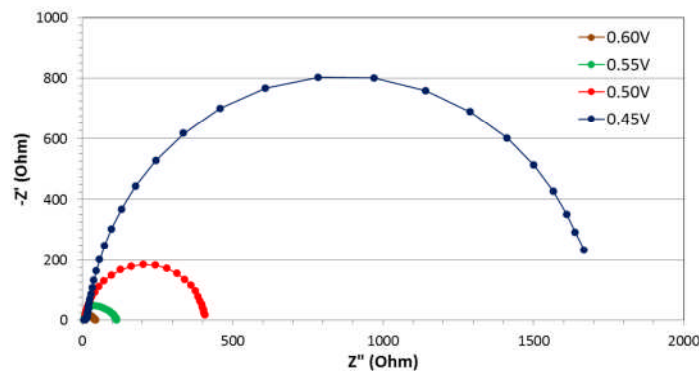


Figure 6.8: Typical IS spectra measured in the dark of ZnO_NR_TG6 cell at various applied potential

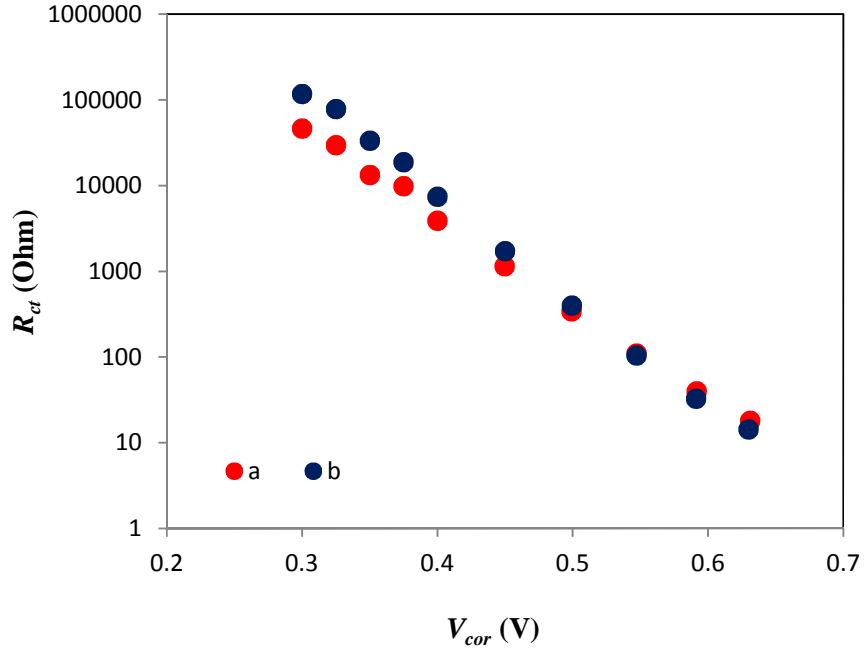


Figure 6.9: Variation of R_{ct} of (a) ZnO_NR_D149 and (b) ZnO_NR_TG6 with V_{cor}

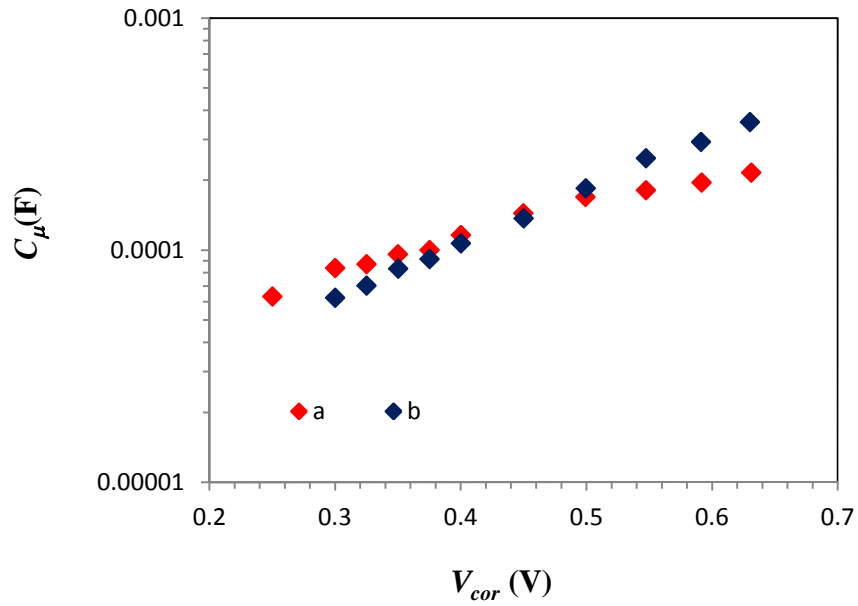


Figure 6.10: Variation of C_{μ} of (a) ZnO_NR_D149 and (b) ZnO_NR_TG6 with V_{cor}

The curve slope of C_{μ} logarithmic plot vs V_{cor} and R_{CT} logarithmic plot vs V_{cor} represent α and β , respectively as written in the equation 2.10 and 2.15 (Chapter II, section II. 1. 3, page 39). The α value of ZnO_NR_D149 and ZnO_NR_TG6 is 0.103 and 0.118 and

β respectively. The α values are slightly lower than the TiO_2 cell (0.18-0.23) and show deeper states in the case of ZnO. The β value of ZnO_NR_D149 and ZnO_NR_TG6 is 0.613 and 0.670, respectively. β lower than 1 is an empirical way to describe sublinear recombination kinetics that takes into account that electrons may be transferred from occupied levels located in the energy gap (Bisquert and Mora-Seró, 2010; Villanueva-Cab et al., 2010)

The electron lifetime, τ_n and the transport time, τ_{tr} have been calculated using the equations 2.16 and 2.17 (Chapter II, section II. 1. 3, page 40), respectively. The results are shown in Figure 6.11 as a function of g (trapped electron concentration). The values of τ_n for both cells are more than one order of magnitude higher than τ_{tr} , a difference that ensures a rather good charge collection at the FTO front contact.

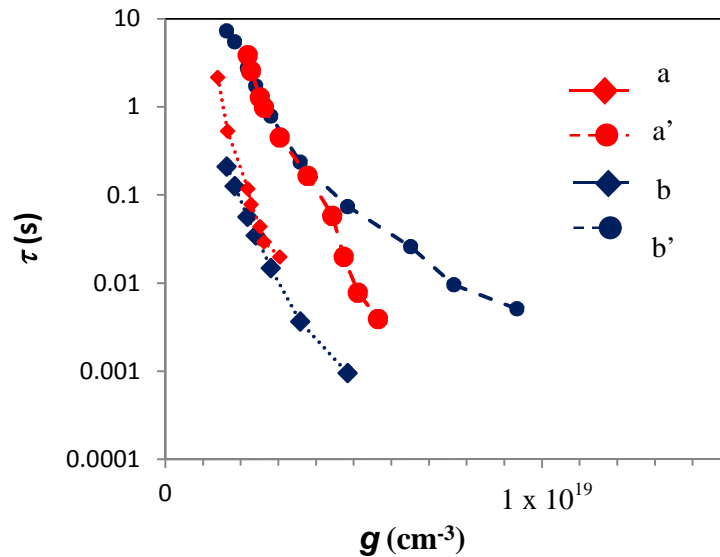


Figure 6.11: The logarithmic plots of τ_{tr} of (a) ZnO_NR_D149 and (b) ZnO_NR_TG6 the plot of τ_n of (a') ZnO_NR_D149 and (b') ZnO_NR_TG6 as a function of g

Both cells have a very high charge collection efficiency (η_{coll}) with values higher than 96% as shown in Figure 6.12. This is the highest value in ZnO-based cell that have been developed in our laboratory at Chimie-Paristech (Hosni, 2014; Magne et al., 2013; Pauporté and Magne, 2014).

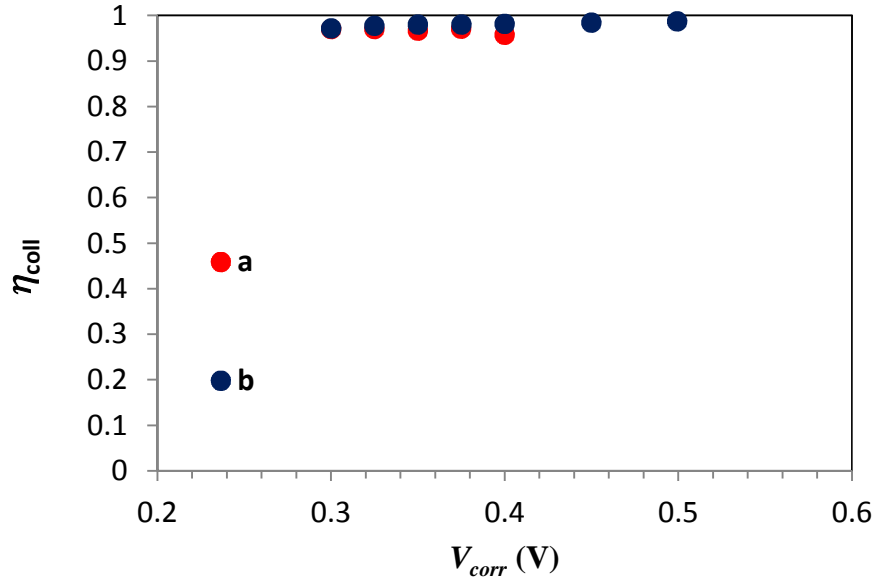


Figure 6.12: The variation of charge collection efficiency (η_{coll}) of (a) ZnO_D149 and (b) ZnO_TG6 with V_{corr}

The conductivity of the ZnO porous layer (σ) is plotted as a function of g in Figure 6.13. Those values are in the range of the reported conductivity values of ZnO nano-particles (Hosni, 2014; Magne et al., 2013; Pauporté and Magne, 2014). The same curve shape is also founded that shows σ increases rapidly with g due to the trap filling. The conductivity of ZnO is higher compare to that of anatase, brookite (see also Figure 4.15) or TiO₂/graphene composite (see also Figure 5.22).

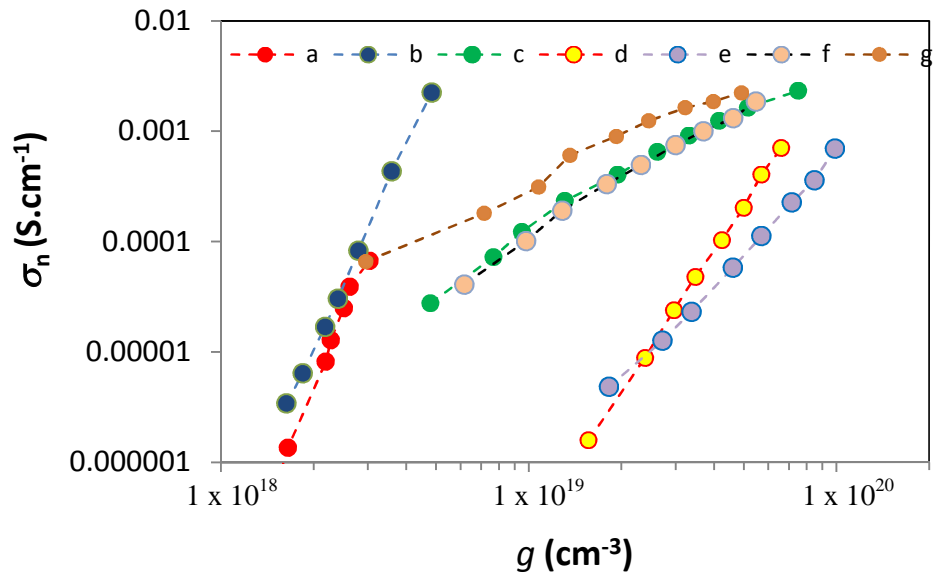


Figure 6.13: The variation of σ with g of (a) ZnO_NR_D149 (b) ZnO_NR_TG6 (c) TiO₂_D (d) TiO₂_B1 (e) TiO₂_B2 (f) TiO₂_A (g) TiO₂_Gr12

Two diffusion parameters of electron transport, namely the electron diffusion coefficient (D_n) and the electron diffusion length (L_n) were calculated using equation 2.20 and 2.21 (Chapter II, section II. I. 3, page 40). These results are gathered in Figure 6.14 and 6.15. They show that electron transport faster in ZnO compare to that in anatase-TiO₂ (example: TiO₂_A)

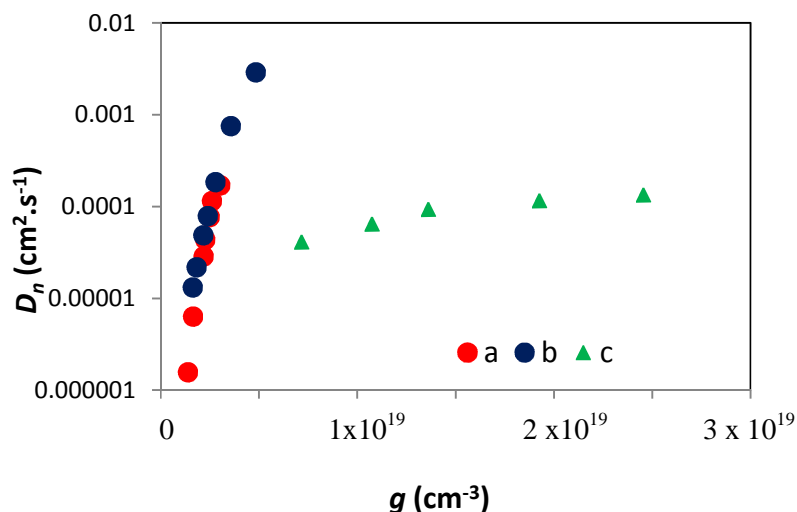


Figure 6.14: Variation of D_n with g of (a) ZnO_NR_D149, (b) ZnO_NR_TG6 and (c) TiO₂_A

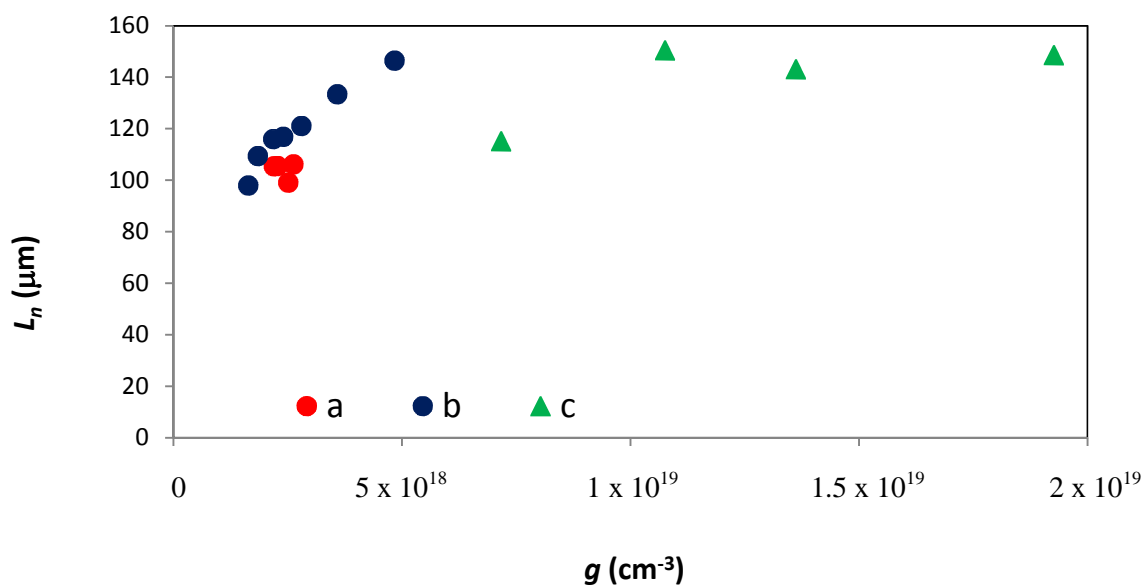


Figure 6.15: Variation of L_n with g of (a) ZnO_NR_D149, (b) ZnO_NR_TG6 and (c) TiO₂_A

IV. 5. Computational investigation of the electronic and optical properties in D149 and TG6 dyes

The calculations were carried out using the Gaussian 09 program package (Frisch et al., 2009) with B3LYP exchange-correlation functional (Becke, 1993a, 1993b; Lee et al., 1988). The dye geometries were optimized using the 6-311G* basis set for C, H, O, N and S atoms (Krishnan et al., 1980; McLean and Chandler, 1980) together with the Los Alamos effective core potential LanL2DZ for Ruthenium (Hay and Wadt, 1985; Wadt and Hay, 1985). Solvation effects were evaluated by the conductor-like polarizable continuum model (C-PCM), (Cossi et al., 2003; Cossi and Barone, 2001) using Dimethylformamide (DMF) as a solvent for D149 and Dichloromethane (CH_2Cl_2) for TG6. The single point TD-DFT calculation (Runge and Gross, 1984) was then carried out to the optimized structure to gain insight into the electronic properties and detailed excited states behavior that contribute to the UV/VIS spectra.

The UV/VIS-absorption spectra of both dyes that resulted from TD-DFT calculations are presented in Figure 6.16 and the calculated electronic transitions with their oscillator strengths are gathered in the Table 6.2 They are in agreement with the experimental measurements performed in the same solvent and also reported in the Figure 6.16.

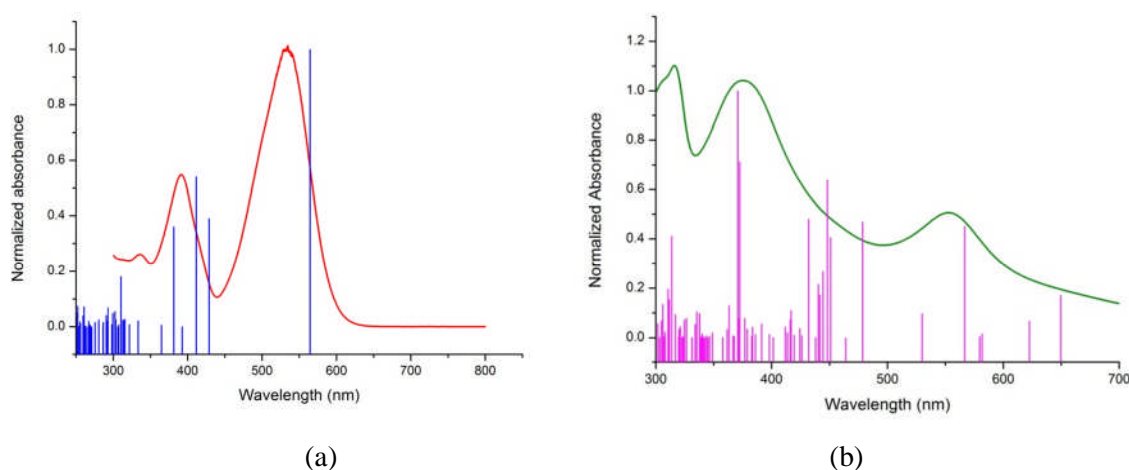


Figure 6.16: UV-Vis spectra of (a) D149 in DMF (Red: experimental; blue: computational) and (b) TG6 in CH_2Cl_2 (Green: experimental, purple: computational)

TD-DFT calculation of D149 dye shows a 30 nm red-shift on UV/VIS-absorption spectrum compared to the experimental one. The maximum wavelength at about 530 nm is

the result of the HOMO to LUMO electron transition. Figure 6.17 shows that the HOMO of D149 is located on the main chain of the molecule (indoline moiety), whereas the LUMO is mainly located on the rhodanine moiety. The separation in the HOMO and LUMO positions indicate that the transition has an ICT (Intra-molecular Charge Transfer) character (Ham and Kim, 2010). This result is in line with the previous one which investigated the electronic structure of the D149 dye (Le Bahers et al., 2009; Kim et al., 2011). The calculation for the TG6 dye informs us that absorption at 566.54 nm results from the electron transition between the HOMO-2 and the LUMO orbitals. Further computational investigation found out that HOMO-2 orbital is composed dominantly by d orbital on ruthenium atom, which indicate that this electronic transition is a metal-to-ligand charge transfer (MLCT) transition (Table 6.2 and Figure 6.18).

Table 6.2. Calculated TD-DFT spectra of TG6 and D149 above 350 nm with oscillator strength, $f > 0.2$

Wavelength, λ (nm)	Oscillator strength, f	Mayor contributions	Percentages of mayor contribution
TG6			
566.54	0.2585	HOMO-2 \rightarrow LUMO	42%
478.41	0.2681	HOMO \rightarrow LUMO+2	89%
450.89	0.2323	HOMO-1 \rightarrow LUMO+2	51%
448.11	0.3656	HOMO \rightarrow LUMO+3	34%
431.91	0.2749	HOMO-5 \rightarrow LUMO	53%
372.50	0.4082	HOMO-5 \rightarrow LUMO+2	84%
370.7	0.5729	HOMO-4 \rightarrow LUMO+2	78%
D149			
564.54	1.0766	HOMO \rightarrow LUMO	98%
428.87	0.4214	HOMO-1 \rightarrow LUMO	74%
411.47	0.5847	HOMO \rightarrow LUMO+1	71%
381.41	0.3892	HOMO-2 \rightarrow LUMO	55%

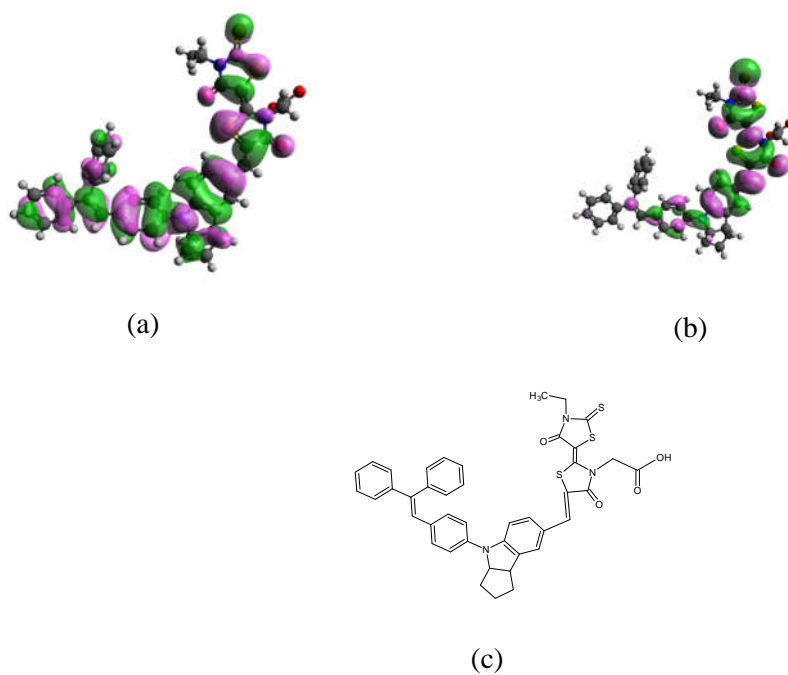


Figure 6.17: (a) HOMO and (b) LUMO orbitals of D149 dye. (c) Molecular structure of D149 dye (positive = green; negative = purple, isovalue = 0.001)

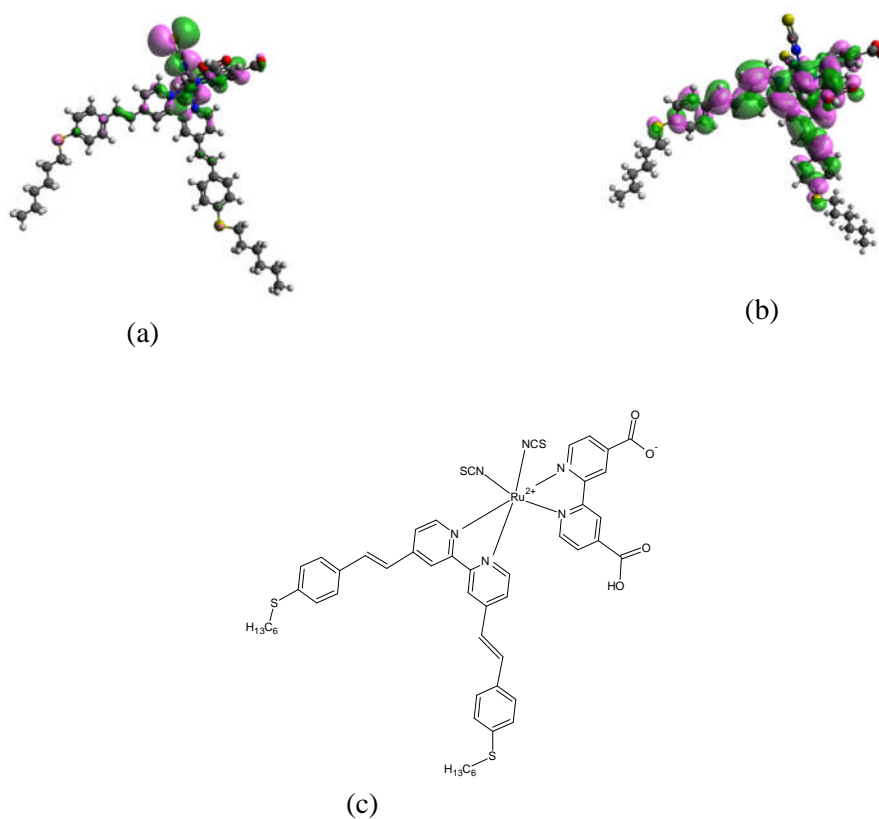


Figure 6.18: (a) HOMO and (b) LUMO orbitals of TG6 dye. (c) Molecular structure of TG6 dye (positive = green; negative = purple, isovalue = 0.001)

The calculated molecular orbital energy levels for both dyes are involved in the main electronic transitions, with the energy level of conduction band (CB) and the valence band (VB) of ZnO together with also the energy position of I^-/I_3^- are presented in Figure 6.19. The energy levels of ZnO were extracted from Ref. (Lee et al., 2011). Figure 6.19 informs us that the position of the LUMO energy of both dyes meet the criteria for an efficient charge injection to the ZnO conduction band. It requires the position of LUMO to be above the semiconductor conduction band. Similarly, for the dye regeneration, the position of the HOMO energy level must be below the electrolyte potential redox. These positions guaranty a sufficient driving force for electrons to flow.

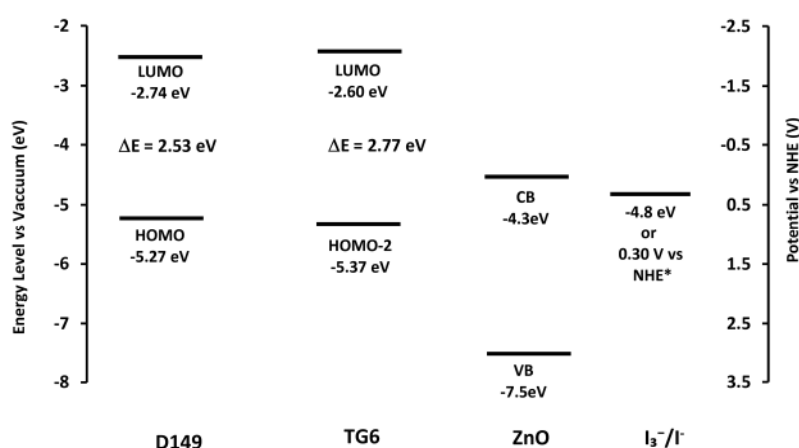


Figure 6.19: Energy diagram of the D149 and TG6 dye orbitals, active in the charge transfer, conduction band (CB) and valence band (VB) of ZnO and I_3^-/I^- redox couple. (*) Calculated with redox concentration in the cell.

Our computational analysis outlines two important differences between the electronic properties of D149 and TG6 dyes. Firstly, from the absorbance spectra, we can see that there are more electronic transitions in TG6 in the UV/Vis range compared to that in D149, which make the TG6 spectrum broader compare to that of D149. Secondly, Figure 6.20 shows us that in TG6 the LUMO orbital is localized closer to the carboxylate anchoring site compared to that of D149, which indicate that the electron will transfer easily from the LUMO to the conduction band of ZnO.

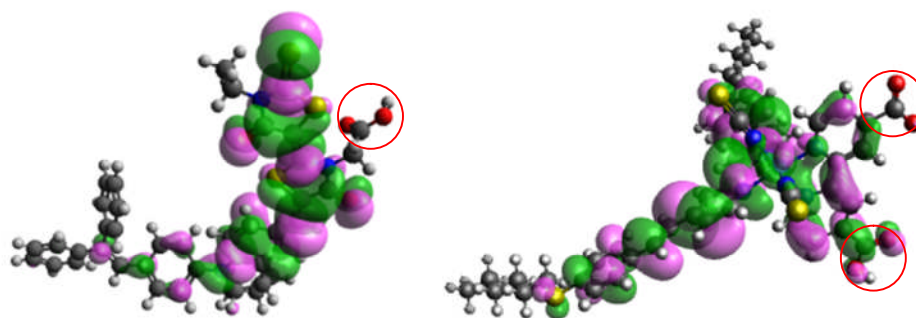


Figure 6.20 Position of anchoring site (carboxylate function) on the dye (show with red circle) in D149 (Left) and TG6 (right)

VI. 6. Use of photoelectrode ZnO_NR for iodine free DSSC

In this section, we investigate three kinds of cells based on sensitizers synthesized by the Université de Bordeaux, Institut des Sciences moléculaires, France: the SD4-cell (use of SD4 as sensitizer), JM131-cell (use of JM131 as sensitizer) and JM164-cell (use of JM164 as sensitizer). They are carbazole dyes that have similarity in structure. The difference lays on the alkyl chain as shown in Figure 6.21. JM131 has two hexyl chains attached on the fluorene ring located in the middle of molecule. JM164 has two hexyl chains the same as JM131 and also has two hexyl chains which are located in the edge of molecule on the opposite side of carboxylate. Endowed with alkyl chains, JM131 and JM164 are good candidates to use as the sensitizer in the cobalt-based DSSC.

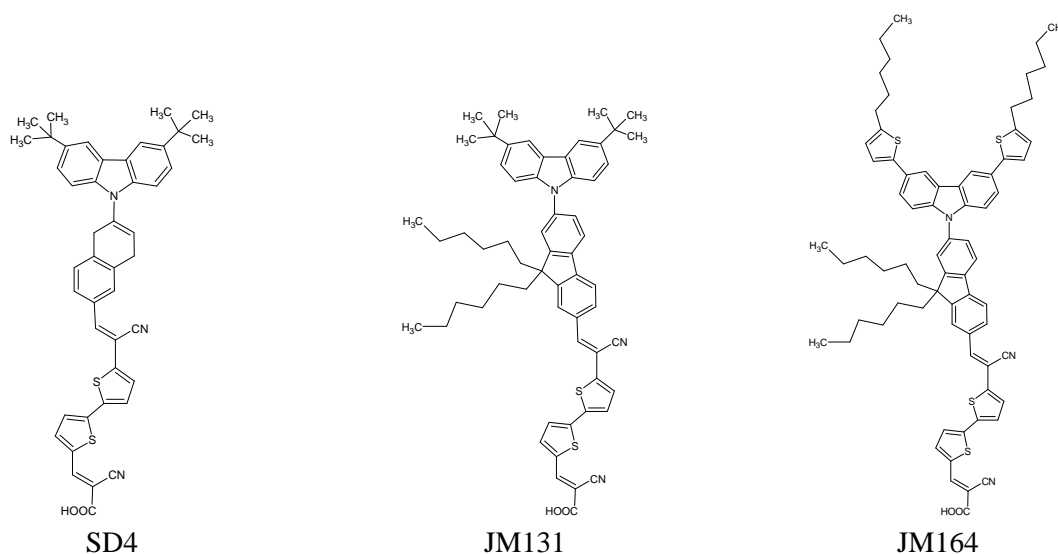


Figure 6.21: Structure of SD4, JM131 and JM164

Before employing ZnO_NR photoelectrode with the three sensitizer and cobalt-based redox couple, we have carried out some optimizations.

First of all, we studied the cell performance using a iodine electrolyte (I₂-2); the photoelectrode thickness was about 10 µm. The results are gathered in Table 6.3 We found that the **SD4-cell was the best cell in iodine-based DSSC**.

Table 6.3 IV characteristics using iodine redox-couple (I₂-2)

Dye Sensitizer	Photoelectrode Thickness (µm)	Cell Measurement			
		V_{oc} (V)	J_{sc} (mA.cm ⁻²)	FF (%)	PCE (%)
SD4	10.9	0.51	6.69	61.5	2.11
JM131	10.3	0.52	4.21	63.7	1.40
JM164	9.8	0.52	5.21	68.6	1.83

I₂-2 electrolyte composition (Chapter III, section III. 2, page 66), ZnO_NR photoanode. The measurement were done 1 hour after cell preparation

In a next step, we tried the SD4-cell, which show the best performances in iodine system, using various cobalt redox-coupled (the preparation of [Co(bpy)₃]²⁺ and [Co(phen)₃]²⁺ are explained in Appendix G. [Co(bpy-pz)₂]²⁺ was obtained from the Université de Bordeaux, Institut des Sciences moléculaires, France) and found **that [Co(bpy-pz)₂]^{2+/3+} showed the best performance**, unfortunately the cell deteriorated after 1 hour. The *I*-*V* measurement of the cell is shown in Table 6.4

Table 6.4 shows that the V_{OC} increases from [Co(bpy)₃]^{2+/3+}; [Co(phen)₃]^{2+/3+} to [Co(bpy-pz)₂]^{2+/3+}. This phenomenon can be explained by the position of their redox potential. The standard redox potential of [Co(bpy)₃]^{2+/3+}; [Co(phen)₃]^{2+/3+} and [Co(bpy-pz)₂]^{2+/3+} vs NHE are 0.56; 0.62 and 0.86 V respectively (Figure 6.22). This value make the different of redox potential and quasi Fermi of ZnO_NR, which is equal to the V_{oc} , is in order as written in Table 6.4.

Table 6.4 I-V characteristics of SD4 using various cobalt redox-couples

Cobalt complex	Cell Measurement					
	Thickness (μm)	Measurement time	V_{oc} (V)	J_{sc} (mA.cm^{-2})	FF (%)	PCE (%)
$[\text{Co}(\text{bpy})_3]^{2+/3+}$	9.5	Just after cell preparation	0.39	7.57	67.92	2.01
		1 hour after cell preparation	0.25	3.91	28.60	0.28
$[\text{Co}(\text{phen})_3]^{2+/3+}$	9.2	Just after cell preparation	0.34	8.33	64.12	1.83
		1 hour after cell preparation	0.33	6.61	66.63	1.47
$[\text{Co}(\text{bpy-pz})_2]^{2+/3+}$	10.5	Just after cell preparation	0.53	6.91	70.05	2.55
		1 hour after cell preparation	0.49	3.78	70.70	1.31

Co-6 electrolyte composition (Chapter III, section III. 2, page 66), ZnO_NR photoanode.

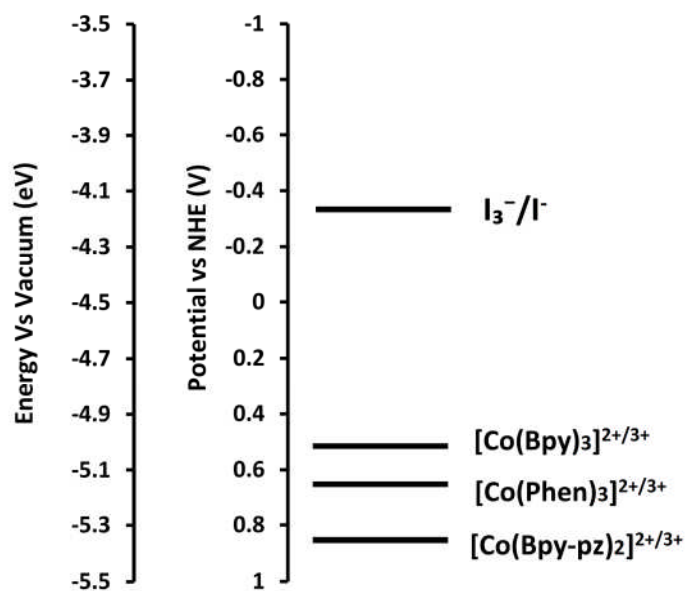


Figure 6.22: The position of E^0 of I_3^-/I^- , $[\text{Co}(\text{bpy})_3]^{2+/3+}$, $[\text{Co}(\text{phen})_3]^{2+/3+}$ and $[\text{Co}(\text{bpy-pz})_2]^{2+/3+}$ redox-couples

Then we tried the other sensitizers, JM131 and JM164 using the best cobalt redox couple, $[\text{Co}(\text{bpy-pz})_2]^{2+/3+}$. The IV characteristics are presented in Table 6.5.

Table 6.5: *I-V* characteristics of JM164- and JM131-based cell using $[\text{Co}(\text{bpy-pz})_2]^{2+/3+}$ and I_3^-/I^- redox-couples

Dye Sensitizer	Redox-couple	Cell Measurement					
		Thickness (μm)	Measurement Time	V_{oc} (V)	J_{sc} (mA.cm^{-2})	FF (%)	PCE (%)
JM131	$[\text{Co}(\text{bpy-pz})_2]^{2+/3+}$	8.9	Just after cell preparation	0.54	6.06	53.94	1.77
			1 hour after cell preparation	0.52	4.64	56.59	1.38
	I_3^-/I^-	8.6	Just after cell preparation	0.47	5.76	58.06	1.58
			1 hour after cell preparation	0.51	4.61	61.39	1.44
JM164	$[\text{Co}(\text{bpy-pz})_2]^{2+/3+}$	10.5	Just after cell preparation	0.64	5.9	68.2	2.60
			1 hour after cell preparation	0.63	6.19	69.0	2.68
	I_3^-/I^-	10.2	Just after cell preparation	0.46	6.1	65.4	1.84
			1 hour after cell preparation	0.54	5.74	68.8	2.12

Co-6 and I_2 -2 electrolyte composition (Chapter III, section III. 2, page 66), ZnO_NR photoanode.

These results show that JM164 is the best sensitizer to be used in combination with the $[\text{Co}(\text{bpy-pz})_2]^{2+/3+}$ redox-couple. It is clearly understand because among three dyes, it has the most bulky structure. It is good point for JM164 when coupled with cobalt redox-couple, as explained above it can avoid cobalt complex to get near into semiconductor surface to have unwanted electron recombination electron. We also found that the JM131- based cell did not show better performance compare to that of SD4, even it has two hexyl chains on the fluorene ring. We suggest those hexyl chains do not make JM131 more bulky compared to that of SD4.

To gain insight into another explanation in relation with the dye-properties effect to cell performance, it is needed to do computational study. We have done this, and the result will be discussed in section VI.6.

Then we continued by testing an electrolyte composition without TBP. The results of I-V measurements of cell without TBP are shown in Table 6.6. It is also completed with

iodine-based cell for the sake of comparison. It shows that the cobalt-based cell without TBP has worse performance compare to that in iodine-based cell. So TBP is needed in the cobalt-based electrolyte. It strongly suggests that TBP has a role avoid cobalt-redox couple to get near into semiconductor surface. In addition, TBP also has a role to facilitate charge transport from Co^{2+} to dye cation (Nakade et al., 2005).

Table 6.6. *I-V* measurement of JM164 cell using $[\text{Co}(\text{bpy-pz})_2]^{2+/3+}$ and I_3^-/I^- as redox couple, without the addition of TBP in electrolyte. The measurement was done just after cell preparation

Redox-couple	Cell Measurement				
	Thickness (μm)	V_{oc} (V)	J_{sc} (mA.cm^{-2})	FF (%)	PCE (%)
$[\text{Co}(\text{bpy-pz})_2]^{2+/3+}$	9.5	0.60	2.65	65.7	1.05
I_3^-/I^-	10.1	0.51	6.6	69.3	2.34

Co-7 and I₂-2 electrolyte composition (Chapter III, section III. 2, page 66). ZnO_NR photoanode.

The next parameter that we optimized was the photoelectrode thickness. We did the test for cell with a 5 μm photoelectrode thickness. The *I-V* measurement results are gathered in Table 6.7. It shows that cell which has 5 μm in photoelectrode thickness has better performance compared to that of 10 μm in photoelectrode thickness. It also shows that the J_{sc} increasing from iodine based cell to cobalt based cell is higher in the cell which has 5 μm in photoelectrode thickness compared to that of cell with a 10 μm in photoelectrode thickness. This result is in line with the statement that cobalt complex-compound easier to diffuse in thinner photoelectrode (Hamann, 2012). However, the usage of too thin photoelectrode will not good due to the lower dye loading.

Table 6.7 The *I-V* chareacteristics of cell with a 5 μm photoelectrode thickness using JM164 sensitizer

Cobalt complex	Cell Measurement					
	Thickness (μm)	Measurement time	V_{oc} (V)	J_{sc} (mA.cm^{-2})	FF (%)	PCE (%)
$[\text{Co}(\text{bpy})_3]^{2+/3+}$	5.3	Just after cell preparation	0.71	5.65	66.13	2.65
		1 hour after cell preparation	0.73	5.42	71.19	2.82
I_2^-/I^-	5.5	Just after cell preparation	0.48	5.44	63.94	1.69
		1 hour after cell preparation	0.58	4.95	64.72	1.86

Co-6 and I₂-2 electrolyte composition (Chapter III, section III. 2, page 66), ZnO_NR photoanode.

I-V curves of the best cells are presented in Figure 6.23.

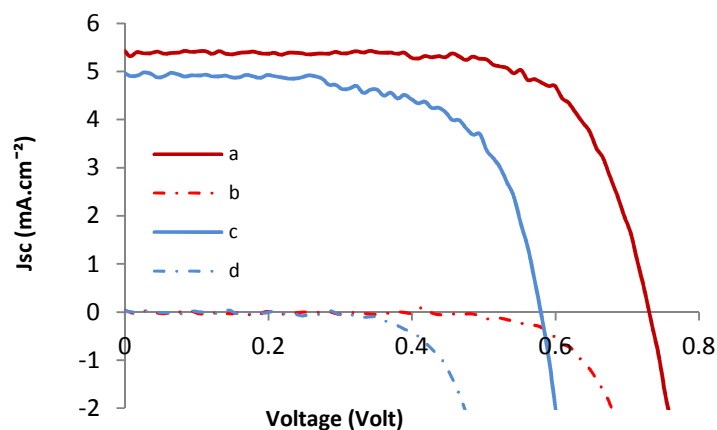


Figure 6.23: *I-V* curve of the best ZnO_NR-based cells using (a) $[\text{Co}(\text{bpy-pz})_2]^{2+/3+}$ and (b) I_3^-/I^- as redox couple; JM164 as sensitizer and has $\sim 5 \mu\text{m}$ photoelectrode thickness. The solid line show the light currents (AM 1.5G 100 mW.cm^{-2}), whereas the dashed lines show the dark currents.

The stability of the cell has been investigated and shows that all *I-V* parameters are stable after at least 2 hours. Those results are presented in Figure 6.24.

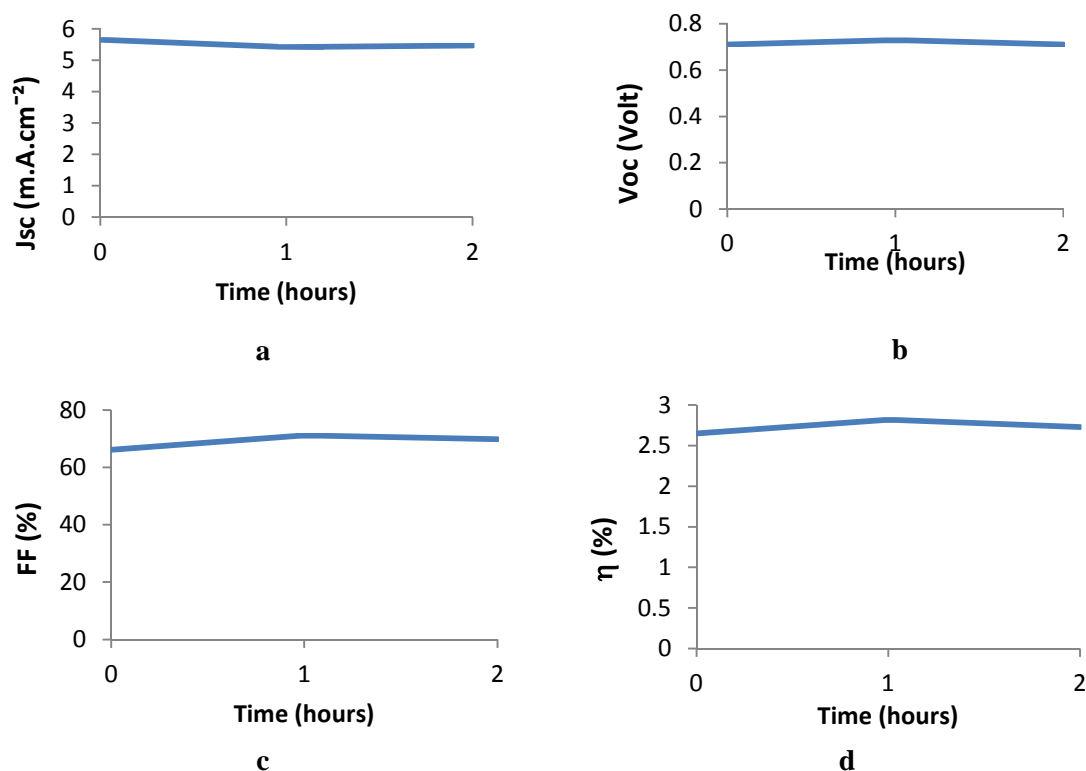


Figure 6.24 The ZnO_NR cell stability of I - V parameters (a) J_{sc} (b) V_{oc} (c) FF and (d) η . The cell use $[\text{Co}(\text{bpy-pz})_2]^{2+/3+}$ as redox-couple and JM164 as sensitizer

We have also checked that the structure of ZnO_NR has an important effect on the cobalt-based cell performances. We did the test for ZnO_C20. This photoelectrode is composed on ZnO commercial nanospherical particles which have an average diameter about 20 nm. A TEM image of these particles is shown in Figure 6.25.

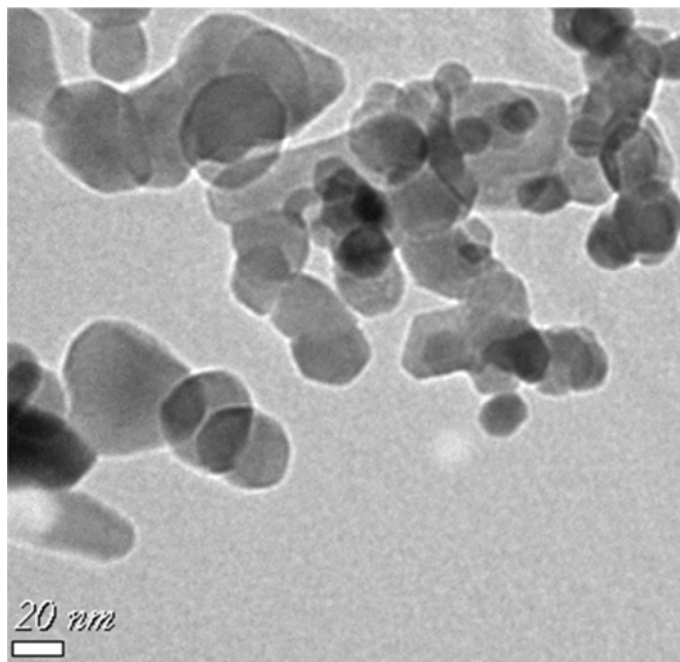


Figure 6.25: TEM Image of ZnO_C20

The I - V measurement results for ZnO_C20-based cell are shown in Table 6.8. Those clearly show that the cell performance of ZnO_C20-based cell using cobalt redox-couple is not good, especially, the V_{oc} and J_{sc} of the cell are reduced. From this result we conclude that the pores size and geometry on ZnO_NR that are well suited for the transport of the cobalt-based redox shuttle through the porous oxide layer.

Table 6.8 The I-V characteristics of JM164 sensitized ZnO_C20 based cells

Redox-couple	Cell Measurement					
	Thickness (μm)	Measurement Time	V_{oc} (V)	J_{sc} (mA.cm^{-2})	FF (%)	PCE (%)
$[\text{Co}(\text{bpy-pz})_2]^{2+/3+}$	5.9	Just after cell preparation	0.63	4.76	71.36	2.15
		1 hour after cell preparation	0.60	4.16	67.15	1.68
I_3^-/I^-	5.7	Just after cell preparation	0.47	4.81	62.75	1.41
		1 hour after cell preparation	0.59	4.36	69.79	1.79
$[\text{Co}(\text{bpy-pz})_2]^{2+/3+}$	9.8	Just after cell preparation	0.63	5.49	69.11	2.38
		1 hour after cell preparation	0.57	3.75	67.73	1.46
I_3^-/I^-	10.2	Just after cell preparation	0.49	5.91	67.11	1.96
		1 hour after cell preparation	0.58	5.12	71.26	2.12

Co-6 and I₂-2 electrolyte composition (Chapter III, section III. 2, page 66), ZnO_NR photoanode.

VI. 7. Computational investigation of the electronic and optical properties of SD4, JM131 and JM164 dyes.

The calculations were carried out using the same code as implemented in section VI.5. The dye geometries were optimized using the 6-311G** basis set for C, H, O, N and S atoms (Krishnan et al., 1980; McLean and Chandler, 1980). Solvation effects were evaluated by the conductor-like polarizable continuum model (C-PCM) (Cossi et al., 2003; Cossi and Barone, 2001) using Dichloromethane (CH_2Cl_2) as solvent. The single point TD-DFT calculation (Runge and Gross, 1984) was also carried out to the optimized structure to gain insight into the electronic properties and detailed excited states behavior that contribute to the UV/VIS spectra. Instead of carrying out the calculations using B3LYP level theory, we also did calculation using ω b97XD (Chai and Head-Gordon, 2008) and CAM-B3LYP (Yanai et al., 2004). We implemented this due to the fact that the observed dyes have long structure that

requires long-range correction for the functionals. We will compare the calculation result using these three level theories and choose the best one.

The comparison of the utilization of level theory B3LYP, ω b97XD and CAM-B3LYP in calculations is shown in Figure 6.26. Both CAM-B3LYP and ω b97XD include Coulomb part in the correlation functional. The non-Coulomb part of exchange correlation functionals typically dies off too rapidly and become inaccurate at large distances, making them unsuitable for modeling processes such as electron excitation to high orbitals (Jungsuttiwong et al., 2013; Kumar et al., 2014; Zhang et al., 2012). It is shown that the spectra calculated by CAM-B3LYP methods have the less shiftiness than the others in respect to the experimental ones. Based on this result we carried out the calculations using CAM-B3LYP level theory for the others dyes. The UV-Vis spectra of SD4, JM131 and JM164 from calculation result compared to the experimental ones are shown in Figure 6.27.

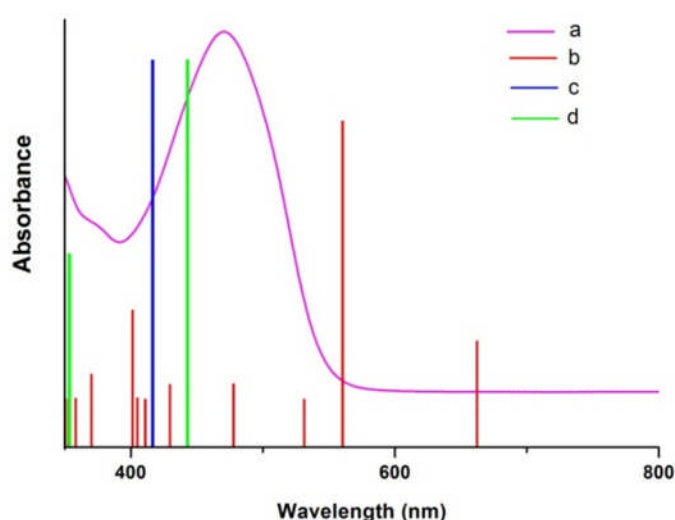


Figure 6.26: Absorbance spectra a of JM164 in UV-Vis range (a) based on experimental measurement and on calculation using TD-DFT method and level theory (b) B3LYP (c) ω b97XD and (d) CAM-B3LYP. All calculations were done using the 6-311G** basis set.

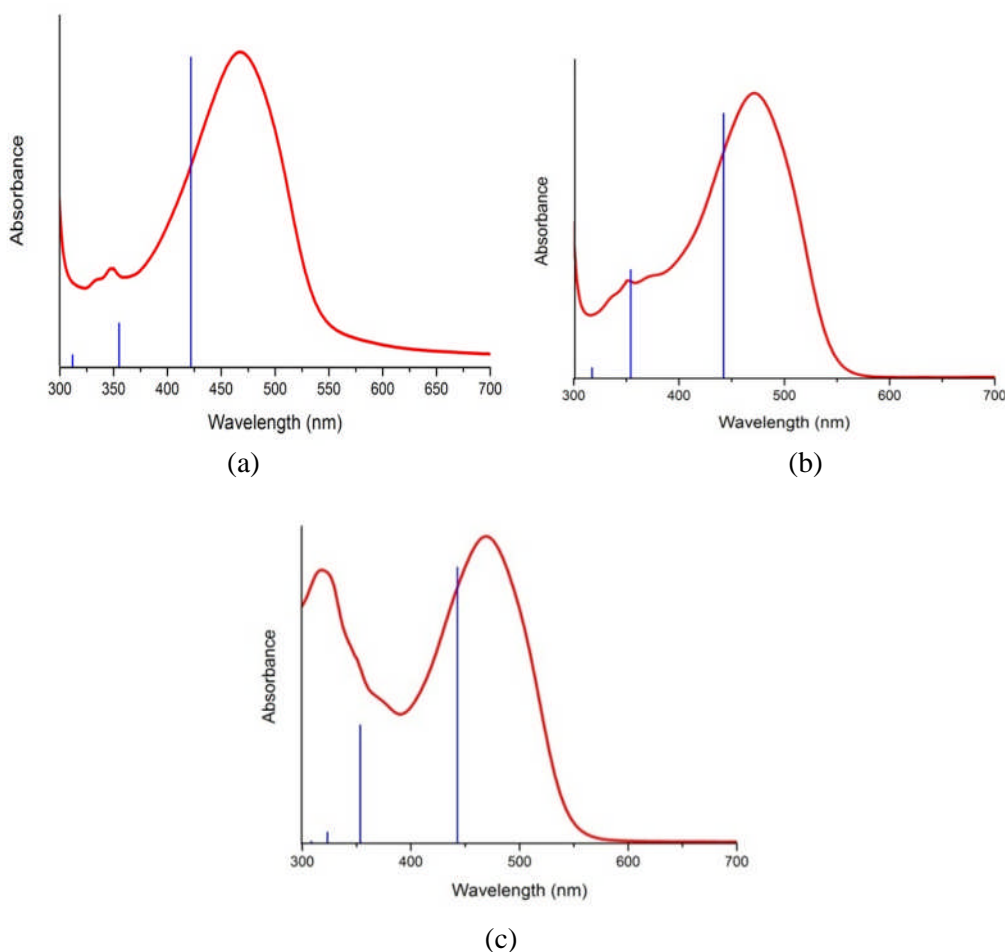


Figure 6.27: Absorbance spectra in UV-Vis range of (a) SD4 (b) JM131 (c) JM164 dyes. The red line is the experimental result and the blue one is the calculation result.

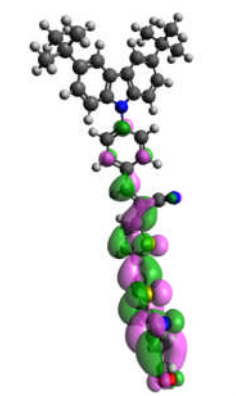
TD-DFT calculation gives the explanation about molecular orbital that involved in the electronic transition. The characters of electronic transition in the UV-Spectra are gathered in Table 6.9. It shows that for all dyes, the electronic transition is contributed majorly by H-1-to-LUMO transition. The visualization of molecular orbital (Figure 6.28) inform us that the charge separation between H-1 and LUMO orbital is not as well as that between HOMO and LUMO. Supported by the information in Table 6.9, that give the contribution of HOMO-to-LUMO transitions is getting higher from SD4, JM131 to JM164 (32% for SD4 and just 9% for JM164), we conclude that the charge separation is getting better from SD4, JM131 to JM164. Moreover, the LUMO positions of SD4 is located above the LUMO position of JM131 and JM164 that give SD4 has the slightly higher the driving force of the electron injection to the oxide surface. It explains why SD4 shows better performance in iodine-based DSSC. However, when using cobalt redox-coupled, poor performances of SD4 appeared due to the bigger chance of cobalt-redox couple to reach the semiconductor surface that provokes

recombination. As we can see in Figure 6.27, JM164 has a bulky structure. This structure can avoid cobalt redox-couple to reach the semiconductor surface then supports the inhibition of charge recombination between cobalt redox-couple and semiconductor

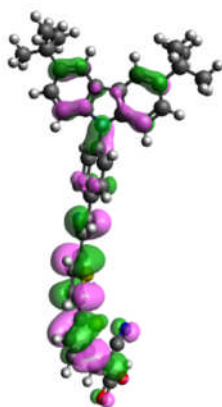
Table 6.9 Calculated TD-DFT spectra of SD4, JM131 and JM164 above 350 nm with oscillator strength, $f > 0.1$

Wavelength , λ (nm)	Oscillator strength, f	Major contributions	Percentages of mayor contribution
SD4			
421.9	1.8554	H-1 \rightarrow LUMO HOMO \rightarrow LUMO	54% 32%
355.17	0.265	HOMO \rightarrow L+1 H -1 \rightarrow LUMO	51% 21%
JM131			
422.34	1.7391	H-1 \rightarrow LUMO HOMO \rightarrow LUMO	60% 24%
354.18	0.7112	HOMO \rightarrow L+1 H-3 \rightarrow LUMO H-1 \rightarrow L+1	31% 23% 21 %
JM164			
442.86	1.7837	H-1 \rightarrow LUMO HOMO \rightarrow LUMO	75% 9%
353.41	0.7622	H-1 \rightarrow L+1 H-3 \rightarrow LUMO	36% 23%

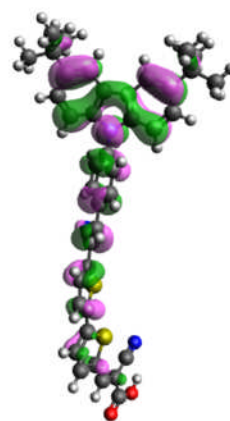
SD4
LUMO, E = -2.06 eV



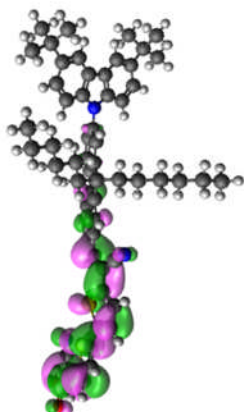
HOMO-1, E = -7.34 eV



HOMO, E = -6.83 eV



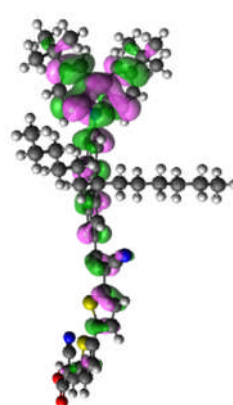
JM131
LUMO, E = -2.13 eV



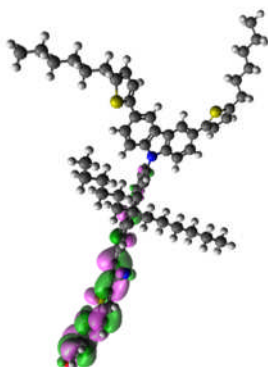
HOMO-1, E = -7.41 eV



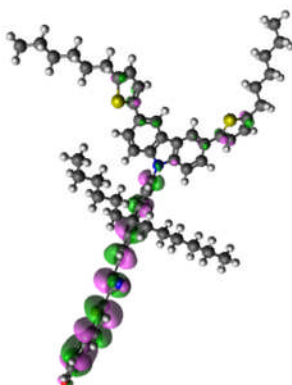
HOMO, E = -7.13 eV



JM164
LUMO, E = -2.14 eV



HOMO-1, E = -7.07 eV



HOMO, E = -6.64 eV

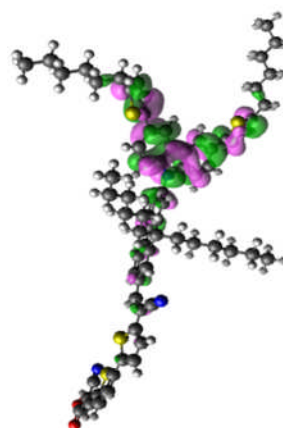


Figure 6.28. LUMO, HOMO-1 and HOMO molecular orbitals of SD4, JM131 and JM164 dyes
(positive = green; negative = purple, isovalue = 0.001)

To quantify the transferred charge (q^{CT}) and the charge transfer distance (d^{CT}) we calculated using the CT model that have been described by Jacquemin et. al. (Jacquemin, et. al., 2012; Ciofini, et. al., 2012; Le Bahers, et. al., 2011). The explanation about the calculation procedure is presented in Appendix J. The calculation results are gathered in Table 6.10, that show the q^{CT} of SD4 and JM131 is not different a lot and JM164 has the highest q^{CT} . This result confirms that the present of alkyl chains attach to fluorine ring in JM131 molecule does not change the charge transfer characteristic, on the contrary the substituent alkyl-thiophene in JM164 improve the q^{CT} from 0.46 e in SD4 to 0.95 e in JM164. Unfortunately, this improvement did not accompany with the d^{CT} improvement, it is shorter a lot in JM164 (5.77 Å) compare to that in SD4 (11.20 Å). The graphical representative of d^{CT} of the dyes is shown in Figure 6.29. It clearly confirms our temporary conclusion mentioned in previous paragraph that state the SD4 has a better charge separation compare to JM164.

Table 6.10 The q^{CT} and d^{CT} of SD4, JM131 and JM164 calculated using CT model

Dye	q^{CT} (e)	d^{CT} (Å)
SD4	0.46	11.20
JM131	0.55	12.10
JM164	0.95	5.77

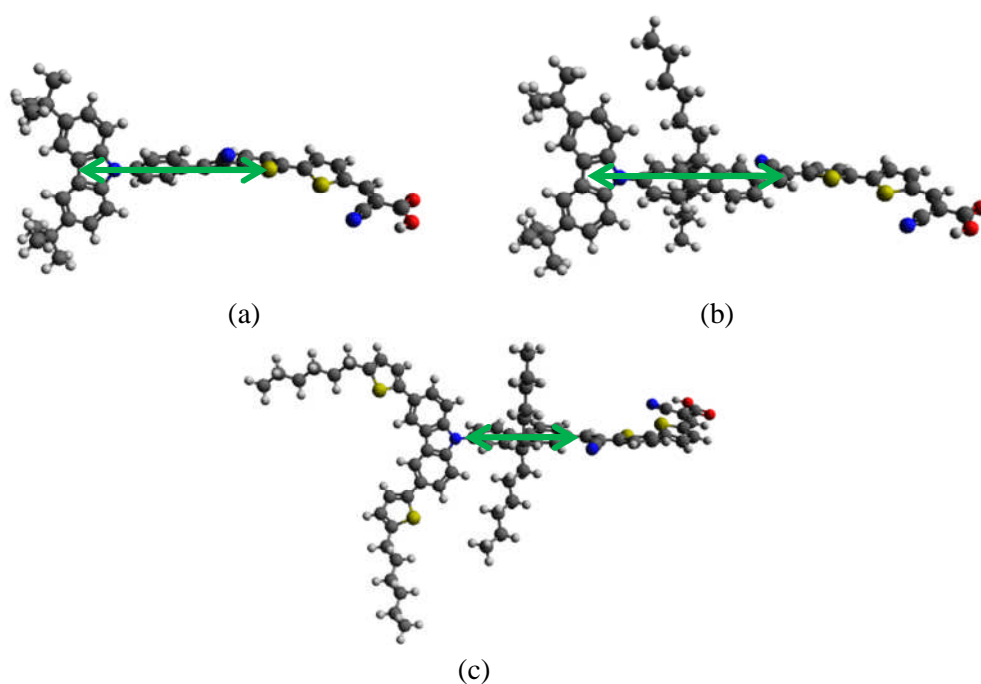


Figure 6.29. Graphical representative of d^{CT} (green arrow) of (a) SD4 (b) JM131 and (c) JM164

The excited state lifetime (radiative lifetime) was computed using the formulae (Le Bahers, et. al., 2009):

$$\tau = \frac{2\pi\epsilon_0 m_e \hbar^2 c^3}{e^4 (E_{\text{fluo}})^2 f} \quad (4.1)$$

where, c is the speed of light, e is the elementary charge, m_e is the electron mass, ϵ_0 is the vacuum permittivity, \hbar is the reduced Planck constant, E_{fluo} is the fluorescence energies and f is oscillator strengths, which represents the transition probability. The E_{fluo} is calculated using Gaussian 09 program package (Frisch et al., 2009). The details of the calculation procedure for determining the E_{fluo} including the calculation results are presented in Appendix J. The results are gathered in Table 6.11

Table 6.11 The calculated excited states lifetime of SD4, JM131 and JM164

Dye	Radiative lifetime (ns)
SD4	2.09
JM131	3.49
JM164	3.20

All the calculated excited-state lifetimes of the dyes are in the order of nanosecond. These results are similar to the calculated excited-state lifetimes of the indoline dyes, 3-5 ns (Le Bahers, et. al., 2009). Excited state lifetime influences the cell performance in relation to the competitive reaction with electron injection from LUMO of dye to the CB of semiconductor. The short electron lifetime accompanied with the slow electron injection will decrease the cell performance due to the excited state decay (Hagfeldt, et. al., 2010; Mishra, et., al., 2009). Since the injection of electron to the oxides are in order of pico second (Hagfeldt, et. al., 2010), thus these results confirm that the excited decay in all observed dyes cannot compete with the injection process.

We observed that the lifetime excited state of JM131 and JM164 are similar and are longer than SD4. We suggest this is due to the alkyl chain of both dyes that make these molecules more flexible. In the presence of solvent, there will be interaction between solvent and the molecule. As a consequence, the more flexible molecule in the excited state need more time to relax due to the solvent effect. This is confirmed by the computed fluorescence in gas phase (Appendix K) of SD4 that has no significant difference between one in the gas phase and one in the present of solvent. On the contrary, the energy fluorescence of JM131 and JM164 in the gas phase is higher than one in the present of solvent.

VI.8 SUMMARY

We have prepared DSSCs using ZnO nanorods prepared by hydrolysis in polyol. ZnO_NR has promising potential to be used as the photoanode in DSSCs. These particles have a high structural quality and provide quite large pores that facilitate much dyes adsorption on their surface. Moreover the IS measurements reveal that ZnO_NR is promising as Electron Transport Layer (ETL). It has higher conductivity and faster electron transport compared to those of anatase TiO₂-layer.

The cell performances using indoline dye (D149) and ruthenium dye (TG6) have been carried out in coupled with redox-couple I₃⁻/I⁻. The cell sensitized with TG6 dye showed better results compared to that of D149. The UV-absorption measurements showed that TG6 more absorb light in a broader wavelength range in the visible region compared to that of D149. Moreover the LUMO orbital of TG6 is localized closer to the anchoring group compare to that of D149. This is a good condition to facilitate a better charge injection from the dye to the semiconductor.

The ZnO_NRs are also promising to be used as photoanode in cobalt-based DSSCs. We have shown that using [Co(Bpy-pz)₂]^{2+/3+} as redox-couple and JM164 as sensitizer, the cell has improvement performance compare to that one using I₃⁻/I⁻ redox couple. The comparison cell performance of ZnO_NR and ZnO_C20 ensures that the large pores in ZnO_NR have an important role in redox-couples transportation. Moreover, the bulky structures of JM164 avoid redox species approaches ZnO this is beneficial to prevent the electron recombination.

References

- Becke, A.D., 1993a. Density-functional thermochemistry. III. The role of exact exchange. *J. Chem. Phys.* 98, 5648–5652. doi:10.1063/1.464913
- Becke, A.D., 1993b. A new mixing of Hartree–Fock and local density-functional theories. *J. Chem. Phys.* 98, 1372–1377. doi:10.1063/1.464304
- Bisquert, J., Mora-Seró, I., 2010. Simulation of Steady-State Characteristics of Dye-Sensitized Solar Cells and the Interpretation of the Diffusion Length. *J. Phys. Chem. Lett.* 1, 450–456. doi:10.1021/jz900297b
- Chai, J.-D., Head-Gordon, M., 2008. Long-range corrected hybrid density functionals with damped atom–atom dispersion corrections. *Phys. Chem. Chem. Phys.* 10, 6615–6620. doi:10.1039/B810189B
- Cossi, M., Barone, V., 2001. Time-dependent density functional theory for molecules in liquid solutions. *J. Chem. Phys.* 115, 4708–4717. doi:10.1063/1.1394921
- Cossi, M., Rega, N., Scalmani, G., Barone, V., 2003. Energies, structures, and electronic properties of molecules in solution with the C-PCM solvation model. *J. Comput. Chem.* 24, 669–681. doi:10.1002/jcc.10189

- Frisch, M.J., Trucks, G.W., Schlegel, H.B., Scuseria, G.E., Robb, M.A., Cheeseman, J.R., Scalmani, G., Barone, V., Mennucci, B., Petersson, G.A., others, 2009. Gaussian 09, Revision A. 1. Wallingford CT: Gaussian, Inc.
- Gao, R., Cui, Y., Liu, X., Wang, L., Cao, G., 2014. A ZnO nanorod/nanoparticle hierarchical structure synthesized through a facile in situ method for dye-sensitized solar cells. *J. Mater. Chem. A* 2, 4765–4770. doi:10.1039/C3TA15276F
- Hamann, T.W., 2012. The end of iodide? Cobalt complex redox shuttles in DSSCs. *Dalton Trans.* 41, 3111. doi:10.1039/c2dt12362b
- Ham, H.W., Kim, Y.S., 2010. Theoretical study of indoline dyes for dye-sensitized solar cells. *Thin Solid Films, Proceedings of the 2nd International Conference on Microelectronics and Plasma Technology – ICMAP 2009* 518, 6558–6563. doi:10.1016/j.tsf.2010.03.048
- Han, J., Fan, F., Xu, C., Lin, S., Wei, M., Duan, X., Wang, Z.L., 2010. ZnO nanotube-based dye-sensitized solar cell and its application in self-powered devices. *Nanotechnology* 21, 405203. doi:10.1088/0957-4484/21/40/405203
- Hay, P.J., Wadt, W.R., 1985. Ab initio effective core potentials for molecular calculations. Potentials for the transition metal atoms Sc to Hg. *J. Chem. Phys.* 82, 270–283. doi:10.1063/1.448799
- Hosni, M., 2014. *Optimisation du Procédé Polyol pour la Synthèse de Nanoparticules d'Oxyde de Zinc : Mise à l'échelle du Procédé et Applications Photovoltaïques*. Doctoral Thesis UNIVERSITE PARIS 13 - Sorbonne Paris Cité-Institut Galilée and UNIVERSITE DE TUNIS EL MANAR-Faculté des Sciences de Tunis. Chapter IV, page 181-234
- Jungsuttiwong, S., Tarsang, R., Sudyoasuk, T., Promarak, V., Khongpracha, P., Namuangruk, S., 2013. Theoretical study on novel double donor-based dyes used in high efficient dye-sensitized solar cells: The application of TDDFT study to the electron injection process. *Org. Electron.* 14, 711–722. doi:10.1016/j.orgel.2012.12.018
- Kim, J.Y., Kim, Y.H., Kim, Y.S., 2011. Indoline dyes with various acceptors for dye-sensitized solar cells. *Curr. Appl. Phys.*, International Conference on Electronic Materials Special Issue: IUMRS-ICEM 2010 International Conference on Electronic Materials 11, S117–S121. doi:10.1016/j.cap.2010.11.098
- Ko, S.H., Lee, D., Kang, H.W., Nam, K.H., Yeo, J.Y., Hong, S.J., Grigoropoulos, C.P., Sung, H.J., 2011. Nanoforest of Hydrothermally Grown Hierarchical ZnO Nanowires for a High Efficiency Dye-Sensitized Solar Cell. *Nano Lett.* 11, 666–671. doi:10.1021/nl1037962
- Krishnan, R., Binkley, J.S., Seeger, R., Pople, J.A., 1980. Self-consistent molecular orbital methods. XX. A basis set for correlated wave functions. *J. Chem. Phys.* 72, 650–654. doi:10.1063/1.438955
- Kumar, G.S., Srinivas, K., Shanigaram, B., Bharath, D., Singh, S.P., Bhanuprakash, K., Rao, V.J., Islam, A., Han, L., 2014. Metal-free organic dyes containing thiadiazole unit for dye-sensitized solar cells: a combined experimental and theoretical study. *RSC Adv.* 4, 13172–13181. doi:10.1039/C3RA47330A
- Lai, Y.-H., Lin, C.-Y., Chen, H.-W., Chen, J.-G., Kung, C.-W., Vittal, R., Ho, K.-C., 2010. Fabrication of a ZnO film with a mosaic structure for a high efficient dye-sensitized solar cell. *J. Mater. Chem.* 20, 9379–9385. doi:10.1039/C0JM01787F
- Le Bahers, T., Pauporté, T., Scalmani, G., Adamo, C., Ciofini, I., 2009. A TD-DFT investigation of ground and excited state properties in indoline dyes used for dye-sensitized solar cells. *Phys. Chem. Chem. Phys.* 11, 11276–11284. doi:10.1039/B914626A
- Lee, C., Yang, W., Parr, R.G., 1988. Development of the Colle-Salvetti correlation-energy formula into a functional of the electron density. *Phys. Rev. B* 37, 785–789. doi:10.1103/PhysRevB.37.785
- Lee, T.-H., Sue, H.-J., Cheng, X., 2011. Solid-state dye-sensitized solar cells based on ZnO nanoparticle and nanorod array hybrid photoanodes. *Nanoscale Res. Lett.* 6, 1–8. doi:10.1186/1556-276X-6-517
- Lu, H., Deng, K., Shi, Z., Liu, Q., Zhu, G., Fan, H., Li, L., 2014. Novel ZnO microflowers on nanorod arrays: local dissolution-driven growth and enhanced light harvesting in dye-sensitized solar cells. *Nanoscale Res. Lett.* 9, 1–8. doi:10.1186/1556-276X-9-183
- Magne, C., Moehl, T., Urien, M., Grätzel, M., Pauporté, T., 2013. Effects of ZnO film growth route and nanostructure on electron transport and recombination in dye-sensitized solar cells. *J. Mater. Chem. A* 1, 2079. doi:10.1039/c2ta00674j
- Martinson, A.B.F., Elam, J.W., Hupp, J.T., Pellin, M.J., 2007. ZnO Nanotube Based Dye-Sensitized Solar Cells. *Nano Lett.* 7, 2183–2187. doi:10.1021/nl070160+

- Matar, F., Ghaddar, T.H., Walley, K., DosSantos, T., Durrant, J.R., O'Regan, B., 2008. A new ruthenium polypyridyl dye, TG6, whose performance in dye-sensitized solar cells is surprisingly close to that of N719, the "dye to beat" for 17 years. *J. Mater. Chem.* 18, 4246–4253. doi:10.1039/B808255C
- McLean, A.D., Chandler, G.S., 1980. Contracted Gaussian basis sets for molecular calculations. I. Second row atoms, Z=11–18. *J. Chem. Phys.* 72, 5639–5648. doi:10.1063/1.438980
- Nakade, S., Makimoto, Y., Kubo, W., Kitamura, T., Wada, Y., Yanagida, S., 2005. Roles of Electrolytes on Charge Recombination in Dye-Sensitized TiO₂ Solar Cells (2): The Case of Solar Cells Using Cobalt Complex Redox Couples. *J. Phys. Chem. B* 109, 3488–3493. doi:10.1021/jp046002d
- Pan, H., Misra, N., Ko, S.H., Grigoropoulos, C.P., Miller, N., Haller, E.E., Dubon, O., 2009. Melt-mediated coalescence of solution-deposited ZnO nanoparticles by excimer laser annealing for thin-film transistor fabrication. *Appl. Phys. A* 94, 111–115. doi:10.1007/s00339-008-4925-0
- Pauporté, T., Magne, C., 2014. Impedance spectroscopy study of N719-sensitized ZnO-based solar cells. *Thin Solid Films*. doi:10.1016/j.tsf.2013.11.121
- Runge, E., Gross, E.K.U., 1984. Density-Functional Theory for Time-Dependent Systems. *Phys. Rev. Lett.* 52, 997–1000. doi:10.1103/PhysRevLett.52.997
- Suh, D.-I., Lee, S.-Y., Kim, T.-H., Chun, J.-M., Suh, E.-K., Yang, O.-B., Lee, S.-K., 2007. The fabrication and characterization of dye-sensitized solar cells with a branched structure of ZnO nanowires. *Chem. Phys. Lett.* 442, 348–353. doi:10.1016/j.cplett.2007.05.093
- Villanueva-Cab, J., Wang, H., Oskam, G., Peter, L.M., 2010. Electron Diffusion and Back Reaction in Dye-Sensitized Solar Cells: The Effect of Nonlinear Recombination Kinetics. *J. Phys. Chem. Lett.* 1, 748–751. doi:10.1021/jz1000243
- Wadt, W.R., Hay, P.J., 1985. Ab initio effective core potentials for molecular calculations. Potentials for main group elements Na to Bi. *J. Chem. Phys.* 82, 284–298. doi:10.1063/1.448800
- Wang, J.X., Wu, C.M.L., Cheung, W.S., Luo, L.B., He, Z.B., Yuan, G.D., Zhang, W.J., Lee, C.S., Lee, S.T., 2010. Synthesis of Hierarchical Porous ZnO Disklike Nanostructures for Improved Photovoltaic Properties of Dye-Sensitized Solar Cells. *J. Phys. Chem. C* 114, 13157–13161. doi:10.1021/jp100637c
- Xi, Y., Wu, W.Z., Fang, H., Hu, C.G., 2012. Integrated ZnO nanotube arrays as efficient dye-sensitized solar cells. *J. Alloys Compd.* 529, 163–168. doi:10.1016/j.jallcom.2012.02.183
- Xu, F., Dai, M., Lu, Y., Sun, L., 2010. Hierarchical ZnO Nanowire–Nanosheet Architectures for High Power Conversion Efficiency in Dye-Sensitized Solar Cells. *J. Phys. Chem. C* 114, 2776–2782. doi:10.1021/jp910363w
- Yanai, T., Tew, D.P., Handy, N.C., 2004. A new hybrid exchange–correlation functional using the Coulomb-attenuating method (CAM-B3LYP). *Chem. Phys. Lett.* 393, 51–57. doi:10.1016/j.cplett.2004.06.011
- Yu, L., Liu, S., Yang, B., Wei, J., Lei, M., Fan, X., 2015. Sn–Ga co-doped ZnO nanobelts fabricated by thermal evaporation and application to ethanol gas sensors. *Mater. Lett.* 141, 79–82. doi:10.1016/j.matlet.2014.11.049
- Zhang, J., Kan, Y.-H., Li, H.-B., Geng, Y., Wu, Y., Su, Z.-M., 2012. How to design proper π -spacer order of the D- π -A dyes for DSSCs? A density functional response. *Dyes Pigments* 95, 313–321. doi:10.1016/j.dyepig.2012.05.02
- Zhang, J., Barboux, P., Pauporté, T., 2014. Electrochemical Design of Nanostructured ZnO Charge Carrier Layers for Efficient Solid-State Perovskite-Sensitized Solar Cells. *Adv. Energy Mater.* 4, 1400932 (1–8). doi: 10.1002/aenm.201400932
- Zhang, Q., Chou, T.P., Russo, B., Jenekhe, S.A., Cao, G., 2008. Aggregation of ZnO Nanocrystallites for High Conversion Efficiency in Dye-Sensitized Solar Cells. *Angew. Chem.* 120, 2436–2440. doi:10.1002/ange.200704919
- Zhang, Q., Dandeneau, C.S., Zhou, X., Cao, G., 2009. ZnO Nanostructures for Dye-Sensitized Solar Cells. *Adv. Mater.* 21, 4087–4108. doi:10.1002/adma.200803827
- Zhang, R., Kumar, S., Zou, S., Kerr, L.L., 2007. High-Density Vertically Aligned ZnO Rods with a Multistage Terrace Structure and Their Improved Solar Cell Efficiency. *Cryst. Growth Des.* 8, 381–383. doi:10.1021/cg700825v
- Zhao, R., Zhu, L., Cai, F., Yang, Z., Gu, X., Huang, J., Cao, L., 2013. ZnO/TiO₂ core–shell nanowire arrays for enhanced dye-sensitized solar cell efficiency. *Appl. Phys. A* 113, 67–73. doi:10.1007/s00339-013-7663-x

Chapter VII

General Conclusions and Suggestions for Future Works

Based on the results that have been obtained, the conclusions of this work are:

1. Three kinds of electron transport layers (ETLs) that composed of nanoparticles: (1) two kinds of TiO₂-brookite nanoparticles, (TiO₂_B1 and TiO₂_B2), (2) composite layers of anatase and graphene (TiO₂_Gr) and (3) nanorods like ZnO nanoparticles (ZnO_NR), have been prepared and show promising potential to be applied as photoelectrode in DSSC. The results in this work point out that ZnO is a promising material to be used as ETL in DSSC application. They have the highest conductivity that leads to the fastest electron transport. Moreover, we have quantified that the ZnO has the deepest trap state. The limited sensitizing time related to its lower stability upon the sensitization by a ruthenium dye could restrict ZnO cell performance. The other disadvantages of ZnO compared to TiO₂ are lie on higher recombination rate, lower dye loading and lower electron injection
2. Brookite based-DSSCs have a higher V_{oc} than that of classical anatase one, because they have higher R_{ct} . The computational results of iodine adsorption on anatase and brookite surface confirm these experimental observations. Unfortunately, the advantage of their performance is limited by their low J_{sc} . The limited capability of brookite to adsorb dye is the primary factor that explains their low J_{sc} . On the other hand, brookite layers are less conducting than anatase ones and it explains the lower charge transport through the photoelectrode. Although the efficiency of brookite based DSSCs ($\eta_{TiO_2_B1} = 5.71\%$, $\eta_{TiO_2_B2} = 5.79\%$) are lower compared to the anatase one ($\eta_{TiO_2_D} = 7.42\%$), but the higher R_{ct} of brookite is the point for brookite that need to develop in the future work.
3. The incorporation of 1.2 wt% graphene into TiO₂ photoelectrode resulted in an increase by 60% in the layer conductivity. This increase induces a faster electron transport in photoelectrode. Moreover, the addition of graphene provokes the improvement of the sensitized-layer light absorbance. Both improvements had an

effect to a J_{sc} enlargement and promising to apply in cobalt-based DSSCs. Finally our TiO₂/graphene cell has about 10% increasing in efficiency compare to the pure TiO₂ one ($\eta_{TiO_2-A} = 6.70\%$, $\eta_{TiO_2-Gr12} = 7.49\%$). TiO₂-Gr12 photoelectrode that was sensitized by the Z907 and was coupled with [Co(phen)₃]^{2+/3+}, showed also better cell performance compared to that one coupled with I₃⁻/I redox couple ($\eta_{TiO_2-A/Co-6} = 4.91\%$, $\eta_{TiO_2-gr12/Co-6} = 5.64\%$). This cell had also a performance comparable to the TiO₂-A (a reference cell that is composed of pure anatase) photoelectrode which was sensitized using the Z907 and was coupled with I₃⁻/I ($\eta_{TiO_2-A/I2-2} = 5.89\%$).

4. The ZnO-NR layer showed the good performance in DSSC. The TG6 sensitized ZnO-NR cells showed a superior performance and reached a PCE of 5.3%. The computational studies have revealed the electronic properties of the utilized sensitizer dye, TG6 and D149. The main differences of their electronic properties that influence DSSC performance are the UV-Vis spectrum of TG6 which is broader than D149 and the location of the LUMO orbital of TG6 which is located closer to the oxide surface compared to D149. We also observed that, the outstanding properties of ZnO-NR lie in their large pore size that facilitates the sensitization by the dye, their attachment to the oxide surface and their high structural properties. Their advantages led us to apply these photoelectrode in cobalt-based DSSC. The cobalt redox-couple species have bulky structures. They need large pores in order to transport through the photoelectrode. Our test, which employed carbazole dyes as the sensitizer, revealed that the ZnO-NR photoelectrode has good performances in cobalt-based redox-couple compared to that of triiodide/iodide. In the similar systems, the efficiency of the cobalt-based DSSCs of ZnO-NR has increased from 1.86% using triiodide/iodide redox-couple to 2.82% using cobalt (II)/(III) one.

The summary of their *I-V* curve characteristic are gathered in Table 7.1

Table 7.1 The summary of I–V curve characteristics of cells investigated in this study

Photoelectrode	Sensitizer	Electrolyte	Photoelectrode thickness (μm)	I-V characteristics			
				V_{oc} (V)	J_{sc} (mA.cm^{-2})	FF (%)	η (%)
TiO ₂ _B1	0.5 mM N719 + 1 eq. TBAH in Acetonitrile/Tert-butanol (50:50)	I ₂ -I	13.4	0.74	9.8	79	5.71
TiO ₂ _B2			13.5	0.72	10.2	79	5.79
TiO ₂ _D (reference of TiO ₂ _B1 and TiO ₂ _B2)			13.4	0.69	14.5	79	7.42
TiO ₂ _Gr12			14.8	0.68	14.4	76.8	7.49
TiO ₂ _A (reference of TiO ₂ _Gr12)			14.1	0.69	13.0	74.8	6.70
TiO ₂ _Gr12	0.5 mM Z907 in Acetonitrile/Tert-butanol	I ₂ -2	10.1	0.66	14.6	73.0	7.06
TiO ₂ _A (reference of TiO ₂ _Gr12)		I ₂ -2	10.3	0.65	12.7	70.9	5.89
TiO ₂ _Gr12		Co-6 Ligand = Phen	9.8	0.72	10.1	77.0	5.64
TiO ₂ _A (reference of TiO ₂ _Gr12)		Co-6 Ligand = Phen	10.4	0.72	8.9	75.0	4.91
ZnO_NR	0.5 mM D149 + 1 mM octanoic acid in Acetonitrile	I ₂ -3	19.4	0.55	12.7	69.3	4.82
ZnO_NR	0.3 mM TG6 in CH ₂ Cl ₂	I ₂ -3	16.6	0.53	15.7	64.2	5.30
ZnO_NR	0.3 mM JM164 + 2 mM CDCA in CH ₂ Cl ₂	I ₂ -2	5.5	0.58	4.95	64.7	1.86
ZnO_NR		Co-6	5.3	0.73	5.42	71.2	2.82

According to the results in this present work, we suggest several works for the future that could be carried out:

1. Combining brookite particles with graphene to improve their cell performances. By incorporating graphene into brookite layers, their conductivity is expected to increase leading to a charge transport improvement. On the other hand, the poor adsorptivity of brookite towards the sensitizer dyes may also be improved by combining with graphene.
2. The improvement of brookite conductivity could also be carried out by doping with other ions/elements, for instance with Nb or Boron.
3. Preparing nanorod-like brookite particles could also be promising to have large pores in nanoparticles in order to improve their dye-sensitization.
4. Improving ZnO-based DSSCs performance, for instance by developing surface passivation technique or by blocking with TiO_2 layer.
5. The further computational researches are also needed in order to support the experimental one, for instance to predict or validate the properties of the brookite/graphene composite and various-ions/elements-doped brookite. The computational study to investigate the electronic properties of organic dye in order to find the best sensitizer dye is still needed.

List of Publications, Seminars and Workshop

Publications:

1. Y. Kusumawati, M. A. Martoprawiro, T. Pauporté. "Effects of Graphene in Graphene/TiO₂ Composite Films Applied to Solar Cell Photoelectrode." *The Journal of Physical Chemistry C* (2014). Vol. 118 (19), p.9974-9981.
2. Y. Kusumawati, M. Hosni, M. A. Martoprawiro, T. Pauporté. "Charge Transport and Recombination in TiO₂ Brookite-based Photoelectrodes." *The Journal of Physical Chemistry. The Journal of Physical Chemistry C. The Journal of Physical Chemistry C* (2014). Vol. 118 (41), p.23459-23467.
3. M. Hosni, Y. Kusumawati, S. Farhat, N. Jouni, T. Pauporté. "Effects of Oxide Nanoparticle Size and Shape on Electronic Structure, Charge Transport, and Recombination in Dye-Sensitized Solar Cell Photoelectrodes." *The Journal of Physical Chemistry C. The Journal of Physical Chemistry C* (2014). Vol. 118 (30), p.16791-16798.
4. M. Hosni, Y. Kusumawati, S. Farhat, N. Jouni, A. L. Ivansyah, M. A. Martoprawiro, T. Pauporté. "Ruthenium Polypyridyl TG6 Dye for the Sensitization of Nanoparticle and Nanocrystalite Spherical Aggregate Photoelectrodes." *ACS Applied Materials and Interfaces* (2015). Vol. 7 (3), p. 1568-1577.
5. Y. Kusumawati, A. L. Ivansyah, B. Prijamboedi, M. A. Martoprawiro, C. L. Radiman, T. Pauporté. "Computational Studies of The Adsorption of I₂ on Anatase (101) and Brookite (210) TiO₂ Surfaces." (In preparation).

Seminars:

1. "Photoactivity increment TiO₂/graphene nanocomposite layer prepared by sol gel technique, oral presentation," symposium G in EMRS (European Material Research Society) Spring Meeting, 26 Mei 2014, Lille, France.
2. "Understanding the role of graphene in TiO₂/graphene nanocomposite photoelectrode in DSSC." Poster session, symposium AA in EMRS (European Material Research Society) Spring Meeting, 26 Mei 2014, Lille, France.

Workshop:

1. Workshop computational chemistry, “Intodcution to Gaussian: Theory and Practice,”
28 July - 1 August 2014. Ulm, Germany.

APPENDIX A: Crystallites Size Determination

Crystallites size has been determined using XRD (X-Ray Diffraction) data and Scherrer formula (Patterson, 1939):

$$d = \frac{K\lambda}{\beta \cos\theta} \quad [\text{A.1}]$$

where,

λ = the wavelength of the incident x-rays

θ = the Bragg angle

K = a numerical constant for which he obtained the value $2(\ln 2/\pi)^{1/2} = 0.93$. It also is defined as a shape factor in which the value may vary from 0.89 – 1.39, depend on the actual shape of the crystallite. In this work we took $K = 0.89$ that represent the shape of our sample, spherical grains.

β = width at half of the maximum of the peak intensity (FWHM). The unit must be in radian

Usually, for more or less spherical crystallites, the size is determined by calculating d for several peaks (at least the three or four peaks) in the XRD pattern then do the average of them.

The example of calculating FWHM is shown in Figure A.1

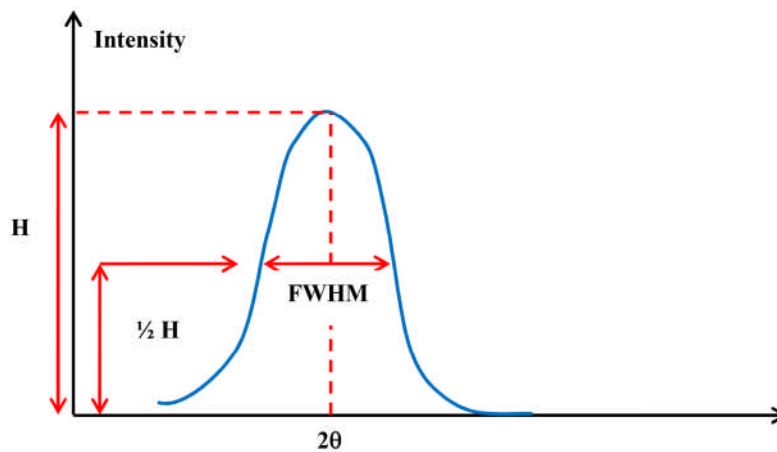


Figure A1. Calculation of FWHM of a XRD peak.

Table A1. Crystallites size in oxide porous film determined from the Scherrer formulae

TiO ₂ _B1 after annealing							
Peaks	2θ	height	FWHM (deg)	cos θ	FWHM(rad)	d (nm)	\bar{d} (nm)
210	25.2303	379.25	0.4368	0.97585905	0.0076236	18.43	18.32
211	30.7721	197.92	0.4992	0.96416003	0.00871268	16.32	
321	48.0387	90.38	0.5616	0.91340804	0.00980177	15.31	
421	55.1348	124.58	0.5112	0.88646704	0.00892212	17.34	
TiO ₂ _B2 after annealing							
Peaks	2θ	height	FWHM (deg)	cos θ	FWHM(rad)	d (nm)	\bar{d} (nm)
210	25.4165	234	0.4992	0.97550288	0.00871268	16.13	Asymmetric particle (see TEM characterizations , page 73)
211	30.8031	120.32	0.4992	0.96408822	0.00871268	16.32	
321	47.9712	102.29	0.4234	0.91364765	0.00738972	20.31	
421	55.178	91.46	0.336	0.88629251	0.00586431	26.38	
TiO ₂ _D after annealing							
Peaks	2θ	height	FWHM (deg)	cos θ	FWHM(rad)	d (nm)	\bar{d} (nm)
101	25.4065	573.29	0.3669	0.97552207	0.00640361	21.95	20.06
200	48.1896	160.4	0.4368	0.91287123	0.0076236	19.70	
105	54.086	99.51	0.4234	0.89066556	0.00738972	20.83	
211	55.2797	86.21	0.4992	0.88588114	0.00871268	17.76	
TiO ₂ _A after annealing							
Peaks	2θ	height	FWHM (deg)	cos θ	FWHM(rad)	d (nm)	\bar{d} (nm)
105	25.317	638.29	0.4556	0.97569353	0.00795172	17.67	19.62
200	47.8263	220.95	0.3744	0.9461269	0.00653451	22.18	
105	53.9899	190.19	0.4997	0.91416095	0.00872141	17.20	
211	55.0499	186.29	0.4672	0.89104654	0.00815418	18.87	
TiO ₂ _Gr12 after annealing							
Peaks	2θ	height	FWHM (deg)	cos θ	FWHM(rad)	d (nm)	\bar{d} (nm)
105	25.3847	678.37	0.3332	0.97559532	0.00581544	24.17	19..9
200	47.8808	229.28	0.4368	0.94598666	0.0076236	19.01	
105	53.9381	214.27	0.4992	0.91334125	0.00871268	17.23	
211	55.0512	139.57	0.5616	0.89102118	0.00980177	15.70	

Reference:

Patterson, A.L., 1939. The Scherrer Formula for X-Ray Particle Size Determination. Phys. Rev. 56, 978–982.

APPENDIX B: Porosity Determination using Direct Method

Porosity has been determined using a direct method. The basic principle of this method calculates this parameter from the layer volume determined by profilometry and the bulk material volume determined by weighting. Procedure: Round-shape of TiO₂ layer is deposited on square glass sheet. The weight of the oxide layer is determined by subtracting glass weight from total weight (oxide layer on glass). From here, we calculate the oxide layer volume using the theoretical density of the oxide with the assumption that the oxide layer is dense. This thickness is noted d_f. The actual thickness of the porous oxide layer (d_t) is measured by profilometry.

Porosity (P) is formulated:

$$p = \frac{d_t - d_f}{d_t} \quad \text{B.1}$$

To have good result, the measurement is done at least three times.

Example:

Table B.1. Porosity determination of TiO₂_D

Sample	m _{glass} (gr)	m _{total} =mf (gr)	m _{oxide} (gr)	d = g/cm ³	volume (cm ³)	diamater (cm)	dense_thickness =df (μm)	actual_thicknes =dt				p	p (average)
								1st	2nd	3rd	mean		
TiO ₂ _D_1	0.25	0.2509	0.0009	3.9	0.000230769	0.8	0.000367133	10.8	10.9	12	0.00112333	0.67	0.65
TiO ₂ _D_2	0.2386	0.2397	0.0011	3.9	0.000282051	0.8	0.000448718	12.8	13.5	12.2	0.00128333	0.65	
TiO ₂ _D_3	0.246	0.2473	0.0013	3.9	0.000333333	0.8	0.000530303	14.9	15	14.9	0.00149333	0.64	

APPENDIX C: Optical Band-gap Calculation

The total transmission and total reflection spectra of the semiconductor layers are measured with the Cary 5000 spectrophotometer equipped with an integrating sphere. The total transmission spectrum (T) is measured using the bare transparent substrate as the baseline. The total reflection (R) is measured placing the sample in a mask, with nothing behind the sample (S position).

By using these two measures, it is possible to get the absorptance (noted A) of the sample:

$$A (\%) = 100 - T (\%) - R(\%) \quad \text{C.1}$$

The energy (expressed in eV) is related to the wavelength, λ (nm), according to:

$$\lambda \text{ (nm)} = \frac{1240}{E \text{ (eV)}} \quad \text{C.2}$$

A semiconductor absorbs light if the wavelength is shorter than a limit value related to the bandgap energy of the semiconductor, E_g : [1]:

$$\lambda \text{ (nm)} < \frac{1240}{E_g \text{ (eV)}} \quad \text{C.3}$$

The light extinction coefficient follows the exponential law:

$$I = I_0 \exp(-\alpha d) \quad \text{C.4}$$

Where d is the thickness of the layer and α is the absorption coefficient.

Then :

$$\ln \frac{I_0}{I} = \alpha d \quad \text{C.4}$$

Where, T the transmittance and R the reflectance.

We have the **absorbance** :

$$a = \log_{10} \left(\frac{100}{R(\%) + T(\%)} \right) \propto \alpha \quad \text{C.5}$$

Near the **absorption edge**, α and then a increases with the photon energy according to:

$$ah\nu = const(h\nu - E_g)^n$$

C.6

With *const* a constant.

For a direct bandgap (ZnO, Rutile TiO₂, Brookite TiO₂) :n=0.5

For an indirect bandgap (Anatase TiO₂): n=2.

Therefore, to get the direct bandgap value, one has to draw : $(ah\nu)^2 = f(h\nu)$, extrapolate the curve to the X-axis and read the bandgap.

To get indirect bandgap value, one has to draw : $(ah\nu)^{1/2} = f(h\nu)$, extrapolate the curve to the X-axis and read the bandgap.

For films with very low reflection, one can draw : $(-\ln(T)*h\nu)^{1/n}$ versus $h\nu$.

Several examples of the band gap calculations are showed in Figure C.1, C.2 and C.3

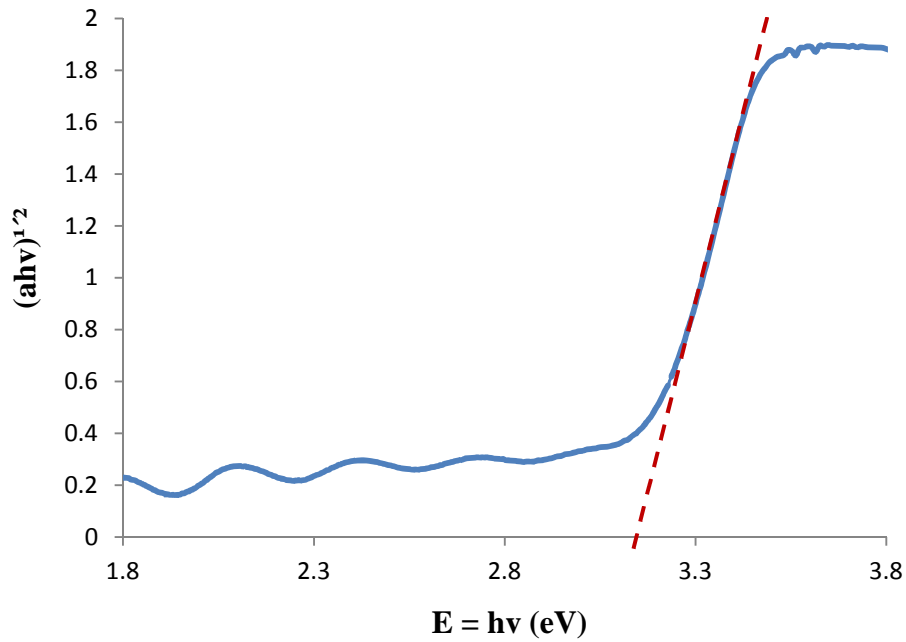


Figure C.1 Bandgap calculation of the TiO₂_A layer

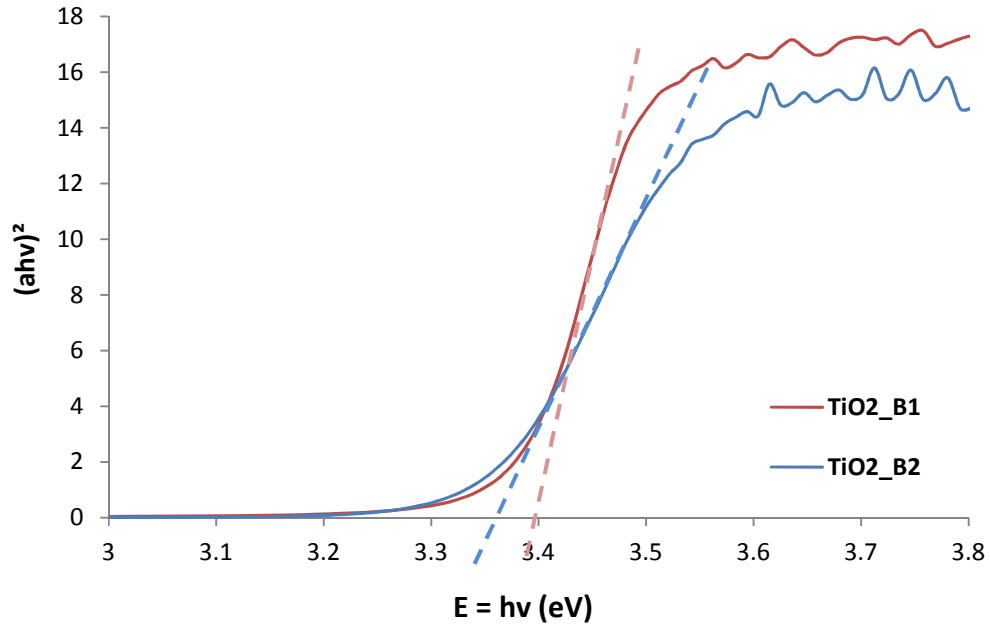


Figure C.2 Bandgap calculation of the TiO₂_B1 nad TiO₂_B2 layer

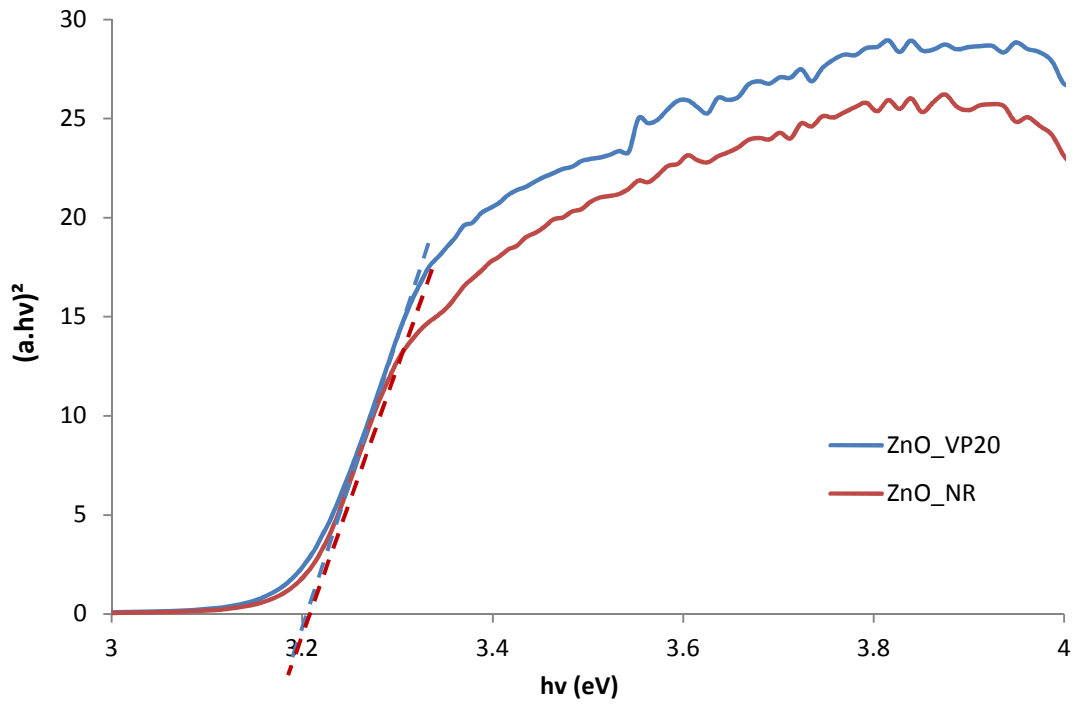


Figure C.3 Bandgap calculation of the ZnO_VP20 and ZnO_NR

The results of band gap calculation of semiconductor layers investigated in the thesis are summarized in Table C.1

Table C.1 Band gap calculation summary

No	Semiconductor	Direct (D)/Indirect (I) bandgap	Bandgap (eV)	Chapter
1	TiO ₂ _D	I	3.25	IV
2	TiO ₂ _B1	D	3.40	IV
3	TiO ₂ _B2	D	3.35	IV
4	TiO ₂ _A	I	3.20	V
5	TiO ₂ _Gr12	I	3.20	V
6	ZnO_C20	D	3.20	VI
7	ZnO_NR	D	3.24	VI

Reference

Hagfeldt, A., Graetzel, M., 1995. Light-Induced Redox Reactions in Nanocrystalline Systems. Chem. Rev. 95, 49–68.

APPENDIX D: Dye Loading Calculation

The dye loading is reported as the density of the dye (nmol/cm²) or as the dye concentration (mM) in the photoelectrode layer. It was determined by doing desorption of sensitized layer in a known volume of a solution. This solution depended on the dye. For N719 we used 0.1 M potassium hydroxide (KOH) (Magne et al., 2012), for D149 we use *Dimethylformamide* (DMF) (Magne et al., 2013), whereas for Z907 we used 10 mM tetrabutyl ammonium hydroxide (TBAOH) in ethanol (Jang et al., 2009). The concentration of the dye in solution then was calculated by measuring the solution absorbance and using the Beer-Lambert law. Then the amount of dye in the layer was determined. Finally, with the film surface, the dye density was calculated whereas the layer volume permitted the calculation of the dye concentration in the layer.

Example: Determination of N719 dye loading N719 in TiO₂_B1 layer

Experimental explanation: The round-shape TiO₂ layer with a diameter of 0.8 cm and a thickness about 5-10 μm was sensitized in the N-719 dye for 24 hours. After that, it was desensitized in 4 mL KOH 1M until the layer became white with all dye dissolved for about 2 hours. The absorbance of the solution was measured using a Varian CARY 5000 Spectrophotometer. Beforehand, the molar extinction coefficient of this dye in KOH 1M was determined using standard solutions of known concentrations (APPENDIX E).

Experimental data

A_{\max} = Absorbance at maximum wavelength = 0.1115

l = cuve width = 1 cm

ϵ = molar extinction coefficient = 13734 mol⁻¹.L.cm⁻¹

Layer thickness (d) = 7.27 μm

Calculation:

In the certain wavelength: $A = \epsilon \cdot C \cdot l$

$$\begin{aligned}\text{We obtain } C &= \frac{A}{\epsilon \cdot l} \\ &= \frac{0.1115}{13734} \\ &= 8.1181 \times 10^{-6} \text{ mol.L}^{-1}\end{aligned}$$

The volume of solution is = 4 mL = 4 x 10⁻³ L,

The amount of the dye is $= 8.1181 \times 10^{-6} \text{ mol.L}^{-1} \times 4 \times 10^{-3} \text{ L}$

$$= 3.247 \times 10^{-8} \text{ mol}$$

$$= 32.47 \text{ nmol}$$

The layer diameter = 0.8 cm (round-shape), so the layer area $= \frac{1}{4} (3.14) \times (0.8)^2 \text{ cm}^2 = 0.5024 \text{ cm}^2$

The layer thickness = 7.27 μm

The layer volume $= 3.65 \times 10^{-4} \text{ cm}^3$

So, the density of the dye in the layer $= 32.47 \text{ nmol} / 0.5024$

$$= 65 \text{ nmol/cm}^2$$

The concentration of the dye $= (32.47/3.65) \times 10^3$

$$= \mathbf{88.9 \text{ mM}}$$

Table D.1 summarizes the dye concentration measured for the layers investigated in this thesis. For each sample, it has been done three measurements. Table D.1 displays the average value.

Table D.1 Dye loading calculation summary

No	Layer	Dye/concentration/ Solvent	Sensitizing time (h)	Dye concentration (mM)	Discussed in Chapter/ section
1	TiO ₂ _B1	N719/0.5mM/ACN+TbuOH	24	80	IV/ IV.3
2	TiO ₂ _B2	N719/0.5mM/ACN+TbuOH	24	86	IV/IV.3
3	TiO ₂ _D	N719/0.5mM/ACN+TbuOH	24	122	IV/IV.3
4	TiO ₂ _D	N719/0.5mM/ACN+TbuOH	4	85.5	IV/IV.3
5	TiO ₂ _A	N719/0.5mM/ACN+TbuOH	24	95	V/V.2 and V.3
6	TiO ₂ _Gr12	N719/0.5mM/ACN+TbuOH	24	111	V/V.2 and V.3
6	TiO ₂ _A	Z907/0.3mM/ACN+TbuOH	24	81.2	V/V.5
7	TiO ₂ _Gr12	Z907/0.3mM/ACN+TbuOH	24	111.7	V/V.5

References:

- Jang, S.-R., Yum, J.-H., Klein, C., Kim, K.-J., Wagner, P., Officer, D., Grätzel, M., Nazeeruddin, M.K., 2009. High Molar Extinction Coefficient Ruthenium Sensitizers for Thin Film Dye-Sensitized Solar Cells. *J. Phys. Chem. C* 113, 1998–2003. doi:10.1021/jp8077562
- Magne, C., Dufour, F., Labat, F., Lancel, G., Durupthy, O., Cassaignon, S., Pauporté, T., 2012. Effects of TiO₂ nanoparticle polymorphism on dye-sensitized solar cell photovoltaic properties. *J. Photochem. Photobiol. Chem.* 232, 22–31. doi:10.1016/j.jphotochem.2012.01.015
- Magne, C., Moehl, T., Urien, M., Grätzel, M., Pauporté, T., 2013. Effects of ZnO film growth route and nanostructure on electron transport and recombination in dye-sensitized solar cells. *J. Mater. Chem. A* 1, 2079–2088. doi:10.1039/C2TA00674J

APPENDIX E: Molar Extinction Coefficient Calculation

Molar extinction coefficient is determined using Beer-Lambert Law:

$$A = \varepsilon \cdot C \cdot l \quad \text{E.1}$$

With,

A = Absorbance at wavelength peak maximum

ε = Molar extinction coefficient

C = Concentration of the solution

l = optical path length, in this case cuvette path length

Procedure:

Three solutions of dye with different concentrations were prepared. The absorbance spectra of each solution was measured using the Varian Cary 5000 Spectrophotometer. From this result we can plot the molar extinction coefficient spectra. Then we can determine the ε_{\max} (molar extinction coefficient at maximum wavelength). The obtained ε_{\max} of each measurement then was averaged.

The ε spectra of the dyes investigated in the thesis are shown in Figure E.1 to E.4 for dyes Z907; SD4; JM131; and JM164, respectively. Table E.1 gather the average value of ε_{\max} of these dyes.

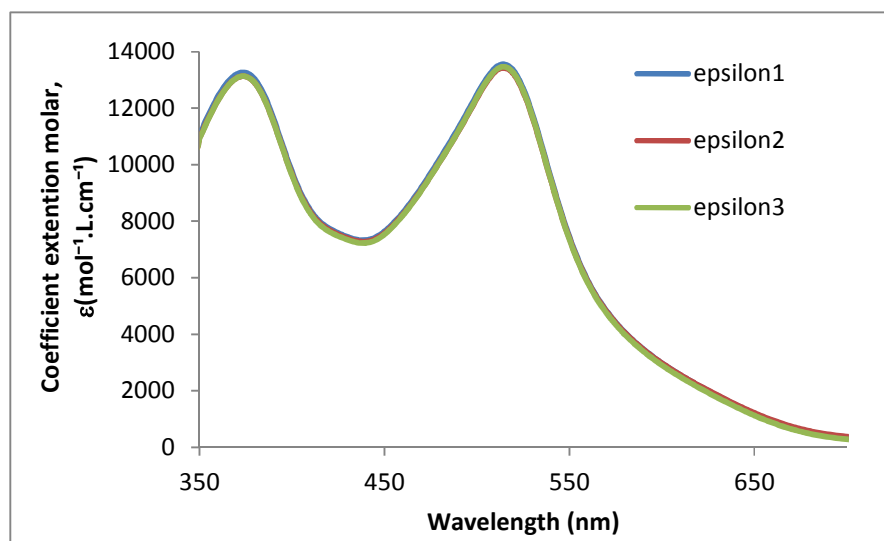


Figure E.1 ε spectra of Z907 dye dissolved in 10 mM TBAOH in ethanol

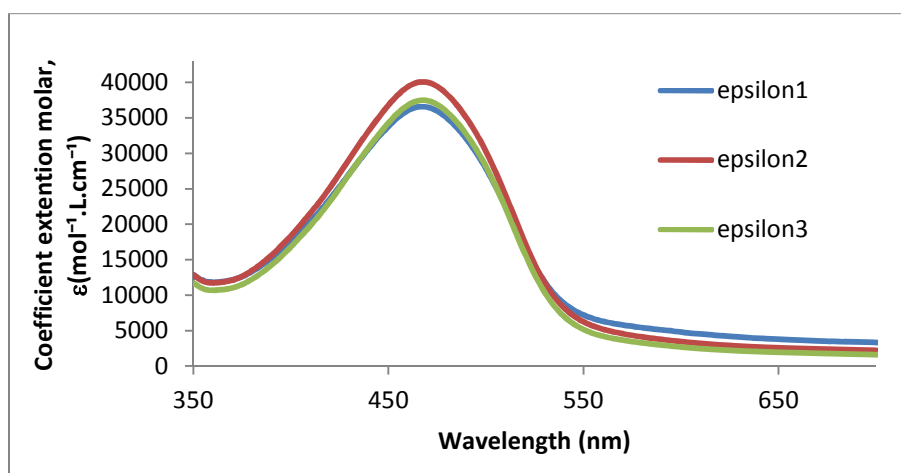


Figure E.2 ϵ spectra of SD4 dye dissolved in CH_2Cl_2

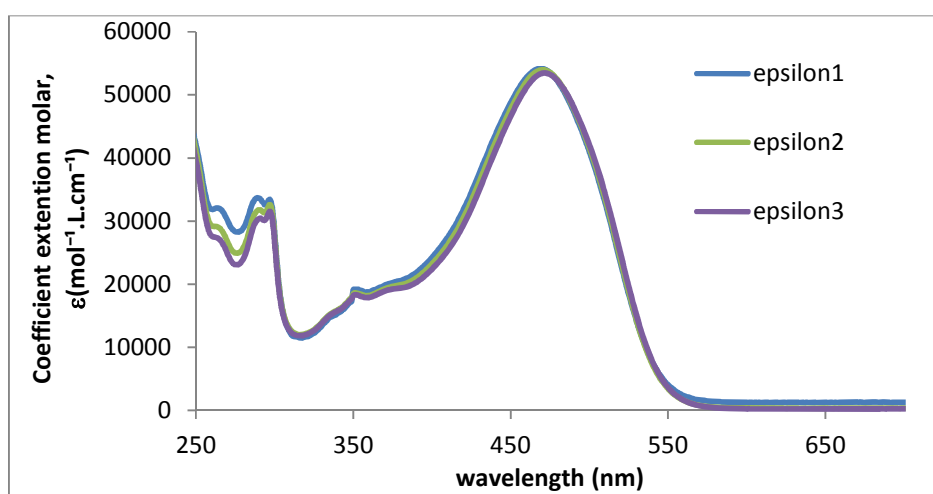


Figure E.3 ϵ spectra of JM131 dye in CH_2Cl_2

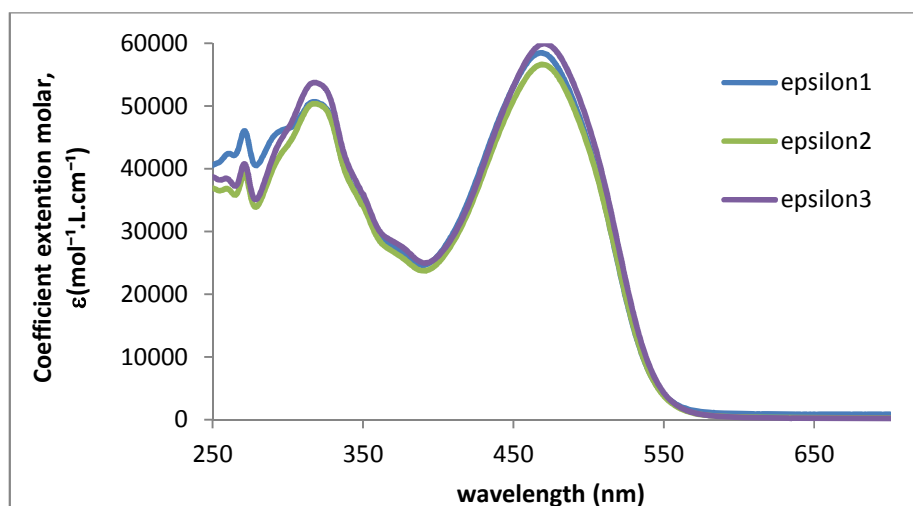


Figure E.4 ϵ spectra of JM164 dye in CH_2Cl_2

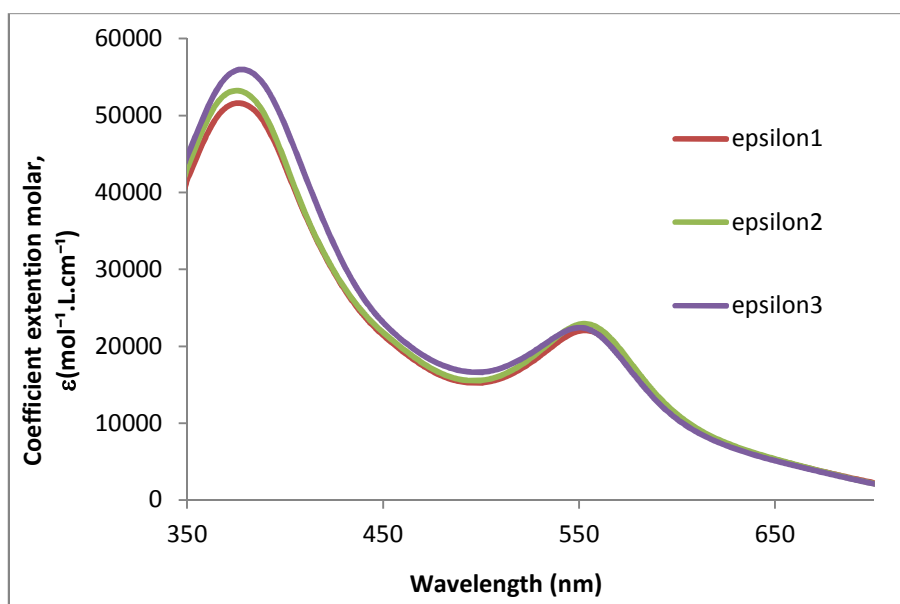


Figure E.5 ϵ spectra of TG6 dye in CH_2Cl_2

Table E.1 ϵ of various dyes in this thesis

No	Dye	ϵ ($\text{mol}^{-1}.\text{L}.\text{cm}^{-1}$)	Solvent	Obtained from
1	N719	13734	0.1 M KOH	(Magne, 2012)
2	D149	72353	DMF	(Magne, 2012)
3	Z907	13389	10 mM TBAOH in ethanol	This study
4	SD4	38048	CH_2Cl_2	This study
5	JM131	54136	CH_2Cl_2	This study
6	JM164	58332	CH_2Cl_2	This study
7	TG6	2245 (at 550 nm)	CH_2Cl_2	This study

Reference

Magne, C. 2012. Optimisation de Couches oxyde Nano-structures pour Applications aux Cellules Solaires à Colorant. Doctoral Thesis. Universite Pierre et Marie Curie, September 30th, 2012. p. 217.

APPENDIX F: Photocatalytic Properties of TiO₂_Gr layer

TiO₂_Gr layer have been tested for the photocatalytic degradation of 4-chlorophenol used as a model compound of an eco-persistent pollutant. The formation of intermediate degradation products, namely hydroquinone and benzoquinone, has been followed. The results show the high photocatalytic activity of the layers and a beneficial effect of graphene for an optimum concentration of 1.2 wt. %.

Experimental explanation

Layer Preparation

The layer was prepared using the same paste as used for preparing the TiO₂_A and TiO₂_Gr (Chapter III, section III. 2. 1. 1). The mass-percentage variation of single graphene oxide (SGO) that was added to the composite is also the same: 0%, 0.6%, 1.2% and 3%. The related prepared porous layers are named after their SGO mass-percentage mentioned as TGr0, TGr6, TGr12 and TGr30.

Microscope soda lime glass slides were used as substrates. They were cleaned with soap and rinsed with distilled water. They were subsequently treated in an ultrasonic bath in acetone and in ethanol for 5 min each. A layer of TiO₂ or TiO₂/SGO paste was coated on the substrates by the doctor blading technique, relaxed and dried at 125°C for 5 min. The step was repeated several times in order to achieve the accurate film thickness. The films were then annealed at 500°C for 15 min (Magne, et. al., 2012; Magne, et. al., 2013)

Layer characterization

The layers characterization as well as their results have been presented in the Chapter V, section V.2

Photocatalytic Test

4-chlorophenol (4-CP) in water with an initial concentration of 0.1 mmol.L⁻¹ was photocatalytically degraded in a quartz cell containing 25 mL of solution. The solution temperature in the vessel was kept at 25°C and no solution bubbling was used. The top of the liquid in the photoreactor was open to air and the solution was stirred by a magnetic stirrer, consequently, the concentration of dissolved oxygen was kept constant during the

experiment owing to its equilibration with oxygen in the ambient air. A Sylvania Lynx-S 11 W BLB lamp irradiated the film surface with UV light (365 nm) at a low power density of 1 mW.cm⁻². The irradiated area of the films was 4.0 cm². For each experiment, eight small aliquots were taken from the solution in the reaction vessel at regular time intervals and analyzed by HPLC (Rathouský, et. al., 2011).

Result and Discussions

All the investigated layers were highly efficient in the photodegradation of 4-chlorophenol and after 5 hours its concentration in solution was almost negligible. The degradation followed a first order kinetics as reported before for pure TiO₂ films (Rathouský, et. al., 2011). The rate constant of degradation as a function of the SGO content is presented in an inset of Figure F.1. A volcano shaped curve is obtained and the maximum was found for the TiO₂_Gr12 sample with 9.31x10⁻² min⁻¹. The rate was improved by 20% compared to pure TiO₂. Adding a larger amount of graphene did not improve the photocatalytic performances, which can be due to the UV light absorption by graphene that becomes detrimental at higher concentration. The addition of too much graphene shields the irradiation light and decreases the photocatalytic activity (Zhang, et. al., 2011; Perera, S. D. et. al., 2012).

Under UV-illumination, electron/hole pairs are generated in the TiO₂ conduction (cb) and valence bands (vb), respectively. Highly reactive oxidizing species such as holes (h⁺), hydroxide radicals (OH[•]), and superoxides (O₂⁻, O₂H) are then produced on TiO₂ surface by the following reactions:



In the case of the TiO₂/graphene composite films, due the work function of graphene (-4.4-4.5 eV) localized below the conduction band of TiO₂ (-4.2 eV), charge transfer may occur between TiO₂ and graphene, followed by oxidizing species production:





The degradation rate for TiO₂_Gr12 is significantly improved compared to TiO₂_A. It is larger than the increase in the specific surface area and overcomes the light shielding by graphene. It suggests that charge separation occurs here and is beneficial for the photocatalytic process.

The degradation reaction of 4-CP is a complex process involving many intermediates species (Theurich, J. et. al., 1996; Li, X. et. al., 1999). In the Figure F.2, the first degradation steps are summarized. There are at least three potential major pathways of degradation: (i) via hydroquinone (HQ)/benzoquinone (ii) via 4-chlorocatechol (4-CC), and (iii) via a chlorinated opened ring intermediates (Rathouský, et. al., 2011; Li, X. et. al., 1999). To understand the mechanism of 4-chlorophenol photocatalytic-degradation, the cyclic intermediates were identified by HPLC titration. 4-CC was not detected. On the other hand, the concentrations of both HQ and BQ have been followed as a function of irradiation time as shown in Figure F.3 and F.4. For all the samples, the HQ concentration was much higher than that of BQ (Figure F.3 and F.4). The profile of HQ concentration shows the same trend for all the examined layers (Figure F.3). It reaches the maximum after about 150 minutes and disappears after more than 300 minutes. On the other hand, the BQ concentration shows different profiles (Figure F.4). For the 1.2 weight % SGO composite, BQ appears faster and is more concentrated. Therefore, graphene, at the optimized concentration, facilitates the formation of BQ.

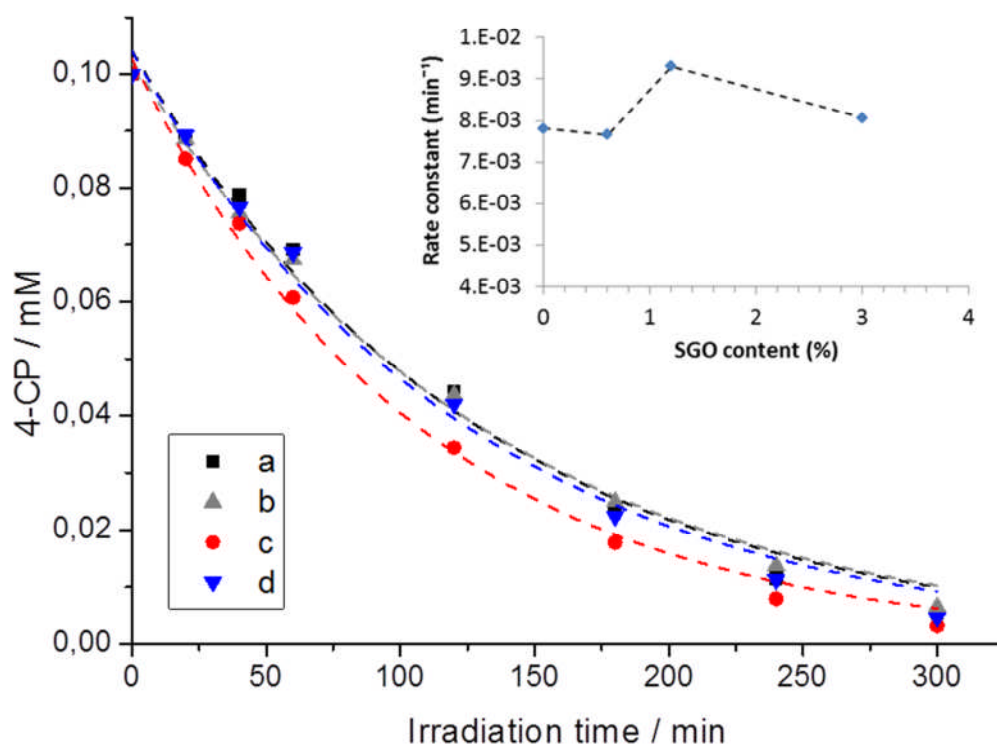


Figure F.1. Effect of SGO content on the photocatalytic degradation of 4-CP.(a) TiO₂_A, (b) TiO₂_Gr06, (c) TiO₂_Gr12 and (d) TiO₂_Gr30. The dashed lines are the fits for a first order kinetic degradation. The inset shows the constant rates as a function of the SGO content.

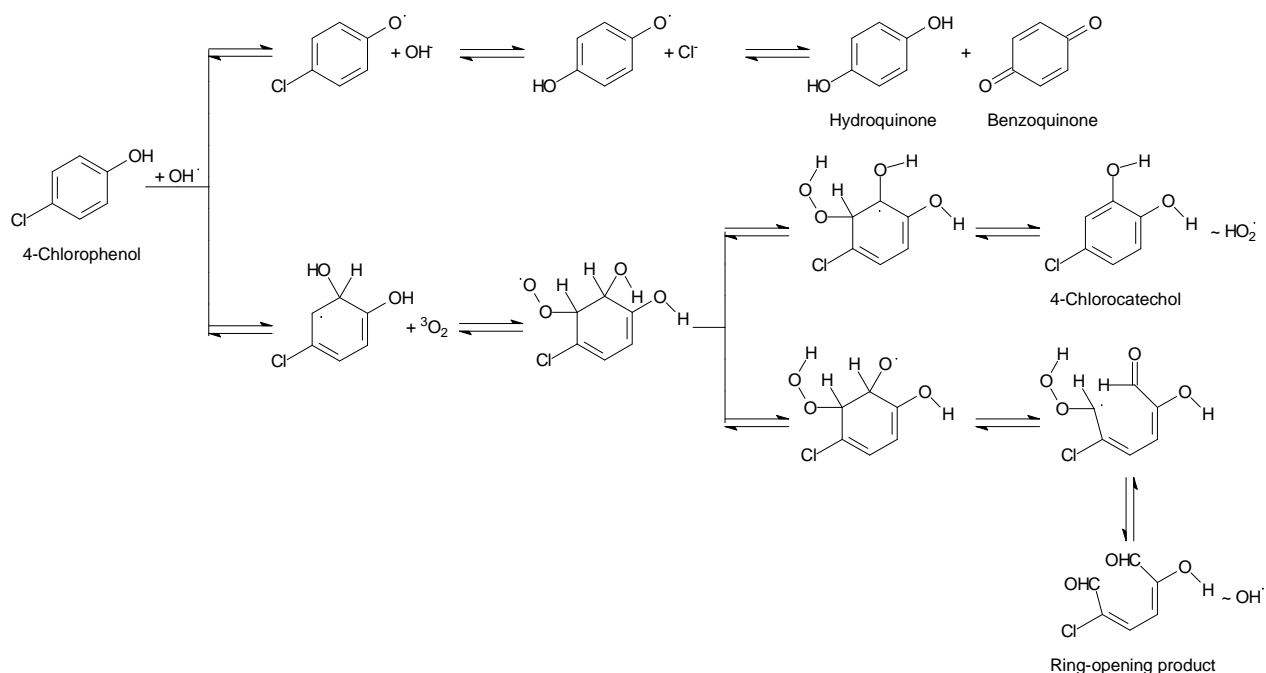


Figure F.2 Scheme of first steps of the 4-chlorophenol photocatalytic degradation pathways.

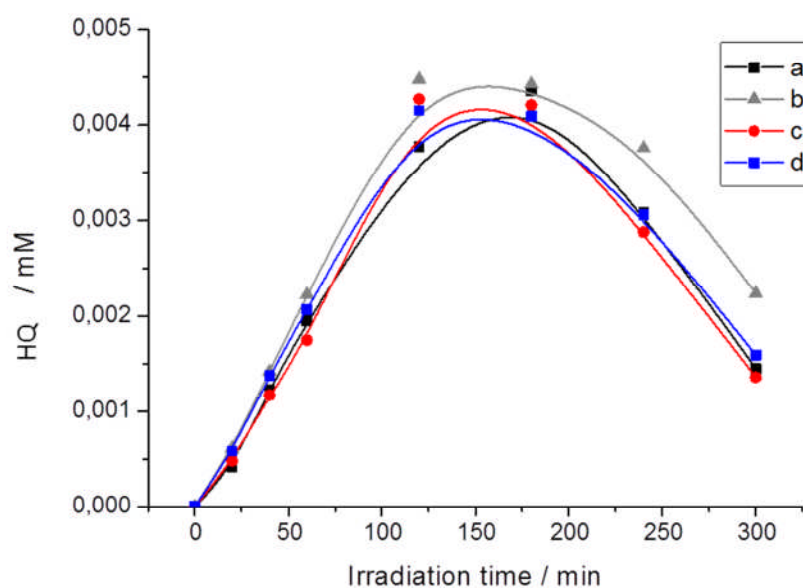


Figure F.3._Concentration profiles of hydroquinone intermediate species during the photocatalytic degradation of 4-chlorophenol. (a) TiO₂_A, (b) TiO₂_Gr06, (c) TiO₂_Gr12 and (d) TiO₂_Gr30

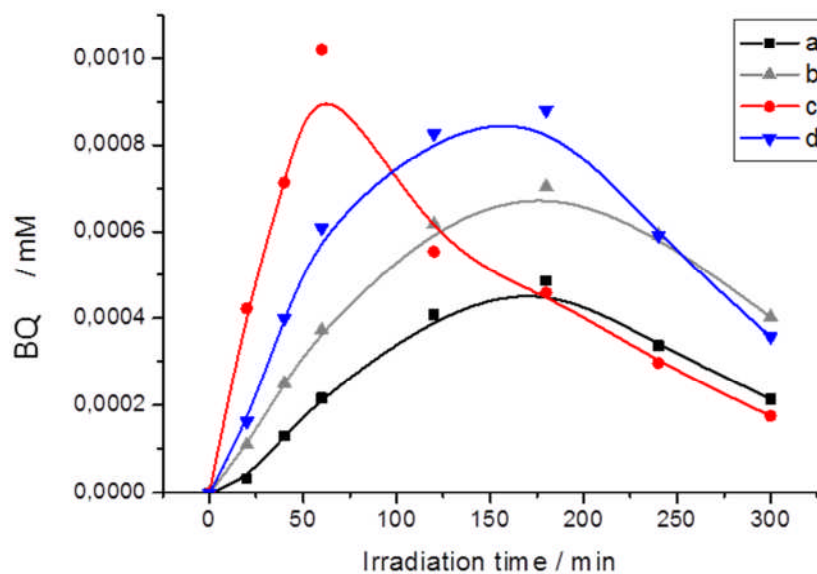


Figure F.4._Concentration profiles of benzoquinone intermediate species during the photocatalytic degradation of 4-chlorophenol. (a) TiO₂_A, (b) TiO₂_Gr06, (c) TiO₂_Gr12 and (d) TiO₂_Gr30

References

- Magne, C., Dufour, F., Labat, F., Lancel, G., Durupthy, O., Cassaignon, S., Pauporté, T., 2012. Effects of TiO₂ nanoparticle polymorphism on dye-sensitized solar cell photovoltaic properties. *J. Photochem. Photobiol. Chem.* 232, 22–31. doi:10.1016/j.jphotochem.2012.01.015
- Magne, C., Moehl, T., Urien, M., Grätzel, M., Pauporté, T., 2013. Effects of ZnO film growth route and nanostructure on electron transport and recombination in dye-sensitized solar cells. *J. Mater. Chem. A* 1, 2079–2088. doi:10.1039/C2TA00674J
- Rathouský, J., Kalousek, V., Kolář, M., Jirkovský, J. Mesoporous films of TiO₂ as efficient photocatalysts for the purification of water. *Photochem. Photobiol. Sci.* 10 (2011) 419–424
- Theurich, J., Lindner, M., Bahnemann, D. W. Photocatalytic Degradation of 4-Chlorophenol in Aerated Aqueous Titanium Dioxide Suspensions: A Kinetic and Mechanistic Study. *Langmuir.* 12 (1996) 6368–6376.
- Perera, S. D., Mariano, R. G., Vu, K., Nour, N., Seitz, O., Chabal, Y., Balkus, Jr., K. J. Hydrothermal Synthesis of Graphene-TiO₂ Nanotube Composites with Enhanced Photocatalytic Activity. *ACS Catal.* 2 (2012) 949–956
- Li, X., Cubbage, J. W., Tetzlaff, T. A., Jenks, W. S. Photocatalytic Degradation of 4-Chlorophenol. 1. The Hydroquinone Pathway. *J. Org. Chem.* 64 (1999) 8509–8524.
- Zhang, Y., Tang, Z-R., Fu, X., Xu, Y-J.. Engineering the Unique 2D Mat of Graphene to Achieve Graphene-TiO₂ Nanocomposite for Photocatalytic Selective Transformation: What Advantage does Graphene Have over Its Forebear Carbon Nanotube? *ACS Nano.* 5 (2011) 7426–7435.

APPENDIX G: Preparation of Cobalt Complexes

Stoichiometrically, for 1 g of $[\text{Co}(\text{bpy})_3](\text{PF}_6)_2$, 0.57 gram of $\text{CoCl}_2 \cdot 6\text{H}_2\text{O}$ is needed to be reacted with minimum 0.29 g of bpy ligand. Whereas for 1 g of $[\text{Co}(\text{phen})_3](\text{PF}_6)_2$, 0.61 g of $\text{CoCl}_2 \cdot 6\text{H}_2\text{O}$ is needed to be reacted with minimum 0.27 g of phen ligand. They were put in Erlenmeyer and diluted with minimal amount of ethanol (~ 10 mL) to obtain ethanolic solution of ligand and ethanolic solution of cobalt (II) chloride hexahydrate.

$[\text{Co}(\text{bpy})_3](\text{PF}_6)_2$ and $[\text{Co}(\text{phen})_3](\text{PF}_6)_2$ were synthesized by adding drop-by-drop an molar excess ethanolic solution of ligand to an ethanolic solution of cobalt (II) chloride hexahydrate under heating (70 °C) and vigorous stirring. The initially blue solution became red. Heating and stirring were maintained during 1 h before cooling of the mixture at room temperature. The complex was then precipitated by addition of saturated aqueous solution of NH_4PF_6 . Theoretically, the minimal amount of NH_4PF_6 that should be added is 0.40 g for $[\text{Co}(\text{bpy})_3](\text{PF}_6)_2$ and 0.37 g for $[\text{Co}(\text{phen})_3](\text{PF}_6)_2$. Small orange crystals appeared after saturated aqueous solution of NH_4PF_6 was added. They were then filtered and washed with diethyl ether (Koussi-Daoud, et. al., 2014). The synthesized product was identified by ^1H -NMR spectra measurement. Figure G.1 and G.2 show the ^1H -NMR Spectra of both cobalt complexes.

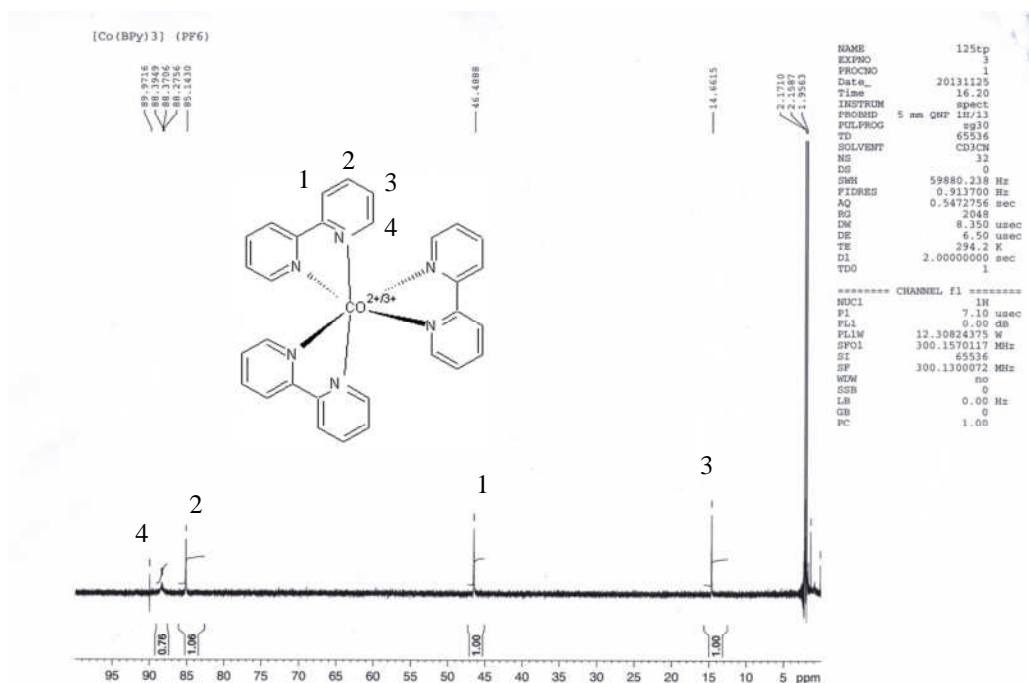


Figure G.1 ^1H -NMR Spectra of $[\text{Co}(\text{bpy})_3]^{2+}$

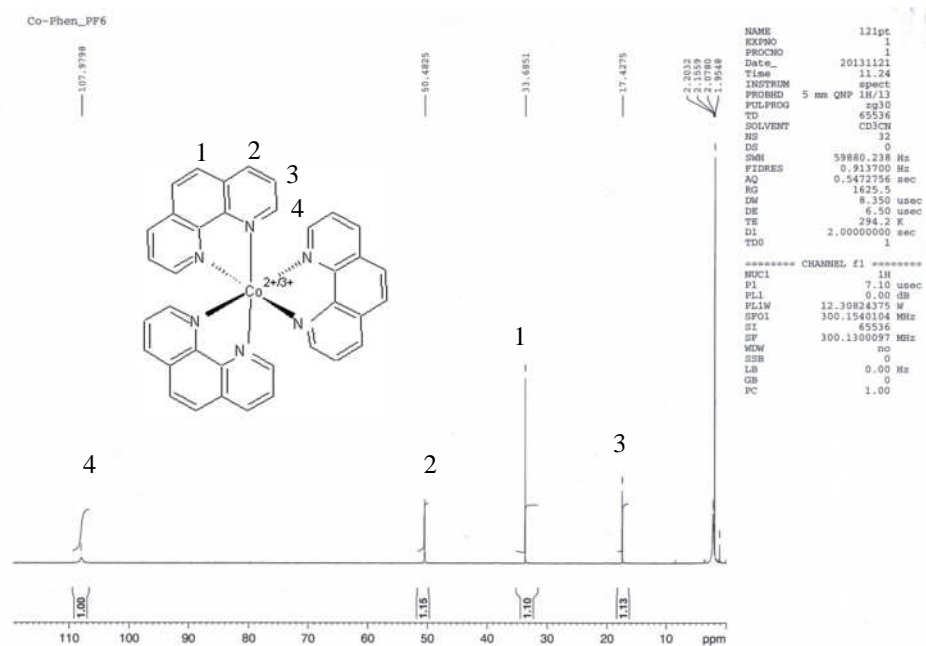


Figure G.2 ^1H -NMR Spectra of $[\text{Co}(\text{phen})_3]^{2+}$

Reference

Koussi-Daoud, S., Schaming, D., Martin, P. & Lacroix, J.-C. Gold nanoparticles and poly(3,4-ethylenedioxythiophene) (PEDOT) hybrid films as counter-electrodes for enhanced efficiency in dye-sensitized solar cells. *Electrochimica Acta* 125, 601–605 (2014).

APPENDIX H: Input File Gaussian Explanation

Example of TG6 dye

#P GFINPUT IOP(6/7=3) B3LYP/GEN → Route section, code for calculation
Pseudo=Read opt test FormCheck (see explanation for each code on the next
SCRF=(CPCM,Read,Solvent=Dichloromethane) page)

TG6_CPCM_1_CH2Cl2

→ Title

-1 1

Ru -1.73724 -3.79701 -0.59156

C 8.35120 -0.00840 0.36601

C 9.39378 -0.90956 0.62976

.....

H C O N S 0

6-311G*

Ru 0

LanL2DZ

Ru 0

LanL2DZ

→ Left = total charge = -1; total multiplicity = 1

→ Molecule coordinate, can be written in Cartesian coordinate or Z-Matrix

→ Basis set of atoms. In this case, we use different basis set for H C O N S and Ru

stoichiometry=CH2Cl2

solventname=dichloromethane

eps=8.93

→ Solvent description. It is added because in root section we use code SCRF

Explanation about route section code:

#P GFINPUT IOP(6/7=3)

Code to create output that can be visualized with some visualization softwares

B3LYP

Level theory that is used in molecule calculation

/GEN Pseudo=Read

It is instructed to read basis set in the section after molecule specification. It is added if there is the different basis set for atoms.

Opt test

The code to instruct optimization calculation

FormCheck

The code to create fchk file. This file is important to visualize orbital molecule using Avogadro

SCRF=(CPCM,Read,Solvent=Dichloromethane)

The code to include solvent effect in calculation

To do another calculation, the code **Opt test** is needed to be replaced. For example, to do TDDFT calculation it is replaced by **TD(Nstates=X)**. In this case, **Nstates** gives the number of each type of states for which to solve. The higher X, the higher calculation cost.

APPENDIX I: Input File CP2K Explanation

&GLOBAL

PROJECT_NAME model

RUN_TYPE GEO_OPT

&END GLOBAL

The section to define the name and type of calculation. For the type of calculation it could be for instance geometry optimization or energy

&FORCE_EVAL

METHOD Quickstep

&DFT

BASIS_SET_FILE_NAME /opt/cp2k-2.6.0/data/
BASIS_MOLOPT

POTENTIAL_FILE_NAME/opt/cp2k-2.6.0/data/ **POTENTIAL**

&MGRID

CUTOFF 400

NGRIDS 4

&END MGRID

&QS

EPS_DEFAULT 1.0E-10

METHOD GPW

EXTRAPOLATION PS

EXTRAPOLATION_ORDER 3

&END QS

&SCF

SCF_GUESS ATOMIC

EPS_SCF 1.0E-5

MAX_SCF 50

&OUTER_SCF

EPS_SCF 1.0E-5

MAX_SCF 20

&END OUTER_SCF

&OT

MINIMIZER DIIS

PRECONDITIONER FULL_SINGLE_INVERSE

&END OT

&END SCF

&XC

&XC_FUNCTIONAL PBE

&END XC_FUNCTIONAL

&END XC

The section to define the calculation methods and the details about it.

<pre> &POISSON PERIODIC XYZ POISSON_SOLVER PERIODIC &END POISSON </pre>		
<pre> &END DFT </pre>		
<pre> &SUBSYS &CELL ABC 20.478518 7.570 26.881174 PERIODIC XYZ ALPHA_BETA_GAMMA 90.000 90.000 90.000 &END CELL </pre>		<p>The section to define the cell parameter</p>
<pre> &COORD @INCLUDE 'model.coord' &END COORD </pre>		<p>The section to define the atom coordinate in system</p>
<pre> &KIND O BASIS_SET DZVP-MOLOPT-GTH POTENTIAL GTH-PBE-q6 &END KIND &KIND Ti BASIS_SET DZVP-MOLOPT-SR-GTH POTENTIAL GTH-PBE-q12 &END KIND &KIND I BASIS_SET DZVP-MOLOPT-SR-GTH POTENTIAL GTH-PBE-q7 &END KIND &END SUBSYS &END FORCE_EVAL </pre>		<p>The section to define the type of atoms in system and their basis set</p>
<pre> &MOTION &GEO_OPT MAX_ITER 100000 OPTIMIZER BFGS &END GEO_OPT &END MOTION </pre>		<p>This section is added for geometry optimisation, to define the geometry optimisation iterations</p>

APPENDIX J: The Computational Procedure to Quantify Charge Transfer

The procedure to quantify charge transfer (CT) of electron from the ground state to the excited one, is adapted from the procedure that has been implemented by Jacquemin, et. al. (Jacquemin, et. al., 2012). This procedure uses a Partially Atomic Charge (PAC) model to approach the localized electron density.

The first step is we need to define the atomic position of the molecule that has an electron transition. For each atom (i) which has Cartesian position $\mathbf{r}_i = (x_i, y_i, z_i)$, the different of excited PAC and ground states one (δq_i):

$$\delta q_i = q_i^{ES} - q_i^{GS} \quad (\text{I.1})$$

Then the atoms are divided into two categories based on the increase/decrease of their PAC, the first category is q^+ , which is defined:

$$q_i^+ = \begin{cases} \delta q_i & \text{if } \delta q_i > 0 \\ 0 & \text{if } \delta q_i < 0 \end{cases} \quad (\text{I.2})$$

the second one, q^- , is defined:

$$q_i^- = \begin{cases} \delta q_i & \text{if } \delta q_i < 0 \\ 0 & \text{if } \delta q_i > 0 \end{cases} \quad (\text{I.3})$$

the amount of charge transferred (q^{CT}) become:

$$q^{CT} = \sum_i q_i^+ = - \sum_i q_i^- \quad (\text{I.4})$$

The two coordinates as the starting and ending position of the charge transfer can be defined by calculating the barycenters corresponding to the q_i^+ and q_i^- functions:

$$\mathbf{r}^+ = (x^+, y^+, z^+) = \frac{\sum_i \mathbf{r}_i q_i^+}{q^{CT}} \quad (\text{I.5})$$

$$\mathbf{r}^- = (x^-, y^-, z^-) = \frac{\sum_i \mathbf{r}_i q_i^-}{q^{CT}} \quad (\text{I.6})$$

The charge separation then can be defined as the distance of these two points,

$$d^{CT} = |\mathbf{r}^+ - \mathbf{r}^-| \quad (\text{I.7})$$

Reference:

Jacquemin, D., Le Bahers., Adamo, C., Ciofini, I., 2012. What is the “best” atomic charge model to describe through-space charge-transfer excitations?. Phys. Chem. Chem. Phys. 14, 5383–5388. doi:10.1039/C2CP40261K

APPENDIX K: Calculation of Fluorescence Energy

The fluorescence energy has been calculated using the procedure that is written in the Gaussian manual using TD-DFT technique and the PCM corrections. Briefly, to determine the fluorescence energy with consider the solvent effect, it need to do 7 steps of calculation.

Step 1: Ground state geometry optimization and frequencies (equilibrium solvation). This is a standard optimization calculation on the ground state including PCM equilibrium solvation. Whereas the frequency calculation is carried out to verify that the optimized geometry is located in local minima

Step 2: Vertical excitation with linear response solvation. This is a TD-DFT calculation of the vertical excitation, therefore at the ground state equilibrium geometry, with the default solvation: linear response, non-equilibrium. We perform a single-point TD-DFT calculation, which defaults to non-equilibrium solvation. The results of this job will be used to identify which state or states are of interest and their ordering. These results give a reasonable description of the solvation of the excited state, but not quite as good as that from a state-specific solvation calculation. In this case, we see that the $n \rightarrow \pi^*$ state is the first excited state. Next, we will use the state-specific method to produce a better description of the vertical excitation step.

Step 3: State-specific solvation of the vertical excitation.

This step calculate the energy of first excited state—at the ground state optimized geometry—from the non-equilibrium solvation state-specific calculation. Subtracting this energy from the ground state energy (from step 1) gives the ground state to first excited state absorption including the state-specific solvation correction.

Step 4: Relaxation of the excited state geometry. Next, we perform a TD-DFT geometry optimization, with equilibrium, linear response solvation, in order to find the minimum energy point on the excited state potential energy surface. Since this is a TD-DFT optimization, the program defaults to equilibrium solvation. As is typical of such cases, the molecule has a plane of symmetry in the ground state but the symmetry is broken in the excited state, so the ground state geometry is perturbed slightly to break symmetry at the start of the optimization.

Step 5: Vibrational frequencies of the excited state structure. It is a frequency calculation to verify that the geometry located in step 4 is a minimum. The results could also be used as part of

Step 6: Emission state-specific solvation (part 1).

This step does state-specific equilibrium solvation of the excited state at its equilibrium geometry, writing out the solvation data for the next step.

The output of this calculation is the energy of first excited state—at its optimized geometry—from the equilibrium solvation state-specific calculation.

Step 7: Emission to final ground state (part 2). Finally, we compute the ground state energy with non-equilibrium solvation, at the excited state geometry and with the static solvation from the excited state.

Here is the energy of ground state from a non-equilibrium solvation calculation in solution, using the first excited state optimized geometry and the solvent reaction field in equilibrium with the first excited state density):

The difference between the energies from steps 6 and 7 gives the vertical emission energy. In this case, the first excited state to ground state emission, including the state-specific solvation correction, is at 396.63 nm.

Steps 1, 2, and 4 would be sufficient to compute the excitation and emission energies in the gas-phase (along with step 5 to confirm the nature of stationary point). They are not sufficient when solvent effects are included because the energies computed in step 4 correspond to the ground state solvent reaction field, while the emission takes place in the reaction field created in response to the excited state charge distribution. This is what is accounted for properly in steps 6 and 7.

The calculation results are gathered in Table J.1

Table J.1 The computed absorbance and fluorescence maxima of SD4, JM131 and JM164

Dyes	Computed absorbance maxima (λ in nm)	Computed fluorescence maxima (λ in nm), in gas phase	Computed fluorescence maxima (λ in nm), in the present of solvent, CH ₂ Cl ₂
SD4	420	460	462
JM131	436	455	579
JM164	437	463	561

References:

- Cossi, M., Barone, V., 2001. Time-dependent density functional theory for molecules in liquid solutions. J. Chem. Phys. 115, 4708–4717. doi:10.1063/1.1394921
- Cossi, M., Rega, N., Scalmani, G., Barone, V., 2003. Energies, structures, and electronic properties of molecules in solution with the C-PCM solvation model. J. Comput. Chem. 24, 669–681. doi:10.1002/jcc.10189
- http://www.gaussian.com/g_tech/g_ur/k_scrf.htm